

**Nematic and Ferronematic Liquid Crystal
Droplets: Effects of Bulk Potentials and
Biaxiality on Canonical Defect Structures**

PhD Thesis

Sophie Elizabeth McLauchlan

Department of Mathematics and Statistics

University of Strathclyde, Glasgow

February 7, 2025

This thesis is the result of the author's original research. It has been composed by the author and has not been previously submitted for examination which has led to the award of a degree.

Chapter 3 contains material published in an article, reference [1]. The material contained therein are a result of the author's original research in collaboration with the article's co-authors, Yucen Han, Matthias Langer, and Apala Majumdar.

The copyright of this thesis belongs to the author under the terms of the United Kingdom Copyright Acts as qualified by University of Strathclyde Regulation 3.50. Due acknowledgement must always be made of the use of any material contained in, or derived from, this thesis.

Signed: Sophie Elizabeth McLauchlan

Date: 07/02/2025

Acknowledgements

Firstly, I would like to thank my supervisor, Apala Majumdar, for her invaluable support and encouragement, and her insightful guidance throughout the last four years. Her expertise and mentorship have been invaluable in shaping this thesis, and I am very grateful for her patience and belief in my work. I would also like to thank Yucen Han for her help and for being so generous with her time as I learned how to implement some of the numerical methods crucial to the success of this research. In addition, I gratefully acknowledge financial support from the EPSRC.

I have had the good fortune of being surrounded by friends over the course of my studies. Special thanks go to Alice and Craig. Thank you both for the adventures we have had, and thank you for your friendship. And to my 'Best Ones' (you know who you are) thank you for the laughs and your good chat.

Next, I would like to thank my family. In particular, I would like to thank my exceptional grandparents, Terry and Isabel, for encouraging me to work hard and always try my best. We all just want to make you proud. To my siblings, Anna and Finlay, and my step-dad, Jonathan, thank you for the fun we all have together.

Finally, my greatest thanks go to my Mum. Thank you for the endless and unwavering support you have provided throughout my whole life. Thank you for your advice, encouragement, sacrifice, and now friendship. None of this would have been possible without you. My success is your success.

Abstract

In this thesis, we study equilibrium configurations in spherical droplets of nematic and ferronematic liquid crystals with strong radial anchoring. In the nematic case, we work with the commonly used fourth-order bulk potential and the more complicated sixth-order bulk potential, which predicts a bulk biaxial phase at sufficiently low temperatures, while the fourth-order bulk potential does not. In the ferronematic case, we work with a ferronematic free energy which contains a Landau–de Gennes contribution for the liquid crystal configuration; terms to account for the spontaneous magnetisation; and a nemato-magnetic coupling term. We prove a collection of analytical results regarding properties of the radial hedgehog solution in both the nematic and ferronematic cases. We use a range of numerical methods to compute critical points of the Landau–de Gennes and ferronematic free energies. We study the stability of the radial hedgehog solution as a function of temperature and droplet radius and compute bifurcation diagrams at fixed temperatures and droplet radii. We place particular emphasis on the effects of the sixth-order bulk potential on the stability of equilibrium configurations in the nematic case; and on the effects of the nemato-magnetic coupling strength in the ferronematic case. We show that the sixth-order bulk potential has a destabilising effect on the nematic radial hedgehog solution; while stronger nemato-magnetic coupling has a stabilising effect on the ferronematic radial hedgehog solution. Moreover, we demonstrate that the solution landscape is richer in ferronematic systems

in comparison to the pure nematic systems. In the final chapter, we introduce random noise into each system, which can account for factors such as material imperfections or uncertainties in experimental set-up, and we investigate the impact of noise on the properties of the nematic and ferronematic radial hedgehog solutions.

Contents

1	Introduction and Literature Review	1
1.1	What are Liquid Crystals?	1
1.1.1	Nematic Liquid Crystals	4
1.1.2	Cholesteric Liquid Crystals	5
1.1.3	Smectic Liquid Crystals	6
1.1.4	Applications of Liquid Crystals	7
1.2	Modelling Nematic Liquid Crystals	13
1.2.1	The Director and the Scalar Order Parameter	14
1.2.2	Continuum Theories	16
1.2.3	Defects	19
1.3	The Landau–de Gennes Theory	21
1.3.1	The \mathbf{Q} -tensor Order Parameter	22
1.3.2	The Landau–de Gennes Free Energy	24
1.3.3	Uniaxiality versus Biaxiality	27
1.4	Thesis Overview	28
1.5	Literature Review	30
1.5.1	The Sixth-Order Bulk Potential	30
1.5.2	The Radial Hedgehog Solution	36

Contents

1.5.3	Equilibrium Configurations on the Sphere	39
1.5.4	Ferronematics	42
1.5.5	Stochastic Effects on Deterministic Landau–de Gennes Solutions	47
2	Preliminary Material	50
2.1	Solutions of the Landau–de Gennes Free Energy	50
2.2	Nondimensionalisation	57
2.2.1	The Landau–de Gennes Free Energy with Sixth-Order Bulk Po- tential	57
2.2.2	The Ferronematic Free Energy	59
2.3	Numerical Methods	60
2.3.1	Symmetry and Boundary Conditions	61
2.3.2	Critical Points of the Landau–de Gennes Free Energy	64
2.3.3	The Morse Index of the Radial Hedgehog Solution	66
2.3.4	The Radial Hedgehog Solution as an Index-1 Transition State . .	67
2.3.5	Bifurcation Diagrams and the HiOSD Method	70
3	The Sixth-Order Bulk Potential	73
3.1	Problem Formulation	73
3.2	The Sixth-Order Bulk Potential	76
3.2.1	Uniaxial Critical Points of the Sixth-Order Bulk Potential	77
3.2.2	Biaxial Critical Points of the Sixth-Order Bulk Potential	79
3.3	Analysis of the Radial Hedgehog Solution	83
3.4	Numerical Results	99
3.4.1	Critical Points of the Landau–de Gennes Free Energy	99
3.4.2	The Morse Index of the Radial Hedgehog Solution	105

Contents

3.4.3	The Radial Hedgehog Solution as an Index-1 Transition State . .	107
3.4.4	Bifurcation Diagrams	109
3.5	Summary	112
4	Critical Points of the Ferronematic Bulk Potential	116
4.1	Uniaxial Critical Points of the Ferronematic Bulk Potential	118
4.1.1	Problem Formulation	118
4.1.2	Results	120
4.1.3	Approximations to the Uniaxial Ferronematic Critical Points . .	131
4.2	Biaxial Critical Points	135
4.2.1	Problem Formulation	137
4.2.2	Critical Points as a Function of Temperature	138
4.2.3	Critical Points as a Function of Nematic-Magnetic Coupling . . .	143
4.2.4	Summary	146
5	The Ferronematic Radial Hedgehog Solution	150
5.1	Problem Formulation	151
5.2	Analysis of the Radial Hedgehog Solution	154
5.2.1	Analytical Results	154
5.2.2	Series Expansion for the Radial Hedgehog Solution	171
5.3	Numerical Results	185
5.3.1	Critical Points of the Ferronematic Free Energy	185
5.3.2	The Morse Index of the Radial Hedgehog Solution	196
5.3.3	The Radial Hedgehog Solution as an Index-1 Transition State . .	198
5.3.4	Bifurcation Diagrams	200
5.4	Summary	207

Contents

6	Stochastic Effects on Deterministic Solutions	211
6.1	Problem Formulation	213
6.2	Numerical Methods	216
6.2.1	Deterministic Solutions	216
6.2.2	Stochastic Solutions	223
6.3	Numerical Results	227
6.3.1	The Nematic Radial Hedgehog Solution	227
6.3.2	The Ferronematic Radial Hedgehog Solution	238
6.4	Summary	252
7	Conclusions and Future Work	254

Chapter 1

Introduction and Literature

Review

1.1 What are Liquid Crystals?

Liquid crystals are classical examples of mesogenic materials which exhibit physical properties that are intermediate between isotropic liquid and solid crystalline states [2]. A solid crystalline state is characterised by a highly ordered, repeating molecular structure in all three spatial dimensions, such that molecules are fixed positionally and orientationally. Solid crystals are typically difficult to deform; cannot flow and can be anisotropic. In contrast, the molecules in an isotropic liquid lack any kind of ordering such that the molecules are free to move and the material will spread out across a surface or conform to the shape of its container. Liquid crystals fall somewhere between these states: the molecules can flow, but the material retains some degree of positional or orientational ordering in at least one dimension [2]. In the context of liquid crystals, positional ordering means the molecules are organised in some kind of regular, repeating pattern, similar to a solid crystal; and orientational ordering means

the molecules are arranged in some average direction throughout the material, but do not necessarily follow any repeating pattern as they would in a solid crystal.

A key driver of the partial ordering in liquid crystalline materials is the shape of the constituent molecules. The molecules are typically strongly anisotropic, with the usual examples being rod-, disc-, or board-shaped molecules [3]–[5]. The anisotropic shape of the molecules forces directionally-dependent molecular interactions and directionally-dependent material responses to external stimuli such as electric and magnetic fields. In particular, the birefringence of liquid crystals leads to striking optical signatures through polarised optical microscopes, and we discuss this property in more detail in Section 1.1.4. We present examples in Figure 1.1, in which the different colours arise due to the varying orientation of liquid crystal molecules throughout the sample. The directionally-dependent behaviour of liquid crystals together with their fluidity makes these materials ideal for a wide range of applications in science and technology [6].

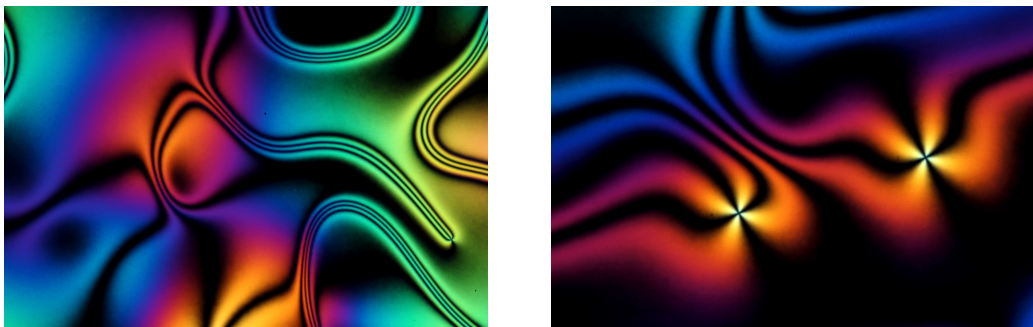


Figure 1.1: Thin films of nematic liquid crystals through a polarising microscope. *Credit: Oleg Lavrentovich, Liquid Crystal Institute, Kent State University, via www.nsf.gov/news/mmg/index.jsp?series_name=image000151.*

The first reported observation of a liquid crystal phase is credited to Austrian botanist and chemist Friederich Reinitzer from experiments carried out in 1888 [3], [7]. Reinitzer was heating a substance called cholesteryl benzoate, which is a solid at room temperature, and was anticipating a phase transition to a clear liquid at some

sufficiently high temperature. However, the solid first melted into a cloudy liquid phase at 145.5°C, and subsequently changed into the anticipated clear fluid at 178.5°C, and these two transitions were observed to be fully reversible. The cloudy liquid, which we now know to be a cholesteric liquid crystal, exhibited unexpected properties, including birefringence, for which material anisotropy is required. Anisotropy was, until then, thought to be a feature of certain solids, only. The second phase transition, where the cloudy liquid crystal became the isotropic liquid, is now referred to as the clearing point for a liquid crystal. Reinitzer shared his findings with the German physicist Otto Lehmann, who coined the term ‘liquid crystal’ in 1900, following a further study of cholesteryl benzoate and similar materials also possessing two transition temperatures [8]. Lehmann is also credited with the first polarised optical microscopy experiments [9], [10]. The German chemist Daniel Vorländer drove progress further, proving that the rigid linear structure of liquid crystal molecules is responsible for their unique characteristics in 1907 [8].

The liquid crystals first observed by Reinitzer are examples of *thermotropic* liquid crystals, which undergo phase transitions due to changes in temperature. Other examples include *N*-(4-Methoxybenzylidene)-4-butylaniline (MBBA) [2] and 4-Cyano-4'-pentylbiphenyl (5CB) [11]. The constituent molecules of thermotropic liquid crystals are generally small, with molecules of MBBA and 5CB being no more than a few nanometres in length. Liquid crystal phases can also be obtained through phase transitions driven by molecular concentration in solvents rather than temperature, and such materials are known as *lyotropic* liquid crystals. Lyotropic liquid crystals comprise much larger molecules compared to thermotropic liquid crystals, in general. For example, the molecules making the material commercially known as Kevlar can be on the order of several nanometres up to micrometres. These molecules form a lyotropic

liquid crystalline phase in sulphuric acid, allowing the material to be spun in to fibres [12]. We will consider only thermotropic liquid crystals in this thesis.

The majority of liquid crystals are in fact more sophisticated than described above, displaying more nuanced behaviour than the two transitions from solid to liquid crystal and liquid crystal to isotropic fluid (and vice-versa). Many liquid crystals can be described as mesogenic, displaying a wider range of intermediate phases, or a higher degree of phase-polymorphism, in the transition from solid to isotropic liquid. The French mineralogist and crystallographer Georges Friedel classified such intermediate phases into three categories in 1922 [13]: the *nematic*, *cholesteric* and *smectic* phases.

1.1.1 Nematic Liquid Crystals

The nematic phase is the simplest liquid crystalline phase. The constituent molecules have long-range orientational order, aligning themselves according to locally preferred directions, but lack any kind of positional order, meaning they can translate freely in space [14]. Typical nematic liquid crystal molecules are elongated, rod-shaped molecules, classed as *calamitic* molecules. Both MBBA and 5CB are examples of calamitic molecules. Nematic liquid crystal molecules can also be disc-shaped, or *discotic*, although these are less-commonly observed [15].

Nematic liquid crystals can be *uniaxial*, meaning there is a single preferred direction throughout the material, which is known as the anisotropic axis, and can be described by a unit vector, \mathbf{n} , known as the director. The schematic in Figure 1.2 illustrates the partial order of a nematic above some melting point, below which the material would become a solid; and below a clearing point, above which the material loses any kind of ordering and becomes an isotropic liquid. Nematic liquid crystals can also have two locally preferred directions. Such phases are known as *biaxial* nematic liquid crystals

[16].

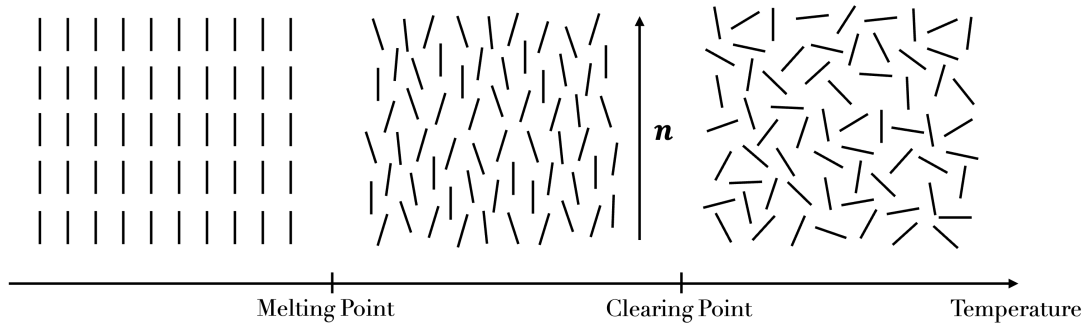


Figure 1.2: A schematic representation of the solid crystalline (left), nematic liquid crystal (centre), and isotropic liquid (right) phases with increasing temperature for calamitic molecules. The average preferred direction of the molecules in the nematic phase is described by the unit vector, \mathbf{n} .

An essential characteristic of nematic liquid crystal molecules is their lack of polarity, or their head-to-tail symmetry. This means that the director, \mathbf{n} , as in Figure 1.2, is equivalent to $-\mathbf{n}$ in this context, so the concept of the director can perhaps be better thought of as a line field [17].

We will focus on nematic liquid crystals throughout this thesis, but give brief descriptions of cholesteric and smectic liquid crystals in the following sections for contrast. More detail on these phases is given in [2] and [14].

1.1.2 Cholesteric Liquid Crystals

Cholesteric liquid crystals are similar to nematic liquid crystals in that they also exhibit orientational ordering that can be described by a director, but the distinguishing feature is that the director twists to form a helical structure, with the helical axis perpendicular to the local director. The distance over which the director rotates 360° is referred to as the pitch of the helix, and we give a schematic representation of a cholesteric liquid crystal in Figure 1.3.

Cholesteric liquid crystals can be formed from chiral, or enantiomorphic, molecules,

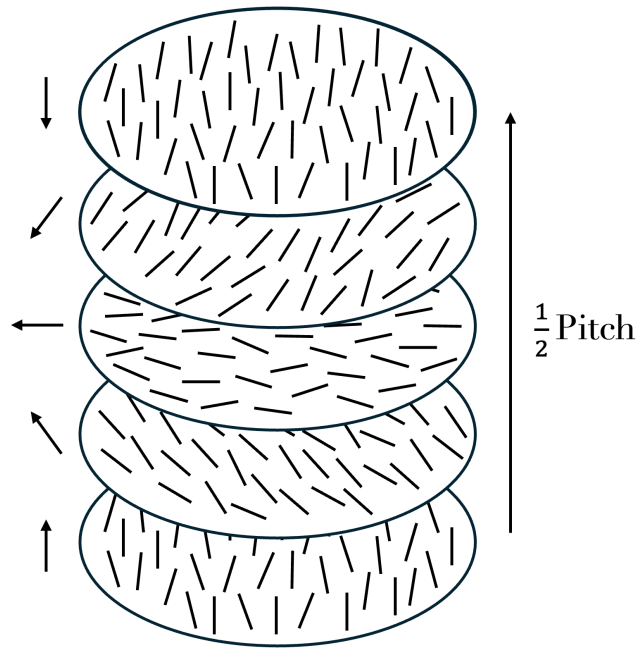


Figure 1.3: A schematic representation of a cholesteric liquid crystal phase. The arrows represent the director, \mathbf{n} , which rotates over 180° , representing half of the pitch of the helical structure.

which cannot be superimposed on their mirror image [14]; or from dissolving chiral molecules in samples of nematic liquid crystals [2]. Despite the name ‘cholesteric’, the substance known as cholesterol cannot form a cholesteric liquid crystal phase. However, many of its derivatives can, including cholesteryl benzoate, the compound studied by Reinitzer. The cholesteric phase is also known as the *chiral nematic* phase, which is perhaps more appropriate, as there are many materials that induce this phase that are not related to cholesterol [18].

1.1.3 Smectic Liquid Crystals

Smectic liquid crystalline phases have both positional and orientational order in that the constituent molecules arrange themselves in layers, and are aligned in some preferred direction within each layer. These layers are independent of one another and the molecules are free to move within each layer. Moreover, each layer has approximately

the same thickness, which can be referred to as the smectic interlayer distance. Since smectic liquid crystal phases have an extra degree of ordering in comparison to nematics, such phases typically occur at lower temperatures than their nematic counterparts in phase-polymorphic materials that can exhibit both phases [14].

Two possible smectic phases are the smectic A and smectic C phases, although other smectic phases have been classified [2]. In the smectic A phase, the director within each layer is parallel to the layer normal, on average. In the smectic C phase, the director is tilted, orienting at an angle to the layer normal [2]. This is illustrated in the schematic of both the smectic A and C phases in Figure 1.4.

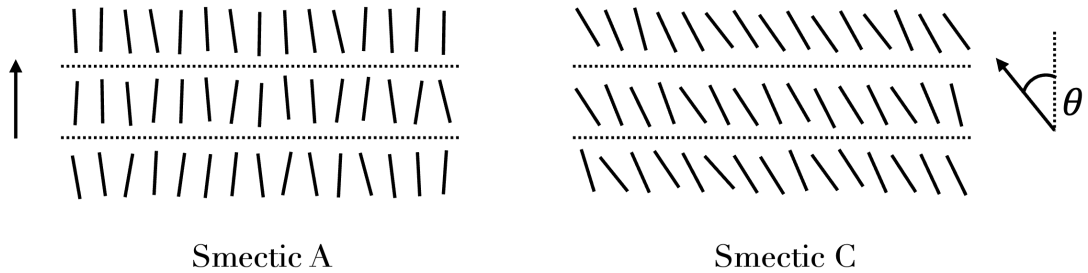


Figure 1.4: A schematic representation of smectic A (left) and smectic C (right) liquid crystal phases. The arrows represent the director, \mathbf{n} , and θ is the angle between the director and layer normal.

1.1.4 Applications of Liquid Crystals

The unique physical, optical, and rheological properties of liquid crystals make them highly versatile for a wide array of applications [6], [9]. Despite this, their full potential has yet to be realised, and there are future applications yet to be imagined that will undoubtedly emerge. As such, the potential applications of liquid crystals drive the need for in-depth mathematical studies to fully understand and harness their capabilities. Here, we briefly discuss a handful of applications of nematic liquid crystals, but

these represent only a small fraction of the potential uses for liquid crystals.

The optical birefringence arising from the anisotropy of liquid crystals is widely exploited in applications. In simple terms, nematic liquid crystals have two refractive indices, in the directions parallel and perpendicular to the nematic director \mathbf{n} . For a typical rod-shaped molecule, the long axis, aligned with the director, is the optical axis. Light travelling along the optical axis will experience some refractive index, n_{\parallel} , and light travelling in any direction perpendicular will experience a different refractive index, n_{\perp} , and in either case will experience a particular phase shift. Light propagating in any other direction is split into two rays: one propagating parallel to the optical axis, and the other perpendicular, both with different phase velocities according to their respective refractive indices [19]. Rays exiting the material that are travelling in different directions can interfere with one another, resulting in various optical effects, and this interference is responsible for the striking colourful pattern captured in Figure 1.1. The difference in refractive indices, $n_{\parallel} - n_{\perp}$, measures the degree of birefringence, and the greater this difference, the stronger the birefringence. The effects of birefringence can be observed when a sample of nematic liquid crystal is sandwiched between two cross-polarisers, as is done to obtain the images in Figure 1.1. In these examples, light is polarised in one direction as it enters the nematic liquid crystal. If the nematic director is parallel or perpendicular to the bottom polariser throughout the thickness of the sample at a given point, the polarisation is unaffected, and thus the light is propagating in a direction perpendicular to the top polariser, which is placed at a right angle to the bottom polariser. In this case, the light is blocked, resulting in a dark patch in the sample. If the nematic director in any other direction, incident polarised light is split into two rays as it passes through the sample, which interfere with one another as light exits the liquid crystal sample and passes through the top polariser,

resulting in different colours depending on the liquid crystal orientation. It is worth noting that the phase lag of the split rays increases with the sample thickness, and as it is impossible to achieve perfect uniform thickness in experiments, some of the colour variation must be attributed to different material thickness at different points.

The birefringence of nematic liquid crystals makes them incredibly useful in applications that exploit this property, including in the multi-billion dollar liquid crystal display industry; and in numerous other applications, including biosensing and lasing [6].

Liquid Crystal Displays

Perhaps one of the most well-known applications of nematic liquid crystals is in liquid crystal displays (LCDs) [6], [20]. LCDs first saw commercial use in the 1970s with the introduction of the twisted nematic display, used in small devices such as calculators and digital watches. A twisted nematic display consists of a sample of liquid crystal in a cell sandwiched between two glass plates, which is then placed between two polarisers which are set at right-angles to one another, as shown in Figure 1.5. The surface of each glass plate is treated to induce a specific director orientation on each plate, usually also orthogonal to one another. This results in an energetically minimising state in which the nematic director twists throughout the sample, so that the optical axis also twists throughout the sample. This causes incident polarised light from the bottom polariser to rotate throughout the sample, so that the light leaving the liquid crystal sample is propagating in the plane perpendicular to that of the incident light, meaning the light will pass through the top polariser, and such a system will appear transparent. As noted in the previous section, the orientation of liquid crystal molecules can lead to colourful patterns observed through cross-polarisers. However, in this specific example,

liquid crystal molecules twist in the plane perpendicular to the incident light rays, and birefringence is responsible for twisting the polarisation of light, but has no noticeable effect on the perceived colour of light passing through the second polariser. This effect is known as the Mauguin regime. As liquid crystals are sensitive to the application of electric fields, and will typically align with the direction of the field [14], an electric field can be applied to reorient the liquid crystal molecules out of the twisted state. As a result, the incident light is no longer rotated throughout the sample, and will be blocked by the top polariser, leading to a dark appearance. Twisted nematic devices form the backbone of more advanced technology, such as LCD TVs, which are made possible by combining twisted nematics with thin-film transistors [20], [21].

One drawback of conventional LCD display devices is that a constant voltage is required to maintain states that deviate from the energetically minimising state. More recent developments, such as zenithal bistable nematic devices [22], [23], allow more than one stable equilibrium state. In these devices, an electric field is required only to switch between stable states, making the system more energetically efficient.

Zenithal bistable nematic devices are an example of a multistable system, which is a system that supports multiple stable equilibria. Systems with multiple stable states have not been extensively utilised in applications, which is a motivating factor behind the research into the solution landscapes of such systems presented in this thesis.

Biology and Biosensing

While it is clear that liquid crystals are highly valuable in technological applications, liquid crystals also occur in nature, playing a significant role in various biological systems. In fact, the liquid crystal observed by Reinitzer in 1888 [7] was not synthetic, but extracted from carrots. Moreover, the combination of fluidity and partial order makes

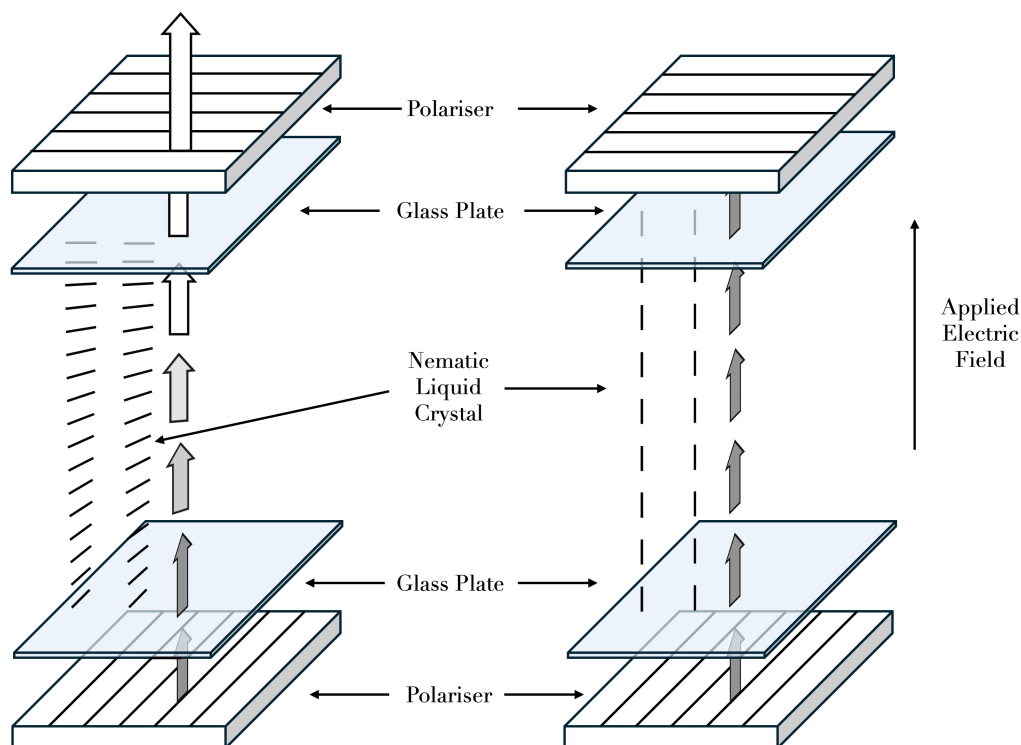


Figure 1.5: A schematic representation of a twisted nematic device. The off state, with no applied electric field, is shown on the left, and the on state, with an applied electric field parallel to the direction of incident light, is shown on the right. Thick shaded arrows indicate the direction and plane of polarisation of light.

liquid crystals the ideal material to form the lipid bilayer that forms the basis of cell membranes [6]; materials such as collagen [24] and DNA [25] can exhibit liquid crystal phases; and suspensions of viruses can form liquid crystal phases under the right conditions [26]. The propensity of organic systems to adopt liquid crystal phases makes liquid crystals well-suited for applications that leverage this behavior, particularly in integrating with and manipulating biological systems.

One such example is in biosensing. Liquid crystal biosensors can be designed so that the orientation of the liquid crystal molecules changes when a compound of interest is present, and are highly effective since liquid crystals are sensitive to the chemical and

physical environment and the optical effects of changing orientation are dramatic [6]. Due to the birefringence of the liquid crystal, these changes are generally detectable through polarised optical microscopy. There are several advantages of using liquid crystals in sensors over other methods: the technology is typically energetically efficient; complex equipment is not required for detection; materials do not need to be labelled for detection; and detection is rapid. One of the first liquid crystal biosensors is described in [27], [28], and was capable of detecting certain proteins and antibodies, via a method that can be applied to the detection of narcotics in biological samples and biomarkers in food, for example. Furthermore, in [29], the authors were able to detect KB cancer cells using emulsions of droplets of 5CB; while a method to detect various bacteria and viruses, also using emulsions of droplets of 5CB, is discussed in [30].

Lasing and Optics

Liquid crystals have recently proven useful in the emerging field of liquid crystal lasers [31], [32]. Experiments have shown that chiral nematic liquid crystals are useful in resonators in mirrorless lasers, and it has been shown that incorporating a chiral dopant into nematic liquid crystals can produce a chiral nematic that can be used in this context [33]. The sensitivity of liquid crystals to stimuli such as external fields and temperature makes them candidates for tunable lasers, which would be useful in settings such as medical imaging. For example, liquid crystal lasers could provide an alternative to existing light sources in fluorescence microscopy, which is currently limited by inconsistent brightness and poor wavelength availability of the light source [34].

Droplets of nematic liquid crystals also show promise as optical microresonators due to their unique optical properties and controllable morphology, as discussed in [35], [36]. The authors demonstrate that droplets of nematic liquid crystals can act as efficient,

tunable optical microresonators, which also have applications in sensing, as well as in other areas such as telecommunications and optical computing [36].

1.2 Modelling Nematic Liquid Crystals

Having discussed liquid crystals and their applications in the preceding sections, it is clear that the study of liquid crystals is multidisciplinary, with key contributions from the likes of chemists, physicists, and engineers. Mathematics also has an important role to play in the field, providing analytical tools and constructing frameworks necessary to understand the complex behavior and phenomena exhibited by liquid crystals, thereby facilitating advances in both fundamental understanding and practical applications. For example, mathematical models can be used to study systems that have not yet been considered experimentally, and provide insight and clues to experimentalists, guiding their exploration of these systems and informing experimental design. Further, a well-designed mathematical model, when integrated with experimental data, can help understand the intricacies of a complex system, offering insights without the need for exhaustive experimentation, thus saving time and resources. The array of mathematical techniques that can be used to model liquid crystals is rich, including but not limited to the calculus of variations; ordinary and partial differential equations; dynamical system theory; stochastic differential equations; numerical methods; and, recently, machine learning.

Nematic liquid crystals can be modelled across various scales, ranging from molecular-level models to continuum approaches, each offering distinct advantages and disadvantages. Molecular-level models consider details such as the shape of the molecules and the nature of the molecular interactions, but become computationally expensive when modelling systems comprising large numbers of molecules, meaning they are poorly

equipped to provide insight into the macroscopic behaviour. Conversely, continuum theories treat liquid crystals as continuous media, where the material properties are described via variables such as the nematic director combined with certain material-specific constants, resulting in a computationally inexpensive model that is well-suited to describing systems involving large numbers of molecules. There also exist so-called mesoscopic models, which fall somewhere in-between, describing liquid crystals at an intermediate length scale, retaining some information regarding molecular interactions, while still being capable of capturing some degree of long-range behaviour. Any mathematical model must compromise in some way to be tractable enough to provide meaningful results. In an ideal scenario, mathematicians should leverage insights from molecular-level models to refine approximations and assumptions within continuum models, providing a more accurate description of the real-world behaviour. However, we model nematic liquid crystals solely within a continuum theory in this thesis, which is sufficient to provide valuable insight on the macroscopic scale.

A range of continuum theories have been used to study systems of nematic liquid crystals. We discuss three continuum theories in the following sections: the Oseen–Frank model; the Ericksen model; and the Landau–de Gennes model. Each of these theories rely on a nematic director and a scalar order parameter.

1.2.1 The Director and the Scalar Order Parameter

In the modelling of nematic liquid crystals, we are interested in capturing the preferred orientation of the molecules at any point in the system. In a uniaxial nematic liquid crystal, with a single preferred direction, we represent the preferred direction by a unit vector, $\mathbf{n} \in \mathbb{S}^2$, known as the *nematic director*, where \mathbb{S}^2 is the unit sphere. The director essentially describes the mean orientation of the molecules and can depend on

both space and time, so that $\mathbf{n} = \mathbf{n}(\mathbf{x}, t)$, for a point \mathbf{x} in space, and some time, t . In static systems, which are the focus of this thesis, the molecular orientation does not evolve in time, so we may write $\mathbf{n} = \mathbf{n}(\mathbf{x})$. For calamitic systems (see Section 1.1.1), the director is the average orientation of the long axes of the molecules [2]; while in discotic systems, the director is the average direction of each disc normal [37]. We note that a disadvantage of the vector representation of the average orientation is that \mathbf{n} and $-\mathbf{n}$ are equivalent in this context.

In addition to measuring the average orientation of nematic liquid crystal molecules, it is useful to measure the degree of ordering about the preferred direction, essentially quantifying how ordered the system is. We do so using the *scalar order parameter*, typically denoted s , where $s \in \mathbb{R}$ and $s = s(\mathbf{x}, t)$, in general. The scalar order parameter depends on the angle of each molecule relative to the director and is defined to be

$$s = \frac{1}{2} \langle 3 \cos^2 \theta_m - 1 \rangle \equiv \frac{1}{2} \int_{\mathcal{B}} (3 \cos^2 \theta_m - 1) \rho(\theta_m) dV. \quad (1.1)$$

The function $\rho(\theta_m)$ is the probability density function describing the probability of the long axis of a given molecule being at an angle θ_m to the director (in calamitic systems), at a point \mathbf{x} , in some appropriately-sized ball, \mathcal{B} [16], such that several molecules are contained in the ball, but not so many that the orientation can vary significantly throughout the ball. The size of such a ball should depend on the molecules in question, but we note that thermotropic liquid crystal molecules are typically on the order of nanometres, so an appropriately-sized ball may be on the order of tens of nanometres.

In a perfectly ordered system, the molecules are fixed and align perfectly with the director so that $\theta_m = 0$, resulting in a scalar order parameter $s = 1$. In an isotropic liquid, molecules orient in random directions so all angles, θ_m , to the director are

equally probable. Therefore, $\rho(\theta_m)$ is a uniform distribution, which causes the scalar order parameter to take the value $s = 0$. If the molecules lie in the plane perpendicular to the director, we must have $\theta_m = \frac{\pi}{2}$ so that $s = -\frac{1}{2}$ [16].

In biaxial nematic liquid crystals, there are two preferred directions, each with associated degrees of ordering [16]. In such a system, we must introduce a second director and its associated scalar order parameter, which we denote as \mathbf{m} and p , respectively in this thesis, when required. We discuss uniaxiality and biaxiality in more detail in Section 1.3.3.

1.2.2 Continuum Theories

The three widely-used continuum theories for nematic liquid crystals in equilibrium are the Oseen–Frank theory; the Ericksen theory; and the Landau–de Gennes theory. Each framework is a variational theory, meaning that physically observable equilibrium configurations minimise an associated free energy subject to appropriate boundary conditions.

The Oseen–Frank Model

The Oseen–Frank model is the simplest of the three continuum models of interest, originally introduced by Carl Wilhelm Oseen [38], and developed further by Frederick Charles Frank [39]. The model assumes a fixed scalar order parameter throughout the system, and the preferred direction of the liquid crystal molecules is modelled using the director, \mathbf{n} , at every point in space. The associated free energy therefore depends only on a single director, meaning this theory can only account for uniaxial phases. The Oseen–Frank model is also poorly equipped to capture defects in the system, which are regions of discontinuity in orientation, or equivalently, discontinuities in the director

field [2], and because the Oseen–Frank theory gives us no information about defects.

For a nematic liquid crystal in a given domain, Ω , in the absence of surface energies and external fields, the Oseen–Frank free energy is given by

$$\mathcal{F}_{OF}[\mathbf{n}] = \int_{\Omega} K_1 (\nabla \cdot \mathbf{n})^2 + K_2 (\mathbf{n} \cdot \nabla \times \mathbf{n})^2 + K_3 (\mathbf{n} \times \nabla \times \mathbf{n})^2 + (K_2 + K_4) \nabla \cdot [(\mathbf{n} \cdot \nabla) \mathbf{n} - (\nabla \cdot \mathbf{n}) \mathbf{n}] d\Omega, \quad (1.2)$$

where K_1, K_2, K_3 , and K_4 are known as the Frank elastic constants [14]. The terms associated with K_1, K_2 , and K_3 correspond to distortions known as *splay*, *twist* and *bend*, respectively, and we give schematic representations of such distortions in Figure 1.6. The term with coefficient $K_2 + K_4$ is known as the *saddle-splay* term. The saddle-splay term can be converted into a surface integral using the divergence theorem if the domain is three-dimensional.

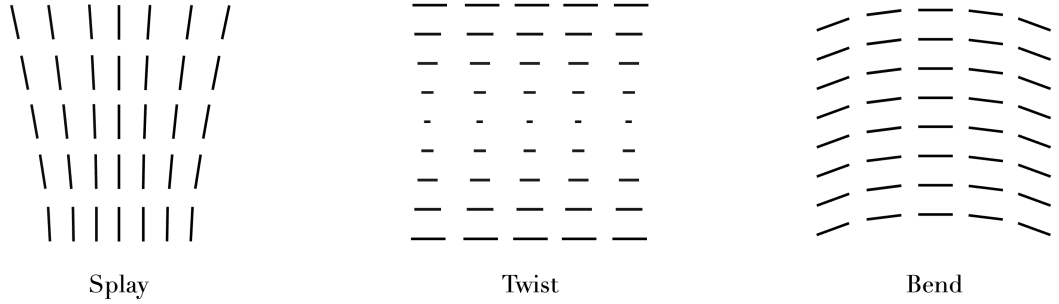


Figure 1.6: A schematic representation of splay (left), twist (centre), and bend (right) distortions in nematic liquid crystals.

The constants K_1, K_2 , and K_3 have been measured in experiments for certain materials. For example, at 22°C, MBBA has elastic constants [40]

$$K_1 = 6 \times 10^{-12} N, \quad K_2 = 2.9 \times 10^{-12} N, \quad K_3 = 7.5 \times 10^{-12} N. \quad (1.3)$$

The elastic constants are temperature-dependent and typically decrease as temperature increases [14]. As demonstrated, the elastic constants can be of the same order of magnitude, so it is reasonable to use the so-called one-constant approximation, where we take $K_1 = K_2 = K_3 =: K$, and $K_4 = 0$ [14], which simplifies the free energy.

While the Oseen–Frank theory has produced some meaningful mathematical insights and is still in use today, it is significantly limited in that it is only applicable to uniaxial systems and cannot be used to effectively characterise defects. Furthermore, since the scalar order parameter is assumed to be constant, the Oseen–Frank model cannot be used to study phase transitions between the isotropic and nematic phases.

The Ericksen Model

In response to the limitations of the Oseen–Frank model in capturing defects, Jerald Ericksen introduced an alternative framework, referred to as the Ericksen model [41]. The associated free energy also depends on a director, \mathbf{n} , but generalises the Oseen–Frank theory by incorporating a varying scalar order parameter, s . Including a varying scalar order parameter regularises the notion of a defect, as the scalar order parameter vanishes in defect regions, where the nematic director is undefined. This removes potential discontinuities in the mathematical description of an equilibrium configuration and describes defects as isotropic regions, where there is no nematic ordering [3].

A one-constant approximation of the Ericksen free energy is also commonly used, and, in the absence of external fields and surface energies, is given by

$$\mathcal{F}[s, \mathbf{n}] = \int_{\Omega} K_E |\nabla s|^2 + s^2 |\nabla \mathbf{n}|^2 + W(s) d\Omega, \quad (1.4)$$

where K_E is an elastic constant and $W(s)$ is a temperature-dependent bulk potential.

We discuss the idea of bulk potentials in Sections 1.3.2 and 1.5.1.

The Ericksen model is more capable of handling defects than the Oseen–Frank model, and the varying scalar order parameter also allows for the modelling of isotropic–uniaxial phase transitions. However, since the Ericksen framework also relies on a single director, it is not able to capture biaxial nematic phases.

The Landau–de Gennes Model

The Landau–de Gennes model is the most sophisticated continuum model for nematic liquid crystals in equilibrium. This framework is capable of fully describing defects in systems of nematic liquid crystals, and can effectively capture biaxiality and the associated phase transitions. We work exclusively within the Landau–de Gennes theory in this thesis, and give a more detailed description in Section 1.3.

1.2.3 Defects

We encountered the notion of a defect in a system of nematic liquid crystals in the previous section. To recap: defects, or disclinations, are localised regions where the nematic director, \mathbf{n} , cannot be defined, and which can be thought of as being locally isotropic, or as regions where the molecular orientation is completely disordered. Such discontinuities in the director may manifest as isolated points, lines, or sheets. Only point and line defects are observed in real systems, since sheet defects are always unstable [2].

Defects can arise simply as a result of confinement, with the preferred liquid crystal orientation competing with the geometry and surface anchoring [42]. However, defects can also arise as a result of phase transitions. For example, when cooling a material from the isotropic phase, or equivalently, when quenching during isotropic–nematic phase transitions, distinct nematic regions may form, with independent director orientations

which do not match when the regions eventually meet as the nematic regions expand [43]. Furthermore, defects can be induced via the application of external stimuli such as electric fields [44], which have the potential to facilitate switching in multistable systems, as has been shown in the case of LCDs [45].

Defects play a crucial role in the mathematical modelling of confined systems, not only because they are often present in such systems, but because their presence causes significant director distortions which substantially affect the character of the system and have distinctive optical signatures through cross-polarisers. For example, the image on the right in Figure 1.1 depicts the director distortions around two point defects which are at the centre of the cross structures.

An example of a confined system which contains defect structures is a spherical droplet of nematic liquid crystals with strong homeotropic anchoring, which we study in Chapters 3, 5 and 6. The liquid crystal molecules are fixed in the radial direction at the droplet surface, which forces the formation of defects. One possible defect in this system is a point defect at the centre of the droplet, known as the radial hedgehog defect, which has a spherically symmetric director profile, as illustrated in Figure 1.7. The radial hedgehog defect is a central focus of this thesis. Alternatively, the droplet might contain a line defect, with the two common classes of line defect being the biaxial torus and the split core configurations, also illustrated in Figure 1.7. The radial hedgehog and biaxial torus configurations are generally the preferred states in this system and these configurations have been observed experimentally [46]. We will discuss the possible equilibrium configurations in spherical droplets with strong homeotropic anchoring in more detail in Section 1.5.3.

The dispersions of nematic droplets used as sensors in [29] and [30], outlined in Section 1.1.4, are prominent examples that leverage the unique properties of defects,

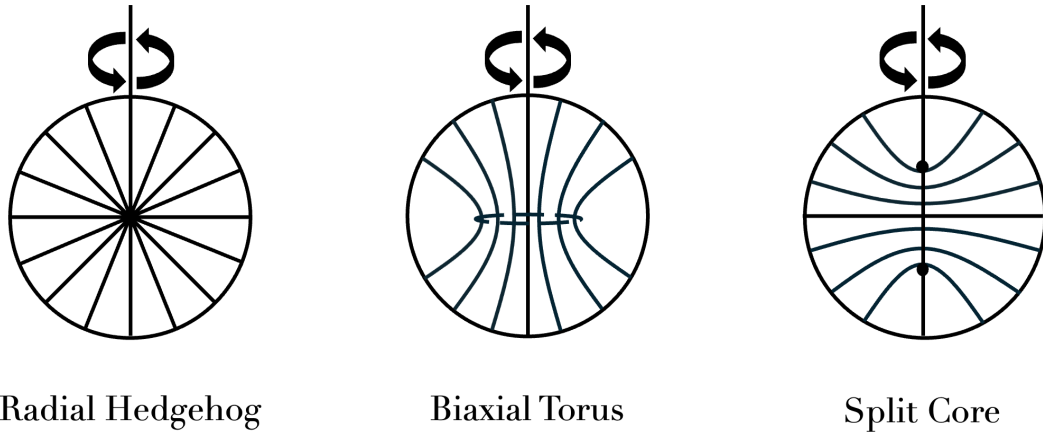


Figure 1.7: A schematic representation of the radial hedgehog (left), biaxial torus (centre), and split core (right) defect configurations in spherical droplets of nematic liquid crystals.

relying on the distinct optical signatures of each defect for detection. The mathematical modelling of these defects can aid similar applications by predicting the conditions under which specific defects might form in practice, leading to better control and optimisation in experiments.

The example of a spherical droplet with strong homeotropic anchoring features defects confined to the interior, but in general confined systems, defects can appear anywhere, including on the boundary, depending on the geometry and surface anchoring. From a mathematical perspective, studying canonical defects in confinement, such as the radial hedgehog defect, is worthwhile, as their properties are often universal. Consequently, insights gained from modelling canonical defects enhance our understanding of defects in broader systems of nematic liquid crystals.

1.3 The Landau–de Gennes Theory

In this thesis, we model nematic liquid crystals within the Landau–de Gennes framework, the most general continuum theory for nematic liquid crystals in equilibrium.

Within this framework, the state of the nematic liquid crystals is described by a \mathbf{Q} -tensor order parameter. The notion of a \mathbf{Q} -tensor was first introduced by Lev Landau [47], as a means to describe phase transitions between solid crystals and isotropic liquids. Pierre-Gilles de Gennes later generalised the theory to encompass liquid crystal phase transitions [48], for which he was awarded the Nobel Prize in physics in 1991. The \mathbf{Q} -tensor can describe isotropic, uniaxial and biaxial phases and the associated phase transitions [16], [49]. Additionally, it is well-suited for characterising defects, which are a central focus of Chapters 3, 5 and 6.

1.3.1 The \mathbf{Q} -tensor Order Parameter

The \mathbf{Q} -tensor is a symmetric, traceless, 3×3 matrix, which can be written

$$\mathbf{Q} = \begin{bmatrix} Q_{11} & Q_{12} & Q_{13} \\ Q_{12} & Q_{22} & Q_{23} \\ Q_{13} & Q_{23} & -Q_{11} - Q_{22} \end{bmatrix}, \quad (1.5)$$

and belongs to the space

$$\mathcal{S}_0 = \{ \mathbf{Q} \in M^{3 \times 3} : \mathbf{Q} = \mathbf{Q}^T, \text{tr } \mathbf{Q} = 0 \}, \quad (1.6)$$

where $M^{3 \times 3}$ is the space of 3×3 matrices.

We may write the \mathbf{Q} -tensor in terms of its eigenvalues and eigenvectors, so that

$$\mathbf{Q} = \lambda_1 \mathbf{e}_1 \otimes \mathbf{e}_1 + \lambda_2 \mathbf{e}_2 \otimes \mathbf{e}_2 + \lambda_3 \mathbf{e}_3 \otimes \mathbf{e}_3. \quad (1.7)$$

We note that $\sum_{i=1}^3 \mathbf{e}_i \otimes \mathbf{e}_i = \mathbf{I}$, where \mathbf{I} is the 3×3 identity matrix. Furthermore, the

tracelessness of \mathbf{Q} implies that $\lambda_3 = -\lambda_1 - \lambda_2$, so we may rewrite the \mathbf{Q} -tensor as

$$\mathbf{Q} = (2\lambda_1 + \lambda_2) \mathbf{e}_1 \otimes \mathbf{e}_1 + (\lambda_1 + 2\lambda_2) \mathbf{e}_2 \otimes \mathbf{e}_2 - (\lambda_1 + \lambda_2) \mathbf{I}. \quad (1.8)$$

Let us set $s = 2\lambda_1 + \lambda_2$, $p = \lambda_1 + 2\lambda_2$, $\mathbf{n} = \mathbf{e}_1$, and $\mathbf{m} = \mathbf{e}_2$, so we may rewrite \mathbf{Q} as

$$\mathbf{Q} = s \left(\mathbf{n} \otimes \mathbf{n} - \frac{1}{3} \mathbf{I} \right) + p \left(\mathbf{m} \otimes \mathbf{m} - \frac{1}{3} \mathbf{I} \right). \quad (1.9)$$

This form of \mathbf{Q} describes the liquid crystal orientation via two directors, \mathbf{n} and \mathbf{m} , with corresponding scalar order parameters, s and p . If s and p are distinct and nonzero, all three eigenvalues of \mathbf{Q} are distinct, and the configuration is biaxial. If one of s and p is zero, or if $s = p \neq 0$, the \mathbf{Q} -tensor has two equal eigenvalues and describes a uniaxial phase. If all three eigenvalues of \mathbf{Q} are equal, we must in fact have $\lambda_1 = \lambda_2 = \lambda_3 = 0$ by the tracelessness of \mathbf{Q} . Therefore, we have that $s = p = 0$, so that $\mathbf{Q} = \mathbf{0}$, and the corresponding material state is isotropic.

There are other, equivalent formulations one might use to represent the \mathbf{Q} -tensor. One such representation relies on a basis for the space \mathcal{S}_0 , namely [50]–[52]:

$$\begin{aligned} \mathbf{E}_1 &= \frac{\sqrt{6}}{2} \left(\mathbf{e}_z \otimes \mathbf{e}_z - \frac{1}{3} \mathbf{I} \right), & \mathbf{E}_2 &= \frac{\sqrt{2}}{2} (\mathbf{e}_x \otimes \mathbf{e}_x - \mathbf{e}_y \otimes \mathbf{e}_y), \\ \mathbf{E}_3 &= \frac{\sqrt{2}}{2} (\mathbf{e}_x \otimes \mathbf{e}_z + \mathbf{e}_z \otimes \mathbf{e}_x), & \mathbf{E}_4 &= \frac{\sqrt{2}}{2} (\mathbf{e}_x \otimes \mathbf{e}_y + \mathbf{e}_y \otimes \mathbf{e}_x), \\ \mathbf{E}_5 &= \frac{\sqrt{2}}{2} (\mathbf{e}_y \otimes \mathbf{e}_z + \mathbf{e}_z \otimes \mathbf{e}_y), \end{aligned} \quad (1.10)$$

where $\mathbf{e}_x = [1, 0, 0]^T$, $\mathbf{e}_y = [0, 1, 0]^T$, and $\mathbf{e}_z = [0, 0, 1]^T$. We then write the \mathbf{Q} -tensor as

$$\mathbf{Q} = \sum_{i=1}^5 q_i(\mathbf{x}) \mathbf{E}_i. \quad (1.11)$$

1.3.2 The Landau–de Gennes Free Energy

The Landau–de Gennes theory hinges on minimising a free energy which depends on the \mathbf{Q} -tensor. In this thesis, we consider a Landau–de Gennes free energy with two contributions: an elastic energy, f_E ; and a thermotropic bulk potential, f_B . Therefore, in the absence of external fields and surface energies, for a nematic liquid crystal confined to some bounded domain, Ω , we write the Landau–de Gennes free energy as

$$\mathcal{F}[\mathbf{Q}] = \int_{\Omega} f_E(\mathbf{Q}) + f_B(\mathbf{Q}) dV. \quad (1.12)$$

The bulk energy, f_B , describes the preferred phase in a spatially homogeneous system. The simplest form of bulk potential that captures a nematic-isotropic phase transition is known as the fourth-order bulk potential, which is a truncated Taylor series in \mathbf{Q} , and can be written as [2], [3]

$$f_B(\mathbf{Q}) = \frac{A}{2} \text{tr} \mathbf{Q}^2 - \frac{B}{3} \text{tr} \mathbf{Q}^3 + \frac{C}{4} (\text{tr} \mathbf{Q}^2)^2, \quad (1.13)$$

where $\text{tr} \mathbf{Q}^2 = Q_{ij}Q_{ij} = |\mathbf{Q}|^2$ and $\text{tr} \mathbf{Q}^3 = Q_{ij}Q_{jk}Q_{ki}$. We use the Einstein summation convention here and in the rest of this thesis, where applicable. The constant A is a temperature-dependent constant given by

$$A = \alpha(T - T^*), \quad (1.14)$$

where $\alpha > 0$ is a material-dependent constant, T is the absolute temperature, and T^* describes the temperature at which the isotropic state becomes unstable [2], [16]. The constants $B, C > 0$ are material-dependent constants. It is commonly accepted that if $B > 0$, the model corresponds to calamitic molecules, while $B < 0$ describes discotic

molecules [53]; and $C > 0$ is required for the stability of the expansion. We note that the fourth-order bulk potential depends only on the invariants of \mathbf{Q} , as these terms do not vary with rotations of the coordinate system.

The fourth-order bulk potential only admits isotropic and uniaxial critical points, and we reproduce a result to this effect in Section 1.5.1. As such, biaxiality arises in the system solely due to geometrical frustration in confinement. In order to consider biaxiality as a bulk effect in the system, we study a confined system with a sixth-order potential in Chapter 3, which we introduce in Section 1.5.1.

The elastic energy, f_E , penalises spatial inhomogeneities, or elastic deformations in the material. In general, it is energetically preferable for a sample of nematic liquid crystal to be uniform in space. However, confinement typically results in direction-dependent material distortions, which are accounted for by the elastic energy density. The most general form of the elastic energy density is given by

$$f_E(\mathbf{Q}) = \frac{L_1}{2} Q_{ij,k} Q_{ij,k} + \frac{L_2}{2} Q_{ij,j} Q_{ik,k} + \frac{L_3}{2} Q_{ik,j} Q_{ij,k} + \frac{L_4}{2} \epsilon_{ijk} Q_{il} Q_{j\ell,k} + \frac{L_5}{2} Q_{\ell k} Q_{ij,\ell} Q_{ij,k}, \quad (1.15)$$

where $Q_{ij,k} = \frac{\partial Q_{ij}}{\partial x_k}$; ϵ_{ijk} is the Levi-Civita symbol; and L_1, \dots, L_5 are material-dependent elastic constants which are related to the Frank elastic constants [16].

Just as in the Oseen–Frank and Ericksen theories, it is common to take a one-constant approximation of the elastic energy. In this case, we set $L := L_1$ and $L_i = 0$ for $i = 2, \dots, 5$, and rewrite the elastic energy as

$$f_E(\mathbf{Q}) = \frac{L}{2} |\nabla \mathbf{Q}|^2, \quad (1.16)$$

where $|\nabla \mathbf{Q}|^2 = Q_{ij,k} Q_{ij,k}$. We work with the one-constant approximation of the elastic

energy density throughout this thesis.

Since the Landau–de Gennes theory is used to model confined systems of nematic liquid crystals, the problems are typically boundary value problems, meaning we need to consider the behaviour at the domain boundary. In this thesis, we work with *strong anchoring*, which means the liquid crystal configuration at the boundary is prescribed using a Dirichlet boundary condition of the form

$$\mathbf{Q} = \mathbf{Q}_b \quad \text{on } \partial\Omega. \quad (1.17)$$

Strong anchoring is often used in scenarios where the surface in contact with the liquid crystal has been treated to induce a specific director orientation; or when the liquid crystal is suspended or coated in some material that enforces a specific director orientation. The anchoring can enforce any director orientation, in theory. If the boundary condition requires the director to be normal to the boundary, the anchoring is *homeotropic* [3]; and if the director is required to be parallel to the boundary, the anchoring is *planar* [16].

An alternative to strong anchoring is *weak anchoring*, which is where there is still a preferred director orientation at the boundary, but it is not as strictly enforced as in the case of strong anchoring. Weak anchoring is arguably more reflective of reality, as it is very difficult to control the director orientation exactly. When weak anchoring is used in the model, it appears as a surface energy in the Landau–de Gennes free energy, but this is beyond the scope of this thesis, so we refer the reader to the likes of [16] for more detail.

1.3.3 Uniaxiality versus Biaxiality

We have come across the notion of biaxiality in earlier sections, but it would be useful to briefly discuss how we characterise and quantify biaxiality.

The idea of biaxiality manifests in two ways in nematic liquid crystalline systems: it is possible to have uniaxial or biaxial molecules; and the arrangement of the molecules can be uniaxial or biaxial [16]. Uniaxial molecules have an axis of rotational symmetry, and include the typical rod- or disc-shaped molecules whose axes of rotational symmetry coincide with the nematic director. Biaxial molecules do not have an axis of rotational symmetry, but rather have three axes of mirror symmetry. An example of a biaxial molecule is a board-shaped molecule. These molecules can still be elongated as we recall they must be strongly anisotropic, and in the case of a board-shaped molecule, the long axis coincides with the nematic director. The Landau–de Gennes framework discussed above is only valid for uniaxial molecules, and the study of biaxial molecules requires a second tensor to describe the orientation of the other molecular axes [54]. As such, we only consider uniaxial molecules, which can exhibit biaxial phases, in this thesis.

We are interested in both uniaxial and biaxial arrangements in this work and we recall that a uniaxial arrangement means the long axes of the molecules approximately align in one direction (for calamitic molecules), while there are two preferred directions for biaxial arrangements. Just as the scalar order parameter quantifies the degree of molecular ordering about the preferred directions, the extent of biaxiality can be similarly measured. We quantify biaxiality via the biaxiality parameter [55]

$$\beta = 1 - 6 \frac{(\text{tr } \mathbf{Q}^3)^2}{(\text{tr } \mathbf{Q}^2)^3}, \quad (1.18)$$

where $0 \leq \beta \leq 1$. If $\beta = 0$, the system is uniaxial, and if $\beta = 1$, the system is ‘maximally’ biaxial, with one of the eigenvalues of the \mathbf{Q} -tensor equal to zero. We reproduce a short proof accordingly [56].

Proposition 1.1. *The quantity $\beta(\mathbf{Q})$, defined in (1.18), satisfies $0 \leq \beta(\mathbf{Q}) \leq 1$.*

Proof. The term $6 \frac{(\text{tr } \mathbf{Q}^3)^2}{(\text{tr } \mathbf{Q}^2)^3}$ is nonnegative, so $\beta(\mathbf{Q}) \leq 1$ is immediate.

We consider a \mathbf{Q} -tensor of the form (1.9) to express $(\text{tr } \mathbf{Q}^3)^2$ and $(\text{tr } \mathbf{Q}^2)^3$ as

$$(\text{tr } \mathbf{Q}^3)^2 = \frac{1}{81} (4s^6 + 4p^6 - 12s^5p - 12sp^5 + 26s^3p^3 - 3s^4p^2 - 3s^2p^4), \quad (1.19)$$

and

$$(\text{tr } \mathbf{Q}^2)^3 = \frac{8}{27} (s^6 + p^6 - 3s^5p - 3sp^5 - 7s^3p^3 + 6s^2p^4 + 6s^4p^2). \quad (1.20)$$

Straightforward calculations then show that

$$(\text{tr } \mathbf{Q}^2)^3 - 6(\text{tr } \mathbf{Q}^3)^2 = 2s^2p^2(s-p)^2 \geq 0, \quad (1.21)$$

which implies that $\beta(\mathbf{Q}) \geq 0$, as required. \square

The implications of the definition of the biaxiality parameter and the above result are that the system is uniaxial when $\text{tr } \mathbf{Q}^2$ is proportional to $\text{tr } \mathbf{Q}^3$. Equivalently, in terms of the scalar order parameters, the system is uniaxial when $s = p$ or when one of s and p is zero, which we recall implies that the system has only one preferred direction.

1.4 Thesis Overview

In Chapter 2, we provide preliminary details and present some key results which contextualise the problems we consider in Chapters 3-6. We then give the nondimensional-

Chapter 1. Introduction and Literature Review

isations for the free energies studied in Chapters 3-5. Finally, we outline key numerical methods employed in Chapters 3 and 5.

We consider uniaxial and biaxial critical points of a sixth-order bulk potential, which we introduce in Section 1.5.1, and their stability in Chapter 3. We then prove a range of analytical results regarding the radial hedgehog solution with a sixth-order bulk potential, building upon the results outlined in Section 1.5.2. The final part of Chapter 3 comprises a numerical exploration of Landau–de Gennes critical points on the sphere with rotational and mirror symmetry. We discuss existing results under a fourth-order bulk potential in Section 1.5.3, and we note that we consider equilibrium configurations with both the fourth- and sixth-order bulk potentials in our study in Chapter 3. Specifically, we investigate the stability of the radial hedgehog solution as a function of temperature and droplet radius; demonstrate that an unstable radial hedgehog solution may act as a transition state in switching processes between two stable states; and construct bifurcation diagrams as a function of temperature for fixed droplet radii, giving a clear picture of the solution landscapes in the parameter regimes studied.

The focus of Chapter 4 is to study critical points of a ferronematic bulk free energy, which we introduce in Section 1.5.4. We consider both uniaxial and biaxial critical points and compute their stability as a function of temperature and nemato-magnetic coupling strength, on which we provide more detail in Section 1.5.4.

We turn our attention to equilibrium configurations on the sphere with rotational and mirror symmetry in a ferronematic system, which we introduce in Section 1.5.4, as noted, in Chapter 5. There are several parallels between the work in Chapters 5 and 3. We first prove a range of analytical results regarding the ferronematic radial hedgehog solution in Chapter 5. We then perform a numerical study analogous to that in Chap-

ter 3, exploring the solution landscape for ferronematic equilibrium configurations with rotational and mirror symmetry. The ferronematic system is richer than the nematic system due to the added complexity of the nemato-magnetic coupling, which we introduce in Section 1.5.4. In the ferronematic framework, we investigate the influence of the nemato-magnetic coupling strength in addition to temperature and droplet radius.

In Chapter 6, we introduce a stochastic term into both the nematic and ferronematic models and study the effects of random noise on the nematic and ferronematic radial hedgehog solutions. We consider the nematic radial hedgehog solution with both the fourth- and sixth-order bulk potentials, and work with three different nemato-magnetic coupling strengths in the ferronematic case. We discuss the details of the stochastic term in Section 1.5.5.

In Chapter 7, we summarise our results, and discuss some potential next steps following the work in this thesis.

In the remainder of this chapter, we review the literature relevant to key concepts considered in this thesis, and motivate the themes studied in subsequent chapters.

1.5 Literature Review

1.5.1 The Sixth-Order Bulk Potential

As discussed in Section 1.3.2, the fourth-order bulk potential,

$$f_B(\mathbf{Q}) = \frac{A}{2} \text{tr } \mathbf{Q}^2 - \frac{B}{3} \text{tr } \mathbf{Q}^3 + \frac{C}{4} (\text{tr } \mathbf{Q}^2)^2, \quad (1.22)$$

is the simplest form of bulk potential that models a first-order isotropic-nematic phase transition. While the fourth-order bulk potential is the most commonly used bulk potential in the literature, it only admits isotropic and uniaxial critical points. We

reproduce a well-known result to this effect, and its proof from [56].

Proposition 1.2. *The critical points of the bulk energy density, f_B , in (1.22), are given by either uniaxial or isotropic \mathbf{Q} -tensors of the form*

$$\mathbf{Q} = s \left(\mathbf{n} \otimes \mathbf{n} - \frac{1}{3} \mathbf{I} \right), \quad (1.23)$$

where s is a scalar order parameter and \mathbf{n} is one of the eigenvectors of \mathbf{Q} .

Proof. We recall that we may express the \mathbf{Q} -tensor as

$$\mathbf{Q} = \lambda_1 \mathbf{e}_1 \otimes \mathbf{e}_1 + \lambda_2 \mathbf{e}_2 \otimes \mathbf{e}_2 + \lambda_3 \mathbf{e}_3 \otimes \mathbf{e}_3, \quad (1.24)$$

where $\{\mathbf{e}_1, \mathbf{e}_2, \mathbf{e}_3\}$ are orthonormal eigenvectors and $\{\lambda_1, \lambda_2, \lambda_3\}$ are their corresponding eigenvalues. Straightforward computations show that $\text{tr } \mathbf{Q}^n = \sum_{i=1}^3 \lambda_i^n$. Therefore, the bulk energy density can be expressed in terms of the eigenvalues, λ_1, λ_2 , and λ_3 , of \mathbf{Q} , only. We recast the bulk energy density, f_B , in terms of the eigenvalues, so that the bulk critical points are in fact equivalent to the critical points of the function $f : \mathbb{R}^3 \rightarrow \mathbb{R}$ given by

$$f(\lambda_1, \lambda_2, \lambda_3) = \frac{A}{2} \sum_{i=1}^3 \lambda_i^2 - \frac{B}{3} \sum_{i=1}^3 \lambda_i^3 + \frac{C}{4} \sum_{i=1}^3 \lambda_i^4 - 2\delta \sum_{i=1}^3 \lambda_i, \quad (1.25)$$

where we include a Lagrange multiplier to account for the tracelessness of \mathbf{Q} .

The critical points are solutions of the system of equations obtained by differentiating (1.25) with respect to each eigenvalue and setting the result equal to zero. We can write the system as

$$\frac{\partial f}{\partial \lambda_i} = 0 \Leftrightarrow A\lambda_i - B\lambda_i^2 + C \left(\sum_{k=1}^3 \lambda_k^2 \right) \lambda_i = 2\delta, \quad \text{for } i = 1, \dots, 3. \quad (1.26)$$

This is equivalent to

$$(\lambda_i - \lambda_j) \left[A - B(\lambda_i + \lambda_j) + C \sum_{k=1}^3 \lambda_k^2 \right] = 0, \quad 1 \leq i < j \leq 3. \quad (1.27)$$

We show that there is no critical point with three distinct eigenvalues via a contradiction argument. Suppose the distinct eigenvalues $\lambda_1 \neq \lambda_2 \neq \lambda_3$ satisfy the system (1.26). We consider equation (1.27) for the pairs (λ_1, λ_2) and (λ_1, λ_3) , without loss of generality, which yields the equations

$$A - B(\lambda_1 + \lambda_2) + C \sum_{k=1}^3 \lambda_k^2 = 0, \quad (1.28)$$

$$A - B(\lambda_1 + \lambda_3) + C \sum_{k=1}^3 \lambda_k^2 = 0. \quad (1.29)$$

Subtracting (1.29) from (1.28), we find that

$$-B(\lambda_2 - \lambda_3) = 0, \quad (1.30)$$

contradicting the initial hypothesis that $\lambda_2 \neq \lambda_3$. Thus, we conclude that any critical point of f_B in (1.22) must have at least two equal eigenvalues. Hence, critical points of f_B are either isotropic or uniaxial, and there can be no biaxial critical points for this particular choice of f_B . \square

Considering the more general biaxial form of the \mathbf{Q} -tensor in (1.9), we see that either $s = p$ or one of s and p is nonzero. Since we are free to choose which of a set of eigenvalues is assigned to λ_1, λ_2 and λ_3 , it suffices to capture uniaxial \mathbf{Q} -tensors with $p = 0$ in (1.9). This corresponds to $\lambda_2 = \lambda_3$ in (1.7) and $s = \frac{3}{2}\lambda_1 = -3\lambda_2$.

We rewrite the bulk potential f_B in terms of the scalar order parameter, s , by

considering \mathbf{Q} -tensors of the form (1.23). We may write

$$f_B(s) = \frac{A}{3}s^2 - \frac{2B}{27}s^3 + \frac{C}{9}s^4, \quad (1.31)$$

where we have used

$$\text{tr } \mathbf{Q}^2 = \frac{2}{3}s^2 \quad \text{and} \quad \text{tr } \mathbf{Q}^3 = \frac{2}{9}s^3, \quad (1.32)$$

and we note that critical points are the solutions of the equation

$$\frac{df_B}{ds} = \frac{2A}{3}s - \frac{2B}{9}s^2 + \frac{4C}{9}s^3 = 0. \quad (1.33)$$

There are three solutions:

$$s = 0, \quad \text{and} \quad s_{\pm} = \frac{B \pm \sqrt{B^2 - 24AC}}{4C}, \quad (1.34)$$

such that

$$f_B(0) = 0, \quad \text{and} \quad f_B(s_{\pm}) = \frac{s_{\pm}^2}{54}(9A - Bs_{\pm}), \quad (1.35)$$

with $f_B(s_-) > f_B(s_+)$. Therefore, the global minimiser of the bulk energy density is either the isotropic state, $\mathbf{Q} = \mathbf{0}$, or the uniaxial nematic state

$$\mathbf{Q} = s_+ \left(\mathbf{n} \otimes \mathbf{n} - \frac{1}{3}\mathbf{I} \right), \quad (1.36)$$

where \mathbf{n} is the eigenvector corresponding to the largest eigenvalue of \mathbf{Q} .

It is possible to check whether a critical point is globally minimising, locally minimising, or locally maximising for any combination of parameters by considering the second derivative, $\frac{d^2 f_B}{ds^2}$, and comparing the value of f_B for each critical point. It can be shown that the isotropic critical point, $s = 0$, is the global minimiser for $A > \frac{B^2}{27C}$;

a local minimiser for $0 < A < \frac{B^2}{27C}$; and a local maximiser $A < 0$. We note that the uniaxial state, $s = s_+$ is undefined for high temperatures corresponding to $A > \frac{B^2}{24C}$; a local minimiser for $\frac{B^2}{27C} < A < \frac{B^2}{24C}$; and the global minimiser for low temperatures corresponding to $A < \frac{B^2}{27C}$. The state $s = s_-$ is also undefined for $A > \frac{B^2}{24C}$; a local maximiser for $0 < A < \frac{B^2}{24C}$; and a local minimiser for $A < 0$.

We note that increasing A corresponds to increasing absolute temperature. There are three important values of A :

- $A = \frac{B^2}{24C}$, the temperature above which the nematic states, s_{\pm} , are undefined, often referred to as the *nematic superheating temperature*;
- $A = \frac{B^2}{27C}$, the temperature at which the isotropic and nematic states have equal energies, so $f_B(0) = f_B(s_+)$, the *nematic-isotropic transition temperature*;
- and $A = 0$, the temperature below which the isotropic state loses stability, commonly known as the *nematic supercooling temperature*.

A key implication of Proposition 1.2 is that any equilibrium configurations exhibiting biaxiality predicted by the Landau–de Gennes free energy with fourth-order bulk potential arise due to the competition between the bulk and elastic energies. In other words, under the fourth-order bulk potential, biaxiality is not a bulk effect, but is introduced as a result of spatial inhomogeneities.

In this thesis we also work with the smallest-order truncated Taylor expansion which admits biaxial critical points: the more general sixth-order bulk potential, which is of the form

$$f_B(\mathbf{Q}) = \frac{A}{2} \operatorname{tr} \mathbf{Q}^2 - \frac{B}{3} \operatorname{tr} \mathbf{Q}^3 + \frac{C}{4} (\operatorname{tr} \mathbf{Q}^2)^2 + \frac{D}{5} \operatorname{tr} \mathbf{Q}^2 \operatorname{tr} \mathbf{Q}^3 + \frac{E}{6} (\operatorname{tr} \mathbf{Q}^2)^3 + \frac{(F-E)}{6} (\operatorname{tr} \mathbf{Q}^3)^2, \quad (1.37)$$

where we require $E \geq 0, F - E > 0$ to ensure the stability of the expansion. The advantage of using this more complicated bulk potential is that biaxiality can arise as a bulk effect, in contrast to the fourth-order bulk potential.

The addition of a sixth-order term in the Landau–de Gennes theory first appears in the early literature in the likes of [57], [58], with works such as [2], [59], [60] laying the foundation for subsequent studies.

In [61], the authors present a detailed study of the stability of the biaxial phase and the possible phase transitions. The authors demonstrate that, contingent on the model parameter regimes, we may expect both first- and second-order isotropic-biaxial and uniaxial-biaxial phase transitions with the sixth-order bulk potential of the form (1.37).

The authors discuss a simpler form of the potential,

$$f_B(\mathbf{Q}) = \frac{A}{2} \text{tr } \mathbf{Q}^2 - \frac{B}{3} \text{tr } \mathbf{Q}^3 + \frac{C}{4} (\text{tr } \mathbf{Q}^2)^2 + \frac{D}{5} \text{tr } \mathbf{Q}^2 \text{tr } \mathbf{Q}^3 + \frac{F}{6} (\text{tr } \mathbf{Q}^3)^2, \quad (1.38)$$

in [2], noting that a biaxial phase is admissible in this simplified parameter space if $CE > 6D^2/25$ and $(2BD - 5AE)^3 > 6(3AD - 5CB)^2$.

The simplest possible form of the sixth-order bulk potential that allows for a biaxial phase is studied in [53], [62] and given by

$$f_B(\mathbf{Q}) = \frac{A}{2} \text{tr } \mathbf{Q}^2 + \frac{B}{3} \text{tr } \mathbf{Q}^3 + \frac{C}{4} (\text{tr } \mathbf{Q}^2)^2 + \frac{F}{6} (\text{tr } \mathbf{Q}^3)^2. \quad (1.39)$$

Assuming $C > 0$, the authors describe various scenarios, dependent on different temperatures and material parameters, which admit first-order isotropic-uniaxial and uniaxial-biaxial phase transitions, and scenarios which admit a second-order uniaxial-biaxial phase transition under this model.

Chapter 3 of this thesis contains our results regarding the sixth-order bulk potential. In Section 3.2, we demonstrate that there are three critical points of the sixth-order bulk potential in (1.37) below some transition temperature in the restricted class of uniaxial \mathbf{Q} -tensors of the form (1.23), analogous to the uniaxial critical points of the fourth-order bulk potential. The key difference, we will show, is that the critical point with negative scalar order parameter is the global minimiser of the sixth-order bulk potential at sufficiently low temperatures in this restricted class. We also complement the existing work on the bulk biaxial phase by considering the critical points of the sixth-order bulk potential with the more general biaxial \mathbf{Q} -tensor

$$\mathbf{Q} = s \left(\mathbf{n} \otimes \mathbf{n} - \frac{1}{3} \mathbf{I} \right) + p \left(\mathbf{m} \otimes \mathbf{m} - \frac{1}{3} \mathbf{I} \right), \quad (1.40)$$

as discussed in Section 1.3.1, and give an example of a parameter regime in which the global minimiser is biaxial at low temperatures.

1.5.2 The Radial Hedgehog Solution

Defects play an important role in the modelling of confined systems of nematic liquid crystals for applications, as discussed in Section 1.2.3. The radial hedgehog solution is a spherically symmetric configuration, characterised by an isolated, isotropic point defect at the centre of a purely uniaxial droplet of nematic liquid crystal. The universality of the character of defects in confined systems, coupled with the analytical tractability of the radial hedgehog solution, has motivated the study of this defect as a means to understand the structure and stability of point defects in more general liquid crystalline systems [63], [64].

Early Landau–de Gennes treatments of the radial hedgehog solution are given in the likes of [65], [66], and it is well known that the radial hedgehog solution is an explicit

solution of the Landau–de Gennes free energy [63], subject to strong homeotropic, or radial, anchoring. In the context of the one-constant Landau–de Gennes free energy with the fourth-order bulk potential in (1.22), the radial hedgehog solution is described by a uniaxial \mathbf{Q} -tensor of the form (1.23). Specifically, we write

$$\mathbf{Q} = s^*(r) \left(\hat{\mathbf{r}} \otimes \hat{\mathbf{r}} - \frac{1}{3} \mathbf{I} \right), \quad (1.41)$$

where $\hat{\mathbf{r}}$ is the unit vector in the radial direction and the scalar order parameter, s^* , is a solution of the ODE

$$L \left(\frac{d^2 s}{dr^2} + \frac{2}{r} \frac{ds}{dr} - \frac{6}{r^2} s \right) = As - \frac{B}{3} s^2 + \frac{2C}{3} s^3. \quad (1.42)$$

The value of s^* on the boundary of a droplet of radius R is taken to be $s^*(R) = \frac{B + \sqrt{B^2 - 24AC}}{4C}$, noting that this is the larger of the two nonzero critical points of the fourth-order bulk potential, (1.22), given in (1.34). The radial hedgehog solution is characterised by the isotropic point defect at the droplet centre, so it must also hold that $s^*(0) = 0$.

Several properties of the radial hedgehog solution with the fourth-order bulk potential have been proven in the literature. The existence of a radial hedgehog solution as critical point of the Landau–de Gennes free energy is shown in [63] and [64], and the authors also show that the scalar order parameter is bounded below by zero and attains its maximum on the droplet boundary. In addition, in [64], the author proves that the radial hedgehog scalar order parameter is monotonic increasing, provided $A < \frac{B^2}{27C}$, and unique if $A < 0$.

A breadth of work on the stability of the radial hedgehog solution has been carried out in the literature [51], [63], [67]–[69], culminating in the consensus that the radial

hedgehog solution is stable in small droplets or at high temperatures, not far from the nematic-isotropic transition temperature. In [63], [70], it is shown that the radial hedgehog solution is unstable to biaxial perturbations in sufficiently large droplets, while in [71], the authors prove that the Landau–de Gennes global minimiser cannot be purely uniaxial at low temperatures. Furthermore, the authors construct a solution with a ring disclination about the origin in [65], and demonstrate that the radial hedgehog solution has higher energy in an infinite domain, and this competing state, often referred to as the biaxial torus solution, is described in [51], [69], [72], among other sources. The authors indicate that the biaxial torus solution is energetically preferable over the radial hedgehog solution at sufficiently low temperatures and in sufficiently large droplets, and we discuss this state in more detail in the next section. These results collectively suggest that the radial hedgehog configuration yields to the emergence of biaxiality, losing stability as temperature decreases or droplet size increases.

We build upon the existing work by studying the radial hedgehog solution with a sixth-order bulk potential of the form (1.37). This allows us to explore the effects of the bulk potential on the properties of the radial hedgehog solution. In Chapter 3, we prove a range of analytical results for the radial hedgehog solution which highlight the parallels and differences in the character of the radial hedgehog solution with the fourth- and sixth-order potentials.

In addition, we consider the radial hedgehog solution in spherical droplets of ferronematic droplets in Chapter 5, and we introduce ferronematic liquid crystals in Section 1.5.4. We study the key properties of the ferronematic radial hedgehog for comparison with the nematic case.

Finally, we introduce uncertainty into our models and study the solutions of stochastic differential equations in Chapter 6, building upon work in [73]. We obtain radial

hedgehog solutions with random noise in the nematic case with both fourth- and sixth-order bulk potentials, and in the ferronematic case. We discuss stochastics in more detail in Section 1.5.5.

1.5.3 Equilibrium Configurations on the Sphere

The study of droplets of nematic liquid crystals is significant in applications such as electro-optical devices [74], [75] due to their anisotropic physical, rheological and optical properties. Furthermore, defects are inherent in spherical droplets with strong radial anchoring, due to geometrical frustration. Given that defects exhibit distinct optical signatures, it is important to be able to control or predict the presence of specific defects in the design of devices which exploit the optical anisotropy of spherical droplets of nematic liquid crystals, for example. This example is one of several which motivate the need to understand competing equilibrium configurations in spherical droplets of nematic liquid crystals and their defect structures, which we can achieve through studying the stability of critical points of the Landau–de Gennes free energy with respect to temperature, droplet size, and material parameters.

The preceding section discusses the radial hedgehog solution and its properties under the fourth-order bulk potential, which is one of the possible equilibrium configurations in a spherical droplet of nematic liquid crystal. The isotropic point defect present in the radial hedgehog configuration is energetically unfavourable at low temperatures, since the isotropic phase is a local maximum of the fourth-order bulk potential below the nematic supercooling temperature. This suggests that other configurations will have lower energy at lower temperatures in spherical droplets with strong homeotropic anchoring. Such alternative Landau–de Gennes critical points have been studied in a batch of papers [51], [66], [69], [72], and our references are not exhaustive. It is well

known that there exist at least two critical points in addition to the radial hedgehog solution, as mentioned in the previous section: the widely reported biaxial torus solution, which is generally energetically preferable in sufficiently large droplets and at sufficiently low temperatures; and the metastable split core solution, first reported in [72]. Both of these configurations have regions of biaxiality and break the spherical symmetry of the radial hedgehog configuration, instead possessing rotational symmetry about some axis of symmetry through the origin and mirror symmetry across the plane perpendicular to the axis of symmetry.

The biaxial torus configuration is characterised by a disclination loop about the origin, rather than a point defect, and has positive uniaxial order at the droplet centre. This loop is surrounded by a torus-shaped region of biaxiality, which acts as a transition region for the nematic director, which is radially aligned towards the edge of the droplet and parallel to the axis of rotational symmetry at the origin [67]. The biaxial torus was first described as an alternative equilibrium configuration in a spherical droplet in [65], [66] and their claims were supported numerically in [51]. Further studies include [67], [69], [70], [72], all of which support the claim that the biaxial torus configuration is the preferred state in a spherical droplet of nematic liquid crystals, modelled via the Landau–de Gennes free energy with the fourth-order bulk potential, except in small droplets and at high temperatures.

The split core configuration was first reported in [72] and has subsequently been discussed in works such as [76]–[78]. The split core configuration features two isotropic point defects on the axis of rotational symmetry, connected by a disclination line. The split core solution exhibits a region of biaxiality about the origin, terminating at these point defects, and the configuration has a negative order parameter at the origin. As the biaxial torus solution is the likely candidate for global minimality when the radial

hedgehog solution is not the global minimiser in the Landau–de Gennes model for nematic liquid crystals with fourth-order bulk potential, the split core solution is only ever expected to be a locally stable configuration whenever it is defined. The authors in [67] are sceptical about the stability and even existence of the split core as an equilibrium configuration in models lacking the imposed rotational and mirror symmetry, suggesting its status as a metastable state could be an artefact of the symmetry class. However, it has since been shown numerically that the split core configuration can be stable in the absence of symmetry assumptions by [76].

In [67], the authors perform a comprehensive numerical study of the possible equilibrium configurations in spherical droplets which possess rotational and mirror symmetry by solving on a quarter circle domain. The authors construct bifurcation diagrams, plotting the value of the scalar order parameter of each configuration at the origin with respect to temperature and droplet radius, which confirm the findings of earlier works such as [51], [65]. The bifurcation diagrams show that the radial hedgehog solution is the global minimiser in small droplets and at temperatures above some transition temperature, while the biaxial torus solution is the global minimiser below this transition temperature and in sufficiently large droplets. These diagrams also show that the split core configuration exists and is locally minimising at sufficiently low temperatures, thus demonstrating the multistability of the system. An ambiguity of this work is in the character of the unstable branch with positive scalar order parameter at the origin, connecting the globally minimising biaxial torus branch and the metastable split core branch. In Chapter 3, we show that this branch corresponds to a second, unstable biaxial torus configuration, thus completing the picture of the admissible equilibrium configurations and their stability in a spherical droplet of nematic liquid crystals with rotational and mirror symmetry.

To understand the impact of biaxiality as a bulk effect under the sixth-order bulk potential on the multistability of the system, we perform a numerical study on the existence and stability of the solutions of the Landau–de Gennes free energy with fourth- and sixth-order bulk potentials in Chapter 3. We impose rotational and mirror symmetry and demonstrate that the radial hedgehog solution can act as a transition state between the biaxial torus and split core solutions at low temperatures under both the fourth- and sixth-order models. This is of physical relevance as it suggests that some switching mechanism between the biaxial torus and split core configurations is mediated by a radial hedgehog solution. Informally, this transition would look like the disclination ring of the biaxial torus shrinking to the isotropic point defect at droplet centre, and subsequently splitting into the two point defects connected by the disclination line of the split core configuration. We also construct a bifurcation diagram to visualise the solution landscape as a function of temperature in an example parameter regime, analogous to that in [72], to understand how the solution landscape is impacted by the enhanced favourability of biaxiality under the sixth-order bulk potential.

In Chapter 5, we complement our work on the ferronematic radial hedgehog solution by performing a numerical study of the solution landscape on a ferronematic spherical droplet. The authors in [67] suggest that magnetisation may have a stabilising effect on the split core configuration, and we give examples to confirm that this can be the case.

1.5.4 Ferronematics

The dielectric response of nematic liquid crystals (NLCs) to electric fields is widely exploited in applications [6], but the same cannot be said for their response to magnetic fields, which is several orders of magnitude weaker [14]. In practice, this means that the

magnetic response of nematic liquid crystals is negligible in comparison, and unrealistically large magnetic fields are required for a meaningful magnetic response, making NLCs poor candidates for use in devices employing magnetic fields. The concept of using dilute suspensions of magnetic colloids in NLCs to enhance magnetic responses instead was initially proposed theoretically in [79]. The authors suggested that these composite nematics may fall into two categories: so-called *compensated* materials, exhibiting improved responses to external magnetic fields; or *ferronematics*, which not only exhibit enhanced responses but also possess spontaneous magnetisation in the absence of external fields. Subsequent theoretical contributions include [80]–[84].

It has been shown experimentally that doping nematic liquid crystals with magnetic nanoparticles (MNPs) can considerably improve the orientational response to magnetic fields [85], [86], with the first experiments reported in [87]. However, the first stable ferronematic suspension with spontaneous magnetisation was not achieved until the work in [88], several decades after the early publications [79], [87], with a more in-depth review given in [89]. Prior studies struggled with MNP aggregation or lacked the hallmark spontaneous magnetisation of ferronematics [90]. The authors in [88], [89] identified that the shape of the MNPs is vital in the preparation of stable suspensions which possess spontaneous magnetisation in the absence of external fields. They report success using nanometre-sized, platelet-shaped magnetic particles, rather than rod- or sphere-shaped particles, for example. More recent experimental studies have since built upon this foundation, bringing us closer to realising the potential for ferronematics in real-world applications. Such work is reported in the likes of [91]–[95].

Multistable nematic systems have found widespread use in various applications, with a prominent example being bistable liquid crystal displays [22], [23], [96]. Analogously, confined systems of ferronematics which support multiple stable states may

hold potential in applications, and the solution landscapes are possibly richer than their nematic counterparts due to the added magnetic order. If stable states can be identified in a ferronematic solution landscape, it is possible that magnetic fields could be applied to guide switching between stable states by following specific transition pathways, thus enhancing the ability to select particular stable states in multistable ferronematic devices.

In Chapters 4 and 5, we consider dilute suspensions of MNPs. We make certain assumptions: the MNPs are significantly smaller than the average distance between them; they are uniformly distributed; and their total volume fraction is small [97]. Despite the absence of external magnetic fields, the system exhibits spontaneous magnetisation due to interactions between the MNPs and NLCs. We model the system via two order parameters: the Landau–de Gennes \mathbf{Q} -tensor to describe the nematic order; and a magnetisation vector, \mathbf{M} , to describe the magnetic field generated by the inclusion of the MNPs.

Dilute suspensions of MNPs in confined nematic systems have been studied using the order parameters \mathbf{Q} and \mathbf{M} in [97]–[99], using a variational model comprising three components: a Landau–de Gennes energy for the nematic liquid crystal, a magnetisation energy, and a nemato-magnetic coupling energy. The authors in [98], [99] numerically investigate the effects of model parameters on solutions in one- and two-dimensions. The authors in [97] further this work in a one-dimensional channel, providing analytical results on existence, uniqueness and stability of solutions, and exploring the multistable ferronematic solution landscape numerically.

In Chapter 5, we work with a free energy similar to that in [98], [99]:

$$\mathcal{F}[\mathbf{Q}, \mathbf{M}] = \int_{\Omega} \left(\frac{L}{2} |\nabla \mathbf{Q}|^2 + \frac{A}{2} \text{tr} \mathbf{Q}^2 - \frac{B}{3} \text{tr} \mathbf{Q}^3 + \frac{C}{4} (\text{tr} \mathbf{Q}^2)^2 + \frac{\kappa}{2} |\nabla \mathbf{M}|^2 + \frac{\alpha}{2} |\mathbf{M}|^2 + \frac{\beta}{4} |\mathbf{M}|^4 + \frac{\alpha^2}{4\beta} - \gamma \mathbf{Q} \mathbf{M} \cdot \mathbf{M} \right) dV, \quad (1.43)$$

where the first four terms are the fourth-order Landau–de Gennes free energy in (1.22). The following four terms comprise the energy associated with the spatially varying magnetisation vector, \mathbf{M} , with associated elastic constant κ , while the constants α and β describe the ferromagnetic transition [88] and the additive constant $\alpha^2/4\beta$ is included for mathematical convenience. The final term captures the nemato-magnetic coupling, with coupling constant γ , which we interpret as a measure of the strength of the coupling (we will replace γ with the rescaled coupling parameter, c , in the dimensionless model given in subsequent chapters). A positive coupling parameter coerces the nematic director to be parallel to the magnetisation vector, \mathbf{M} ; while a negative coupling parameter indicates the coupling energy favours that they be perpendicular.

Until the work in [98], ferronematics in confinement had been modelled using a unit vector to describe the nematic order together with a magnetisation vector [81], [83], [88], [100]. The authors in [98] replace the nematic director with the Landau–de Gennes \mathbf{Q} -tensor and include an elastic energy density in \mathbf{M} to penalise inhomogeneities or jumps in \mathbf{M} to arrive at free energy of the form (1.43). The authors work with a coupling energy density analogous to that proposed in [81], which is reasonable to use as the NLC-MNP interactions and the microscopic properties of the MNPs can be homogenised in the dilute limit [83].

In Chapter 4, we look for critical points of the ferronematic bulk energy:

$$f_{FB}(\mathbf{Q}, \mathbf{M}) = \frac{A}{2} \text{tr} \mathbf{Q}^2 - \frac{B}{3} \text{tr} \mathbf{Q}^3 + \frac{C}{4} (\text{tr} \mathbf{Q}^2)^2 + \frac{\alpha}{2} |\mathbf{M}|^2 + \frac{\beta}{4} |\mathbf{M}|^4 + \frac{\alpha^2}{4\beta} - \gamma \mathbf{Q} \mathbf{M} \cdot \mathbf{M}, \quad (1.44)$$

with \mathbf{Q} -tensor and magnetisation vector of the form

$$\mathbf{Q} = \begin{bmatrix} q_1 - q_3 & q_2 & 0 \\ q_2 & -q_1 - q_3 & 0 \\ 0 & 0 & 2q_3 \end{bmatrix}, \quad \text{and} \quad \mathbf{M} = \begin{bmatrix} m_1 \\ m_2 \\ m_3 \end{bmatrix}, \quad (1.45)$$

respectively. We are interested in whether the inclusion of MNPs can induce biaxiality as a bulk effect, and we find that this is in fact the case for both positive and negative coupling parameters.

In Chapter 5, we complement existing work on the nematic radial hedgehog with fourth-order bulk potential outlined in Section 1.3.2 and our work with the sixth-order bulk potential in Chapter 3 by studying the ferronematic radial hedgehog solution. The radial hedgehog solution is described by the usual \mathbf{Q} -tensor of the form (1.41), with associated magnetisation vector $\mathbf{M} = m(r)\hat{\mathbf{r}}$, recalling that $\hat{\mathbf{r}}$ is the unit vector in the radial direction. As we do in the nematic case with the sixth-order bulk potential in Chapter 3, we prove a collection of analytical results for the ferronematic radial hedgehog solution to understand how the nemato-magnetic coupling influences the properties of the radial hedgehog solution. Later in Chapter 5, we explore the ferronematic solution landscape on a spherical droplet with rotational and mirror symmetry to understand how the system is affected by the NLC-MNP coupling. In particular, we show that the radial hedgehog solution remains a transition state between split core and biaxial

torus solutions and we construct bifurcation diagrams as a function of temperature for a range of droplet radii and positive coupling strengths. As suggested in [67], it is possible that the coalignment of the preferred orientation of the nematic liquid crystals and the magnetic field could enhance the stability of the split core solution, and we find that this is the case in instances with strong enough nemato-magnetic coupling. We also find example scenarios where a new, unstable split core solution becomes admissible in the system, which could be an alternative candidate to the radial hedgehog solution as a transition state in switching mechanisms in such scenarios.

1.5.5 Stochastic Effects on Deterministic Landau–de Gennes Solutions

In Chapters 3-5, we study droplets of nematic and ferronematic liquid crystals with deterministic Landau–de Gennes models. This work is rooted in a solid foundation in the literature which employs these methods, and such studies provide valuable and valid insights into the behaviour of these systems, informing experiments and applications. Nonetheless, deterministic models rely on assumptions and simplifications by design, meaning they are likely to overlook any potential imperfections, uncertainties and nuances intrinsic in physical systems. Stochastic models can expose the shortcomings of a deterministic model by revealing more complex or nuanced behaviour. Conversely, they can also be used to endorse the reliability of deterministic models if their conclusions are in approximate agreement.

We work with stochastic Landau–de Gennes models for the nematic and ferronematic radial hedgehog solution in Chapter 6, which may be able to capture this inherent variability via the inclusion of additive random noise modelled by a Q -Wiener process, which we discuss in more detail below, and thus offer insights that are closer to the

true behaviour of these systems. Specifically, additive noise is implemented via an additional term in the relevant gradient flow equations and does not depend on the unknown variable.

The vast majority of existing research concerning nematic and ferronematic liquid crystals in confined systems relies on deterministic models, including the continuum theories such as the Oseen–Frank, Ericksen, and Landau–de Gennes models discussed in Section 1.2.2, alongside other approaches. There are a limited number of studies employing stochastic continuum models for nematic liquid crystals. A stochastic Ericksen–Leslie equation with multiplicative noise, i.e. noise which depends on the unknown variable, has been studied analytically in [101]–[105]. The authors prove a host of analytical results, including existence and uniqueness of solutions, but do not focus on specific model examples. The only paper to date which considers a Landau–de Gennes model with stochastic terms is [73]. The authors numerically explore the solution landscape on two-dimensional square domains with both multiplicative and additive noise. They also perform a preliminary numerical study of the radial hedgehog solution with the fourth-order bulk potential with additive noise.

In [73], noise is incorporated via an additional term in the gradient flow equations, and this noise is generated via a Q -Wiener stochastic process [106]. A Q -Wiener process exhibits randomness in space and time and is characterised by random increments at points in space that are correlated. This means that fluctuations in the liquid crystal alignment at one point influences the alignment of nearby molecules, making a Q -Wiener process an appropriate choice to capture the effects of the likes of material imperfections, thermal fluctuations, or variations in experimental measurements.

The work in Chapter 6 is a direct extension of the findings outlined in [73] concerning the radial hedgehog solution. In the existing work, the authors worked with

a Landau–de Gennes model with the fourth-order bulk potential and incorporated additive noise. They demonstrated that the perfect rotational symmetry of the radial hedgehog solution is broken when random noise is introduced. Notably, the influence of noise was found to be more pronounced on smaller domains compared to larger domains. We expand upon this work by studying the radial hedgehog solution with the sixth-order bulk potential in the nematic case and in the ferronematic case under the influence of random noise. We consider domains of different sizes at a range of temperatures, and a range of coupling strengths in the ferronematic case, and incorporate noise of different strengths. We confirm that symmetry is broken and properties such as the monotonicity of the radial hedgehog scalar order parameter can be violated in certain scenarios, but otherwise find that the stochastic models agree well with the deterministic models discussed in Chapters 3-5.

Despite the inherent randomness in the stochastic simulations, the qualitative behavior of stochastic solutions presented in Chapter 6 remains largely consistent with the deterministic predictions, and stochastic solutions generally agree with the shape of radial hedgehog scalar order parameter profiles. We observe certain scenarios in which the value of the scalar order parameter is reduced in the droplet bulk in the stochastic case, and speculate that this reduction in ordering reflects real-world scenarios in which the perfect conditions assumed under a deterministic model are rarely met. These observations lead us to conclude that stochastic results corroborate the deterministic model and enrich our understanding by incorporating some of the variability and randomness inherent in real-world systems. The primary qualitative features remain unchanged, validating deterministic predictions, while providing an arguably more nuanced and realistic depiction of the radial hedgehog solution.

Chapter 2

Preliminary Material

In this chapter, we outline some details that contextualise the problems we study in later chapters; and provide an overview of the methods employed. We begin by giving a review of some of the properties of critical points of the Landau–de Gennes free energy in Section 2.1. We then discuss the nondimensionalisation of the Landau–de Gennes free energy with the sixth-order bulk potential and the ferronematic free energy in Section 2.2. Finally, in Section 2.3, we outline the numerical methods we use in Chapters 3 and 5.

2.1 Solutions of the Landau–de Gennes Free Energy

In this section, we review key results concerning the Landau–de Gennes free energy with the fourth-order bulk potential. In subsequent chapters, these results are generalised to a Landau–de Gennes free energy with a sixth-order bulk potential and a ferronematic free energy.

We work in a ball of radius R centred at the origin,

$$B(0, R) = \{\mathbf{x} \in \mathbb{R}^2 : |\mathbf{x}| \leq R\}. \quad (2.1)$$

We consider critical points of the Landau–de Gennes free energy with the fourth-order bulk potential in the absence of surface energies and external fields:

$$\mathcal{F}[\mathbf{Q}] = \int_{B(0,R)} \frac{L}{2} |\nabla \mathbf{Q}|^2 + f_B(\mathbf{Q}) \, dV, \quad (2.2)$$

where f_B denotes the bulk energy density

$$f_B(\mathbf{Q}) = \frac{A}{2} \operatorname{tr} \mathbf{Q}^2 - \frac{B}{3} \operatorname{tr} \mathbf{Q}^3 + \frac{C}{4} (\operatorname{tr} \mathbf{Q}^2)^2. \quad (2.3)$$

We enforce strong homeotropic anchoring, following [63], [64], [67], that ensures the bulk energy density, f_B , is minimised on the boundary, denoted by the Dirichlet boundary condition

$$\mathbf{Q} = \mathbf{Q}_{s_+} := s_+ \left(\hat{\mathbf{r}} \otimes \hat{\mathbf{r}} - \frac{1}{3} \mathbf{I} \right) \quad \text{on } \partial B(0, R), \quad (2.4)$$

where

$$s_+ = \frac{B + \sqrt{B^2 - 24AC}}{4C}, \quad (2.5)$$

and $\hat{\mathbf{r}}$ is the unit vector in the radial direction in three dimensions. The admissible space for critical points of (2.2) is defined to be

$$\mathcal{A}_{\mathbf{Q}} = \left\{ \mathbf{Q} \in W^{1,2}(B(0, R), \mathcal{S}_0) : \mathbf{Q} = \mathbf{Q}_{s_+} \text{ on } \partial B(0, R) \right\}, \quad (2.6)$$

and we recall that \mathcal{S}_0 is the space of symmetric, traceless 3×3 matrices and the Sobolev space $W^{1,2}(B(0, R), \mathcal{S}_0)$ is given by

$$W^{1,2}(B(0, R), \mathcal{S}_0) = \left\{ \mathbf{Q} \in \mathcal{S}_0 : \int_{B(0,R)} |\mathbf{Q}|^2 + |\nabla \mathbf{Q}|^2 \, dV < \infty \right\}. \quad (2.7)$$

In simple terms, this is the space of square-integrable \mathbf{Q} -tensors in \mathcal{S}_0 which have square-

integrable first derivatives. This space is a common choice in the study of variational problems.

A key question in the study of functionals of the form (2.2) is the existence of a global minimiser that belongs to the admissible space, $\mathcal{A}_{\mathbf{Q}}$. Without existence, any other results regarding properties of minimisers of (2.2) in $\mathcal{A}_{\mathbf{Q}}$ are irrelevant. The existence of a global minimiser can be proven via the direct methods in the calculus of variations [107], [108]. There are three key steps: demonstrating that the admissible space, $\mathcal{A}_{\mathbf{Q}}$, is nonempty; proving weak lower semi-continuity of the Landau–de Gennes free energy (2.2); and proving coercivity of (2.2). We reproduce an existence result in the fourth-order case here [56], [108], which can be generalised to a Landau–de Gennes free energy with a sixth-order bulk potential and a ferronematic free energy.

Proposition 2.1. *There exists a global minimiser, \mathbf{Q}^* , of \mathcal{F} in (2.2) in the admissible space, $\mathcal{A}_{\mathbf{Q}}$ in (2.6).*

Proof. Firstly, the admissible space, $\mathcal{A}_{\mathbf{Q}}$, is nonempty since $\mathbf{Q}_{s+} \in \mathcal{A}_{\mathbf{Q}}$. Next, the free energy in (2.2) is weakly lower-semicontinuous, meaning

$$\liminf_{n \rightarrow \infty} \mathcal{F}[\mathbf{Q}_n] \geq \mathcal{F}[\mathbf{Q}] \quad (2.8)$$

when $\mathbf{Q}_n \rightharpoonup \mathbf{Q}$ in $W^{1,2}(B(0, R); \mathcal{S}_0)$, since the elastic energy density is convex in $\nabla \mathbf{Q}$ (see Chapter 8, Theorem 1 in [107]). Finally, since the bulk energy density, f_B , is a polynomial in $|\mathbf{Q}|$, it is bounded from below, and we may write

$$\frac{L}{2} |\nabla \mathbf{Q}|^2 + \frac{A}{2} \operatorname{tr} \mathbf{Q}^2 - \frac{B}{3} \operatorname{tr} \mathbf{Q}^3 + \frac{C}{4} (\operatorname{tr} \mathbf{Q}^2)^2 \geq a_1 |\nabla \mathbf{Q}|^2 + a_2, \quad (2.9)$$

for some positive constants $a_1, a_2(A, B, C)$. Therefore, we may conclude that

$$\mathcal{F}[\mathbf{Q}] \geq a_3 \|\nabla \mathbf{Q}\|_{L^2(B(0,R))}^2 + a_4, \quad (2.10)$$

for positive constants a_3, a_4 , which guarantees coercivity, which means that

$$\frac{\mathcal{F}[\mathbf{Q}]}{|\mathbf{Q}|} \rightarrow \infty \quad \text{as} \quad |\mathbf{Q}| \rightarrow \infty, \quad (2.11)$$

which implies that \mathcal{F} grows faster than $|\mathbf{Q}|$. Therefore, there must exist a global minimiser of (2.2) in the admissible space $\mathcal{A}_{\mathbf{Q}}$. \square

Any critical point of (2.2) satisfies the associated Euler–Lagrange equations [49], which are obtained via the equations

$$\frac{\partial}{\partial x_k} \frac{\partial \mathcal{E}}{\partial Q_{ij,k}} = \frac{\partial \mathcal{E}}{\partial Q_{ij}}, \quad i, j = 1, 2, 3, \quad (2.12)$$

where \mathcal{E} is the integrand of the energy functional (2.2), and can be expressed as

$$L\Delta Q_{ij} = A Q_{ij} - B \left(Q_{ik} Q_{kj} - \frac{1}{3} \delta_{ij} \operatorname{tr} \mathbf{Q}^2 \right) + C Q_{ij} \operatorname{tr} \mathbf{Q}^2, \quad i, j = 1, 2, 3, \quad (2.13)$$

where

$$\frac{B}{3} \delta_{ij} \operatorname{tr} \mathbf{Q}^2 \quad (2.14)$$

is a Lagrange multiplier for the tracelessness constraint. Furthermore, solutions of the Euler–Lagrange equations are real analytic in $B(0, R)$ (see Proposition 13 in [49]). We present Euler–Lagrange equations in the nematic case with the sixth-order bulk potential and in the ferronematic case in Chapters 3 and 5, respectively.

The extension of the existence result in Proposition 2.1 to a Landau–de Gennes free

energy with a sixth-order potential as in (1.37) is immediate, since the elastic energy is unchanged, and the sixth-order potential is also a polynomial in $|\mathbf{Q}|$, meaning it is bounded below and coercivity holds. Extending the existence result to the ferronematic free energy in (1.43) is more delicate. Weak lower-semicontinuity holds since the energy density is convex in the gradient of the \mathbf{Q} -tensor and in the gradient of the magnetisation vector. The added complication is the lower-boundedness of the nemato-magnetic coupling term, which requires a more careful argument, and we provide further details in Chapter 5.

Equipped with existence and analyticity, we now consider the notion of a maximum principle for solutions of the above Euler–Lagrange equations and reproduce an important result below, which is proven in [56] and [49]. This result yields natural upper bounds for the scalar order parameters of a global minimiser of the Landau–de Gennes free energy in terms of temperature and the bulk constants, and implies that the degree of ordering in the interior of the droplet is at most equal to that on the edge of the droplet. Furthermore, this upper bound helps to identify regimes of agreement between the Landau–de Gennes definition of the \mathbf{Q} -tensor and the statistical interpretation of the \mathbf{Q} -tensor as the second moment of a probability distribution function, as discussed in [56]. It is pointed out in [56] that bounds on the scalar order parameters of equilibrium configurations can be derived from the probabilistic definition of the \mathbf{Q} -tensor order parameter, and these constraints indicate what is physical. Comparison with the upper bound described below can indicate when equilibrium scalar order parameters and, by extension, certain parameter regimes are not physical.

Proposition 2.2. *Suppose \mathbf{Q} is a global minimiser of the Landau–de Gennes energy*

functional \mathcal{F} in (2.2) in the admissible space $\mathcal{A}_{\mathbf{Q}}$ in (2.6). Then

$$|\mathbf{Q}|^2 \leq \frac{2}{3}s_+^2, \quad (2.15)$$

where s_+ is defined in (2.5).

Proof. Suppose for a contradiction that $|\mathbf{Q}|^2$ attains its maximum at some point $\mathbf{r}^* \in \overline{B(0, R)}$, and $|\mathbf{Q}(\mathbf{r}^*)|^2 > \frac{2}{3}s_+^2$. Hence we have that

$$\Delta\left(\frac{1}{2}|\mathbf{Q}|^2\right)(\mathbf{r}^*) \leq 0. \quad (2.16)$$

Multiplying both sides of the Euler–Lagrange equations (2.13) by Q_{ij} , we write

$$LQ_{ij}\Delta Q_{ij} = A \operatorname{tr} \mathbf{Q}^2 - B \operatorname{tr} \mathbf{Q}^3 + C (\operatorname{tr} \mathbf{Q}^2)^2, \quad (2.17)$$

where we have used the tracelessness of \mathbf{Q} . Next, we use the fact that $\Delta\left(\frac{1}{2}|\mathbf{Q}|^2\right) = Q_{ij}\Delta Q_{ij} + |\nabla \mathbf{Q}|^2$ to write

$$L\Delta\left(\frac{1}{2}|\mathbf{Q}|^2\right) = L|\nabla \mathbf{Q}|^2 + A \operatorname{tr} \mathbf{Q}^2 - B \operatorname{tr} \mathbf{Q}^3 + C (\operatorname{tr} \mathbf{Q}^2)^2. \quad (2.18)$$

We recall the definition of the biaxiality parameter, β :

$$\beta = 1 - 6 \frac{(\operatorname{tr} \mathbf{Q}^3)^2}{(\operatorname{tr} \mathbf{Q}^2)^3}, \quad (2.19)$$

with $\beta \in [0, 1]$. The nonnegativity of β implies that $\operatorname{tr} \mathbf{Q}^3 \leq \frac{1}{\sqrt{6}}|\mathbf{Q}|^3$, using the fact that $\operatorname{tr} \mathbf{Q}^2 = |\mathbf{Q}|^2$. Then, from (2.18), we may write

$$L\Delta\left(\frac{1}{2}|\mathbf{Q}|^2\right) \geq L|\nabla \mathbf{Q}|^2 + A|\mathbf{Q}|^2 - \frac{B}{\sqrt{6}}|\mathbf{Q}|^3 + C|\mathbf{Q}|^4, \quad (2.20)$$

and it is straightforward to show that

$$h(|\mathbf{Q}|) := A|\mathbf{Q}|^2 - \frac{B}{\sqrt{6}}|\mathbf{Q}|^3 + C|\mathbf{Q}|^4 > 0 \quad (2.21)$$

when $|\mathbf{Q}| > \sqrt{\frac{2}{3}}s_+$, by considering the zeros of h , the largest of which is $\sqrt{\frac{2}{3}}s_+$, and noting that $h(|\mathbf{Q}|) \rightarrow +\infty$ as $|\mathbf{Q}| \rightarrow \infty$. Therefore, we must have that

$$\Delta\left(\frac{1}{2}|\mathbf{Q}|^2\right)(r^*) > 0, \quad (2.22)$$

which is a contradiction. Hence, $|\mathbf{Q}|^2 \leq \frac{2}{3}s_+^2$. \square

Proposition 2.2 essentially tells us that the maximum ordering occurs on the boundary of the droplet. Or in other words, the strong anchoring on the boundary of the droplet enforces the highest degree of ordering, and the degree of ordering is weaker throughout the rest of the droplet.

We derive maximum principles for the minimisers of the Landau–de Gennes free energy and the ferronematic free energy in Chapters 3 and 5, respectively. We prove a maximum principle for uniaxial global minimisers in the sixth-order case, which follows a similar contradiction argument and considers the roots of an analogous polynomial in $|\mathbf{Q}|$. In the ferronematic case in Chapter 5, we prove a maximum principle for the ferronematic radial hedgehog solution below the nematic supercooling temperature, also via a contradiction argument, which relies on the specific form of the radial hedgehog solution to make the problem tractable.

2.2 Nondimensionalisation

It is common practice to nondimensionalise and rescale models before performing any analysis. As such, we nondimensionalise the Landau–de Gennes free energy with the sixth-order bulk potential and the ferronematic free energy; and we rescale the domain in each case to the unit ball,

$$B(0, 1) = \{\mathbf{x} \in \mathbb{R}^3 : |\mathbf{x}| \leq 1\}, \quad (2.23)$$

before proceeding.

2.2.1 The Landau–de Gennes Free Energy with Sixth-Order Bulk Potential

In Sections 1.3 and 1.5.1, we introduce a Landau–de Gennes free energy, which takes the form

$$\mathcal{F}[\mathbf{Q}] = \int_{B(0,R)} \frac{L}{2} |\nabla \mathbf{Q}|^2 + f_B(\mathbf{Q}) dV, \quad (2.24)$$

where f_B can be either the fourth- or sixth-order bulk potential.

In Chapters 3 and 6, we work with a nondimensionalised version of the above free energy, inspired by [76]. Let

$$\tilde{\mathbf{x}} = \frac{1}{R} \mathbf{x}, \quad \tilde{\mathbf{Q}} = \sqrt{\frac{27C^2}{2B^2}} \mathbf{Q}. \quad (2.25)$$

The dimensionless free energy with the fourth-order bulk potential is then given by

$$\mathcal{F}_4 = \tilde{\mathcal{F}}[\tilde{\mathbf{Q}}] = \int_{B(0,1)} \frac{\varepsilon^2}{2} |\nabla \tilde{\mathbf{Q}}|^2 + \frac{t}{2} \operatorname{tr} \tilde{\mathbf{Q}}^2 - \sqrt{6} \operatorname{tr} \tilde{\mathbf{Q}}^3 + \frac{1}{2} (\operatorname{tr} \tilde{\mathbf{Q}}^2)^2 d\tilde{V}, \quad (2.26)$$

and with the sixth-order bulk potential is given by

$$\begin{aligned} \mathcal{F}_6 = \tilde{\mathcal{F}}[\tilde{\mathbf{Q}}] = \int_{B(0,1)} & \frac{\varepsilon^2}{2} |\nabla \tilde{\mathbf{Q}}|^2 + \frac{t}{2} \operatorname{tr} \tilde{\mathbf{Q}}^2 - \sqrt{6} \operatorname{tr} \tilde{\mathbf{Q}}^3 + \frac{1}{2} (\operatorname{tr} \tilde{\mathbf{Q}}^2)^2 \\ & + \frac{d}{5} \tilde{\mathbf{Q}}^2 \operatorname{tr} \tilde{\mathbf{Q}}^3 + \frac{e}{6} (\operatorname{tr} \tilde{\mathbf{Q}}^2)^3 + \frac{(f-e)}{6} (\operatorname{tr} \tilde{\mathbf{Q}}^3)^2 d\tilde{V}, \end{aligned} \quad (2.27)$$

where the characteristic length scale is given by $\xi = \sqrt{\frac{27CL}{B^2}}$ with $\varepsilon = \frac{\xi}{R}$, and

$$t = \frac{27AC}{B^2}, \quad d = \frac{2\sqrt{6}BD}{9C^2}, \quad e = \frac{4B^2E}{27C^3}, \quad f = \frac{4B^2F}{27C^3}. \quad (2.28)$$

We note that this rescaling reduces the domain to the unit ball in three dimensions, $B(0,1)$, and the geometrical properties are captured by the parameter ε . We refer to t as the temperature for convenience, although it is, more precisely, a function of the absolute temperature. We drop the tildes for brevity in the rest of this thesis and all results are interpreted in terms of the dimensionless variables.

We adopt this particular rescaling of the Landau–de Gennes free energy and capture the effects of temperature through the parameter t , referred to as the reduced temperature. Furthermore, since we have rescaled the domain to the unit ball, the computational domain remains constant in our numerical simulations and we instead capture a changing radius through the parameter ε .

While there are no current values obtained for the constants D, E and F in the literature, there are known values for the constants B and C for a range of commonly used liquid crystals. In particular, for MBBA, the values are [109]

$$B = 0.64 \times 10^6 Nm^{-2}, \quad C = 0.35 \times 10^6 Nm^{-2}. \quad (2.29)$$

In practice, one would know the values for B, C, D, E and F for a given material, then

these could be translated into our dimensionless coefficients. In this thesis, we choose values for the dimensionless coefficients to describe mathematical scenarios, which may be applicable to liquid crystals which one day may be synthesised.

2.2.2 The Ferronematic Free Energy

The dimensional ferronematic free energy introduced in Section 1.5.4 is of the form

$$\begin{aligned} \mathcal{F}[\mathbf{Q}, \mathbf{M}] = \int_{B(0,R)} & \frac{L}{2} |\nabla \mathbf{Q}|^2 + \frac{A}{2} \operatorname{tr} \mathbf{Q}^2 - \frac{B}{3} \operatorname{tr} \mathbf{Q}^3 + \frac{C}{4} (\operatorname{tr} \mathbf{Q}^2)^2 \\ & + \frac{\kappa}{2} |\nabla \mathbf{M}|^2 + \frac{\alpha}{2} |\mathbf{M}|^2 + \frac{\beta}{4} |\mathbf{M}|^4 + \frac{\alpha^2}{4\beta} - \gamma \mathbf{Q} \mathbf{M} \cdot \mathbf{M} \, dV. \end{aligned} \quad (2.30)$$

Inspired by [98], we introduce the scaling

$$\tilde{\mathbf{x}} = \frac{\mathbf{x}}{R}, \quad \tilde{\mathbf{Q}} = \sqrt{\frac{27C^2}{2B^2}} \mathbf{Q}, \quad \tilde{\mathbf{M}} = \sqrt{\frac{\beta}{|\alpha|}} \mathbf{M}, \quad (2.31)$$

and arrive at the dimensionless free energy

$$\begin{aligned} \mathcal{F}_F = \tilde{\mathcal{F}}[\tilde{\mathbf{Q}}, \tilde{\mathbf{M}}] = \int_{B(0,1)} & \xi_1 \left(\frac{\ell_1}{2} |\nabla \tilde{\mathbf{Q}}|^2 + \frac{t}{2} \operatorname{tr} \tilde{\mathbf{Q}}^2 - \sqrt{6} \operatorname{tr} \tilde{\mathbf{Q}}^3 + \frac{1}{2} (\operatorname{tr} \tilde{\mathbf{Q}}^2)^2 \right) \\ & + \xi_2 \left(\frac{\ell_2}{2} |\nabla \tilde{\mathbf{M}}|^2 + \frac{1}{4} (|\tilde{\mathbf{M}}|^2 - 1)^2 - c \tilde{\mathbf{Q}} \tilde{\mathbf{M}} \cdot \tilde{\mathbf{M}} \right) d\tilde{V}, \end{aligned} \quad (2.32)$$

where

$$\begin{aligned} t = \frac{27AC}{B^2}, \quad \xi_1 = \frac{2B^3}{27^2 C^3}, \quad \xi_2 = \frac{\alpha^2}{\beta B}, \\ \ell_1 = \frac{27LC}{B^2 R^2}, \quad \ell_2 = \frac{\kappa}{|\alpha| R^2}, \quad c = \gamma \sqrt{\frac{2}{27C^2}} \frac{|\alpha|}{\beta}. \end{aligned} \quad (2.33)$$

We note that we have again rescaled the domain to the unit ball, $B(0, 1)$, and capture temperature via the reduced temperature t and different radii via the parameters ℓ_1 and ℓ_2 . Again, we drop the tildes for brevity in the rest of this thesis and interpret all

results in terms of the dimensionless variables. We also set $\xi_1 = \xi_2 = 1$ and $\ell_1 = \ell_2 =: \ell$ in this thesis, for simplicity. The scaling parameters ξ_1 and ξ_2 measure the strength of the nematic and magnetic energies. In setting $\xi_1 = \xi_2 = 1$, we assume the energies are equal in strength; while in setting $\ell_1 = \ell_2 =: \ell$, we assume that the nematic and magnetic elastic constants have comparable magnitude, or are both very small. The physical meaning of these assumptions are that equilibrium configurations are not dominated by the preferred liquid crystal behaviour, nor the preferred magnetisation behaviour (as may be the case if ξ_1 and ξ_2 differed in magnitude); and that the effects of spatial homogeneities on the liquid crystal configuration and the magnetisation are comparable.

We note that we assume that the magnetisation is independent of temperature in this model. While magnetisation is generally temperature-dependent, we assume here that the effects of temperature on the magnetisation are negligible in this case in comparison to the effects of temperature on the liquid crystals.

2.3 Numerical Methods

In Chapters 3 and 5, we numerically compute equilibrium configurations on spherical droplets of nematic and ferronematic liquid crystals, and study their stability. We employ finite element [110], gradient flow, continuation [111], and HiOSD [112] methods to solve for numerical solutions and construct a picture of the solution landscapes in the nematic cases with fourth- and sixth-order bulk potentials; as well as in the ferronematic case. We outline the numerical framework and methods in the sections below.

We present the problem formulation and numerical methods in the nematic case with the fourth-order bulk potential here. The numerical framework is analogous in the nematic case with the sixth-order bulk potential and in the ferronematic case. We

present the specific details of the numerical methods in these cases in Sections 3.4 and 5.2, respectively, noting that they are direct extensions of the nematic case with fourth-order bulk potential.

The content in this section is adapted from [1].

2.3.1 Symmetry and Boundary Conditions

Following previous work in [67], we numerically compute critical points of the Landau–de Gennes free energy in (2.26) with rotational symmetry about the z -axis, and mirror symmetry across the xy -plane. In this case, our domain is reduced to a quarter circle. We work in cylindrical polar coordinates (r, θ, z) , where $r \in [0, 1]$ and $z \in [0, 1]$, while θ is the angle in the xy -plane.

We recall that the \mathbf{Q} -tensor order parameter has five degrees of freedom in the most general setting, and it is possible to represent the \mathbf{Q} -tensor in terms of five basis tensors, as in (1.10) in Section 1.3.1 [51]. However, in our numerical framework, following the work in [67] and related papers, the \mathbf{Q} -tensor always has an eigenvector in the direction \mathbf{e}_θ , normal to the rz -plane, which is a consequence of the symmetry assumptions described above. With a fixed eigenvector, the degrees of freedom reduce from five to three, with one degree of freedom associated with the free eigenvectors in the rz -plane and two degrees of freedom associated with the eigenvalues of a traceless \mathbf{Q} -tensor. Hence, we express the \mathbf{Q} -tensor in terms of just three basis tensors as

$$\mathbf{Q}(r, z) = q_1(r, z)\mathbf{E}_1 + q_2(r, z)\mathbf{E}_2 + q_3(r, z)\mathbf{E}_3, \quad (2.34)$$

where

$$\mathbf{E}_1 = \frac{\sqrt{6}}{6} \begin{bmatrix} -1 & 0 & 0 \\ 0 & -1 & 0 \\ 0 & 0 & 2 \end{bmatrix}, \quad \mathbf{E}_2 = \frac{\sqrt{2}}{2} \begin{bmatrix} 1 & 0 & 0 \\ 0 & -1 & 0 \\ 0 & 0 & 0 \end{bmatrix}, \quad \mathbf{E}_3 = \frac{\sqrt{2}}{2} \begin{bmatrix} 0 & 0 & 1 \\ 0 & 0 & 0 \\ 1 & 0 & 0 \end{bmatrix}. \quad (2.35)$$

We assume that the three degrees of freedom, q_1, q_2 , and q_3 , are independent of θ , consistent with our assumptions of rotational symmetry about the z -axis and mirror symmetry about $z = 0$.

We then rewrite the Landau–de Gennes free energy (2.26) in terms of q_1, q_2 , and q_3 . First, the \mathbf{Q} -tensor in (2.34) can be written in terms of r, θ , and z by

$$\mathbf{Q}(r, \theta, z) = \mathbf{R}(\theta) \mathbf{Q}(r, z) \mathbf{R}(\theta)^T, \quad (2.36)$$

where \mathbf{R} is the rotation matrix

$$\mathbf{R}(\theta) = \begin{bmatrix} \cos \theta & -\sin \theta & 0 \\ \sin \theta & \cos \theta & 0 \\ 0 & 0 & 1 \end{bmatrix}. \quad (2.37)$$

Then the \mathbf{Q} -tensor is given by

$$\mathbf{Q}(r, \theta, z) = \begin{bmatrix} -\frac{\sqrt{6}q_1}{6} + \frac{\sqrt{2}q_2}{2} (\cos^2 \theta - \sin^2 \theta) & \sqrt{2}q_2 \cos \theta \sin \theta & \frac{\sqrt{2}}{2} q_3 \cos \theta \\ \sqrt{2}q_2 \cos \theta \sin \theta & -\frac{\sqrt{6}q_1}{6} + \frac{\sqrt{2}q_2}{2} (\sin^2 \theta - \cos^2 \theta) & \frac{\sqrt{2}q_3}{2} \sin \theta \\ \frac{\sqrt{2}q_3}{2} \cos \theta & \frac{\sqrt{2}q_3}{2} \sin \theta & \frac{\sqrt{6}q_1}{3} \end{bmatrix}. \quad (2.38)$$

The Landau–de Gennes free energy in (2.26) is then rewritten as

$$\begin{aligned} \mathcal{F}[\mathbf{Q}] = \int_{B(0,1)} & \left(\frac{t}{2} (q_1^2 + q_2^2 + q_3^2) - q_1^3 + 3q_1q_2^2 - \frac{3}{2}q_1q_3^2 - \frac{3\sqrt{3}}{2}q_2q_3^2 \right. \\ & + \frac{1}{2} (q_1^4 + q_2^4 + q_3^4 + 2q_1^2q_2^2 + 2q_1^2q_3^2 + 2q_2^2q_3^2) \\ & \left. + \frac{\varepsilon^2}{2} \left(q_{1,r}^2 + q_{2,r}^2 + q_{3,r}^2 + q_{1,z}^2 + q_{2,z}^2 + q_{3,z}^2 + \frac{1}{r^2} (4q_2^2 + q_3^2) \right) \right) dV. \end{aligned} \quad (2.39)$$

We also specify boundary conditions for q_1, q_2 , and q_3 with our symmetry assumptions. We work with the Dirichlet boundary condition (2.4) on $r^2 + z^2 = 1$, which can be translated into conditions for q_1, q_2 , and q_3 . The unit vector $\hat{\mathbf{r}}$ can be written as $\hat{\mathbf{r}} = r\mathbf{e}_r + z\mathbf{e}_z$, where $\mathbf{e}_r = [\cos \theta, \sin \theta, 0]^T$, $\mathbf{e}_z = [0, 0, 1]^T$, so that

$$s_+ \left(\hat{\mathbf{r}} \otimes \hat{\mathbf{r}} - \frac{1}{3} \mathbf{I} \right) = s_+ \begin{bmatrix} r^2 \cos^2 \theta - \frac{1}{3} & r^2 \cos \theta \sin \theta & rz \cos \theta \\ r^2 \cos \theta \sin \theta & r^2 \sin^2 \theta - \frac{1}{3} & rz \sin \theta \\ rz \cos \theta & rz \sin \theta & z^2 - \frac{1}{3} \end{bmatrix}, \quad (2.40)$$

where s_+ is defined in (2.5). Comparing with (2.38), we obtain

$$q_1 = \frac{\sqrt{6}}{6} (2 - 3r^2) s_+, \quad q_2 = \frac{\sqrt{2}}{2} r^2 s_+, \quad q_3 = \sqrt{2} r z s_+ \quad \text{on } r^2 + z^2 = 1. \quad (2.41)$$

There are additional boundary conditions to account for the assumed rotational and mirror symmetry [67]:

$$q_{1,z} = q_{2,z} = q_3 = 0 \quad \text{on } z = 0 \quad (2.42)$$

for mirror symmetry across the xy -plane, and

$$q_{1,r} = q_2 = q_{2,r} = q_3 = 0 \quad \text{on } r = 0 \quad (2.43)$$

for rotational symmetry about the z -axis.

It is worth briefly explaining how the boundary conditions on $r = 0$ and $z = 0$ arise. Firstly, we include $q_2 = q_3 = 0$ on $r = 0$ to regularise the problem as there is a singularity in (2.39) at $r = 0$. The other conditions all arise as a result of the Dirichlet boundary conditions in (2.41). We note that the boundary values q_1 and q_2 in (2.41) are even functions in r and z , so we require $q_{1,r} = q_{2,r} = 0$ on $r = 0$ and $q_{1,z} = q_{2,z} = 0$ on $z = 0$ to match the boundary conditions. Furthermore, q_3 in (2.41) is an odd function of r and z , and in theory we require $q_3(r, z) = -q_3(r, -z)$ on $r^2 + z^2 = 1$, leading to the additional condition $q_3 = 0$ on $z = 0$.

2.3.2 Critical Points of the Landau–de Gennes Free Energy

We use a finite element method [110] to solve for Landau–de Gennes critical points. The finite element method discretises the domain into smaller elements and solves for the unknowns within each element, yielding approximate (but often very accurate) solutions to complex systems. In our context, we apply the finite element method to the weak formulations associated with the Landau–de Gennes free energy (2.39) with the fourth-order bulk potential (and the equivalent energies in the sixth-order bulk and

ferronematic cases), which are given by

$$\begin{aligned}
 F_1 &= \int_{B(0,1)} \varepsilon^2 \nabla q_1 \cdot \nabla v_1 \\
 &\quad + v_1 \left(tq_1 - 3q_1^2 + 3q_2^2 - \frac{3}{2}q_3^2 + 2q_1^3 + 2q_1q_2^2 + 2q_1q_3^2 \right) dV \\
 F_2 &= \int_{B(0,1)} \varepsilon^2 \nabla q_2 \cdot \nabla v_2 \\
 &\quad + v_2 \left(tq_2 + 6q_1q_2 - \frac{3\sqrt{3}}{2}q_3^2 + 2q_1^2q_2 + 2q_2^3 + 2q_2q_3^2 + \frac{4}{r^2}\varepsilon^2q_2 \right) dV, \\
 F_3 &= \int_{B(0,1)} \varepsilon^2 \nabla q_3 \cdot \nabla v_3 \\
 &\quad + v_3 \left(tq_3 - 3q_1q_3 - 3\sqrt{3}q_2q_3 + 2q_1^2q_3 + 2q_2^2q_3 + 2q_3^3 + \frac{1}{r^2}\varepsilon^2q_3 \right) dV,
 \end{aligned} \tag{2.44}$$

where v_1, v_2 , and v_3 are test functions.

We present the weak formulations with the sixth-order bulk potential and in the ferronematic case in Chapters 3 and 5, respectively.

The finite element method is implemented in the open-source computing package FEniCS [110], which uses Newton's method to find solutions; and the visualisation is carried out in an open-source post-processing visualisation application, ParaView [113].

We plot the biaxiality parameter, β in (1.18), of the numerically computed critical points, since biaxiality often labels defects and biaxiality also distinguishes the sixth-order bulk potential from the fourth-order bulk potential. The radial hedgehog solution is purely uniaxial with $\beta = 0$ everywhere, while the split core and biaxial torus solutions have signature regions of biaxiality near the origin (see Section 1.5.3 for more in-depth discussion of equilibrium configurations on the sphere with the fourth-order bulk potential). We also plot the leading eigenvector of the \mathbf{Q} -tensor, which is the eigenvector with the largest positive eigenvalue and models the preferred direction of orientation of the nematic liquid crystal molecules.

A further useful property to consider is the sign of the scalar order parameter at the origin. However, since we set $q_2 = q_3 = 0$ at the origin in (2.43), the sign of the scalar order parameter is given by the sign of q_1 at the origin. The radial hedgehog solution is isotropic at the origin so that $q_1(0, 0) = 0$; while the split core solution is negatively ordered at the origin, requiring $q_1(0, 0) < 0$; and the biaxial torus solution is positively ordered at the origin, requiring $q_1(0, 0) > 0$.

2.3.3 The Morse Index of the Radial Hedgehog Solution

We characterise the stability of Landau–de Gennes critical points using the Morse index, which is the number of negative real eigenvalues of the associated Hessian of the Landau–de Gennes free energy evaluated at the critical point [114]. The Morse index is calculated using the SLEPc eigenvalue solver [115]. An index-0 critical point, with no negative eigenvalues, is at least locally stable. All index- k critical points, with $k > 0$, are unstable. We numerically compute the Morse index of the radial hedgehog solution with the fourth- and sixth-order bulk potentials in the nematic case in Chapter 3, and in the ferronematic case in Chapter 5, and tabulate the results across a range of temperatures and droplet radii.

As it is difficult to converge to the radial hedgehog solution at low temperatures and in droplets with large radii, we solve for \mathbf{Q} -tensors in the further restricted class described by $\mathbf{q}^* = [q_1, q_2, q_3]^T$ such that

$$q_1 = \frac{\sqrt{6}}{6} \left(2 - \frac{3r^2}{r^2 + z^2} \right) s^*, \quad q_2 = \frac{\sqrt{2}r^2}{2(r^2 + z^2)} s^*, \quad q_3 = \frac{\sqrt{2}rz}{r^2 + z^2} s^*, \quad (2.45)$$

where s^* is a solution of the ODE

$$\varepsilon^2 \Delta s = ts - \sqrt{6}s^2 + \frac{4}{3}s^3 + \frac{6\varepsilon^2 s}{r^2 + z^2}, \quad (2.46)$$

which is equivalent to the dimensionless version of the ODE in (1.42):

$$\varepsilon^2 \left(\frac{d^2 s}{dr^2} + \frac{2}{r} \frac{ds}{dr} - \frac{6}{r^2} s \right) = ts - \sqrt{6} s^2 + \frac{4}{3} s^3, \quad (2.47)$$

recalling that (1.42), and therefore (2.47), are given in spherical polar coordinates.

This reduces the problem to solving the weak formulation

$$F_s = \int_{B(0,1)} \varepsilon^2 \nabla s \cdot \nabla v + v \left(ts - \sqrt{6} s^2 + \frac{4}{3} s^3 + \frac{6\varepsilon^2 s}{r^2 + z^2} \right) dV, \quad (2.48)$$

where v is a test function, for the function $s = s^*(r, z)$ in the fourth-order case, and we present the analogous weak formulations in the sixth-order bulk and ferronematic cases in Chapters 3 and 5, respectively. Having solved for s^* , we then construct the \mathbf{Q} -tensor from the relations (2.45), and compute the Morse index of the solution in the more general class of \mathbf{Q} -tensors described by (2.38).

2.3.4 The Radial Hedgehog Solution as an Index-1 Transition State

We attempt to identify situations in which the radial hedgehog solution acts as an index-1 saddle point, because these points are often referred to as transition states, potentially mediating switching processes between stable equilibrium states [116]. Our aim is to compute the transition pathway between two index-0 Landau–de Gennes critical points, which are potentially physically observable, through an index-1 radial hedgehog solution, \mathbf{q}^* , in (2.45), thus identifying example regimes in which the radial hedgehog solution mediates switching processes as an index-1 saddle point.

We use a gradient flow method, a well-established numerical method which iteratively takes steps in the direction of steepest descent from the initial point to find local minima [117]. We work with values of t and ε for which the radial hedgehog solution

is an index-1 saddle point and take small perturbations of the radial hedgehog solution in the unstable direction, or along the direction of the eigenvector associated with the negative eigenvalue of the Hessian, as an initial condition. We solve the initial value problem

$$\begin{aligned}\frac{\partial \mathbf{q}}{\partial \tau} &= -\nabla \mathcal{F}(\mathbf{q}, \nabla \mathbf{q}) \quad \text{in } B(0, 1) \text{ for } \tau > 0, \\ \mathbf{q} &= \mathbf{q}_0 = \mathbf{q}^* \pm \lambda \mathbf{u}, \quad \text{in } B(0, 1) \text{ at } \tau = 0,\end{aligned}\tag{2.49}$$

with boundary conditions (2.41)-(2.43), where \mathcal{F} is the Landau–de Gennes free energy (2.39); the quantity λ is a small positive constant; and \mathbf{u} is the unstable eigendirection of the radial hedgehog solution. The initial value problem, (2.49), will converge to two different index-0 solutions for the two different initial conditions.

Remark: In the spatially discretised domain, we have n grid points on which we solve the problem numerically. In this framework, rather than working with a tensor at each grid point, we solve for a vector, $\tilde{\mathbf{q}}$, with $3n$ elements such that $\tilde{q}_{3(i-1)} = q_1^i$, $\tilde{q}_{3(i-1)+1} = q_2^i$, $\tilde{q}_{3(i-1)+2} = q_3^i$ for $i = 1, \dots, n$, where q_1^i is the value of q_1 on the i^{th} grid point. Hence, the notion of adding a vector to perturb the radial hedgehog solution is sensible, since computed eigenvectors are of length $3n$.

Solving the above initial value problem is equivalent to solving the coupled, nonlinear, τ -dependent PDEs

$$\begin{aligned}\frac{\partial q_1}{\partial \tau} &= \varepsilon^2 \Delta q_1 - tq_1 + 3q_1^2 - 3q_2^2 + \frac{3}{2}q_3^2 - 2q_1^3 - 2q_1q_2^2 - 2q_1q_3^2, \\ \frac{\partial q_2}{\partial \tau} &= \varepsilon^2 \Delta q_2 - tq_2 - 6q_1q_2 + \frac{3\sqrt{3}}{2}q_3^2 - 2q_1^2q_2 - 2q_3^3 - 2q_2q_3^2 - \frac{4}{r^2}\varepsilon^2q_2, \\ \frac{\partial q_3}{\partial \tau} &= \varepsilon^2 \Delta q_3 - tq_3 + 3q_1q_3 + 3\sqrt{2}q_2q_3 - 2q_1^2q_3 - 2q_2^2q_3 - 2q_3^3 - \frac{1}{r^2}\varepsilon^2q_3.\end{aligned}\tag{2.50}$$

To solve the above PDEs with the finite element method, we time-discretise the problem

using an implicit Euler method [118], approximating time derivatives by

$$\frac{\partial q_i}{\partial \tau}(\tau_n) \approx \frac{q_{i,n} - q_{i,n-1}}{\Delta \tau}, \quad q_i(\tau_n) \approx q_{i,n}, \quad (2.51)$$

for $i = 1, 2, 3$, where $\tau_n = n\Delta\tau$. We use Euler's method as it is a computationally efficient method to obtain approximate solutions for systems of partial differential equations, and it is straightforward to implement. We use the implicit Euler method as it is numerically stable in comparison with the explicit Euler method, and therefore more robust, despite being more computationally expensive than the explicit Euler method [118].

The weak formulations of the discretised versions of (2.50) are given by

$$\begin{aligned} F_1 &= \int_{B(0,1)} (q_{1,n} - q_{1,n-1}) v_1 + \Delta\tau \varepsilon^2 \nabla q_{1,n} \cdot \nabla v_1 \\ &\quad + \Delta\tau \left(tq_{1,n} - 3q_{1,n}^2 + 3q_{2,n}^2 - \frac{3}{2}q_{3,n}^2 + 2q_{1,n}^3 + 2q_{1,n}q_{2,n}^2 + 2q_{1,n}q_{3,n}^2 \right) v_1 dV, \\ F_2 &= \int_{B(0,1)} (q_{2,n} - q_{2,n-1}) v_2 + \Delta\tau \varepsilon^2 \nabla q_{2,n} \cdot \nabla v_2 \\ &\quad + \Delta\tau \left(tq_{2,n} + 6q_{1,n}q_{2,n} - \frac{3\sqrt{3}}{2}q_{3,n}^2 + 2q_{1,n}^2q_{2,n} \right. \\ &\quad \left. + 2q_{2,n}^3 + 2q_{2,n}q_{3,n}^2 + \frac{4}{r^2}\varepsilon^2q_{2,n} \right) v_2 dV, \\ F_3 &= \int_{B(0,1)} (q_{3,n} - q_{3,n-1}) v_3 + \Delta\tau \varepsilon^2 \nabla q_{3,n} \cdot \nabla v_3 \\ &\quad + \Delta\tau \left(tq_{3,n} - 3q_{1,n}q_{3,n} - 3\sqrt{3}q_{2,n}q_{3,n} \right. \\ &\quad \left. + 2q_{1,n}^2q_{3,n} + 2q_{2,n}^2q_{3,n} + 2q_{3,n}^3 + \frac{1}{r^2}\varepsilon^2q_{3,n} \right) v_3 dV. \end{aligned} \quad (2.52)$$

2.3.5 Bifurcation Diagrams and the HiOSD Method

We construct bifurcation diagrams as a function of temperature to understand the nature of the solution landscapes in the nematic case with fourth- and sixth-order bulk potentials; as well as in the ferronematic case. The branches of the bifurcation diagrams are computed via continuation methods [111]. Loosely speaking, a critical point is found at a given temperature, and used as an initial condition at a slightly lower or slightly higher temperature. The resulting solution is then used as an initial condition for the next temperature, and this process is repeated across the full temperature range of interest. Stable solutions can generally be computed via the finite element or gradient flow methods outlined in Sections 2.3.2 and 2.3.4, respectively. We use a high-index optimisation-based shrinking dimer (HiOSD) method [112] to compute unstable solutions, which are generally difficult to obtain via other methods.

The HiOSD method is a local search algorithm designed to compute saddle points with any Morse index. This method can be used to construct solution landscapes of confined systems and reveal how critical points are connected. In this sense, it can be viewed as a generalisation of the idea of the gradient flow method in Section 2.3.4. The gradient flow method we use takes a small perturbation of an index-1 saddle point and searches in a given eigendirection to find an index-0 minimiser. The HiOSD method is more powerful in the sense that we start from an index- m critical point, where $m \geq 0$, and search in a given eigendirection for an index- k critical point, where $k \geq 0$, $k \neq m$. This allows us to find critical points of a specific index, including obtaining higher-index critical points than that which we start with, which is not possible with the gradient flow method. Note that the HiOSD can be used for an *upward* search, perturbing an index- m critical point and searching in a given eigendirection for an index- k critical point, where $m < k$; or for a *downward* search, where $m > k$ [119]. We illustrate the

ideas behind the HiOSD method in Figure 2.1, in which we present an example of a solution landscape and its associated energy landscape.

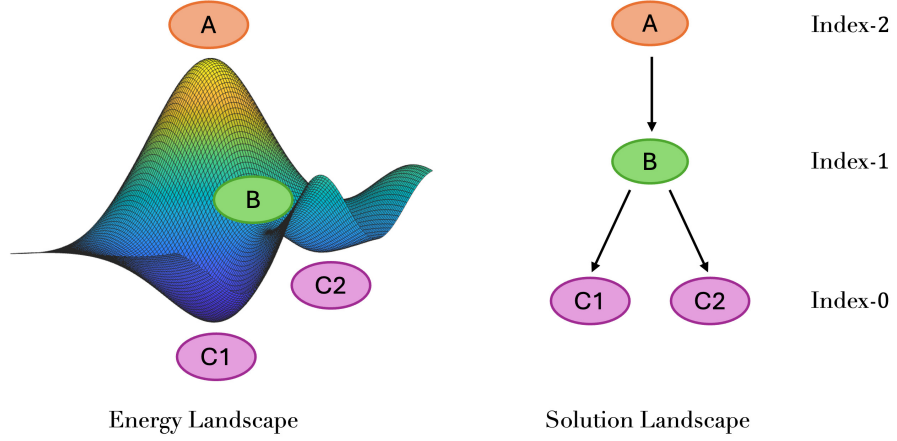


Figure 2.1: An example of an energy landscape and the associated solution landscape. The point A is an index-2 maximum; B is an index-1 saddle point; and C1 and C2 are index-0 minima.

The Hessian, $\mathbb{H}(\mathbf{Q}) := \nabla^2 \mathcal{F}[\mathbf{Q}]$ for \mathcal{F} in (2.39), associated with an index- m critical point has exactly m negative eigenvalues, with associated unit eigenvectors $\mathbf{v}_1, \dots, \mathbf{v}_m$ such that $\mathbf{v}_i \cdot \mathbf{v}_j = \delta_{ij}$ for $1 \leq i, j \leq m$. To obtain an index- k critical point via an upward search method, we perturb an index- m critical point such that $k > m$ in the direction of a linear combination of $k - m$ eigenvectors corresponding to the $k - m$ smallest positive eigenvalues of the Hessian associated with the index- m critical point. To obtain an index- k saddle via a downward search when $k < m$, we perturb the index- m critical point along a linear combination of the eigenvectors corresponding to the $m - k$ eigenvectors corresponding to the negative eigenvalues with smallest magnitude.

Noting again that we work with a vector $\tilde{\mathbf{q}}$ rather than a tensor in the spatially discretised numerical framework, the numerical search for an index- k critical point

then follows the dynamical system [112]

$$\begin{cases} \beta^{-1}\dot{\tilde{\mathbf{q}}} &= \left(\mathbf{I} - \sum_{i=1}^k 2\mathbf{v}_i\mathbf{v}_i^T\right) \mathcal{F}[\tilde{\mathbf{q}}], \\ \gamma^{-1}\dot{\mathbf{v}}_i &= -\left(\mathbf{I} - \mathbf{v}_i\mathbf{v}_i^T - \sum_{j=1}^{i-1} 2\mathbf{v}_j\mathbf{v}_j^T\right) \mathbb{H}[\tilde{\mathbf{q}}], \quad i = 1, \dots, k. \end{cases} \quad (2.53)$$

Here, $\beta, \gamma > 0$ are relaxation parameters and $\mathbf{v}_1, \dots, \mathbf{v}_k$ are the same eigenvectors along which the index- m critical point is perturbed. In this thesis, we set $\beta = \gamma = \Delta\tau$, where $\Delta\tau$ is the step size used in the gradient flow method in Section 2.3.4. We note that we use $\mathcal{F}[\tilde{\mathbf{q}}]$ and $\mathbb{H}[\tilde{\mathbf{q}}]$ for consistency in (2.53), but these are notionally equivalent to $\mathcal{F}[\mathbf{Q}]$ in (2.39) and the associated Hessian, $\mathbb{H}[\mathbf{Q}]$, respectively.

Chapter 3

The Sixth-Order Bulk Potential

This chapter is based on McLauchlan, Han, Langer and Majumdar (2024) [1].

We investigate biaxiality as a bulk effect on Landau–de Gennes critical points by considering a sixth-order bulk potential in this chapter. In Section 3.2, we consider critical points of the sixth-order bulk potential in the uniaxial and biaxial cases, and compare with the critical points of the fourth-order bulk potential. We prove a range of analytical results for the radial hedgehog solution with the sixth-order bulk potential in Section 3.3, by analogy with results outlined in Section 2.1. Finally, we perform a parallel analysis of equilibrium configurations on the sphere with the fourth- and sixth-order bulk potentials numerically in Section 3.4.

3.1 Problem Formulation

We discuss the nondimensionalisation and rescaling of the Landau–de Gennes free energy in Section 2.2, and we recall that the dimensionless Landau–de Gennes free energy with the sixth-order bulk potential, in the absence of surface energies and external

fields, is given by

$$\begin{aligned} \mathcal{F}[\mathbf{Q}] = \int_{B(0,1)} & \frac{\varepsilon^2}{2} |\nabla \mathbf{Q}|^2 + \frac{t}{2} \operatorname{tr} \mathbf{Q}^2 - \sqrt{6} \operatorname{tr} \mathbf{Q}^3 + \frac{1}{2} (\operatorname{tr} \mathbf{Q}^2)^2 \\ & + \frac{d}{5} \operatorname{tr} \mathbf{Q}^2 \operatorname{tr} \mathbf{Q}^3 + \frac{e}{6} (\operatorname{tr} \mathbf{Q}^2)^3 + \frac{(f-e)}{6} (\operatorname{tr} \mathbf{Q}^3)^2 dV, \end{aligned} \quad (3.1)$$

and we recall that the effects of temperature are captured by the reduced temperature, t , which is proportional to the absolute temperature; while different droplet radii are captured by the parameter ε^2 , which is inversely proportional to the droplet radius.

We again impose strong homeotropic anchoring in both the fourth- and sixth-order bulk potential cases via the Dirichlet boundary condition [67]

$$\mathbf{Q} = \mathbf{Q}_{s_+} := s_+ \left(\hat{\mathbf{r}} \otimes \hat{\mathbf{r}} - \frac{1}{3} \mathbf{I} \right), \quad \text{on } \partial B(0,1), \quad (3.2)$$

where $\hat{\mathbf{r}}$ is the unit vector in the radial direction. The quantity s_+ is the largest minimiser of

$$\left\{ f_B(\mathbf{Q}) : \mathbf{Q} = s \left(\mathbf{n} \otimes \mathbf{n} - \frac{1}{3} \mathbf{I} \right); \mathbf{n} \in \mathbb{R}^3; |\mathbf{n}| = 1, s \geq 0 \right\}, \quad (3.3)$$

where f_B is the fourth- or sixth-order bulk potential. In the fourth-order case, the dimensionless bulk potential is given by

$$f_B(\mathbf{Q}) = \frac{t}{2} \operatorname{tr} \mathbf{Q}^2 - \sqrt{6} \operatorname{tr} \mathbf{Q}^3 + \frac{1}{2} (\operatorname{tr} \mathbf{Q}^2)^2, \quad (3.4)$$

and s_+ has the explicit expression

$$s_+ = \sqrt{\frac{3}{2} \frac{3 + \sqrt{9 - 8t}}{4}} \quad (3.5)$$

Chapter 3. The Sixth-Order Bulk Potential

when $t \leq \frac{9}{8}$. The dimensionless sixth-order bulk potential is given by

$$f_B(\mathbf{Q}) = \frac{t}{2} \operatorname{tr} \mathbf{Q}^2 - \sqrt{6} \operatorname{tr} \mathbf{Q}^3 + \frac{1}{2} (\operatorname{tr} \mathbf{Q}^2)^2 + \frac{d}{5} \operatorname{tr} \mathbf{Q}^2 \operatorname{tr} \mathbf{Q}^3 + \frac{e}{6} (\operatorname{tr} \mathbf{Q}^2)^3 + \frac{f-e}{6} (\operatorname{tr} \mathbf{Q}^3)^2, \quad (3.6)$$

and in this case, s_+ is the largest positive minimiser of the function

$$g(s) := \frac{t}{3} s^2 - \frac{2\sqrt{6}}{9} s^3 + \frac{2}{9} s^4 + \frac{4d}{135} s^5 + \frac{4e}{81} s^6 + \frac{2(f-e)}{243} s^6. \quad (3.7)$$

We note that the function g is the potential (3.6), restricted to uniaxial \mathbf{Q} -tensors.

Critical points of the Landau–de Gennes free energy then belong to the admissible space [63]

$$\mathcal{A}_{\mathbf{Q}} = \{ \mathbf{Q} \in W^{1,2}(B(0,1), \mathcal{S}_0) : \mathbf{Q} = \mathbf{Q}_{s_+} \text{ on } \partial B(0,1) \}. \quad (3.8)$$

We note that this admissible space is simply a generalisation of the admissible space (2.6), discussed in Section 2.1, and we refer the reader to this section for the definition of the Sobolev space $W^{1,2}(B(0,1), \mathcal{S}_0)$. Furthermore, critical points of the free energy with the sixth-order bulk potential satisfy the Euler–Lagrange equations

$$\begin{aligned} \varepsilon^2 \Delta Q_{ij} &= tQ_{ij} - 3\sqrt{6} \left(Q_{ik}Q_{kj} - \frac{1}{3} \delta_{ij} \operatorname{tr} \mathbf{Q}^2 \right) + 2Q_{ij} \operatorname{tr} \mathbf{Q}^2 \\ &\quad + \frac{2d}{5} Q_{ij} \operatorname{tr} \mathbf{Q}^3 + \frac{3d}{5} \operatorname{tr} \mathbf{Q}^2 \left(Q_{ik}Q_{kj} - \frac{1}{3} \delta_{ij} \operatorname{tr} \mathbf{Q}^2 \right) \\ &\quad + eQ_{ij} (\operatorname{tr} \mathbf{Q}^2)^2 + (f-e) \operatorname{tr} \mathbf{Q}^3 \left(Q_{ik}Q_{kj} - \frac{1}{3} \delta_{ij} \operatorname{tr} \mathbf{Q}^3 \right), \end{aligned} \quad (3.9)$$

where

$$\sqrt{6} \delta_{ij} \operatorname{tr} \mathbf{Q}^2, \quad \text{and} \quad \frac{1}{3} \delta_{ij} \operatorname{tr} \mathbf{Q}^2 \left(3\sqrt{6} - \frac{3d}{5} \operatorname{tr} \mathbf{Q}^2 - (f-e) \operatorname{tr} \mathbf{Q}^3 \right) \quad (3.10)$$

Chapter 3. The Sixth-Order Bulk Potential

are Lagrange multipliers for the tracelessness constraint. Solutions with the fourth-order bulk potential satisfy the above equations with $d = e = f = 0$, which are the dimensionless equivalent to the Euler–Lagrange equations (2.13) in Section 2.1. Furthermore, solutions of the Euler–Lagrange equations are analytic by analogy with Proposition 13 in [49].

We focus on an exact solution of the Euler–Lagrange equations (3.9) in the admissible space, $\mathcal{A}_{\mathbf{Q}}$: the radial hedgehog solution, which can be written explicitly as

$$\mathbf{Q}^*(\mathbf{r}) = s^*(r) \left(\hat{\mathbf{r}} \otimes \hat{\mathbf{r}} - \frac{1}{3} \mathbf{I} \right). \quad (3.11)$$

As discussed in earlier chapters, the radial hedgehog solution is a purely uniaxial solution with a scalar order parameter that depends only on the radial distance, r , from the centre of the droplet. The admissible space for the scalar order parameter, s^* , is [63]

$$\mathcal{A}_s = \{s \in W^{1,2}([0, 1], \mathbb{R}) : s(1) = s_+\}, \quad (3.12)$$

where s_+ is again the largest minimiser of (3.3).

3.2 The Sixth-Order Bulk Potential

In this section, we study the critical points of the sixth-order bulk potential, (3.6). We first consider critical points in the restricted space of uniaxial \mathbf{Q} -tensors; and then in the whole space \mathcal{S}_0 , which includes biaxial \mathbf{Q} -tensors.

We note two key differences in the sixth-order case in comparison to the fourth-order case. Firstly, in the restricted class of uniaxial \mathbf{Q} -tensors, the sixth-order bulk potential, (3.6), has two nonzero critical points below $t = 0$: one with positive scalar order parameter, s_+ , and the other with negative scalar order parameter, s_- . The same

is true in the fourth-order case, but the difference is that s_- is the globally minimising scalar order parameter for low temperatures in the sixth-order case, while s_+ is the global minimiser at all temperatures in the fourth-order case. Secondly, in the space \mathcal{S}_0 , the sixth-order bulk potential admits biaxial critical points, while the fourth-order bulk potential does not, and the global minimiser of the sixth-order bulk potential is biaxial at sufficiently low temperatures.

3.2.1 Uniaxial Critical Points of the Sixth-Order Bulk Potential

In what follows, we work in a parameter regime so that $f_B(\mathbf{Q})$ in (3.6), restricted to uniaxial \mathbf{Q} -tensors, has an isotropic critical point and two well-defined nonzero critical points for low temperatures. We consider the quartic polynomial

$$\frac{g'(s)}{s} = \frac{2t}{3} - \frac{2\sqrt{6}}{3}s + \frac{8}{9}s^2 + \frac{4d}{27}s^3 + \frac{8e}{27}s^4 + \frac{4(f-e)}{81}s^4, \quad (3.13)$$

where the function g is defined in (3.7). We determine the roots of this quartic polynomial by considering its discriminant [120].

$$\begin{aligned} \Delta = & \frac{512}{59049} (5e+f)^3 t^3 \\ & + \frac{1024}{177147} \left(-\frac{512}{27} (5e+f)^2 - d^4 + \frac{32}{3} (5e+f) + \frac{32\sqrt{6}}{9} d(5e+f)^2 \right) t^2 \\ & + \frac{1024}{6561} \left(-\frac{64}{243} (5e+f) + \frac{32}{9} (5e+f)^2 \right. \\ & \quad \left. - \frac{2}{27} d^2 (5e+f) - \sqrt{6} d^2 + \frac{320\sqrt{6}}{243} d(5e+f) \right) t \\ & + \frac{1024}{2187} \left(-\frac{64}{81} (5e+f) + \frac{4\sqrt{6}}{81} d^3 + \frac{2}{3} d(5e+f) + \frac{8}{81} d^2 - (5e+f)^2 \right), \end{aligned} \quad (3.14)$$

and the quantity

$$P = 16(5e+f) - 3d^2. \quad (3.15)$$

The signs of the discriminant, Δ , and the quantity P characterise the roots of $g'(s)/s$. For $P > 0$, a quartic polynomial has two real roots and two complex conjugate roots if $\Delta < 0$; two pairs of complex conjugate roots if $\Delta > 0$; and a real double root and two complex conjugate roots if $\Delta = 0$.

We restrict the parameters d , e , and f to satisfy one of the three sets of conditions for all values of t and ε . Figure 3.1 demonstrates that for the specific choice $d = 1$, $e = 0$, $f = 1$, and $P > 0$, there is some transition temperature t_0 such that $\Delta < 0$ when $t < t_0$; $\Delta = 0$ when $t = t_0$; and $\Delta > 0$ when $t > t_0$. These results can be translated into properties of the function g in (3.7). Specifically, under these conditions, the function g will have one real critical point, $s = 0$, above some transition temperature t_0 ; two real critical points at $t = t_0$; and three real critical points at temperatures below t_0 . In particular, we note that g , plotted in Figure 3.2, is a double-welled potential at lower temperatures $t < t_0$ for which there is at least a positive local minimiser $s = s_+$ of the sixth-order polynomial $g(s)$. In the remainder of this chapter, and in Chapter 6, we use $e = 0$ and $d = f = 1$ as an illustrative example.

In Figure 3.2, we plot the function g for five different temperatures. One can clearly see that the isotropic state is the global minimiser for the high temperature $t = 5$; $s_+ > 0$ is the global minimiser for the low temperature $t = -25$; and as the temperature further decreases to $t = -100$, $s = s_- < 0$ is the global minimiser of g . Nonzero critical points first appear at the transition temperature $t_0 \approx 0.97$, where Δ changes sign, and the minimisers s_+ and s_- have the same energy at the transition temperature $t^* \approx -48.6$. This is further illustrated in Figure 3.3, where we plot the critical points of g as a function of t , and indicate their stability. We observe that for $t < 0$, there are two local minimisers of $g(s)$: $s = s_+ > 0$ and $s = s_- < 0$; and $s = s_-$ is the global minimiser of g for $t < -48.6$. As such, we conclude that

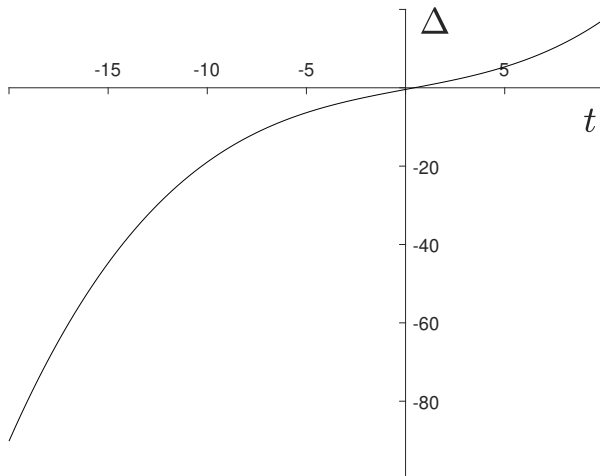


Figure 3.1: The function Δ for $d = 1$, $e = 0$, $f = 1$ and temperature from $t = -20$ to $t = 5$.

the sixth-order bulk potential restricted to uniaxial \mathbf{Q} -tensors indeed has an isotropic critical point and two real nonzero critical points at low temperatures in the parameter regime $d = 1$, $e = 0$, $f = 1$, per the requirements at the beginning of this section. In the absence of experimentally calibrated values of the sixth-order bulk potential parameters, we choose $d = f = 1$ for convenience and $e = 0$ to reduce computational time for the numerical results presented later in this chapter.

3.2.2 Biaxial Critical Points of the Sixth-Order Bulk Potential

Next we consider critical points of f_B in (3.6) in the full class of Landau–de Gennes \mathbf{Q} -tensors of the form

$$\mathbf{Q} = s \left(\mathbf{n} \otimes \mathbf{n} - \frac{1}{3} \mathbf{I} \right) + p \left(\mathbf{m} \otimes \mathbf{m} - \frac{1}{3} \mathbf{I} \right). \quad (3.16)$$

Chapter 3. The Sixth-Order Bulk Potential

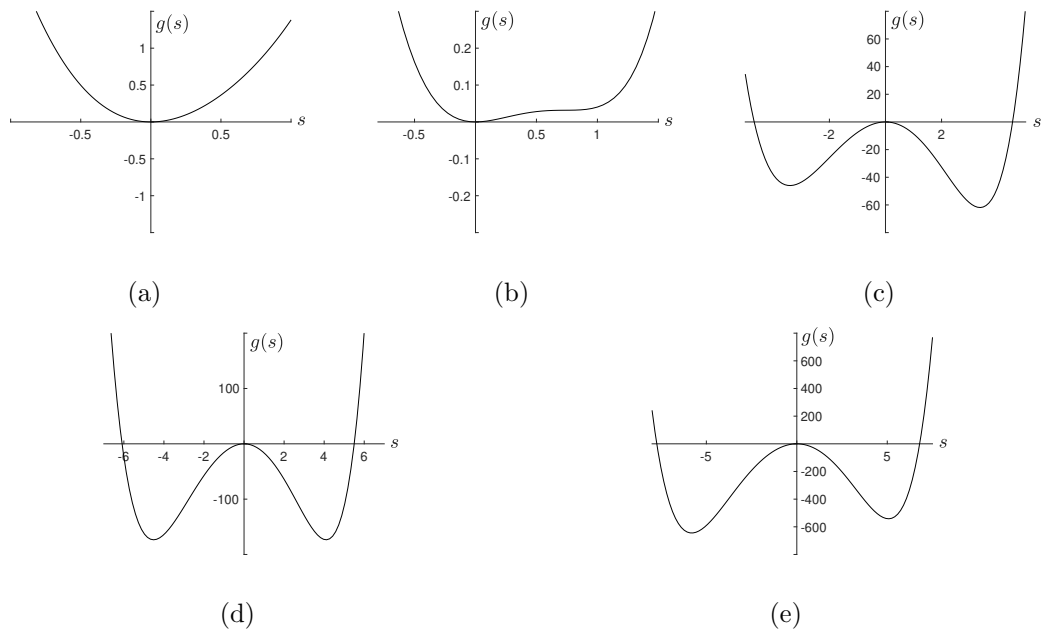


Figure 3.2: The function g in (3.7) with $d = 1$, $e = 0$, and $f = 1$ at (a) $t = 5$; (b) $t = t_0 \approx 0.97$; (c) $t = -25$; (d) $t = t^* \approx -48.6$; and (e) $t = -100$.

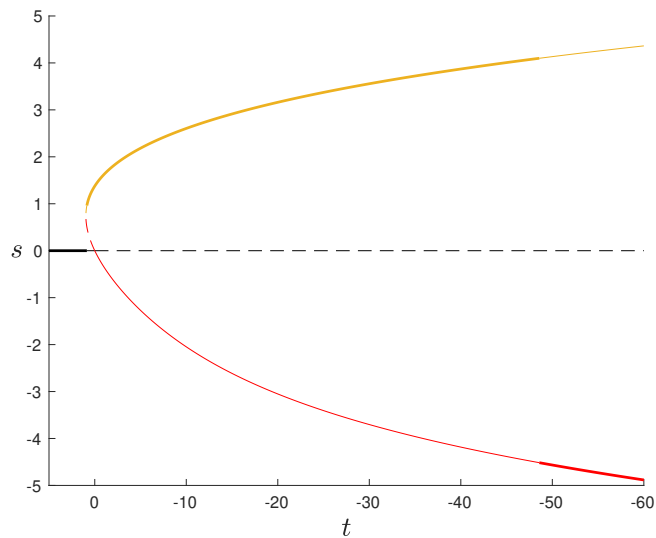


Figure 3.3: The critical points of the function g in (3.7) for decreasing temperature, with $d = 1$, $e = 0$, and $f = 1$. Bold lines indicate a global minimum, thin solid lines indicate a local minimum and dashed lines indicate instability (negative second derivative of g).

Chapter 3. The Sixth-Order Bulk Potential

We substitute (3.16) into (3.6) and compute the critical points in terms of the pairs (s, p) .

There are no biaxial critical points of the fourth-order bulk potential (see Proposition 1.2). In Figure 3.4, we plot the critical points of the fourth-order bulk potential, (3.4). The isotropic phase is the global minimiser above $t = 1.125$, and below this temperature there are four critical points, two of which are global minimisers: one minimiser has positive s and zero p (yellow solid line in Figure 3.4); and the other minimiser has $s = p < 0$ (red solid line in Figure 3.4). Both minimisers correspond to uniaxial \mathbf{Q} -tensors and are rotations of each other. The same relationship holds for the two unstable critical points: both correspond to a uniaxial configuration with a negative order parameter. Thus, Figure 3.4 shows that below $t = 1.125$, there is one stable uniaxial critical point with positive order parameter, and one unstable critical point with negative order parameter; there are no biaxial critical points; and the isotropic phase loses stability for $t < 0$. These facts are well-known in the literature regarding the fourth-order bulk potential.

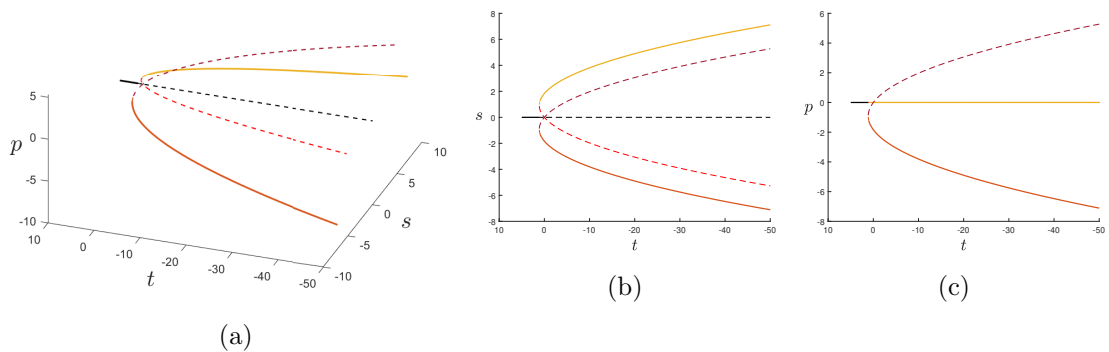


Figure 3.4: Critical points of the fourth-order bulk potential for the temperature range $t = 5$ to $t = -50$. (a) Both scalar order parameters, s and p , plotted against t . (b) Scalar order parameter s plotted against t . (c) Scalar order parameter p plotted against t .

Chapter 3. The Sixth-Order Bulk Potential

We fix $d = 1$, $e = 0$, and $f = 1$ and plot the critical points of the sixth-order bulk potential (3.6) in Figure 3.5. There are certain similarities to Figure 3.4: the isotropic phase is the global minimiser at high temperatures; there are four nonzero critical points for moderate temperatures below some transition temperature; and the isotropic phase loses stability below $t = 0$. These critical points correspond to one uniaxial global minimiser and one unstable uniaxial critical point for the same reasons as the fourth-order case, as detailed above. The two uniaxial critical points emerge at the approximate transition temperature $t = t_0 \approx 0.97$, with $(s, p) = (s_+, 0)$ being the global minimiser (red and yellow solid lines in Figure 3.5), and $(s, p) = (s_-, 0)$ being the unstable critical point (purple and red dashed lines), where s_+ and s_- are defined above. The critical point $(s_+, 0)$ remains stable until biaxial critical points appear at approximately $t = -11.6$, at which point (unlike with the fourth-order potential (3.4)) there are no stable uniaxial critical points and there is a unique global biaxial minimiser of (3.6), corresponding to the three blue solid lines in Figure 3.5, which are rotations of one another.

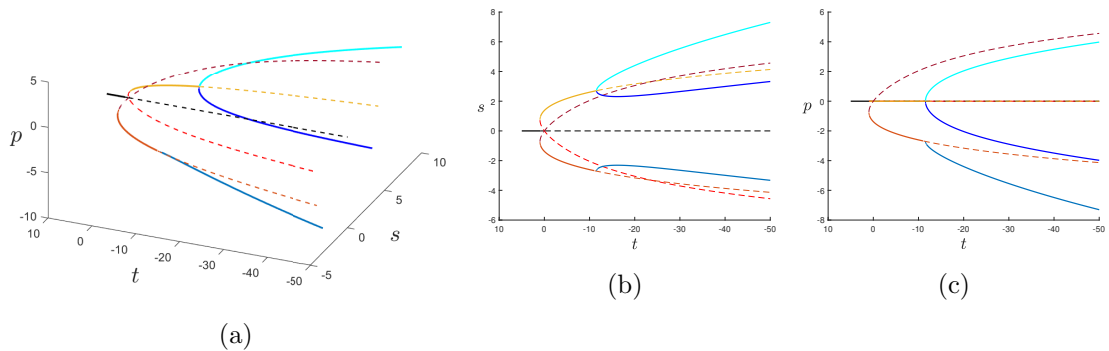


Figure 3.5: Critical points of the sixth-order bulk potential with $d = 1$, $e = 0$, and $f = 1$, for $t = 5$ to $t = -50$. (a) Scalar order parameters, s and p , plotted against t . (b) The scalar order parameter s plotted against t . (c) The scalar order parameter p plotted against t . Yellow, orange, red and maroon lines label uniaxial critical points; and blue lines label biaxial critical points.

3.3 Analysis of the Radial Hedgehog Solution

The radial hedgehog solution has been studied extensively with the fourth-order bulk potential in the literature, and we discuss some key properties and results in Sections 1.5.2 and 2.1. In particular, for the Landau–de Gennes free energy with the fourth-order bulk potential in (2.26), there are strong analytical results regarding the existence of the radial hedgehog solution. It has been shown that the radial hedgehog scalar order parameter is positive away from the origin; is monotonic and bounded above and below; and there is a unique radial hedgehog solution for $t < 0$ [63], [64]. Furthermore, it is known that the radial hedgehog solution is stable for sufficiently small droplets, and is unstable for large droplets and for low temperatures [63], [68], [70], [71]. In this section, we study the radial hedgehog solution with the sixth-order bulk potential (3.6) to understand how the choice of bulk potential affects the radial hedgehog solution, and the impact of the more general nature of the sixth-order bulk potential. We note that we make the reasonable assumption that the function g , which is equivalent to the sixth-order bulk potential, (3.6), restricted to uniaxial \mathbf{Q} -tensors, is a double-welled potential below some transition temperature t_0 at points in this section.

First, we prove a general existence result for the Landau–de Gennes free energy with the sixth-order bulk potential, which is a direct extension of Proposition 2.1 in Chapter 2. We provide an outline of the proof, which is analogous to that of Proposition 2.1.

Proposition 3.1. *There exists a global minimiser, \mathbf{Q}^* , of \mathcal{F} in (3.1) in the admissible space, $\mathcal{A}_{\mathbf{Q}}$, in (3.8).*

Proof. The admissible space, $\mathcal{A}_{\mathbf{Q}}$, is nonempty, since $\mathbf{Q}_{s_+} \in \mathcal{A}_{\mathbf{Q}}$, where \mathbf{Q}_{s_+} is defined in (3.2).

Furthermore, the free energy (3.1) is weakly lower-semicontinuous since the elastic

energy density is convex in $\nabla\mathbf{Q}$.

Finally, since the bulk energy density, f_B in (3.6), is a polynomial in $|\mathbf{Q}|$ and bounded from below, the free energy (3.1) is coercive.

Therefore, there must exist a global minimiser of (3.1) in the admissible space, $\mathcal{A}_{\mathbf{Q}}$. □

Our next result concerns the existence of the radial hedgehog solution and is analogous to Proposition 2.1 in [63]. We omit the proof as it is similar to that in [63].

Proposition 3.2. (a) *Consider the energy functional*

$$I[s] = \int_0^1 \left(\varepsilon \left(\frac{1}{2} \left(\frac{ds}{dr} \right)^2 + \frac{2}{r^2} s^2 \right) + \frac{t}{3} s^2 - \frac{2\sqrt{6}}{9} s^3 + \frac{2}{9} s^4 + \frac{4d}{135} s^5 + \frac{4e}{81} s^6 + \frac{2(f-e)}{243} s^6 \right) r^2 dr, \quad (3.17)$$

defined for functions $s \in \mathcal{A}_s$ for I . There exists a global minimiser $s^* \in \mathcal{A}_s$ for I .

The function s^* is a solution of the ordinary differential equation

$$\varepsilon^2 \left(\frac{d^2 s}{dr^2} + \frac{2}{r} \frac{ds}{dr} - \frac{6}{r^2} s \right) = ts - \sqrt{6}s^2 + \frac{4}{3}s^3 + \frac{2d}{9}s^4 + \frac{4e}{9}s^5 + \frac{2(f-e)}{27}s^5, \quad (3.18)$$

subject to the boundary conditions

$$s(0) = 0, \quad s(1) = s_+. \quad (3.19)$$

The global minimiser s^* is analytic for all $r \geq 0$.

(b) *The radial hedgehog solution is defined in (3.11), where s^* is a global minimiser of I in the admissible space \mathcal{A}_s in (3.12), and is a critical point of the Landau–de Gennes energy functional (3.1) for all ε , t , d , e , and f .*

(c) The function s^* satisfies $s^{*'}(0) = 0$.

Next, we derive a maximum principle which yields upper bounds for s^* in (3.11).

Proposition 3.3. *A global minimiser, \mathbf{Q}^* , of the Landau–de Gennes free energy (3.1), in the class of uniaxial \mathbf{Q} -tensors, in the admissible space, $\mathcal{A}_{\mathbf{Q}}$ in (3.8), satisfies the upper bound $|\mathbf{Q}^*|^2 \leq \frac{2}{3} \max \{s_+^2, s_-^2\}$ on $B(0, 1)$, where s_+ and s_- are the two nonzero critical points of (3.7).*

Proof. We consider two subsets:

$$\Omega_+ = \{\mathbf{r} \in B(0, 1) : s(\mathbf{r}) \geq 0\}, \quad \text{and} \quad \Omega_- = \{\mathbf{r} \in B(0, 1) : s(\mathbf{r}) < 0\}. \quad (3.20)$$

Suppose that the subset

$$\tilde{\Omega} = \left\{ \mathbf{r} \in B(0, 1) : |\mathbf{Q}^*(\mathbf{r})|^2 > \frac{2}{3} \max \{s_+^2, s_-^2\} \right\}, \quad (3.21)$$

where $\tilde{\Omega} \subset B(0, 1) \setminus \partial B(0, 1) \subset \Omega_+ \cup \Omega_-$, is nonempty. The subset $\tilde{\Omega}$ does not intersect $\partial B(0, 1)$ since $\max \{s_+^2, s_-^2\} \geq s_+^2$. Moreover, we assume that the function $|\mathbf{Q}^*| : \overline{B(0, 1)} \rightarrow \mathbb{R}$ attains a strict maximum at an interior point $\mathbf{r}^* \in \tilde{\Omega}$.

We multiply the Euler–Lagrange equations in (3.9) by Q_{ij}^* to find that

$$\begin{aligned} \varepsilon^2 \left(\frac{1}{2} \Delta |\mathbf{Q}^*|^2 - |\nabla \mathbf{Q}^*|^2 \right) &= t |\mathbf{Q}^*|^2 - 3\sqrt{6} \operatorname{tr} \mathbf{Q}^{*3} + 2 |\mathbf{Q}^*|^4 \\ &\quad + d |\mathbf{Q}^*|^2 \operatorname{tr} \mathbf{Q}^{*3} + e |\mathbf{Q}^*|^6 + \frac{(f - e)}{6} (\operatorname{tr} \mathbf{Q}^{*3})^2, \end{aligned} \quad (3.22)$$

since $|\nabla \mathbf{Q}^*|^2 + Q_{ij}^* \Delta Q_{ij}^* = \frac{1}{2} \Delta |\mathbf{Q}^*|^2$. We note that $\frac{1}{2} \Delta |\mathbf{Q}^*(\mathbf{r}^*)|^2 - |\nabla \mathbf{Q}^*(\mathbf{r}^*)|^2 \leq 0$ at the interior maximum.

Chapter 3. The Sixth-Order Bulk Potential

Let us label

$$h(\mathbf{Q}) := t|\mathbf{Q}|^2 - 3\sqrt{6}\operatorname{tr}\mathbf{Q}^3 + 2|\mathbf{Q}|^4 + d|\mathbf{Q}|^2\operatorname{tr}\mathbf{Q}^3 + e|\mathbf{Q}|^6 + \frac{(f-e)}{6}(\operatorname{tr}\mathbf{Q}^3)^2. \quad (3.23)$$

The aim is to show that h is positive at $\mathbf{Q}^*(\mathbf{r}^*)$ for a contradiction. First, consider the case where $\mathbf{r}^* \in \Omega_+$. Then we may write

$$\begin{aligned} h(\mathbf{Q}^*(\mathbf{r}^*)) &= t|\mathbf{Q}^*(\mathbf{r}^*)|^2 - 3|\mathbf{Q}^*(\mathbf{r}^*)|^3 + 2|\mathbf{Q}^*(\mathbf{r}^*)|^4 \\ &\quad + \frac{d}{\sqrt{6}}|\mathbf{Q}^*(\mathbf{r}^*)|^5 + e|\mathbf{Q}^*(\mathbf{r}^*)|^6 + \frac{(f-e)}{6}|\mathbf{Q}^*(\mathbf{r}^*)|^6 \end{aligned} \quad (3.24)$$

since $\operatorname{tr}\mathbf{Q}^{*3} = \frac{1}{\sqrt{6}}|\mathbf{Q}^*|^3$, because \mathbf{Q}^* is uniaxial and $\mathbf{r}^* \in \Omega_+$. Note that

$$h(\mathbf{Q}) = \sqrt{\frac{3}{2}}|\mathbf{Q}|g'\left(\sqrt{\frac{3}{2}}|\mathbf{Q}|\right), \quad \text{and} \quad \sqrt{\frac{3}{2}}|\mathbf{Q}| = |s|, \quad (3.25)$$

for an arbitrary uniaxial \mathbf{Q} -tensor of the form

$$\mathbf{Q}_s = s\left(\mathbf{n} \otimes \mathbf{n} - \frac{1}{3}\mathbf{I}\right). \quad (3.26)$$

Therefore, the sign of $h(\mathbf{Q})$ is dictated by the sign of $g'(|s|)$, where g is defined in (3.7).

Let us write $|\mathbf{Q}^*(\mathbf{r})| = \sqrt{\frac{2}{3}}|s^*(\mathbf{r})|$. We have noted in Section 3.2.1 that we are working in a parameter regime such that the function g is a double-welled potential with $g'(s_-) = g'(s_+) = 0$ below some transition temperature t_0 . Moreover, we choose e and f so that $g(s) \rightarrow +\infty$ as $|s| \rightarrow +\infty$, and since $|s^*(\mathbf{r}^*)| > \max\{s_+, |s_-|\}$, then we may conclude that $g'(|s^*(\mathbf{r}^*)|) > 0$ at the interior maximum $\mathbf{r}^* \in \tilde{\Omega}$. Hence $h(\mathbf{Q}^*(\mathbf{r}^*)) > 0$, and there cannot be a strict interior maximum at $\mathbf{r}^* \in \Omega_+$.

Chapter 3. The Sixth-Order Bulk Potential

Now consider the case where $\mathbf{r}^* \in \Omega_-$. We may write

$$h(\mathbf{Q}^*(\mathbf{r}^*)) = t|\mathbf{Q}^*(\mathbf{r}^*)|^2 + 3|\mathbf{Q}^*(\mathbf{r}^*)|^3 + 2|\mathbf{Q}^*(\mathbf{r}^*)|^4 - \frac{d}{\sqrt{6}}|\mathbf{Q}^*(\mathbf{r}^*)|^5 + e|\mathbf{Q}^*(\mathbf{r}^*)|^6 + \frac{(f-e)}{6}|\mathbf{Q}^*(\mathbf{r}^*)|^6, \quad (3.27)$$

since $\text{tr } \mathbf{Q}^{*3} = -\frac{1}{\sqrt{6}}|\mathbf{Q}^*|^3$, because \mathbf{Q}^* is uniaxial and $\mathbf{r}^* \in \Omega_-$, and we note that $h(\mathbf{Q}) = -\sqrt{\frac{3}{2}}|\mathbf{Q}|g'(-\sqrt{\frac{3}{2}}|\mathbf{Q}|)$. Therefore, the sign of $h(\mathbf{Q})$ is dictated by the sign of $-g'(-|s|)$. Then, since g is a double-welled potential with $g'(s_-) = g'(s_+) = 0$ such that $g(s) \rightarrow +\infty$ as $|s| \rightarrow +\infty$, and $|s^*(\mathbf{r}^*)| > \max\{s_+, |s_-|\}$, then we may conclude that $-g'(-|s^*(\mathbf{r}^*)|) > 0$ at the interior maximum $\mathbf{r}^* \in \tilde{\Omega}$. Hence $h(\mathbf{Q}^*(\mathbf{r}^*)) > 0$, and there cannot be a strict interior maximum at $\mathbf{r}^* \in \Omega_-$.

Thus, we combine the above two cases to find that the set $\tilde{\Omega}$ must be empty and the global minimiser \mathbf{Q}^* in the class of uniaxial \mathbf{Q} -tensors must satisfy the upper bound

$$|\mathbf{Q}^*|^2 \leq \frac{2}{3} \max\{s_+^2, s_-^2\}. \quad (3.28)$$

□

In the next proposition, we assume that $16(5e + f) > 3d^2$ and work within a temperature regime for which the potential (3.6) has a uniaxial global minimiser with positive order parameter s_+ , consistent with the imposed Dirichlet condition in (3.2). In this case, we can prove that s^* is bounded, positive, monotonic and unique, analogous to the results for (2.26). The differences emerge at low temperatures, for which (3.6) has a biaxial global minimiser and no stable uniaxial critical points. At the end of this section, we show numerically that s^* can be negative and non-monotonic deep in the nematic phase. Recall that s_+ is the largest positive minimiser of the function g in

(3.7). Since $g(s) \rightarrow +\infty$ as $s \rightarrow +\infty$, then $g'(s) > 0$ for $s > s_+$. Furthermore, the value s_+ is in fact the largest positive root of $g'(s)/s$ in (3.13), and increases in magnitude as the magnitude of t increases when t is negative. Therefore, s_+ increases as $|t|$ increases for $t < 0$ and bounds on s_+ can be translated into bounds for t .

Proposition 3.4. *Let s^* be the global minimiser of I in (3.17) in the moderately low temperature regime for which (3.6) has a global uniaxial minimiser, characterised by $t < 0$,*

$$s_+^2 - \frac{15\sqrt{6}}{2d} < 0, \quad (3.29)$$

with $d > 0$, and $s_+ \geq s_-$. It holds that s^ is nonnegative for $r \geq 0$ and positive for $r > 0$; unique; and monotonic increasing for $r \geq 0$.*

The proof of Proposition 3.4 follows from analogous arguments used for the fourth-order bulk potential in [64], precisely because the sixth-order bulk potential in (3.6) has a uniaxial global minimiser in the temperature range specified by (3.29). However, these arguments do not apply when the minimiser of (3.6) is biaxial at lower temperatures.

Proof. We prove nonnegativity via a contradiction argument with the assumption that there exists an interior measurable subset

$$\Gamma = \{r \in (0, 1) : s^*(r) < 0\} \subset [0, 1], \quad (3.30)$$

with $s^*(r) = 0$ on $\partial\Gamma$. We define the perturbation

$$\bar{s}^* = \begin{cases} s^*(r), & r \in [0, 1] \setminus \Gamma, \\ -s^*(r), & r \in \Gamma. \end{cases} \quad (3.31)$$

Then

$$I[\bar{s}^*] - I[s^*] = \int_{\Gamma} \left(\frac{4\sqrt{6}}{9} s^{*3} - \frac{8d}{135} s^{*5} \right) r^2 dr < 0, \quad (3.32)$$

where I is defined in (3.17), if $s^{*2} < \frac{15\sqrt{6}}{2d}$ for $d > 0$ since $s^*(r) < 0$ on Γ by assumption. Also, since $s^{*2} \leq s_+^2$ by Proposition 3.3, we can guarantee that $I[\bar{s}^*] - I[s^*] < 0$ if $s_+^2 < \frac{15\sqrt{6}}{2d}$. However, this contradicts the energy minimality of s^* . It follows that $s^*(r) \geq 0$ for $r \in [0, 1]$ if $s_+^2 < \frac{15\sqrt{6}}{2d}$.

To show that $s^*(r) > 0$ for $r > 0$, assume for a contradiction that there exists some $r_0 \in (0, 1]$ such that $s^*(r_0) = 0$. Since we have already shown that $s^*(r) \geq 0$ on $[0, 1]$, the function s^* must therefore have a minimum at r_0 . Then

$$\left. \frac{ds^*}{dr} \right|_{r=r_0} = 0 \quad \text{and} \quad \left. \frac{d^2s^*}{dr^2} \right|_{r=r_0} \geq 0. \quad (3.33)$$

However, if we substitute $s^*(r_0)$ into (3.18), we find that $\left. \frac{d^2s^*}{dr^2} \right|_{r=r_0} = 0$. We can differentiate (3.18) and repeat this process to find that, in fact, $\left. \frac{d^n s^*}{dr^n} \right|_{r=r_0} = 0$ for all $n \in \mathbb{N}$. However, this cannot be true because we know from Proposition 3.2 that s^* is analytic and we have the boundary condition $s^*(1) = s_+$. Therefore, we have reached a contradiction, so $s^*(r) > 0$ in $(0, 1]$.

We prove uniqueness via a contradiction argument, relying on a Pohozaev identity

$$\begin{aligned} \varepsilon^2 \left(\frac{1}{2} \int_{B(0,1)} Q_{ij,\ell} Q_{ij,\ell} dV \right. \\ \left. + \int_{\partial B(0,1)} Q_{ij,k} x_k Q_{ij,\ell} x_\ell dS - \frac{1}{2} \int_{\partial B(0,1)} Q_{ij,\ell} Q_{ij,\ell} dS \right) \\ = \int_{\partial B(0,1)} f_B(\mathbf{Q}) dS - 3 \int_{B(0,1)} f_B(\mathbf{Q}) dV, \quad (3.34) \end{aligned}$$

which is obtained from the Euler–Lagrange equations (3.9) as is done in [49].

Chapter 3. The Sixth-Order Bulk Potential

We rewrite (3.34) as

$$\begin{aligned} \mathcal{F}[\mathbf{Q}] + 2 \int_{B(0,1)} f_B(\mathbf{Q}) dV \\ = \int_{\partial B(0,1)} f_B(\mathbf{Q}) dS + \frac{1}{2} \int_{\partial B(0,1)} Q_{ij,\ell} Q_{ij,\ell} dS - \int_{\partial B(0,1)} (Q_{ij,k} x_k)^2 dS. \end{aligned} \quad (3.35)$$

Suppose for a contradiction that there exist $s_1, s_2 \in \mathcal{A}_s, s_1 \neq s_2$, satisfying

$$I[s_1] = I[s_2] = \min_{\mathcal{A}_s} I. \quad (3.36)$$

We apply (3.35) to \mathbf{Q}_{s_1} and \mathbf{Q}_{s_2} , simplify the resulting equations to obtain two equations involving s_1 and s_2 , and subtract the second from the first to obtain the relation

$$6 \int_0^1 r^2 (g(s_1) - g(s_2)) dr = (s_2'(1))^2 - (s_1'(1))^2, \quad (3.37)$$

recalling that $s_1(1) = s_2(1) = s_+$.

The two functions, s_1 and s_2 , are distinct solutions of the Euler–Lagrange equation (3.18) corresponding to the minimisation of I . Hence Lemma 2 in [64] ensures they cannot coincide on a neighbourhood of zero.

Suppose, without loss of generality, that $s_1 < s_2$ on $(0, \varepsilon)$. To show that we must in fact have $s_1 < s_2$ on $(0, 1)$, suppose for a contradiction that there exists an $r_0 \in (0, 1)$ such that $s_1(r_0) = s_2(r_0)$. We define the function \tilde{s} by

$$\tilde{s}(r) = \begin{cases} s_2(r), & r \in (0, r_0], \\ s_1(r), & r \in (r_0, 1), \end{cases} \quad (3.38)$$

and we show that \tilde{s} is a minimiser of I . Denoting by $h[s]$ the energy density ($I[s] =$

$\int_0^1 h[s] dr$), and setting

$$\bar{s}(r) = \begin{cases} s_1(r), & r \in (0, r_0], \\ s_2(r), & r \in (r_0, 1), \end{cases} \quad (3.39)$$

we find that

$$I[s_2] \leq I[\bar{s}] = \int_0^{r_0} h[s_1] dr + \int_{r_0}^1 h[s_2] dr, \quad (3.40)$$

since s_2 is a minimiser and \bar{s} lies in the admissible space. Therefore, it holds that

$$\int_0^{r_0} h[s_2] dr \leq \int_0^{r_0} h[s_1] dr, \quad (3.41)$$

since

$$I[s_2] = \int_0^{r_0} h[s_2] dr + \int_{r_0}^1 h[s_2] dr \leq \int_0^{r_0} h[s_1] dr + \int_{r_0}^1 h[s_2] dr. \quad (3.42)$$

Adding $\int_{r_0}^1 h[s_1] dr$ to both sides of the inequality (3.41) yields $I[\tilde{s}] \leq I[s_1]$, so we may conclude that \tilde{s} is a minimiser. Since \tilde{s} is a minimiser, it must be analytic by Proposition 3.2. Therefore, at r_0 , all of its right derivatives are equal to those of s_1 . This tells us that $\tilde{s} = s_1$ on a neighbourhood of r_0 , which implies that $s_1 = s_2$. This contradicts the assumption that $s_1 < s_2$ on $(0, \varepsilon)$. Therefore, we find that $s_1 < s_2$ on $(0, 1)$. This implies, together with $s_1(1) = s_2(1)$, that

$$s_1'(1) \geq s_2'(1), \quad (3.43)$$

so the right-hand side of (3.37) is nonpositive.

On the other hand, we prove that g is decreasing on $[0, s_+]$. Let us consider the derivative of g , given by

$$g'(s) = \frac{2t}{3}s - \frac{2\sqrt{6}}{3}s^2 + \frac{8}{9}s^3 + \frac{4d}{27}s^4 + \frac{8e}{27}s^5 + \frac{4(f-e)}{81}s^5. \quad (3.44)$$

Chapter 3. The Sixth-Order Bulk Potential

By Descartes' rule of signs, which states that the number of positive roots of a polynomial is at most equal to the number of sign changes in the sequence of the coefficients, excluding zero coefficients, and that the difference between the number of roots and the number of sign changes is always even, we conclude that g' has at most one positive root, s_+ , since $t < 0$. Furthermore, $s = 0$ is a local maximum when $t < 0$, hence the function g must be decreasing on $[0, s_+]$. Then since $s_1 < s_2$, we find that

$$\int_0^1 r^2 (g(s_1) - g(s_2)) dr > 0. \quad (3.45)$$

Therefore, the left-hand side of (3.37) is positive, and we have reached our contradiction. Hence, the global minimiser of I in (3.17) must be unique in this temperature regime.

We prove monotonicity using an argument analogous to Proposition 3 in [64]. \square

The next result shows that the radial hedgehog solution is the sole Landau–de Gennes critical point for droplets of sufficiently small radius with the sixth-order bulk potential, and is therefore globally stable in this regime. This follows from the local convexity of the Landau–de Gennes free energy with polynomial bulk potentials for small domains.

Proposition 3.5. *For ε sufficiently large, the radial hedgehog solution, \mathbf{Q}^* in (3.11), is the unique critical point, and hence, is the global minimiser of the Landau–de Gennes free energy (3.1).*

Proof. First, we show that a critical point, \mathbf{Q}^* , of \mathcal{F} in the admissible space (3.8) satisfies the upper bound

$$|\mathbf{Q}^*| \leq \max \{M(d, e, f), |\mathbf{Q}_{s_+}| \} =: M' \quad (3.46)$$

Chapter 3. The Sixth-Order Bulk Potential

on $\overline{B(0, 1)}$, where M is a constant depending only on t, d, e , and f .

We assume that the function $|\mathbf{Q}^*| : B(0, 1) \rightarrow \mathbb{R}$ attains its maximum at the interior point $\mathbf{r}^* \in B(0, 1)$. Recall that \mathbf{Q}^* is a solution of the Euler–Lagrange equations (3.9).

We multiply both sides of (3.9) by Q_{ij} to find

$$\begin{aligned} \frac{\varepsilon^2}{2} \Delta |\mathbf{Q}^*|^2 &= t |\mathbf{Q}^*|^2 - 3\sqrt{6} \operatorname{tr} \mathbf{Q}^{*3} + 2 |\mathbf{Q}^*|^4 \\ &\quad + d |\mathbf{Q}^*|^2 \operatorname{tr} \mathbf{Q}^{*3} + e |\mathbf{Q}^*|^6 + \frac{(f - e)}{6} (\operatorname{tr} \mathbf{Q}^{*3})^2 \end{aligned} \quad (3.47)$$

at \mathbf{r}^* , since $|\nabla \mathbf{Q}^*| + Q_{ij}^* \Delta Q_{ij}^* = \frac{1}{2} \Delta |\mathbf{Q}^*|^2$, and $|\nabla \mathbf{Q}^*| = 0$ at \mathbf{r}^* . Note that $\Delta |\mathbf{Q}^*|^2 \leq 0$ at $\mathbf{r}^* \in B(0, 1)$ by assumption. Define

$$h(\mathbf{Q}) = t |\mathbf{Q}|^2 - 3\sqrt{6} \operatorname{tr} \mathbf{Q}^3 + 2 |\mathbf{Q}|^4 + d |\mathbf{Q}|^2 \operatorname{tr} \mathbf{Q}^3 + e |\mathbf{Q}|^6 + \frac{(f - e)}{6} (\operatorname{tr} \mathbf{Q}^3)^2. \quad (3.48)$$

Recalling that $-\frac{1}{\sqrt{6}} |\mathbf{Q}|^3 \leq \operatorname{tr} \mathbf{Q}^3 \leq \frac{1}{\sqrt{6}} |\mathbf{Q}|^3$, by Lemma 1 in [56]. Consider the polynomial

$$H|\mathbf{Q}| := \frac{\min\{f - e, 0\}}{36} |\mathbf{Q}|^6 + e |\mathbf{Q}|^6 - \frac{d}{\sqrt{6}} |\mathbf{Q}|^5 + 2 |\mathbf{Q}|^4 - 3 |\mathbf{Q}|^3 + t |\mathbf{Q}|^2. \quad (3.49)$$

The function $H(|\mathbf{Q}|)$ has $n \leq 6$ real roots, $\{|\mathbf{Q}_i|\}_{i=1}^n$, with $|\mathbf{Q}_1| \leq \dots \leq |\mathbf{Q}_n|$, and H is positive for $|\mathbf{Q}| > |\mathbf{Q}_n|$ since $e > 0$. If $|\mathbf{Q}^*(\mathbf{r}^*)| > |\mathbf{Q}_n|$, then $\Delta |\mathbf{Q}^*|^2 > 0$ at \mathbf{r}^* , which is a contradiction. We set $M(t, d, e, f) := |\mathbf{Q}_n|$, so we may conclude that $|\mathbf{Q}^*| \leq \max\{M(t, d, e, f), |\mathbf{Q}_{s_+}|\}$ on $\overline{B(0, 1)}$.

Next, we demonstrate the local convexity of the Landau–de Gennes free energy, (3.1), for sufficiently large ε , closely following arguments in [64]. Let

$$X = \{\mathbf{Q} \in W^{1,2}(B(0, 1), \bar{S}) : \mathbf{Q} = \mathbf{Q}_{s_+} \text{ on } \partial B(0, 1); |\mathbf{Q}| \leq M'\}. \quad (3.50)$$

Chapter 3. The Sixth-Order Bulk Potential

Then for $\mathbf{Q}_u, \mathbf{Q}_v \in X$,

$$\begin{aligned} \mathcal{F} \left[\frac{1}{2}(\mathbf{Q}_u + \mathbf{Q}_v) \right] &= \int_{B(0,1)} \left(\frac{\varepsilon^2}{8} |\nabla \mathbf{Q}_u + \nabla \mathbf{Q}_v|^2 + f_B \left(\frac{1}{2}(\mathbf{Q}_u + \mathbf{Q}_v) \right) \right) dV \\ &= \frac{1}{2} \mathcal{F}[\mathbf{Q}_u] + \frac{1}{2} \mathcal{F}[\mathbf{Q}_v] - \frac{\varepsilon^2}{8} \|\nabla(\mathbf{Q}_u - \mathbf{Q}_v)\|_{L^2}^2 \\ &\quad + \int_{B(0,1)} \left(f_B \left(\frac{1}{2}(\mathbf{Q}_u + \mathbf{Q}_v) \right) - \frac{1}{2} f_B(\mathbf{Q}_u) - \frac{1}{2} f_B(\mathbf{Q}_v) \right) dV, \end{aligned} \quad (3.51)$$

where we have used the fact that $|\nabla \mathbf{Q}_u + \nabla \mathbf{Q}_v|^2 = 2|\nabla \mathbf{Q}_u|^2 + 2|\nabla \mathbf{Q}_v|^2 - |\nabla \mathbf{Q}_u - \nabla \mathbf{Q}_v|^2$.

By the Poincaré inequality, we have that

$$-\frac{1}{8} \|\nabla(\mathbf{Q}_u - \mathbf{Q}_v)\|_{L^2}^2 \leq -c_1 \|\mathbf{Q}_u - \mathbf{Q}_v\|_{L^2}^2, \quad (3.52)$$

for some positive constant, c_1 . Therefore,

$$\begin{aligned} \mathcal{F} \left[\frac{1}{2}(\mathbf{Q}_u + \mathbf{Q}_v) \right] &\leq \frac{1}{2} \mathcal{F}[\mathbf{Q}_u] + \frac{1}{2} \mathcal{F}[\mathbf{Q}_v] - c_1 \varepsilon^2 \|\mathbf{Q}_u - \mathbf{Q}_v\|_{L^2}^2 \\ &\quad + \int_{B(0,1)} \left(f_B \left(\frac{1}{2}(\mathbf{Q}_u + \mathbf{Q}_v) \right) - \frac{1}{2} f_B(\mathbf{Q}_u) - \frac{1}{2} f_B(\mathbf{Q}_v) \right) dV. \end{aligned} \quad (3.53)$$

Furthermore, we note that

$$f_B \left(\frac{x+y}{2} \right) - \frac{1}{2} f_B(x) - \frac{1}{2} f_B(y) \leq \|f_B\|_{W^{2,\infty}(\{z \in \bar{S}; |z| \leq M'\})} |x-y|^2, \quad (3.54)$$

for x, y satisfying $|x|, |y| \leq M'$ [64]. Hence, for some $c_2 := c_2(M', f_B(t, d, e, f)) > 0$, we may write

$$\mathcal{F} \left[\frac{1}{2}(\mathbf{Q}_u + \mathbf{Q}_v) \right] \leq \frac{1}{2} \mathcal{F}[\mathbf{Q}_u] + \frac{1}{2} \mathcal{F}[\mathbf{Q}_v] + (-c_1 \varepsilon^2 + c_2) \|\mathbf{Q}_u - \mathbf{Q}_v\|_{L^2}^2. \quad (3.55)$$

Then, if $\varepsilon^2 > \frac{c_2}{c_1}$, we find that

$$\mathcal{F} \left[\frac{1}{2}(\mathbf{Q}_u + \mathbf{Q}_v) \right] < \frac{1}{2}\mathcal{F}[\mathbf{Q}_u] + \frac{1}{2}\mathcal{F}[\mathbf{Q}_v], \quad (3.56)$$

$\forall \mathbf{Q}_u, \mathbf{Q}_v \in X, \mathbf{Q}_u \neq \mathbf{Q}_v$. Thus, \mathcal{F} is strictly convex on X .

Let us assume for the remainder of the proof that we are working with ε large enough to guarantee strict convexity of \mathcal{F} in (3.1). To show that a critical point of \mathcal{F} is unique, let us assume that there exist two distinct solutions, \mathbf{Q}_1 and \mathbf{Q}_2 , of (3.9) in X , as is done in the proof of Lemma 8.3 in [121]. Then, for $v \in [0, 1]$, the derivative of $\mathcal{F}[v\mathbf{Q}_1 + (1-v)\mathbf{Q}_2]$ vanishes at $v = 0$ and $v = 1$. However, the strict convexity of \mathcal{F} implies that \mathcal{F} can have only one critical point. Therefore, \mathbf{Q}_1 and \mathbf{Q}_2 cannot both be solutions of the Euler–Lagrange equations (3.9), so a critical point of \mathcal{F} must be unique.

Finally, Proposition 3.2 guarantees the existence of a radial hedgehog solution for any ε , and we are also guaranteed the existence of a global Landau–de Gennes energy minimiser of (3.1) for all ε by Proposition 3.1, so the radial hedgehog configuration, \mathbf{Q}^* in (3.11), is the unique critical point, and consequently, the unique global minimiser of the Landau–de Gennes free energy (3.1) when ε is sufficiently large. \square

Next, we demonstrate that the radial hedgehog solution is not globally minimising for the Landau–de Gennes free energy (3.1) in the low temperature regime by constructing a biaxial perturbation with lower energy, following arguments in Proposition 3.3 in [63].

Proposition 3.6. *The radial hedgehog solution, \mathbf{Q}^* in (3.11), is not the global minimiser of the Landau–de Gennes free energy (3.1) in the admissible space, $\mathcal{A}_{\mathbf{Q}}$, when*

$t < 0$ and $|t|$ is sufficiently large. In particular, the biaxial state,

$$\hat{\mathbf{Q}}(\mathbf{r}) = \begin{cases} \mathbf{Q}^*(\mathbf{r}) + \frac{1-10r}{(r^2+12)^2} \left(\mathbf{z} \otimes \mathbf{z} - \frac{1}{3}\mathbf{I} \right), & 0 \leq r \leq 0.1, \\ \mathbf{Q}^*(\mathbf{r}), & 0.1 \leq r \leq 1, \end{cases} \quad (3.57)$$

where \mathbf{z} is the unit vector in the z -direction, has lower Landau–de Gennes free energy than \mathbf{Q}^* .

Proof. We consider a general biaxial perturbation

$$\hat{\mathbf{Q}}(\mathbf{r}) = \begin{cases} \mathbf{Q}^*(\mathbf{r}) + \tilde{p}(r) \left(\mathbf{z} \otimes \mathbf{z} - \frac{1}{3}\mathbf{I} \right), & 0 \leq r < 0.1, \\ \mathbf{Q}^*(\mathbf{r}), & 0.1 \leq r \leq 1, \end{cases} \quad (3.58)$$

where $\tilde{p} : [0, 1] \rightarrow \mathbb{R}$ is nonzero for $0 \leq r < 0.1$, and $\tilde{p}(r) = 0$ for $0.1 \leq r \leq 1$, and \mathbf{Q}^* is the radial hedgehog solution. We find that

$$\begin{aligned} & \frac{1}{4\pi} \left(\mathcal{F}[\hat{\mathbf{Q}}] - \mathcal{F}[\mathbf{Q}^*] \right) \\ & \leq \int_0^{0.1} \frac{\varepsilon^2}{3} \left(\frac{d\tilde{p}}{dr} \right)^2 + \frac{t}{3}\tilde{p}^2 - \frac{2\sqrt{6}}{9}\tilde{p}^3 + \frac{28}{45}s^{*2}\tilde{p}^2 + \frac{2}{9}\tilde{p}^4 \\ & \quad + \frac{d}{5} \left(\frac{4}{27}s^{*3}\tilde{p}^2 + \frac{52}{135}s^{*2}\tilde{p}^3 + \frac{4}{27}\tilde{p}^5 \right) \\ & \quad + \frac{e}{6} \left(\frac{8}{5}s_+^4\tilde{p}^2 + \frac{128}{945}s^{*3}\tilde{p}^3 + \frac{8}{5}s^{*2}\tilde{p}^4 + \frac{16}{9}s^*\tilde{p}^5 + \frac{8}{27}\tilde{p}^6 \right) \\ & \quad + \frac{(f-e)}{6} \left(\frac{4}{45}s_+^4\tilde{p}^2 + \frac{112}{405}s^{*3}\tilde{p}^3 + \frac{4}{45}s^{*2}\tilde{p}^4 + \frac{4}{81}\tilde{p}^6 \right) r^2 dr. \end{aligned} \quad (3.59)$$

For large negative t , we can approximate s_+ by

$$s_+ \approx \left(\frac{-27t}{2(f+5e)} \right)^{1/4}, \quad (3.60)$$

by rearranging

$$\frac{3}{2} \frac{g'(s)}{s} = t - \sqrt{6}s + \frac{4}{3}s^2 + \frac{2d}{9}s^3 + \frac{4e}{9}s^4 + \frac{2(f-e)}{27}s^4 = 0, \quad (3.61)$$

where g is defined in (3.7), to

$$s^4 = \frac{27}{2(f+5e)} \left(-t + \sqrt{6}s - \frac{4}{3}s^2 - \frac{2d}{9}s^3 \right) \quad (3.62)$$

and neglecting terms independent of t for large negative t . Suppose we are working with large negative t . Then substituting

$$\tilde{p}(r) = \frac{1 - 10r}{(r^2 + 12)^2} \quad (3.63)$$

into the above, we find that $\frac{1}{4\pi} (\mathcal{F}[\hat{\mathbf{Q}}] - \mathcal{F}[\mathbf{Q}^*]) < 0$ if

$$t \lesssim \frac{500\varepsilon^2(77184e + 16437f)}{428440e - 32975f}. \quad (3.64)$$

Therefore we may conclude that the biaxial perturbation, (3.57), with $\tilde{p}(r)$ as in (3.63) has lower free energy than the radial hedgehog solution in the low temperature regime.

□

The above results make evident many parallels between the radial hedgehog solution with the fourth-order bulk potential in the literature and the radial hedgehog solution with the sixth-order bulk potential for moderately low temperatures. Key differences are that we do not have an explicit expression for s_+ with the sixth-order bulk potential, (3.6); and that there exist parameter regimes where the radial hedgehog scalar order parameter, s^* , might not be unique and monotonic, and may take negative values for

$r \in (0, 1)$.

We demonstrate numerically that the radial hedgehog scalar order parameter can take negative values deep in the nematic phase, and that a profile with negative values has lower energy than a nonnegative profile in this scenario. We work in a parameter regime for which $g(s)$ in (3.7) has two minimisers: a positive local minimiser, s_+ , and a negative global minimiser, s_- . We set $d = 1$, $e = 0$, and $f = 1$ and compute solutions of the ODE (3.18) for $t = -100$ in a large droplet specified by $\varepsilon = 0.1$. From the initial guess $s(r) = 0$, $r \in [0, 1]$, we obtain the positive profile in Figure 3.6a. The negative profile in Figure 3.6b is obtained from the initial guess $s(r) = 0.5s_-$, where s_- is the negative minimiser of (3.7) at $t = -100$. We verify numerically that the profile in Figure 3.6b has lower energy than the nonnegative profile in Figure 3.6a by computing the value of the free energy for each profile. This is a significant departure from the nature of the radial hedgehog scalar order parameter with the fourth-order bulk potential, which is required to be nonnegative and monotonic.

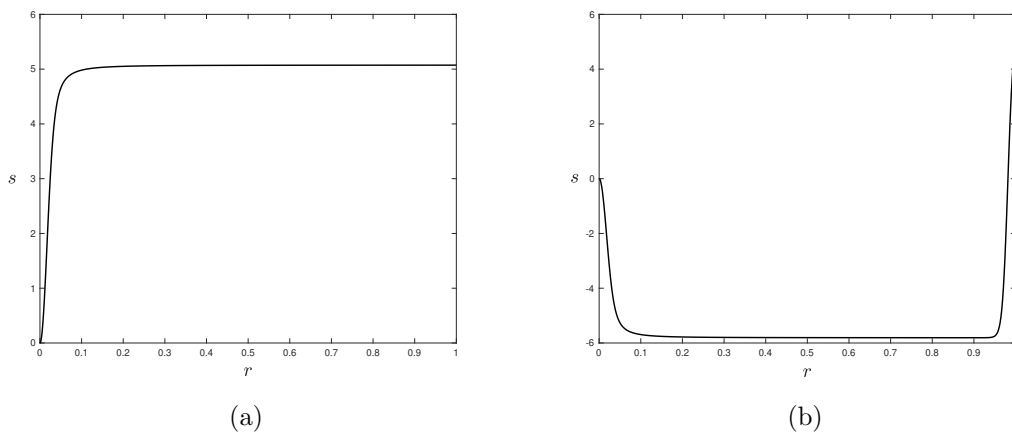


Figure 3.6: Radial hedgehog scalar order parameter profiles which solve the ODE (3.18) from the initial guess (a) $s(r) = 0$, $r \in [0, 1]$, and (b) $s(r) = 0.5s_-$, $r \in [0, 1]$.

3.4 Numerical Results

The critical points of the Landau–de Gennes free energy with the fourth-order bulk potential have been well-studied to date in the likes of [51], [67], among other works. As discussed in Section 1.5.3, it is well-known that there exist at least two critical points in addition to the radial hedgehog solution for large droplets and at low temperatures: the biaxial torus and split core solutions. Both of these configurations have small biaxial regions near the droplet centre and possess rotational symmetry and mirror symmetry across the plane perpendicular to the axis of rotational symmetry.

In this section, we address whether the split core and biaxial torus solutions survive as critical points of the Landau–de Gennes free energy with the sixth-order bulk potential. If they are present as critical points, this implies that their existence is a consequence of the symmetries of the problem, and is less influenced by the specific form of the bulk potential. In Section 3.4.1, we compute critical points of the Landau–de Gennes free energy with the sixth-order bulk potential. We consider the stability of the radial hedgehog solution in this framework in Section 3.4.2 by computing the Morse index of the radial hedgehog solution across a range of temperatures and droplet radii with both the fourth- and sixth-order bulk potentials. In Section 3.4.3, we demonstrate that an unstable radial hedgehog solution may act as a transition state between two equilibrium configurations via a gradient flow method. Finally, in Section 3.4.4, we visualise the solution landscape in both the fourth- and sixth-order bulk potential cases by computing bifurcation diagrams as a function of temperature.

3.4.1 Critical Points of the Landau–de Gennes Free Energy

Following work in [67], we numerically compute critical points of the Landau–de Gennes free energy in (3.1) with rotational symmetry about the z -axis and mirror symmetry

Chapter 3. The Sixth-Order Bulk Potential

across the xy -plane. We have outlined the symmetry assumptions, boundary conditions, and numerical methods in the fourth-order case in Sections 2.3.1 and 2.3.2. The symmetry assumptions and boundary conditions in the sixth-order bulk potential case are the same, with the key difference being that the Landau–de Gennes free energy is rewritten as

$$\begin{aligned}
\mathcal{F}[\mathbf{Q}] = \int_{B(0,1)} & \left(\frac{\varepsilon^2}{2} \left(q_{1,r}^2 + q_{2,r}^2 + q_{3,r}^2 + q_{1,z}^2 + q_{2,z}^2 + q_{3,z}^2 + \frac{1}{r^2} (4q_2^2 + q_3^2) \right) \right. \\
& + \frac{t}{2} (q_1^2 + q_2^2 + q_3^2) - q_1^3 + 3q_1q_2^2 - \frac{3}{2}q_1q_3^2 - \frac{3\sqrt{3}}{2}q_2q_3^2 \\
& + \frac{1}{2} (q_1^4 + q_2^4 + q_3^4 + 2q_1^2q_2^2 + 2q_1^2q_3^2 + 2q_2^2q_3^2) \\
& + \frac{d}{5} \left(\frac{\sqrt{6}}{6}q_1^5 - \frac{\sqrt{6}}{3}q_1^3q_2^2 + \frac{5\sqrt{6}}{12}q_1^3q_3^2 - \frac{\sqrt{6}}{2}q_1q_2^4 - \frac{\sqrt{6}}{4}q_1q_2^2q_3^2 \right. \\
& \quad \left. + \frac{\sqrt{6}}{4}q_1q_3^4 + \frac{3\sqrt{2}}{4}q_1^2q_2q_3^2 + \frac{3\sqrt{2}}{4}q_2^3q_3^2 + \frac{3\sqrt{2}}{4}q_2q_3^4 \right) \\
& + \frac{e}{6} (q_1^6 + q_2^6 + q_3^6 + 3q_1^4q_2^2 + 3q_1^4q_3^2 + 3q_1^2q_2^4 \\
& \quad + 3q_1^2q_3^4 + 3q_2^4q_3^2 + 3q_2^2q_3^4 + 6q_1^2q_2^2q_3^2) \\
& + \frac{(f-e)}{6} \left(\frac{1}{6}q_1^6 - q_1^4q_2^2 + \frac{1}{2}q_1^4q_3^2 + \frac{\sqrt{3}}{2}q_1^3q_2q_3^2 \right. \\
& \quad + \frac{3}{2}q_1^2q_2^4 - \frac{3}{2}q_1^2q_2^2q_3^2 - \frac{3\sqrt{3}}{2}q_1q_2^3q_3^2 \\
& \quad \left. + \frac{3}{8}q_1^2q_3^4 + \frac{3\sqrt{3}}{4}q_1q_2q_3^4 + \frac{9}{8}q_2^2q_3^4 \right) \Big) dV. \tag{3.65}
\end{aligned}$$

with the associated weak formulations in this case given by

$$\begin{aligned}
 F_1 = & \int_{B(0,1)} \varepsilon^2 \nabla q_1 \cdot \nabla v_1 \\
 & + v_1 \left(t q_1 - 3 q_1^2 + 3 q_2^2 - \frac{3}{2} q_3^2 + 2 q_1^3 + 2 q_1 q_2^2 + 2 q_1 q_3^2 \right. \\
 & \quad + \frac{d}{5} \left(\frac{5\sqrt{6}}{6} q_1^4 - \sqrt{6} q_1^2 q_2^2 + \frac{5\sqrt{6}}{5} q_1^2 q_3^2 \right. \\
 & \quad \quad \left. \left. - \frac{\sqrt{6}}{2} q_2^4 - \frac{\sqrt{6}}{4} q_2^2 q_3^2 + \frac{\sqrt{6}}{4} q_3^4 + \frac{3\sqrt{2}}{2} q_1 q_2 q_3^2 \right) \right. \\
 & \quad + e (q_1^5 + 2 q_1^3 q_2^2 + 2 q_1^3 q_3^2 + q_1 q_2^4 + q_1 q_3^4 + 2 q_1 q_2^2 q_3^2) \\
 & \quad \left. + \frac{(f-e)}{6} \left(q_1^5 - 4 q_1^3 q_2^2 + 2 q_1^3 q_3^2 + \frac{3\sqrt{3}}{2} q_1^2 q_2 q_3^2 + 3 q_1 q_2^4 \right. \right. \\
 & \quad \quad \left. \left. - 3 q_1 q_2^2 q_3^2 - \frac{3\sqrt{3}}{2} q_2^3 q_3^2 + \frac{3}{4} q_1 q_3^4 + \frac{3\sqrt{3}}{4} q_2 q_3^4 \right) \right) dV,
 \end{aligned}$$

$$\begin{aligned}
 F_2 = & \int_{B(0,1)} \varepsilon^2 \nabla q_2 \cdot \nabla v_2 \\
 & + v_2 \left(\frac{4}{r^2} \varepsilon^2 q_2 + t q_2 + 6 q_1 q_2 - \frac{3\sqrt{3}}{2} q_3^2 + 2 q_1^2 q_2 + 2 q_2^3 + 2 q_2 q_3^2 \right. \\
 & \quad + \frac{d}{5} \left(-\frac{2\sqrt{6}}{3} q_1^3 q_2 - 2\sqrt{6} q_1 q_2^3 - \frac{\sqrt{6}}{2} q_1 q_2 q_3^2 \right. \\
 & \quad \quad \left. \left. + \frac{3\sqrt{2}}{4} q_1^2 q_3^2 + \frac{9\sqrt{2}}{4} q_2^2 q_3^2 + \frac{3\sqrt{2}}{4} q_3^4 \right) \right. \\
 & \quad + e (q_2^5 + q_1^4 q_2 + 2 q_1^2 q_2^3 + 2 q_2^3 q_3^2 + q_2 q_3^4 + 2 q_1^2 q_2 q_3^2) \\
 & \quad \left. + \frac{(f-e)}{6} \left(-2 q_1^4 q_2 + \frac{\sqrt{3}}{2} q_1^3 q_3^2 + 6 q_1^2 q_2^3 - 3 q_1^2 q_2 q_3^2 \right. \right. \\
 & \quad \quad \left. \left. - \frac{9\sqrt{3}}{2} q_1 q_2^2 q_3^2 + \frac{3\sqrt{3}}{4} q_1 q_3^4 + \frac{9}{4} q_2 q_3^4 \right) \right) dV,
 \end{aligned}$$

$$\begin{aligned}
 F_3 = & \int_{B(0,1)} \varepsilon^2 \nabla q_3 \cdot \nabla v_3 \\
 & + v_3 \left(\frac{1}{r^2} \varepsilon^2 q_3 + t q_3 - 3q_1 q_3 - 3\sqrt{3} q_2 q_3 + 2q_1^2 q_3 + 2q_2^2 q_3 + 2q_3^3 \right. \\
 & \quad + \frac{d}{5} \left(\frac{5\sqrt{6}}{6} q_1^3 q_3 - \frac{\sqrt{6}}{2} q_1 q_2^2 q_3 + \sqrt{6} q_1 q_3^3 \right. \\
 & \quad \quad \left. \left. + \frac{3\sqrt{2}}{2} q_1^2 q_2 q_3 + \frac{3\sqrt{2}}{2} q_2^3 q_3 + 3\sqrt{2} q_2 q_3^3 \right) \right. \\
 & \quad + e (q_3^5 + q_1^4 q_3 + 2q_1^2 q_3^3 + q_2^4 q_3 + 2q_2^2 q_3^3 + 2q_1^2 q_2^2 q_3) \\
 & \quad \left. + \frac{(f-e)}{6} \left(q_1^4 q_3 + \sqrt{3} q_1^3 q_2 q_3 - 3q_1^2 q_2^2 q_3 \right. \right. \\
 & \quad \quad \left. \left. - 3\sqrt{3} q_1 q_2^3 q_3 + \frac{3}{2} q_1^2 q_3^3 + 3\sqrt{3} q_1 q_2 q_3^3 + \frac{9}{2} q_2^2 q_3^3 \right) \right) dV, \tag{3.66}
 \end{aligned}$$

where v_1, v_2, v_3 are test functions.

The boundary conditions on the edge of the droplet in the sixth-order case are also given by

$$q_1 = \frac{\sqrt{6}}{6} (2 - 3r^2) s_+, \quad q_2 = \frac{\sqrt{2}}{2} r^2 s_+, \quad q_3 = \sqrt{2} r z s_+ \quad \text{on } r^2 + z^2 = 1, \tag{3.67}$$

with s_+ being the largest positive minimiser of the function g in (3.7).

We numerically compute critical points of the Landau–de Gennes free energy with the fourth- and sixth-order bulk potentials by solving the weak formulations (2.44) and (3.66), respectively. We plot the biaxiality parameter,

$$\beta = 1 - 6 \frac{(\text{tr } \mathbf{Q}^3)^2}{(\text{tr } \mathbf{Q}^2)^3}, \tag{3.68}$$

of the numerically computed critical points, and we recall that we first discuss the notion of the biaxiality parameter in 1.3.3. We also plot the leading eigenvector of the \mathbf{Q} -tensor in the examples below, which is the eigenvector associated with the largest

positive eigenvalue of \mathbf{Q} , giving an indication of the preferred direction of the nematic liquid crystal molecules. In addition, we consider the sign of the scalar order parameter at the origin, which is another good indicator of which configuration we have obtained. As discussed in Section 2.3.2, this is equivalent to considering the sign of q_1 at the origin. The radial hedgehog solution has $q_1(0, 0) = 0$, while the split core and biaxial torus solutions have $q_1(0, 0) < 0$ and $q_1(0, 0) > 0$, respectively.

In Figures 3.7a-3.7c, we plot the biaxiality parameter, β , and the leading eigenvector of the radial hedgehog, split core, and biaxial torus configurations obtained with the fourth-order bulk potential. We plot the radial hedgehog configuration in Figure 3.7a with $t = 0$ and $\varepsilon = 1$. The radial hedgehog solution has $\beta = 0$ everywhere, with an isotropic point at $r = 0$, meaning $q_1 = 0$ at $(r, z) = (0, 0)$, while the leading eigenvector is the radial unit vector. We plot the split core and biaxial torus solutions for $t = -10$, $\varepsilon = 0.5$ in Figures 3.7b and 3.7c, respectively. We observe the signature regions of biaxiality associated with the split core and biaxial torus solutions, indicated by the red regions. Moreover, we find that $q_1(0, 0) < 0$ for the split core and $q_1(0, 0) > 0$ for the biaxial torus. We compute the Morse index, which is defined in Section 2.3.3, of each configuration in Figures 3.7a-3.7c, and find that each is at least a locally stable critical point of the Landau–de Gennes free energy with the fourth-order bulk potential, (2.26), for the specified values of t and ε . Local stability of a Landau–de Gennes critical point implies that it is potentially observable in experiments and applications.

We repeat the same numerical investigation with the Landau–de Gennes free energy with the sixth-order bulk potential. The behaviour and trends are expected to be similar to those observed with the fourth-order bulk potential, at least for moderately low temperatures, as suggested by the analysis in Section 3.3. In Figures 3.7d-3.7f, we plot the biaxiality parameter and leading eigenvector of critical points of (3.65)

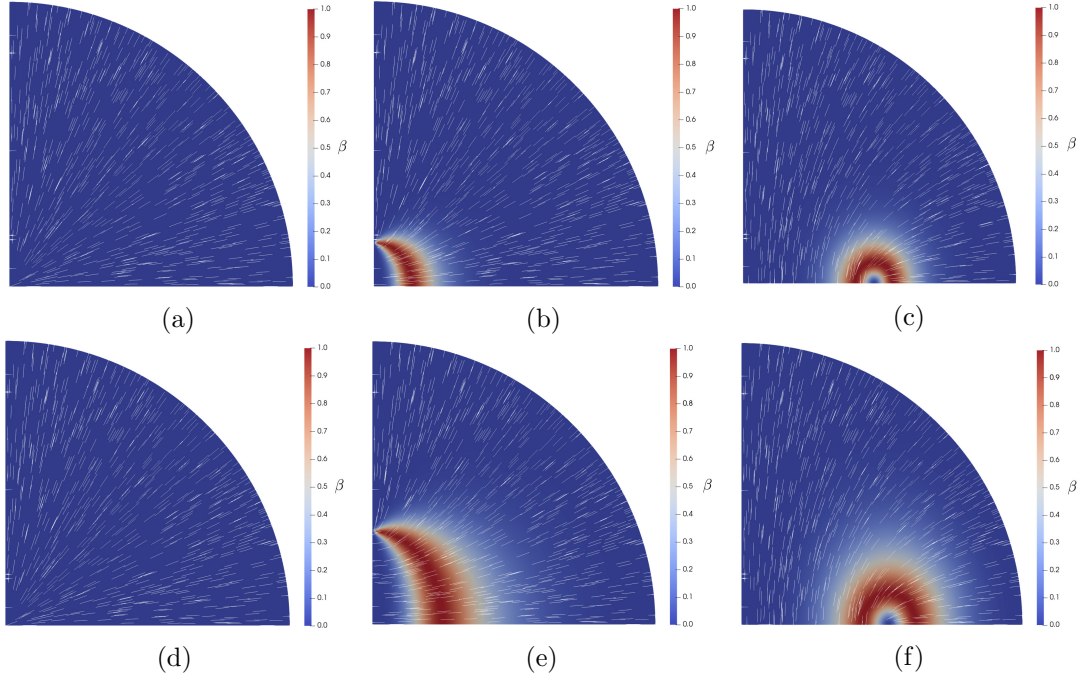


Figure 3.7: Biaxiality parameter, β , and leading eigenvector of (a)-(c) Landau–de Gennes critical points of (2.39); and (d)-(f) Landau–de Gennes critical points of (3.65) with $d = 1$, $e = 0$, and $f = 1$. (a), (d) Radial hedgehog solution with $t = 0$, $\varepsilon = 1$. (b), (e) Split core solution with $t = -10$, $\varepsilon = 0.5$. (c), (f) Biaxial torus solution with $t = -10$, $\varepsilon = 0.5$. We plot $r \in [0, 1]$ on the horizontal axis and $z \in [0, 1]$ on the vertical axis.

with $d = 1$, $e = 0$, and $f = 1$. We plot the radial hedgehog solution at $t = 0$ and $\varepsilon = 1$ in Figure 3.7d, and the split core and biaxial torus solutions at $t = -10$ and $\varepsilon = 0.5$ in Figures 3.7e and 3.7f, respectively. We verify numerically that $q_1(0, 0) = 0$ for the radial hedgehog solution, while q_1 is negative at the origin for the split core solution and positive at the origin for the biaxial torus solution, although we do not quote the figures here. Comparing Figures 3.7e and 3.7f obtained with a sixth-order bulk potential with Figures 3.7b and 3.7c, respectively, which are obtained with the fourth-order bulk potential at the same values of t and ε , we observe that the regions of biaxiality of the split core and biaxial torus solutions are larger with the sixth-order bulk potential, which suggests that bulk biaxiality is more favourable under the

sixth-order bulk potential in comparison to the fourth-order bulk potential. We again compute the Morse index of each critical point in Figures 3.7d-3.7f, and find that each is also at least a locally stable critical point of the Landau–de Gennes free energy with the sixth-order bulk potential.

3.4.2 The Morse Index of the Radial Hedgehog Solution

We characterise the stability of the Landau–de Gennes critical points using the Morse index, which we introduced in Section 2.3.3. We recall that an index-0 critical point is at least locally stable, while all index- k critical points, with $k > 0$, are unstable. We numerically compute the Morse index of the radial hedgehog solution across a range of temperatures and droplet radii (recalling that ε is inversely proportional to droplet radius), to study the effects of temperature and droplet size on the stability of the radial hedgehog solution. We note that our study is limited to the class of \mathbf{Q} -tensors with three degrees of freedom, as discussed in Section 2.3.1.

As outlined in Section 2.3.3, we solve for the particular form of the \mathbf{Q} -tensor with

$$q_1 = \frac{\sqrt{6}}{6} \left(2 - \frac{3r^2}{r^2 + z^2} \right) s^*, \quad q_2 = \frac{\sqrt{2}r^2}{2(r^2 + z^2)} s^*, \quad q_3 = \frac{\sqrt{2}rz}{r^2 + z^2} s^*, \quad (3.69)$$

where s^* is a solution of the ODE (2.46) with the fourth-order bulk potential; and solves the ODE (3.18) in the sixth-order case.

In Figures 3.8a and 3.8b, we tabulate the Morse index of the radial hedgehog solution with the fourth- and sixth-order bulk potentials, respectively, with $d = 1$, $e = 0$, and $f = 1$, for a range of values of t and ε .

We make some general observations: the Morse index of the radial hedgehog solution is lower for higher values of t and ε in both cases. This is consistent with the

Chapter 3. The Sixth-Order Bulk Potential

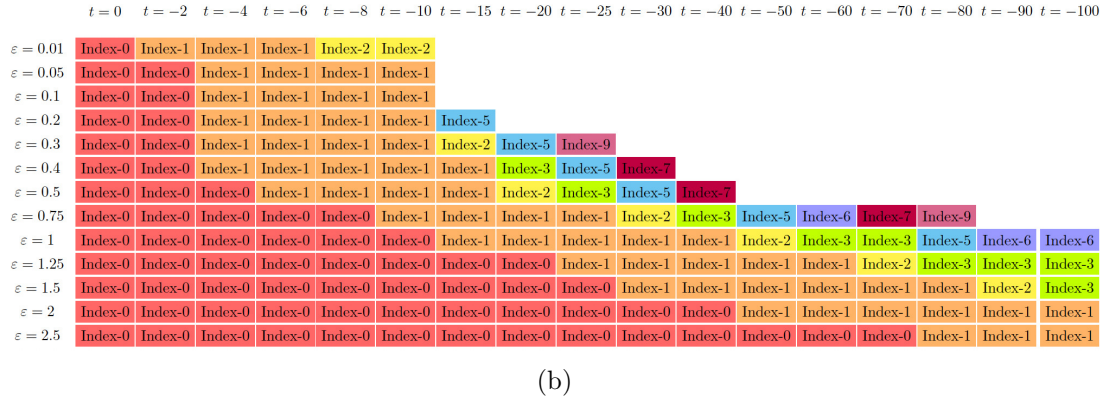
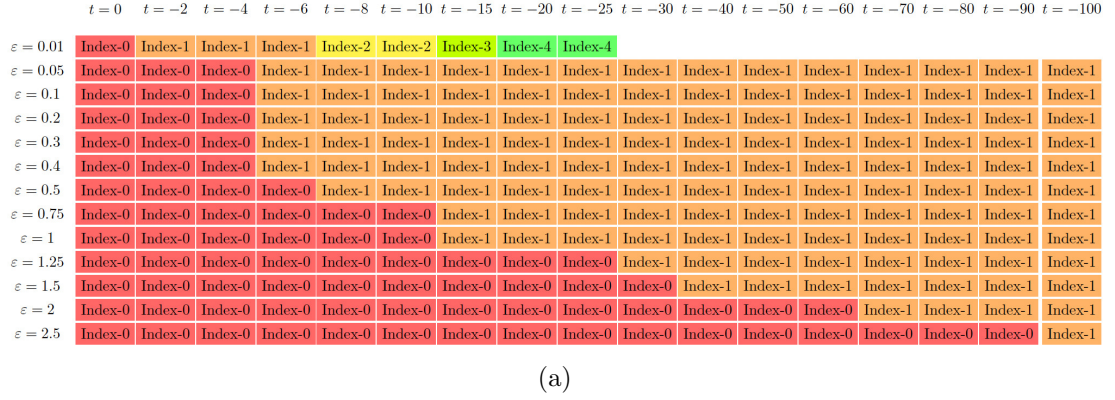


Figure 3.8: Morse index of the radial hedgehog solution for the given value of t and ε , as a critical point of the Landau–de Gennes free energy with the (a) fourth-order bulk potential, (2.39); and (b) the sixth-order bulk potential, (3.65), with $d = 1$, $e = 0$, $f = 1$. Each index is assigned a different colour for readability. Blank spaces in the tables correspond to cases for which all ten computed eigenvalues are negative, or when the solver fails to compute the ten smallest eigenvalues.

fact that the radial hedgehog solution is stable closer to the isotropic-nematic transition temperature (where the nematic phase gains stability) and for smaller droplets. Comparing the indices with the fourth- and sixth-order bulk potentials, we note that the radial hedgehog solution has higher index in the sixth-order case compared to the fourth-order case. This suggests that the sixth-order bulk potential has a destabilising effect on the radial hedgehog solution, likely because it admits biaxial critical points. Consequently, the radial hedgehog solution has more unstable biaxial eigendirections, resulting in a higher Morse index compared to the fourth-order bulk potential, which

does not admit biaxial critical points.

3.4.3 The Radial Hedgehog Solution as an Index-1 Transition State

In this section, we attempt to identify scenarios in which the radial hedgehog solution acts as an index-1 saddle point, because index-1 saddle points can be referred to as *transition states*, which are relevant for switching between two locally stable states [116]. In practice, this means that the index-1 state mediates the transition between stable states and may be observable in the non-equilibrium dynamics.

We work with values of t and ε for which the radial hedgehog solution is an index-1 critical point of the Landau–de Gennes free energies (2.39) and (3.65), and we can easily identify such scenarios from the tables in Figures 3.8a and 3.8b. We compute the transition pathway between two index-0 Landau–de Gennes critical points, through an index-1 radial hedgehog solution, \mathbf{q}^* , described in Section 3.4.2. We use a gradient flow method and take small perturbations of the radial hedgehog solution along the direction of the eigenvector associated with the negative eigenvalue of the Hessian as an initial condition, we solve the initial value problem

$$\begin{aligned} \frac{\partial \mathbf{q}}{\partial \tau} &= -\nabla \mathcal{F}(\mathbf{q}, \nabla \mathbf{q}) \quad \text{in } B(0, 1) \text{ for } \tau > 0, \\ \mathbf{q} &= \mathbf{q}_0 = \mathbf{q}^* \pm \lambda \mathbf{u}, \quad \text{in } B(0, 1) \text{ at } \tau = 0, \end{aligned} \tag{3.70}$$

with boundary conditions (2.41)-(2.43), where \mathcal{F} is the Landau–de Gennes free energy with the fourth- or sixth-order bulk potential, given by (2.39) or (3.65), respectively; the quantity λ is a small positive constant; and \mathbf{u} is the unstable eigendirection of the radial hedgehog solution. We refer the reader to Section 2.3.4 for more details on the above initial value problem in the fourth-order bulk potential case, which we use as an illustrative example as the methods are easily extended to the sixth-order case.

As an example, the unstable eigendirection of the radial hedgehog solution as a critical point of (3.65) with $t = -12$, $\varepsilon = 0.5$, $d = 1$, $e = 0$, and $f = 1$ is $\mathbf{u} = [6.11 \times 10^{-2}, 3.34 \times 10^{-18}, 1.15 \times 10^{-18}]^T$, at the origin. A perturbation of the radial hedgehog solution, $\mathbf{q}_0 = \mathbf{q}^* + \lambda \mathbf{u}$, yields the biaxial torus configuration, while a perturbation $\mathbf{q}_0 = \mathbf{q}^* - \lambda \mathbf{u}$, yields the split core configuration. This is in agreement with the fact that $q_1 > 0$ at the origin for a biaxial torus solution and $q_1 < 0$ at the origin for a split core solution.

Figure 3.9a shows an example of two index-0 critical points of the Landau–de Gennes free energy with the fourth-order bulk potential, (2.39), while Figure 3.9b shows an example of two index-0 critical points of the Landau–de Gennes free energy with the sixth-order bulk potential, (3.65), in both cases obtained via a gradient flow method with the perturbed index-1 radial hedgehog solution as an initial condition. This strongly suggests that there are transition pathways via the index-1 radial hedgehog solutions between the index-0 biaxial torus and split core solutions at $t = -12$ and $\varepsilon = 0.5$.

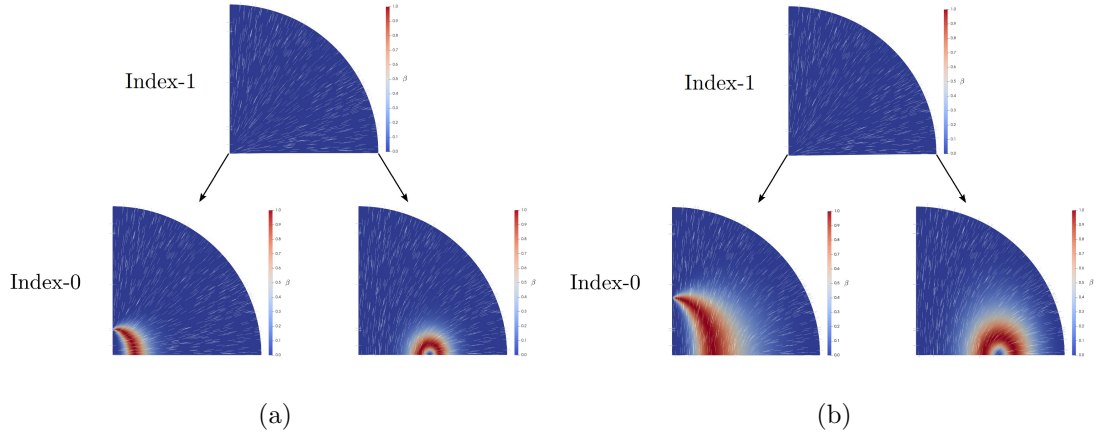


Figure 3.9: The transition pathways between two stable states. Index-0 split core and biaxial torus solutions via index-1 transition state radial hedgehog with (a) the fourth-order bulk potential (2.39) at $t = -12$ and $\varepsilon = 0.5$, and (b) the sixth-order bulk potential (3.65) with $t = -12$, $\varepsilon = 0.5$, $d = 1$, $e = 0$, and $f = 1$. We plot $r \in [0, 1]$ on the horizontal axis and $z \in [0, 1]$ on the vertical axis.

Note that the split core solution may not be index-0 in the full class of admissible \mathbf{Q} -tensors without the symmetry constraints, as suggested in [67]. Nevertheless, we speculate that these reduced examples can be generalised to show that the radial hedgehog solution can act as a transition state between two index-0 Landau–de Gennes critical points in the admissible space (3.8), without the symmetry constraints and exploiting the full five degrees of freedom.

3.4.4 Bifurcation Diagrams

We numerically compute bifurcation diagrams as a function of temperature with the Landau–de Gennes free energies (2.39) and (3.65) in Figures (3.10a) and (3.10b), respectively, using the numerical methods outlined in Section 2.3.5. We plot the value of the scalar order parameter, s , of each configuration at the origin against temperature, noting that $s(0, 0) = \sqrt{\frac{3}{2}}q_1(0, 0)$ and that all configurations are uniaxial at the origin due to the boundary conditions (2.42) and (2.43). In what follows, we consider only radial hedgehog solutions with positive scalar order parameter profiles, recalling that the global minimiser of (3.17) can be negative for low temperatures, as demonstrated in Section 3.3.

The two bifurcation diagrams are qualitatively similar and the bifurcation points are simply shifted. The radial hedgehog solution, with $s(0, 0) = 0$, is the unique critical point for high temperatures; the radial hedgehog and biaxial torus configurations are stable at intermediate temperatures, where we also observe an unstable biaxial torus configuration; and the radial hedgehog configuration loses stability at low temperatures, while the globally minimising biaxial torus remains stable, accompanied by the emergence of a locally stable split core configuration. As expected, the radial hedgehog solution loses stability at a higher temperature in the sixth-order case, compared to the

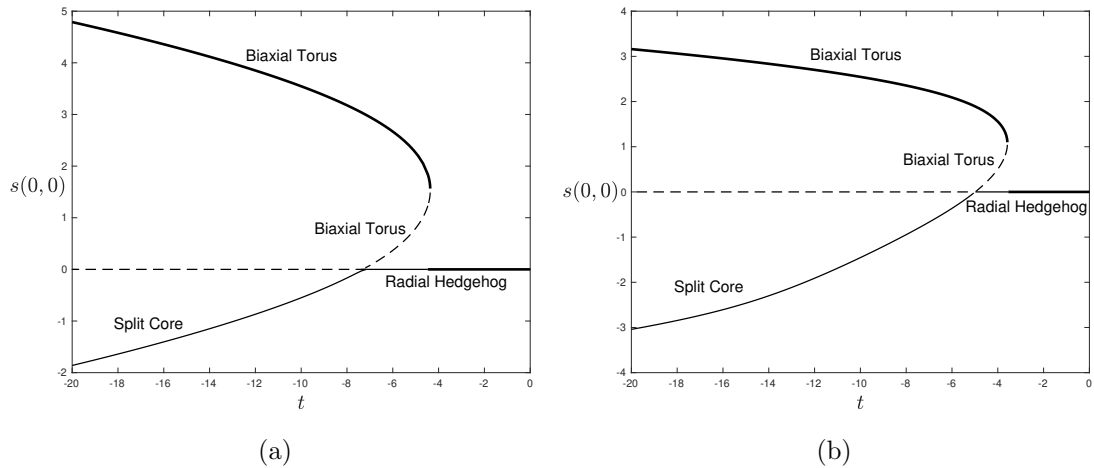


Figure 3.10: Bifurcation diagrams for the Landau–de Gennes free energies for $\varepsilon = 0.5$ with (a) fourth-order bulk potential (2.39), and (b) sixth-order bulk potential (3.65) with $d = 1$, $e = 0$, and $f = 1$. We plot the scalar order parameter of each configuration. Bold solid lines indicate the global minimiser; thin solid lines indicate local stability/minimality; and dashed lines indicate instability.

fourth-order case, so that the radial hedgehog configuration is unstable over a wider temperature range with the sixth-order bulk potential. We outline the methods used to compute the bifurcation diagrams in Section 2.3.5.

We plot the stable and unstable biaxial torus configurations with the fourth-order bulk potential at $t = -6.5$ with $\varepsilon = 0.5$ in Figures 3.11a and 3.11b respectively; and with the sixth-order bulk potential at $t = -4$ with $\varepsilon = 0.5$, $d = 1$, $e = 0$, and $f = 1$ in the sixth-order case in Figures 3.11c and 3.11d. The key difference is that the biaxial region is closer to the origin in the unstable biaxial torus configuration. Furthermore, the unstable biaxial torus is an index-1 critical point of the Landau–de Gennes free energy, and is accompanied by stable biaxial torus and radial hedgehog solutions at temperatures at which it is observed. Therefore, it is reasonable to speculate that the unstable, index-1 biaxial torus could act as a transition state between the stable, index-0 biaxial torus and radial hedgehog solutions.

From this numerical investigation, we deduce that there are only qualitative dif-

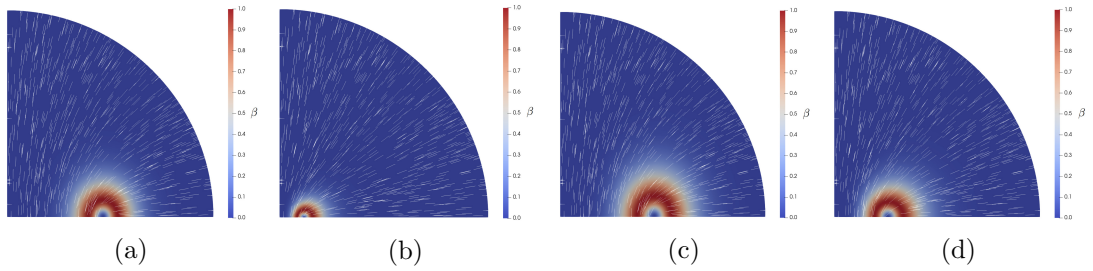


Figure 3.11: (a) Stable biaxial torus configuration; and (b) unstable biaxial torus configuration for (2.39) with the fourth-order bulk potential, with $t = -6.5$ with $\varepsilon = 0.5$. (c) Stable biaxial torus, and (d) unstable biaxial torus configuration for (3.65) with the sixth-order bulk potential, for $t = -4$ and $\varepsilon = 0.5$, $d = 1$, $e = 0$, and $f = 1$. We plot $r \in [0, 1]$ on the horizontal axis and $z \in [0, 1]$ on the vertical axis.

ferences between the critical points of the Landau–de Gennes free energies (2.39) and (3.65). Key differences are that uniaxial critical points are more unstable, or have higher Morse indices, in the sixth-order case; and that the biaxial critical points have larger ranges of stability with respect to temperature and droplet size, and larger biaxial regions in the sixth-order case compared to the fourth-order case. We note that the biaxial torus solution is predominantly uniaxial away from the characteristic disclination line, and hence, it would be interesting to investigate its stability when (3.6) strongly favours a bulk biaxial phase, with and without the symmetry constraints (2.42) and (2.43). Indeed, we give an example of a biaxial torus configuration which is a stable critical point of the Landau–de Gennes free energy with the sixth-order bulk potential at the low temperature $t = -50$, with $\varepsilon = 0.5$, $d = 1$, $e = 0$, and $f = 1$ which possesses a large biaxial region at the low temperature $t = -50$ in Figure 3.12. Referring to Figure 3.5, we note that the global minimiser of the sixth-order bulk potential, (3.6), is biaxial at this low temperature. This suggests that the biaxial region corresponding to the biaxial torus grows as temperature decreases and the bulk behaviour dominates. Furthermore, this suggests that the liquid crystal configuration approaches a purely biaxial state, approximating the global minimiser of the sixth-order bulk potential. In

fact, by direct analogy with [49], it is possible to prove that global minimisers of (3.1) will converge to minimisers of (3.6) almost everywhere, with the exception of defects and boundary layers, for sufficiently large domains and hence are expected to demonstrate bulk biaxiality. This is of particular interest because bulk biaxiality is typically elusive and difficult to detect experimentally.

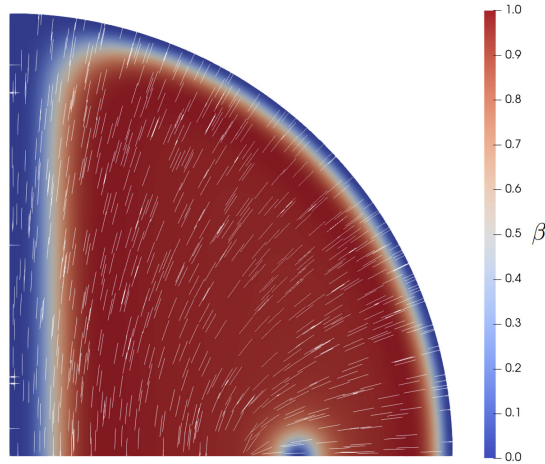


Figure 3.12: Biaxial torus configuration at $t = -50$, $\varepsilon = 0.5$, with $d = 1$, $e = 0$, and $f = 1$. We plot $r \in [0, 1]$ on the horizontal axis and $z \in [0, 1]$ on the vertical axis.

3.5 Summary

In this chapter, we perform some analytical and numerical studies of critical points of a Landau–de Gennes free energy with a sixth-order bulk potential, (3.1), in contrast to the majority of studies in the literature, which depend on the fourth-order bulk potential. We demonstrate that the sixth-order bulk potential, (3.6), admits a biaxial minimiser for sufficiently low temperatures, and does not admit stable uniaxial critical points deep in the nematic phase in Section 3.2, reinforcing the conclusions that were previously reached in [61]. This in contrast to the critical points of the fourth-order bulk potential, which are exclusively uniaxial. Furthermore, we have demonstrated that the

sixth-order bulk potential can have a uniaxial global minimiser with a negative scalar order parameter at low temperatures when restricted to the class of uniaxial \mathbf{Q} -tensors, which is also in contrast to the behaviour of critical points of the fourth-order bulk potential, which has a uniaxial global minimiser with positive scalar order parameter at all temperatures at which it has nonzero critical points.

Our analytical results in Section 3.3 show that there are many analogies between the properties of the radial hedgehog solution with the fourth- versus the sixth-order bulk potential at moderately low temperatures, where the global minimiser of (3.6) is uniaxial with positive scalar order parameter. We prove uniqueness, monotonicity and nonnegativity of the radial hedgehog scalar order parameter in a moderate temperature regime. Key differences arise at low temperatures, where these arguments fail. We no longer have uniqueness of the radial hedgehog solution, and demonstrate the multiplicity of radial hedgehog solutions at low temperatures by finding a globally minimising radial hedgehog solution with a negative scalar order parameter. The radial hedgehog solution with a negative scalar order parameter in the interior describes a uniaxial state in which the nematic liquid crystal molecules align orthogonally to the radial direction, and one can draw comparisons between this behaviour and the transitions from homeotropic to planar orientations on nematic shells upon cooling in experiments discussed in [122].

The physical implications of the results in Section 3.3 are unclear as yet, and one could argue that the Landau–de Gennes model with the sixth-order bulk potential is not necessarily valid for low temperatures.

Our numerical results in Section 3.4.2 indicate that the radial hedgehog solution with the sixth-order bulk potential has a smaller domain of stability than its counterpart with the fourth-order bulk potential. This is to be expected, since (3.6) favours bulk

biaxiality at sufficiently low temperatures, while the radial hedgehog solution is purely uniaxial with the exception of the isotropic point defect at the droplet centre. We also numerically compute the biaxial torus and split core solutions as critical points of (2.39) and (3.65) for comparison, with the key differences being that biaxial regions are larger under the sixth-order bulk potential; and that both the biaxial torus and split core solutions have larger domains of stability with the sixth-order bulk potential, which is evident from the bifurcation diagrams in Section 3.4.4. We also provide numerical evidence in Section 3.4.3 to support the notion that an unstable radial hedgehog solution mediates transitions between stable split core and biaxial torus solutions, suggesting that the radial hedgehog configuration might be physically observable in switching processes between these two stable states.

The critical points studied in this chapter exploit only three of the five degrees of freedom, and the biaxial torus and split core solutions are only ‘locally’ biaxial solutions. In [1], we find a new biaxial critical point of (3.6), which exploits the full five degrees of freedom and lacks rotational and mirror symmetry. The solution is almost maximally biaxial in the droplet interior, with the exception of the imposed uniaxial boundary condition and the defect structures. An interesting next step would be to conduct a more in-depth numerical investigation of the critical points of the Landau–de Gennes free energies (2.26) and (3.6) without the imposed rotational and mirror symmetry. However, we note that this is significantly more computationally expensive, making the problem prohibitive with the methods we have used.

The results in this chapter provide a reference for future experiments, and may help indicate whether the fourth-order bulk potential is sufficient to capture the behaviour of nematic liquid crystals; or whether the extra terms in the sixth-order bulk potential should be incorporated into the theory. We indicate the stability of equilibrium con-

Chapter 3. The Sixth-Order Bulk Potential

figurations according to temperature and droplet size, and note that there are some quantitative differences between the predictions of the fourth- and sixth-order bulk potentials. Future experiments could investigate which equilibrium configurations are stable under different conditions to discern which set of predictions physical systems agree better with.

A physically relevant question is whether the sixth-order bulk potential better captures the liquid crystal behaviour than the fourth-order bulk potential. A key next step in answering this question is to identify realistic values of the parameters d , e and f . With realistic values for these parameters, one could conduct experiments on the experimentally observable phases in temperatures regimes for which the sixth-order bulk potential favours uniaxiality and biaxiality, respectively, testing for bulk biaxiality. Such a comparison to experiments would allow us to assess the suitability and validity of both the fourth- and sixth-order bulk potentials.

Chapter 4

Critical Points of the Ferronematic Bulk Potential

In Chapter 3, we study purely nematic liquid crystals. We noted in Section 1.5.4 that nematic liquid crystals respond poorly to external magnetic fields, and introduced the idea of ferronematic liquid crystals. We recall that ferronematic liquid crystals are nematic liquid crystals which are doped with magnetic nanoparticles, which exhibit spontaneous magnetisation in the absence of external fields, and have a heightened response to the application of external magnetic fields in comparison to pure nematic liquid crystals. The mathematical modelling of ferronematic liquid crystals with a Landau–de Gennes-type free energy, first introduced in Section 1.5.4, is the focus of this chapter and the next.

In Section 3.2, we compute critical points of a sixth-order bulk potential in the class of uniaxial \mathbf{Q} -tensors, and in a more general class of \mathbf{Q} -tensors. We recall that with the fourth-order bulk potential, the global minimiser has a positive scalar order parameter in the class of uniaxial \mathbf{Q} -tensors, and that the global minimiser cannot ever be biaxial under the fourth-order bulk potential. In Section 3.2, we demonstrate that the global

Chapter 4. Critical Points of the Ferronematic Bulk Potential

minimiser of the sixth-order bulk potential has a negative scalar order parameter at low temperatures in the class of uniaxial \mathbf{Q} -tensors; and that the global minimiser is biaxial in the more general class of \mathbf{Q} -tensors at low temperatures.

In this chapter, we study critical points of the dimensionless ferronematic bulk potential [98], [99]

$$f_F(\mathbf{Q}, \mathbf{M}) = \frac{t}{2} \text{tr } \mathbf{Q}^2 - \sqrt{6} \text{tr } \mathbf{Q}^3 + \frac{1}{2} (\text{tr } \mathbf{Q}^2)^2 + \frac{1}{4} (|\mathbf{M}|^2 - 1)^2 - c \mathbf{Q} \mathbf{M} \cdot \mathbf{M}, \quad (4.1)$$

where the first three terms comprise the nematic fourth-order bulk potential, and t is the reduced temperature; the fourth term is a potential associated with the spontaneous magnetisation; and the final term is the nemato-magnetic coupling energy, with coupling strength, c .

In Section 4.1, we focus on uniaxial critical points of the ferronematic bulk potential with nonnegative nemato-magnetic coupling. We investigate how the stability of uniaxial critical points of the ferronematic bulk potential are influenced by temperature and the nemato-magnetic coupling strength, c .

In Section 4.2, we extend our analysis to a more general \mathbf{Q} -tensor and explore whether nemato-magnetic coupling induces biaxiality in spatially homogeneous systems. Recall that in Chapter 3, we discuss how the preference for biaxiality under the sixth-order bulk potential destabilises the nematic radial hedgehog solution and results in split core and biaxial torus configurations with larger regions of biaxiality. Analogously, our aim in Section 4.2 is to understand if and when the ferronematic bulk potential prefers biaxiality in spatially homogeneous systems, which could impact the stability of the ferronematic radial hedgehog solution and the extent of biaxial regions in other critical points discussed in Chapter 5.

On the whole, the goal of this chapter is to investigate how nemato-magnetic cou-

pling alters the bulk behaviour, shedding light on the characteristics of ferronematic liquid crystals. We first investigate if nemato-magnetic coupling alters the qualitative behaviour of uniaxial critical points with a fourth-order bulk potential. And secondly, we investigate if the magnetic order parameter facilitates biaxiality with a fourth-order bulk potential in a spatially homogeneous system, recalling that the fourth-order bulk potential cannot accommodate biaxiality in purely nematic systems.

4.1 Uniaxial Critical Points of the Ferronematic Bulk Potential

4.1.1 Problem Formulation

We first consider critical points, (\mathbf{Q}, \mathbf{M}) , of (4.1) of the form

$$\mathbf{Q} = s \left(\mathbf{n} \otimes \mathbf{n} - \frac{1}{3} \mathbf{I} \right), \quad \mathbf{M} = m \mathbf{n}, \quad \mathbf{n} \in \mathbb{R}^3, \quad (4.2)$$

where we describe both \mathbf{Q} and \mathbf{M} with a unit vector, \mathbf{n} , to reduce the problem to solving for pairs (s, m) . Note that working with \mathbf{Q} and \mathbf{M} of this form means that the nematic director and magnetisation vector are co-aligned, and the nemato-magnetic coupling parameter, c , simply influences the values s and m in this context. In this case, the preferred orientation of the liquid crystal molecules and the magnetic field are oriented in the radial direction. We substitute (4.2) into (4.1) which reduces f_F to the function

$$g_F(s, m) := \frac{t}{3} s^2 - \frac{2\sqrt{6}}{9} s^3 + \frac{2}{9} s^4 + \frac{1}{4} (m^4 - 2m^2 + 1) - \frac{2}{3} c s m^2, \quad (4.3)$$

Chapter 4. Critical Points of the Ferronematic Bulk Potential

which has first partial derivatives

$$\frac{\partial g_F}{\partial s} = \frac{2t}{3}s - \frac{2\sqrt{6}}{3}s^2 + \frac{8}{9}s^3 - \frac{2}{3}cm^2, \quad (4.4)$$

$$\frac{\partial g_F}{\partial m} = m^3 - m - \frac{4}{3}csm. \quad (4.5)$$

Critical points of g_F are solutions of

$$\frac{\partial g_F}{\partial s} = \frac{\partial g_F}{\partial m} = 0, \quad (4.6)$$

and are given by $(s, m) = (0, 0)$ and

$$m = 0, \quad s = \sqrt{\frac{3}{2}} \frac{3 \pm \sqrt{9 - 8t}}{4} =: s_{\pm}, \quad (4.7)$$

noting that the values s_{\pm} correspond to the nonzero critical points of the pure nematic system with the fourth-order bulk potential, which are given in Section 1.5.1; and

$m = \pm \sqrt{1 + \frac{4}{3}cs}$, where s is a solution of

$$h(s) := s^3 - \frac{3\sqrt{6}}{4}s^2 + \left(\frac{3t}{4} - c^2\right)s - \frac{3c}{4} = 0. \quad (4.8)$$

In this section, we work only with nonnegative values of the nemato-magnetic coupling parameter, c . We note that we take the largest positive root of the above polynomial, h , as the boundary value on the droplet surface when we study spherical droplets of ferronematic liquid crystals in Chapter 5.

4.1.2 Results

We first determine the nature of the roots of the polynomial h in (4.8) by considering its discriminant [123],

$$\Delta = -\frac{27}{16}t^3 + \left(\frac{27}{4}c^2 + \frac{243}{128}\right)t^2 + \left(\frac{243\sqrt{6}}{32}c - 9c^4 - \frac{81}{16}c^2\right)t + 4c^6 + \frac{27}{8}c^4 - \frac{81\sqrt{6}}{8}c^3 - \frac{243}{16}c^2 - \frac{243\sqrt{6}}{32}c. \quad (4.9)$$

The sign of the discriminant, Δ , characterises the roots of the cubic polynomial h , which correspond to ferronematic bulk critical points. The cubic polynomial, h , has three distinct real roots if $\Delta > 0$; two real roots if $\Delta = 0$; and one real root and two complex conjugate roots if $\Delta < 0$. We plot Δ as a function of t in Figure 4.1, with the fixed values $c = 0$, $c = 0.01$, $c = 0.1$, $c = 1$, and $c = 10$.

In all five cases plotted, we observe that $\Delta > 0$ for low temperatures $t \rightarrow -\infty$, meaning that h in (4.8) has three real, distinct roots at low temperatures, corresponding to six real, distinct critical points of the ferronematic bulk free energy with nonzero m (since we work with positive and negative values of m), deep in the nematic phase. Thus, if we restrict our temperature range to, say, $t < -5$, we will be working with six real, distinct ferronematic critical points with nonzero m , regardless of the value of c .

Moreover, in the very strong coupling case, $c = 10$, we observe that $\Delta < 0$ only at very high, and potentially unrealistic temperatures, suggesting that h in (4.8) will have three real, distinct roots at physically relevant temperatures in models with large, positive c . However, it is worth noting that large values of the coupling parameter, c , may themselves be unrealistic, meaning that working with large c is simply a mathematical exercise.

Finally, we observe that there are small temperature ranges with $t > 0$ for which

Chapter 4. Critical Points of the Ferronematic Bulk Potential

$\Delta > 0$ in the cases $c = 0$, $c = 0.01$, and $c = 0.1$, so that there are three real, distinct ferronematic bulk critical points in these high temperature ranges. In the nonzero c cases, $c = 0.01$ and $c = 0.1$, as temperature decreases, the number of critical points reduces to one in some intermediate temperature range in each case; but as temperature decreases further, three real, distinct critical points re-emerge. In the uncoupled, $c = 0$ case, the discriminant is zero at $t = 0$, so the number of real, distinct critical points is reduced to two at $t = 0$; and there are three real, distinct critical points for $t < 0$.

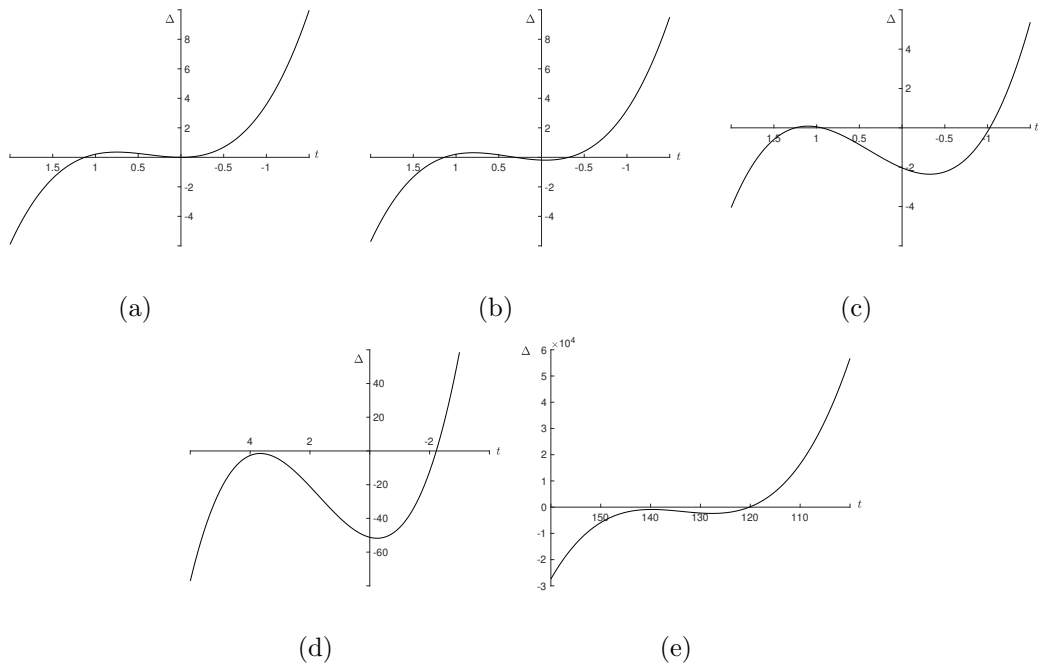


Figure 4.1: The discriminant, Δ , with (a) $c = 0$; (b) $c = 0.01$; (c) $c = 0.1$; (d) $c = 1$; and (e) $c = 10$. The horizontal axis is decreasing in temperature, t , from left to right.

We further explore the nature of the roots of the cubic h in (4.8) by plotting h in the case $c = 0.1$ at the temperatures $t = 1.2$, $t = -0.5$, and $t = -2$ in Figure 4.2. We plot h at $t = 1.2$ in Figure 4.2a, which belongs to the temperature range above $t = 0$ in Figure 4.1c where $\Delta > 0$, and demonstrates that h has three positive roots in this temperature range. Figure 4.2b is h at $t = -0.5$, and corresponds to the intermediate

Chapter 4. Critical Points of the Ferronematic Bulk Potential

temperature range which includes $t = 0$ in Figure 4.1c, where $\Delta < 0$, and we observe that h has just one root, which is positive. Finally, Figure 4.2c is plotted at $t = -2$, a temperature at which $\Delta > 0$ in Figure 4.1c, and we observe that h has one positive and two negative roots.

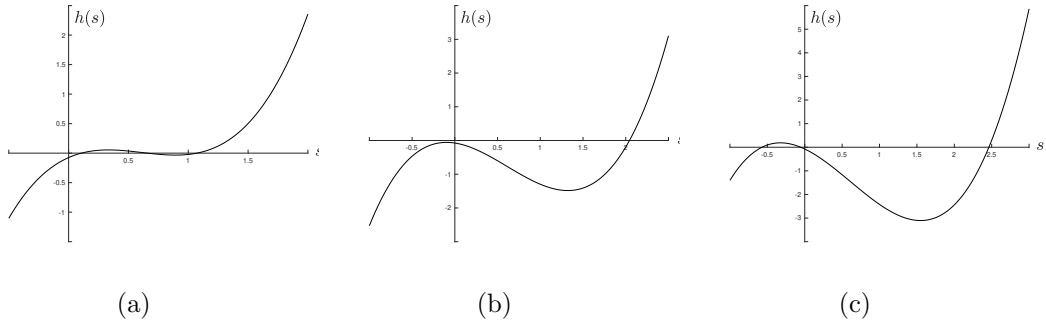


Figure 4.2: The cubic function h with $c = 0.1$ at the temperatures (a) $t = 1$; (b) $t = -0.5$; and (c) $t = -2$.

We plot the critical points of (4.3) with $c = 0$, $c = 0.01$, $c = 0.1$, and $c = 1$ in Figures 4.3, 4.4, 4.5 and 4.6, respectively.

We first consider the uncoupled case, $c = 0$, in Figure 4.3. There are three critical points at temperatures above $t = \frac{9}{8}$: the unstable isotropic point, $(s, m) = (0, 0)$, and the globally stable points, $(s, m) = (0, \pm 1)$. At $t = \frac{9}{8}$, the critical points which are nonzero in s emerge. The points $(s, m) = (s_{\pm}, 0)$ are always unstable, where s_{\pm} are given in (4.7). The points $(s, m) = (s_{+}, \pm 1)$ are local minimisers for $1 < t < \frac{9}{8}$ and global minimisers for $t < 1$. The points $(s, m) = (s_{-}, \pm 1)$ are unstable for $0 < t < \frac{9}{8}$ and local minimisers for $t < 1$. Finally, the points $(s, m) = (0, \pm 1)$ are local minimisers for $0 < t < \frac{9}{8}$ and unstable for $t < 0$.

The behaviour in s in the uncoupled case is identical to that in the pure uniaxial nematic case, in that there is a stable isotropic point at high temperatures, and s_{+} has lower energy than s_{-} for all temperatures at which they are defined. An interesting difference, however, is that nonzero magnetisation is required for stability in the spatially

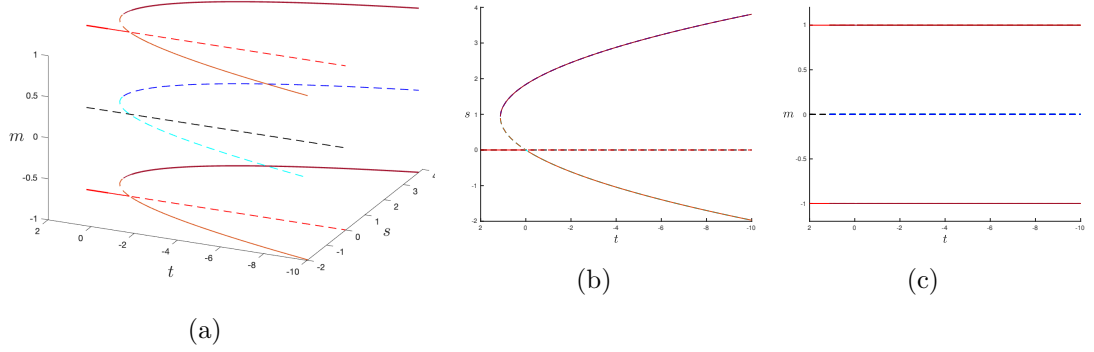


Figure 4.3: Critical points of the ferronematic bulk potential with $c = 0$ for the temperature range $t = 5$ to $t = -10$. (a) Both parameters, s and m , plotted against t . (b) Order parameter, s , plotted against t . (c) Magnetisation parameter, m , plotted against t . The line $m = 0$ in (c) represents three unstable critical points, with $s = 0$ and $s = s_{\pm}$.

homogeneous ferronematic system in the uncoupled case.

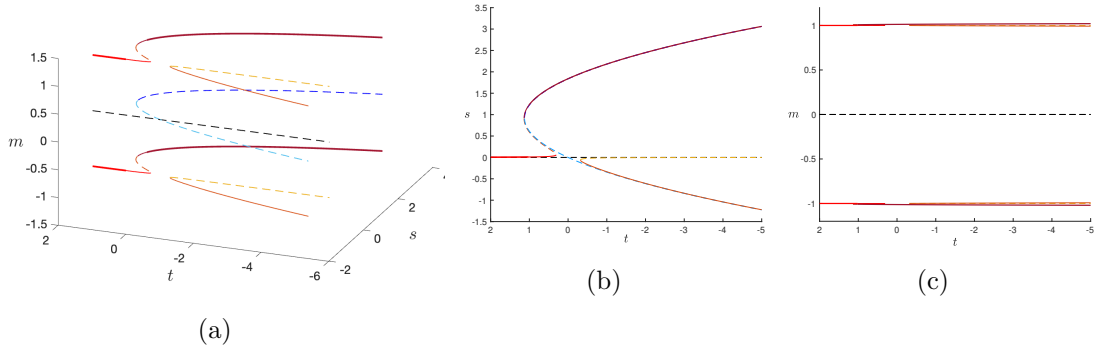


Figure 4.4: Critical points of the ferronematic bulk potential with $c = 0.01$ for the temperature range $t = 2$ to $t = -5$. (a) Both parameters, s and m , plotted against t . (b) Order parameter, s , plotted against t . (c) Magnetisation parameter, m , plotted against t . The line $m = 0$ in (c) represents three unstable critical points, with $s = 0$ and $s = s_{\pm}$.

Next, we plot the uniaxial ferronematic critical points in the very weak coupling case, $c = 0.01$, in Figure 4.4. For clarity, let us label the roots of h in (4.8), which have been plotted with the corresponding values of m in (4.8), before proceeding. We observe that h has one positive root at high temperatures (solid red line in Figure 4.4).

Let us label this root s_0 . As temperature decreases, two further roots emerge, both positive and larger than s_0 (solid maroon line and dashed orange line in Figure 4.4). Let us label the largest root s_1 and the intermediate root s_2 . Furthermore, there is an intermediate temperature range containing $t = 0$ in which the only real root of h is s_1 (solid maroon line in Figure 4.4). At low temperatures, h again has three real roots: the positive root, s_1 , and two negative roots (dashed yellow and solid orange lines in Figure 4.4). Let us label the negative root which is smaller in magnitude s_3 , and the other s_4 . Each root of h in (4.8) of course has a corresponding value of m in the context of the critical points of g_F in (4.3), which we label m_0, \dots, m_4 , accordingly.

We note that the weakly coupled case, $c = 0.01$, largely approximates the uncoupled case, and the similarities are as follows. There are three critical points at temperatures above $t \approx \frac{9}{8}$: the unstable isotropic point, $(s, m) = (0, 0)$, and the globally minimising points $(s, m) = (s_0, \pm m_0) \approx (0, \pm 1)$. At $t \approx \frac{9}{8}$, six further critical points which are nonzero in m emerge. Namely, these are $(s, m) = (s_1, \pm m_1)$, $(s, m) = (s_2, \pm m_2)$, and $(s, m) = (s_{\pm}, 0)$. The critical points $(s_1, \pm m_1)$ are local minimisers for $0.3 \lesssim t \lesssim \frac{9}{8}$ and global minimisers for $t \lesssim 0.3$, while the points $(s_{\pm}, 0)$ are unstable for the temperature range plotted. We note that the points $(s_1, \pm m_1)$ replace the points $(s_+, \pm 1)$ as the global minimisers in comparison to the uncoupled case, but we observe that $(s_1, \pm m_1)$ closely approximate $(s_+, \pm 1)$. We next consider the critical points which most closely approximate the points $(s_-, \pm 1)$, namely $(s_2, \pm m_2)$ above $t \approx 0.3$ and $(s_4, \pm m_4)$ below $t \approx -0.3$. These points approximate the points $(s_-, \pm 1)$ and are unstable for $0.3 \lesssim t \lesssim \frac{9}{8}$, and locally minimising for $t \lesssim -0.3$ (we discuss the the situation for $-0.3 \lesssim t \lesssim 0.3$ in the next paragraph). Finally, the points $(s, m) = (s_3, m_3) \approx (0, \pm 1)$ are unstable for $t \lesssim -0.3$.

The key difference between the $c = 0$ and $c = 0.01$ cases is in the temperature range

$-0.3 \lesssim t \lesssim 0.3$. Here, there is only one root of h in (4.8) with $c = 0.01$, s_1 , so the total number of critical points is reduced to five in this temperature range: the points $(s, m) = (0, 0)$, $(s, m) = (s_{\pm}, 0)$, and $(s, m) = (s_1, m_1) \approx (s_+, \pm 1)$; and four at $t = 0$, since $s_- = 0$, so $(s_-, 0) = (0, 0)$ at $t = 0$. In contrast, there are six critical points at $t = 0$ in the uncoupled case, and nine otherwise within the same temperature range. This can be explained by the fact that the discriminant of h in the case $c = 0.01$ in Figure 4.1b is negative for $-0.3 \lesssim t \lesssim 0.3$, meaning that h has only one real root within this temperature range. In contrast, the discriminant with $c = 0$ in Figure 4.1a is zero at $t = 0$ and positive elsewhere within the same temperature range, meaning there are two real roots of h at $t = 0$ ($s = 0$ and $s = s_+$), and three, otherwise ($s = 0$, $s = s_+$, and $s = s_-$).

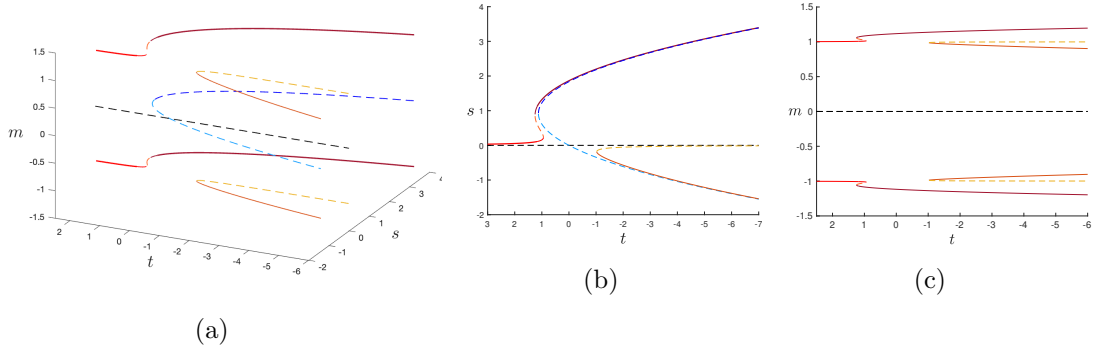


Figure 4.5: Critical points of the ferronematic bulk potential with $c = 0.1$ for the temperature range $t = 2.5$ to $t = -7$. (a) Both parameters, s and m , plotted against t . (b) Order parameter s plotted against t . (c) Magnetisation parameter m plotted against t . The line $m = 0$ in (c) represents three unstable critical points, with $s = 0$ and $s = s_{\pm}$.

Next, we plot the case $c = 0.1$ in Figure 4.5. The qualitative behaviour of the critical points is the same as in the weakly coupled, $c = 0.01$ case, so we use the same labels for the critical points corresponding to the roots of h in (4.8) and summarise our observations in the next paragraph.

There are three critical points at high temperatures: the unstable critical point $(s, m) = (0, 0)$; and the two global minimisers, $(s_0, \pm m_0)$, which are positive in s and nonzero in m , and are such that $(s, m) \rightarrow (0, \pm 1)$ as $t \rightarrow \infty$. There are seven critical points in the temperature range $\frac{9}{8} < t \lesssim 1.3$: the unstable point $(0, 0)$; and six critical points which are positive in s and nonzero in m : $(s_0, \pm m_0)$, $(s_1, \pm m_1)$, and $(s_2, \pm m_2)$. The points $(s_1, \pm m_1)$ are the global minimisers; while the points $(s_0, \pm m_0)$ are local minimisers; and the points $(s_2, \pm m_2)$ are unstable. At $t = \frac{9}{8}$, the number of critical points increases to nine with the emergence of the critical points $(s, m) = (s_{\pm}, 0)$, which are both unstable across the temperature range plotted. Analogously to the $c = 0.01$ case, the number of critical points reduces to five in the temperature range $-1 \lesssim t \lesssim 0.95$, where the discriminant of h in Figure 4.1c is negative, except at $t = 0$, where there are four critical points, since again $s_- = 0$. Finally, the discriminant in Figure 4.1c is positive for $t \lesssim -1$, where there are again nine critical points: the unstable zero solution; the two global minimisers $(s, m) = (s_1, \pm m_1)$; the unstable critical points $(s, m) = (s_{\pm}, 0)$ and $(s, m) = (s_3, \pm m_3)$; and the two local minimisers, $(s, m) = (s_4, \pm m_4)$. We note that the globally minimising value of s , s_1 , converges to s_+ as $t \rightarrow -\infty$.

Finally, we plot the critical points in the case $c = 1$ in Figure 4.6. The qualitative behaviour of the critical points is slightly different to that in the cases with $c = 0.01$ and $c = 0.1$. In particular, h in (4.8) has only one positive root at all temperatures in the range plotted in Figure 4.6. We label the corresponding critical points $(s_1, \pm m_1)$, and use the same labels, $(s_3, \pm m_3)$ and $(s_4, \pm m_4)$, for the critical points corresponding to the negative roots of h . We note that we do not use the labels $(s_0, \pm m_0)$ or $(s_2, \pm m_2)$ for any critical points in the $c = 1$ case.

Elements of Figure 4.6 are qualitatively similar to the $c = 0.1$ case in Figure 4.5.

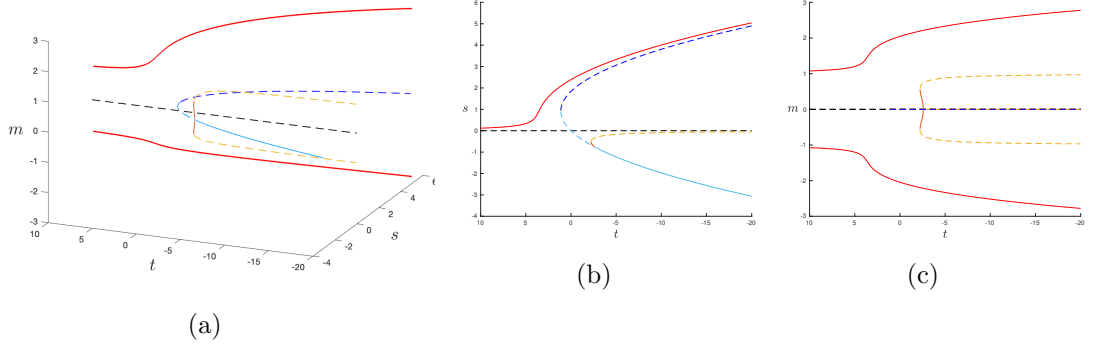


Figure 4.6: Critical points of the ferronematic bulk potential with $c = 1$ for the temperature range $t = 10$ to $t = -20$. (a) Both parameters, s and m , plotted against t . (b) Order parameter s plotted against t . (c) Magnetisation parameter m plotted against t . The line $m = 0$ in (c) represents three critical points: the two unstable critical points with $s = 0$ and $s = s_+$; and the critical point with $s = s_-$, which is unstable at higher temperatures and locally stable at sufficiently low temperatures.

Specifically, the solution $(s, m) = (0, 0)$ is an unstable critical point for all temperatures; unstable critical points, $(s, m) = (s_3, \pm m_3)$ emerge at sufficiently low temperatures such that $s_3 \rightarrow 0$ and $m_3 \rightarrow 1$ as $t \rightarrow -\infty$; the critical point $(s, m) = (s_+, 0)$ emerges at $t = \frac{9}{8}$ and is always unstable; and the globally minimising value of s , namely s_1 , converges to s_+ as $t \rightarrow -\infty$.

As noted above, there are several key differences between the $c = 1$ case and the other cases plotted in Figures 4.3, 4.4 and 4.5, and this is related to the fact that the discriminant for $c = 1$ in Figure 4.1d only crosses the x -axis once, rather than three times. This means that h in (4.8) with $c = 1$ has one root above some critical temperature, $t \approx -2.1$, and three below this temperature. Furthermore, the critical point $(s, m) = (s_-, 0)$ becomes a local minimiser at sufficiently low temperatures, and there is only a small temperature regime in which there are three critical points with nonzero m . This is because $m = \sqrt{1 + \frac{4}{3}cs}$ becomes complex for $s < -\frac{3}{4c}$, so the larger negative root of h , s_4 , has a complex associated magnetisation vector, and we lose the

critical points $(s_4, \pm m_4)$ at sufficiently low temperatures. We note that this relation can be satisfied for any nonzero c , but the required magnitude of the largest negative root of h for m to be complex increases for smaller c , so the associated value of m is real over a larger temperature range for smaller c .

We note certain overall trends as the nemato-magnetic coupling strength, c , increases. For any positive c , the global minimiser at high temperatures is nonzero in s and m and the isotropic state $(0, 0)$ is unstable, but the globally minimising value of s tends to zero as $t \rightarrow +\infty$.

Furthermore, the globally minimising branches $(s_+, \pm 1)$ for $t < \frac{9}{8}$ in the $c = 0$ case are replaced by the globally minimising branches $(s_1, \pm m_1)$ when c is positive. The value of s_1 is larger for larger c , but in each case, $s_1 \rightarrow s_+$ as $t \rightarrow -\infty$. However, the corresponding values for m do not converge to ± 1 . Additionally, the branches $(s_{\pm}, 0)$ are unstable for all values of c considered.

Another trend we note is that for all positive c , there is a temperature below $t = 0$ at which two negative roots of h in (4.8) emerge, s_3 and s_4 , and this temperature decreases for increasing c . The critical points of $(s_3, \pm m_3)$ correspond to unstable branches such that $s_3 < 0$, $(s_3, \pm m_3) \rightarrow (0, \pm 1)$ as $t \rightarrow -\infty$. The other critical points, $(s_4, \pm m_4)$, correspond to locally minimising branches such that $s_4 \rightarrow s_- < 0$ as $t \rightarrow -\infty$; and the magnitude of m_4 decreases with temperature and eventually becomes complex, as noted in the $c = 1$ case above. The temperature at which the values of m become complex is higher for larger c , so this happens beyond the ranges we have plotted in Figures 4.4 and 4.5, corresponding to $c = 0.01$ and $c = 0.1$. When m_4 becomes complex, the branch $(s_-, 0)$ gains local stability.

The instability of the isotropic critical point, $(s, m) = (0, 0)$, in the ferronematic case is in contrast to its behaviour in the nematic case studied in Section 3.2, in which

the isotropic point, $(s, m) = (0, 0)$, is globally stable at high temperatures. We confirm the instability of the isotropic critical point for all temperatures via the second partial derivatives of the function g_F in (4.3), which are given by

$$\frac{\partial^2 g_F}{\partial s^2} = \frac{2t}{3} - \frac{4\sqrt{6}}{3}s + \frac{8}{3}s^2, \quad \frac{\partial^2 g_F}{\partial m^2} = 3m^2 - 1 - \frac{4}{3}cs, \quad \frac{\partial^2 g_F}{\partial s \partial m} = -\frac{4}{3}cm^2. \quad (4.10)$$

We consider the determinant of the Hessian,

$$\mathcal{H} = \begin{bmatrix} \frac{\partial^2 g_F}{\partial s^2} & \frac{\partial^2 g_F}{\partial s \partial m} \\ \frac{\partial^2 g_F}{\partial s \partial m} & \frac{\partial^2 g_F}{\partial m^2} \end{bmatrix}, \quad (4.11)$$

which is given by

$$\mathcal{D}(s, m) := \frac{\partial^2 g_F}{\partial s^2} \frac{\partial^2 g_F}{\partial m^2} - \left(\frac{\partial^2 g_F}{\partial s \partial m} \right)^2, \quad (4.12)$$

the sign of which, together with the sign of $\frac{\partial^2 g_F}{\partial s^2}$, indicates the nature of the critical points.

We note that $\mathcal{D}(0, 0) = -\frac{2t}{3}$. If $t > 0$, $\mathcal{D}(0, 0) < 0$, which indicates that the critical point $(s, m) = (0, 0)$ is a saddle point and hence unstable. If $t < 0$, then $\mathcal{D}(0, 0) > 0$ and $\frac{\partial^2 g_F}{\partial s^2} = \frac{2t}{3} < 0$, which indicates that the critical point $(0, 0)$ is a local maximum of the function g_F in (4.3). Furthermore, it is straightforward to show that the eigenvalues of \mathcal{H} with $(s, m) = (0, 0)$ are $\{\frac{2t}{3}, -1\}$, with corresponding eigenvectors $\{[1, 0]^T, [0, 1]^T\}$. Hence, when $t > 0$, the unstable direction is $[0, 1]^T$, which indicates that the system tolerates $s = 0$ at high temperatures, but prefers a nonzero value of m for stability. This is reflected in Figure 4.3, where we see that $(s, m) = (0, \pm 1)$ is at least locally stable for $t > 0$.

It is interesting to note that the critical point $(s_+, 0)$ is never stable since

$$\mathcal{D}(s_+, 0) = \frac{4t}{3} - \frac{3}{2} - \frac{\sqrt{9-8t}}{2} + \frac{(2t-27)\sqrt{6} + (4t-9)\sqrt{6(9-8t)}}{3} c < 0, \quad (4.13)$$

if $t < \frac{9}{8}$ recalling that s_+ is undefined for $t > \frac{9}{8}$. This is despite s_+ being the global minimiser in the nematic case with the fourth-order bulk potential, yet the critical point $(s_-, 0)$ gains local stability at low temperatures for sufficiently large and positive c when the value of m corresponding to the critical point with nonzero m and largest negative s becomes complex in m , as can be seen in Figure 4.6. This is in contrast to the fourth-order nematic case in Section 3.2, where we observe that the critical point $(s, m) = (s_-, 0)$ is never stable. As an example, taking $t = -5$, $c = 1$, we find that

$$\mathcal{D}(s_-, 0) = \frac{28\sqrt{6} - 42}{9} > 0, \quad \text{and} \quad \frac{\partial^2 g_F}{\partial s^2} = \frac{14}{3} > 0, \quad (4.14)$$

where \mathcal{D} is defined in (4.12), confirming the local stability of $(s_-, 0)$ with $t = -5$, $c = 1$.

However, we illustrate in Figure 4.7, in the case $c = 1$, that the energy of $(s_-, 0)$ is higher than that of $(s_+, 0)$, which is in turn higher than the energy of the global minimiser, $(s_1, \pm\sqrt{1 + \frac{4}{3}cs_1})$.

Another key contrast to the nematic case is the presence of a global minimiser which is nonzero in s and m at high temperatures with $t > \frac{9}{8}$. In the fourth-order nematic case, discussed in Section 3.2, the only critical point above $t = \frac{9}{8}$ is the isotropic critical point. Recalling that the critical points which are nonzero in s are solutions of h in (4.8), let us consider the limit $t \rightarrow \infty$. Noting that, by neglecting terms independent of t when the magnitude of t is sufficiently large such that the magnitude of terms

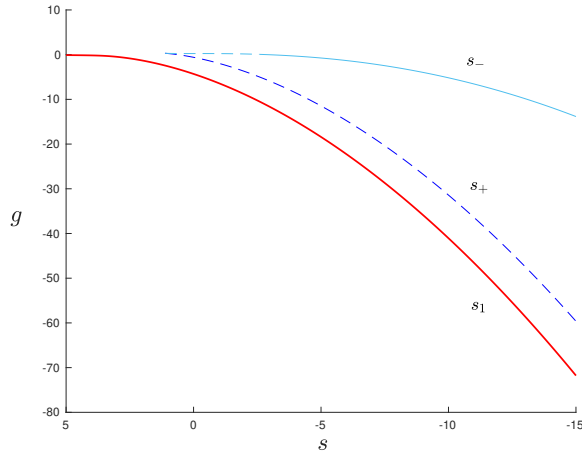


Figure 4.7: Value of the function g_F for the critical points, $(s_1, \pm m_1)$, $(s_+, 0)$, and $(s_-, 0)$ of the ferronematic bulk potential with $c = 1$ for the temperature range $t = 5$ to $t = -15$.

independent of t are negligible in comparison, we find that

$$h(s) \rightarrow \frac{3t}{4}s \quad \text{and} \quad m \rightarrow \pm 1 \quad \text{as} \quad t \rightarrow \infty, \quad (4.15)$$

which indicates that $s \rightarrow 0$ and $m \rightarrow 1$ as $t \rightarrow \infty$. In other words, the global minimiser is approximately isotropic at sufficiently high temperatures in the ferronematic case. This is in agreement with the pure nematic case, which is isotropic at high temperatures, and the magnetisation being constant at high temperatures indicates that the magnetisation is not influenced by the liquid crystal molecules in the absence of nematic ordering.

4.1.3 Approximations to the Uniaxial Ferronematic Critical Points

We note that, for small c , we can approximate the roots of h in (4.8), which we label s_0, \dots, s_4 in the previous section, and the corresponding values of m via polynomial

expansions of the form

$$\tilde{s}_0 = a_0 c + b_0 c^2, \quad \tilde{s}_1 = s_+ + a_1 c + b_1 c^2, \quad \tilde{s}_2 = s_- + a_2 c + b_2 c^2. \quad (4.16)$$

Substituting \tilde{s}_0, \tilde{s}_1 , and \tilde{s}_2 into (4.8) in turn and neglecting $o(c^2)$ terms, we find that we may write

$$\tilde{s}_0 = \frac{1}{t}c + \frac{\sqrt{6}}{t^3}c^2, \quad \tilde{m}_0 = \pm\sqrt{1 + \frac{4}{3}c\tilde{s}_0}, \quad (4.17)$$

$$\tilde{s}_1 = s_+ + \frac{1}{t - 2\sqrt{6}s_+}c + \frac{(1 - 16ts_+)\sqrt{6} + 4t^2s_+ + 96s_+^3 - 4s_+}{(t - 2\sqrt{6}s_+)^2(4s_+^2 - 2\sqrt{6}s_+ + t)}c^2, \quad \tilde{m}_1 = \pm\sqrt{1 + \frac{4}{3}c\tilde{s}_1}, \quad (4.18)$$

$$\tilde{s}_2 = s_- + \frac{1}{t - 2\sqrt{6}s_-}c + \frac{(1 - 16ts_-)\sqrt{6} + 4t^2s_- + 96s_-^3 - 4s_-}{(t - 2\sqrt{6}s_-)^2(4s_-^2 - 2\sqrt{6}s_- + t)}c^2, \quad \tilde{m}_2 = \pm\sqrt{1 + \frac{4}{3}c\tilde{s}_2}. \quad (4.19)$$

We illustrate how $(\tilde{s}_0, \tilde{m}_0)$, $(\tilde{s}_1, \tilde{m}_1)$, and $(\tilde{s}_2, \tilde{m}_2)$ approximate the roots of the cubic in (4.8) and the corresponding values of m in the case $c = 0.01$. It suffices to only consider the positive values of the critical values of m . We revisit the critical points plotted in Figure 4.4 and plot the functions \tilde{s}_0 and \tilde{m}_0 , \tilde{s}_1 and \tilde{m}_1 , and \tilde{s}_2 and \tilde{m}_2 against the roots of h and the corresponding values of m in Figures 4.8, 4.9, and 4.10, respectively. The solid and dashed curves are the same as the curves in Figure 4.4 with the same colour. We note that each of the bulk critical points plotted in Figures 4.8-4.10 are originally plotted in Figure 4.4. We do not reproduce the critical points $(s, m) = (s_{\pm}, 0)$.

We observe that the pairs $(\tilde{s}_0, \tilde{m}_0)$, $(\tilde{s}_1, \tilde{m}_1)$, and $(\tilde{s}_2, \tilde{m}_2)$ approximate the ferrone-

Chapter 4. Critical Points of the Ferronematic Bulk Potential

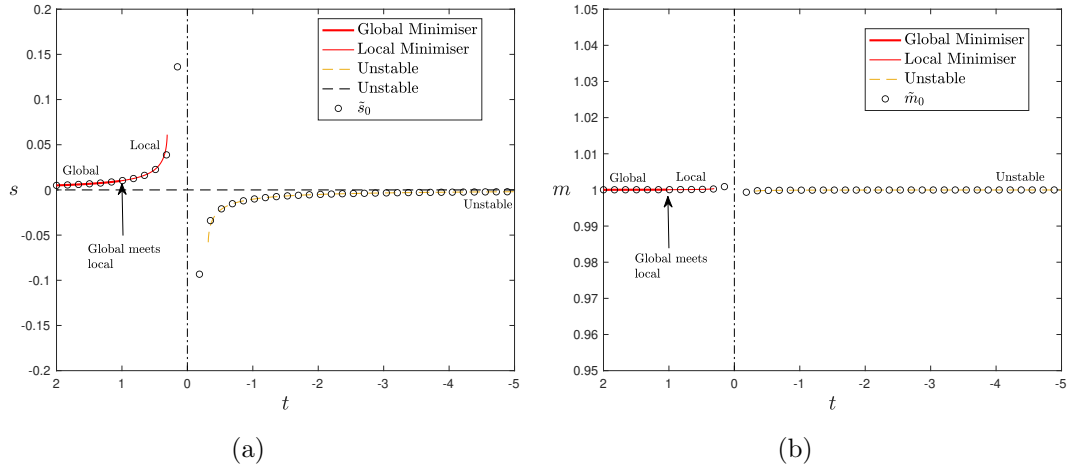


Figure 4.8: The approximation $(\tilde{s}_0, \tilde{m}_0)$ plotted against the closest ferronematic bulk critical points. The point $(\tilde{s}_0, \tilde{m}_0)$ approximates the stable critical point (s_0, m_0) above $t \approx 0.3$ and the unstable critical point (s_3, m_3) below $t \approx -0.3$.

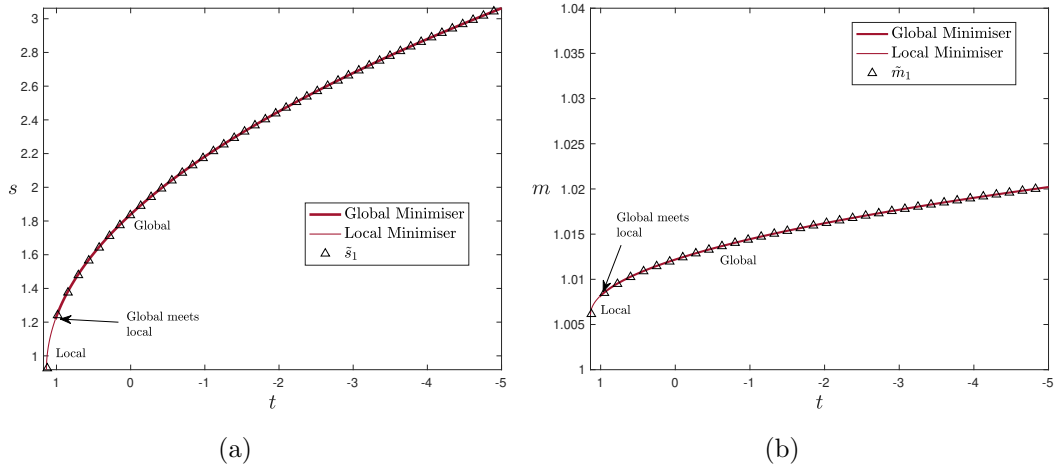


Figure 4.9: The approximation $(\tilde{s}_1, \tilde{m}_1)$ plotted against the closest ferronematic bulk critical point. The point $(\tilde{s}_1, \tilde{m}_1)$ approximates the stable critical point (s_1, m_1) .

matic critical points well, with the exception of the region close to $t = 0$.

Let us first consider the pair $(\tilde{s}_0, \tilde{m}_0)$. From Figure 4.8a, it is clear that \tilde{s}_0 approximates the globally minimising value for s , s_0 , above $t \approx \frac{9}{8}$, where h has only one root, and \tilde{m}_0 approximates the corresponding value for m , m_0 , in Figure 4.8b. At $t \approx \frac{9}{8}$, the discriminant of h in Figure 4.1b becomes positive, and h has three real roots. The

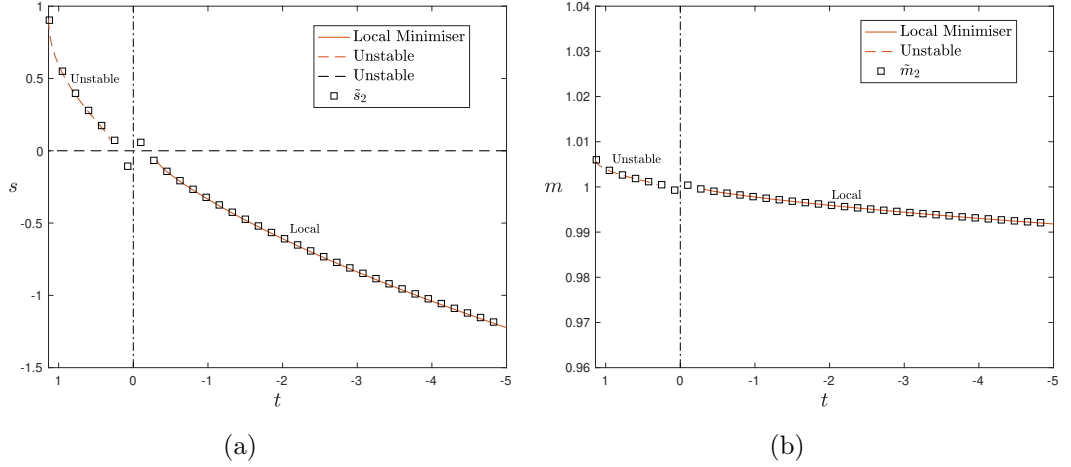


Figure 4.10: The approximation $(\tilde{s}_2, \tilde{m}_2)$ plotted against the closest ferronematic bulk critical points. The point $(\tilde{s}_2, \tilde{m}_2)$ approximates the unstable critical point (s_2, m_2) above $t \approx 0.3$ and the local minimiser (s_4, m_4) below $t \approx -0.3$. We include the unstable critical point $(0, 0)$ for reference.

smallest, s_0 , is still approximated by \tilde{s}_0 . The discriminant in Figure 4.1b becomes negative again around $t \approx 0.3$, and only the largest, globally minimising value of s , s_1 , remains. Below $t \approx -0.3$, the discriminant in Figure 4.1b is again positive, and there are three roots of h : the globally minimising, positive value, s_1 ; and two negative roots, s_3 and s_4 . We observe in Figure 4.8a that the pair $(\tilde{s}_0, \tilde{m}_0)$ approximates the negative, unstable value of s , s_3 , and the corresponding value for m , m_3 , below $t \approx -0.3$. The approximation fails for $-0.3 \lesssim t \lesssim 0.3$: there is only one root of h in this temperature range, and we have that

$$\tilde{s}_0 = a_0 c + b_0 c^2 = \frac{1}{t} c + \frac{\sqrt{6}}{t^3} \rightarrow \infty \text{ as } t \rightarrow 0 \text{ from above,} \quad (4.20)$$

$$\text{and } \tilde{s}_0 = a_0 c + b_0 c^2 = \frac{1}{t} c + \frac{\sqrt{6}}{t^3} \rightarrow -\infty \text{ as } t \rightarrow 0 \text{ from below.} \quad (4.21)$$

Now let us consider the pair $(\tilde{s}_2, \tilde{m}_2)$, which is plotted in Figure 4.10. We observe that $(\tilde{s}_2, \tilde{m}_2)$ approximates the unstable critical point, (s_2, m_2) in the temperature

range $0.3 \lesssim t \lesssim \frac{9}{8}$, which corresponds to the intermediate root of h in this temperature range. Moreover, $(\tilde{s}_2, \tilde{m}_2)$ appears to approximate the locally minimising critical point for $t \lesssim -0.3$, (s_4, m_4) . Similarly to the case of $(\tilde{s}_0, \tilde{m}_0)$, the approximation fails in the temperature range $-0.3 \lesssim t \lesssim 0.3$, where h has only one real root, and we note that

$$a_2c + b_2c^2 \rightarrow \frac{1}{t}c - \frac{\sqrt{6}}{t^3}c^2 \rightarrow -\infty \text{ as } t \rightarrow 0 \text{ from above,} \quad (4.22)$$

$$\text{and } a_2c + b_2c^2 \rightarrow \frac{1}{t}c - \frac{\sqrt{6}}{t^3}c^2 \rightarrow \infty \text{ as } t \rightarrow 0 \text{ from below,} \quad (4.23)$$

so that $\tilde{s}_2 \rightarrow -\infty$ as $t \rightarrow 0$ from above, and $\tilde{s}_2 \rightarrow \infty$ as $t \rightarrow 0$ from below

Finally, consider the simpler case, $(\tilde{s}_1, \tilde{m}_1)$, plotted in Figure 4.9. We observe that $(\tilde{s}_1, \tilde{m}_1)$ approximates the largest positive root of h , s_1 , and the associated value of m , m_1 , for all temperatures below $t \approx \frac{9}{8}$. The largest positive root is the locally minimising critical point for $t \approx \frac{9}{8}$ to $t \approx 1$, and the global minimiser for all $t \lesssim 1$.

4.2 Biaxial Critical Points

In this section, we investigate whether the ferronematic bulk potential can admit bulk biaxial critical points for given temperatures and nemato-magnetic coupling. We work with a more general form of the \mathbf{Q} -tensor and magnetisation vector. We consider a \mathbf{Q} -tensor of the form

$$\mathbf{Q} = q_1(\mathbf{x} \otimes \mathbf{x} - \mathbf{y} \otimes \mathbf{y}) + q_2(\mathbf{x} \otimes \mathbf{y} + \mathbf{y} \otimes \mathbf{x}) + q_3(2\mathbf{z} \otimes \mathbf{z} - \mathbf{x} \otimes \mathbf{x} - \mathbf{y} \otimes \mathbf{y}), \quad (4.24)$$

where $\mathbf{x} = [1, 0, 0]^T$, $\mathbf{y} = [0, 1, 0]^T$, and $\mathbf{z} = [0, 0, 1]^T$, so

$$\mathbf{Q} = \begin{bmatrix} q_1 - q_3 & q_2 & 0 \\ q_2 & -q_1 - q_3 & 0 \\ 0 & 0 & 2q_3 \end{bmatrix}. \quad (4.25)$$

We note that this \mathbf{Q} -tensor can be biaxial, with eigenvalues

$$\lambda_1 = -q_3 + \sqrt{q_1^2 + q_2^2}, \quad \lambda_2 = -q_3 - \sqrt{q_1^2 + q_2^2}, \quad \lambda_3 = 2q_3. \quad (4.26)$$

We choose this form of \mathbf{Q} -tensor as it is a combination of three orthonormal vectors.

We also work with a magnetisation vector of the form $\mathbf{M} = [m_1, m_2, m_3]^T$.

The authors in [124] demonstrate bulk biaxiality in systems with a negative coupling parameter, c . We find examples of globally minimising biaxial bulk critical points with negative nemato-magnetic coupling, supporting the findings in [124], and, in addition, we find examples of locally stable biaxial critical points within positively coupled systems. We note that the authors in [124] claim that positively coupled, spatially homogeneous systems can only be uniaxial. Our results prove otherwise as we will show, with the existence of both locally stable and unstable biaxial critical points in our spatially homogeneous, positively coupled systems. However, it is worth pointing out that we only find biaxial global minimisers in negatively coupled systems; and the locally stable biaxial critical points in the positively coupled systems are very small in magnitude. Moreover, our methods differ from those used in [124].

4.2.1 Problem Formulation

To reduce the complexity of the problem and make it computationally feasible with our methods, we set $q_2 = m_2 = 0$ before substituting the \mathbf{Q} -tensor and magnetisation vector into the ferronematic bulk potential f_F in (4.1), so that the \mathbf{Q} -tensor has eigenvalues

$$\lambda_1 = q_1 - q_3, \quad \lambda_2 = -q_1 - q_3, \quad \lambda_3 = 2q_3. \quad (4.27)$$

Therefore, the \mathbf{Q} -tensor is biaxial provided $q_1 \neq 0$ and $q_1 \neq \pm 3q_3$. Moreover, setting $q_2 = 0$ results in the preferred directions being aligned with \mathbf{x} , \mathbf{y} and \mathbf{z} , rather than being tilted.

We rewrite the bulk potential as

$$\begin{aligned} f_F(q_1, q_3, m_1, m_3) = & t(q_1^2 + 3q_3^2) + 6\sqrt{6}(q_1^2q_3 - q_3^3) + 2(q_1^4 + 6q_1^2q_3^2 + 9q_3^4) \\ & + \frac{1}{4}\left((m_1^2 + m_3^2)^2 - 1\right)^2 - c(q_1m_1^2 - q_3m_1^2 + 2q_3m_3^2). \end{aligned} \quad (4.28)$$

To obtain critical points of the ferronematic bulk potential above, we solve the coupled equations

$$\frac{\partial f_F}{\partial q_1} = 0, \quad \frac{\partial f_F}{\partial q_3} = 0, \quad \frac{\partial f_F}{\partial m_1} = 0, \quad \frac{\partial f_F}{\partial m_3} = 0, \quad (4.29)$$

numerically for the critical points of the ferronematic bulk potential in this restricted

regime, where the partial derivatives are given by

$$\frac{\partial f_F}{\partial q_1} = 2tq_1 + 12\sqrt{6}q_1q_3 + 8(q_1^3 + 3q_1q_3^2) - cm_1^2, \quad (4.30)$$

$$\frac{\partial f_F}{\partial q_3} = 6tq_3 + 6\sqrt{6}(q_1^2 - 3q_3^2) + 24(q_1^2q_3 + 3q_3^3) + c(m_1^2 - 2m_3^2), \quad (4.31)$$

$$\frac{\partial f_F}{\partial m_1} = 2m_1(m_1^2 + m_3^2) \left((m_1^2 + m_3^2)^2 - 1 \right) - 2cm_1(q_1 - q_3), \quad (4.32)$$

$$\frac{\partial f_F}{\partial m_3} = 2m_3(m_1^2 + m_3^2) \left((m_1^2 + m_3^2)^2 - 1 \right) - 4cq_3m_3. \quad (4.33)$$

We use the function *vpasolve()* in MATLAB [125] to find solutions of the coupled system (4.29).

We compute the stability of each critical point by considering the eigenvalues of their associated Hessian matrix, which is given by

$$\mathcal{H} = \begin{bmatrix} \frac{\partial^2 f_F}{\partial q_1^2} & \frac{\partial^2 f_F}{\partial q_1 \partial q_3} & \frac{\partial^2 f_F}{\partial q_1 \partial m_1} & \frac{\partial^2 f_F}{\partial q_1 \partial m_3} \\ \frac{\partial^2 f_F}{\partial q_1 \partial q_3} & \frac{\partial^2 f_F}{\partial q_3^2} & \frac{\partial^2 f_F}{\partial q_3 \partial m_1} & \frac{\partial^2 f_F}{\partial q_3 \partial m_3} \\ \frac{\partial^2 f_F}{\partial q_1 \partial m_1} & \frac{\partial^2 f_F}{\partial m_1 \partial q_3} & \frac{\partial^2 f_F}{\partial m_1^2} & \frac{\partial^2 f_F}{\partial m_1 \partial m_3} \\ \frac{\partial^2 f_F}{\partial q_1 \partial m_3} & \frac{\partial^2 f_F}{\partial m_3 \partial q_3} & \frac{\partial^2 f_F}{\partial m_3 \partial m_1} & \frac{\partial^2 f_F}{\partial m_3^2} \end{bmatrix} \quad (4.34)$$

There are three possible classifications of a critical point based on the eigenvalues. If all eigenvalues are positive, the critical point is at least a local minimum. If all eigenvalues are negative, the critical point is a local maximum. Finally, if some eigenvalues are positive and others negative, the critical point is a saddle point. The results are inconclusive if none of the three stated cases are fulfilled.

4.2.2 Critical Points as a Function of Temperature

In this section, we numerically compute critical points of the ferronematic bulk potential in (4.28) as a function of temperature, forming part of the picture of how bulk

ferronematic critical points are influenced by temperature and coupling strength. We consider the cases $c = 1, 0.1, 0, -0.1$, and -1 , and find at least three biaxial critical points in every case except for $c = 0$. In Figure 4.11, we plot the biaxiality parameter,

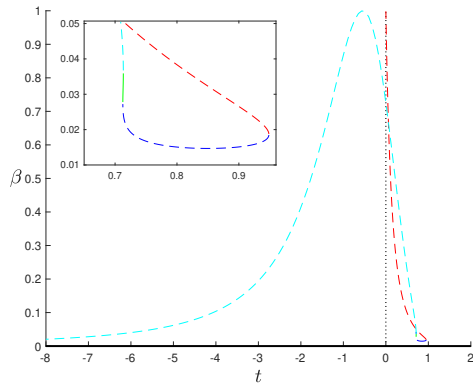
$$\beta = 1 - 6 \frac{(\text{tr } \mathbf{Q}^3)^2}{(\text{tr } \mathbf{Q}^2)^3}, \quad (4.35)$$

which is first introduced in 1.3.3, for each of the critical points for each value of c . We also plot the eigenvalues of the \mathbf{Q} -tensor, which are given by (4.27). We plot the eigenvalues of the biaxial critical points, given in (4.27), in each case in Figure 4.12. We plot the norm of the magnetisation vector, $|\mathbf{M}| = \sqrt{m_1^2 + m_3^2}$, for each value of c in Figure 4.13.

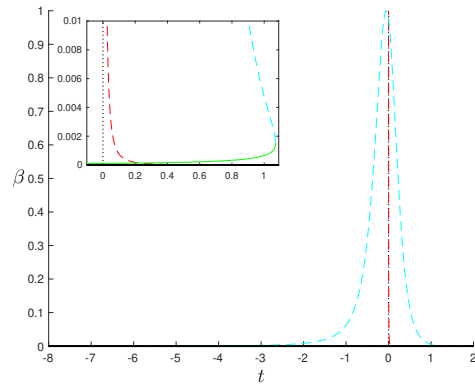
The visualisation of the biaxiality of the critical points in Figure 4.11 offers several key insights into the role of biaxiality as a ferronematic bulk effect. We note that there exist biaxial critical points in all cases, with the exception of the uncoupled case. This is to be expected, as the critical points in the absence of nemato-magnetic coupling are essentially the critical points of the fourth-order nematic bulk potential, which we study in Section 3.2, and which cannot be biaxial by Proposition 1.2. What is of significance is that we observe at least locally stable biaxial critical points in all cases with nonzero coupling, suggesting that biaxiality can be a preferred bulk effect with both the positive and negative coupling, at least in theory.

Let us consider the positive coupling cases in Figures 4.11a and 4.11b. There exist locally stable biaxial critical points in these scenarios, with the global minimiser being uniaxial, with $\beta = 0$, at all temperatures in the range plotted. However, in the $c = 1$ case, the stable biaxial critical point (solid green line in Figure 4.11a) only exists over a very narrow temperature range just above $t = 0.7$ with biaxiality of around $\beta = 0.03$. Furthermore, in the $c = 0.1$ case, the locally stable biaxial critical point (solid green

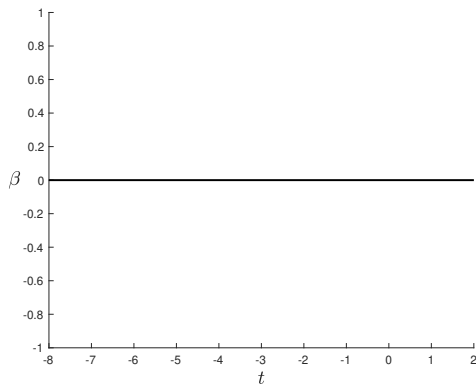
Chapter 4. Critical Points of the Ferronematic Bulk Potential



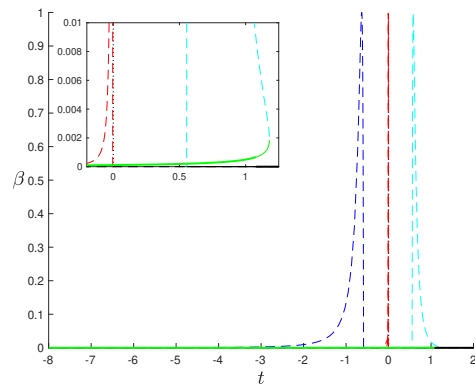
(a) $c = 1$



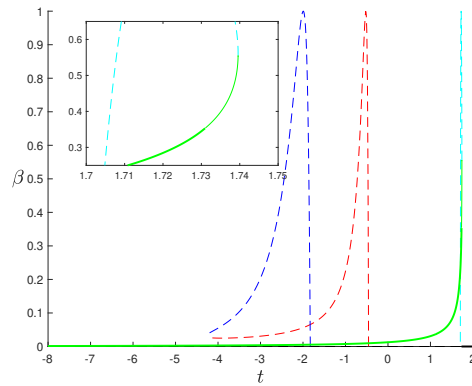
(b) $c = 0.1$



(c) $c = 0$



(d) $c = -0.1$



(e) $c = -1$

Figure 4.11: The biaxiality parameter, β , associated with biaxial critical points of (4.28) for fixed c and $t \in [-8, 2]$. Thick solid lines indicate global minimality; thin solid lines indicate local minimality, and dashed lines indicate instability. The vertical dotted black line in (a), (b) and (d) indicates $t = 0$.

line in Figure 4.11b) exists over a broader temperature range, but has a maximum biaxiality of less than $\beta = 0.002$, and β tends to zero as t decreases. We note that we have three unstable biaxial critical points in the case $c = 1$, and two unstable biaxial critical points in the case $c = 0.1$. In both cases, two of these unstable critical points take significantly larger values of the biaxiality parameter, β , in comparison to the respective stable critical points, and in fact approach maximal biaxiality, which is described by $\beta = 1$, at particular temperatures. However, since these critical points are unstable, they do not correspond to potentially physically observable bulk effects. The above observations suggest that, in the positive coupling case, it is very unlikely that one will observe biaxiality as a bulk effect, and if biaxiality is observed, it will be so weak that it approximates uniaxiality.

The negative coupling cases, $c = -0.1$ and $c = -1$, are given in Figures 4.11d and 4.11e, respectively. We observe that both cases have globally minimising biaxial critical points. In the $c = -0.1$ case, the behaviour of the stable biaxial critical point (solid green line in Figure 4.11d) is similar to that of the stable biaxial critical point in the $c = 0.1$ case: it first appears and is locally stable just above $t = 1$; has biaxiality of at most $\beta = 0.002$; and β tends to zero as t decreases, meaning there is in fact no significant biaxiality. The key difference in comparison to the positive coupling case, $c = 0.1$, is that the stable biaxial critical point in this case is locally minimising over a small temperature range and is then globally minimising for sufficiently low temperatures.

The most interesting result is arguably in the $c = -1$ case, shown in Figure 4.11e. In this case, a stable biaxial critical point emerges just below $t = 1.74$ (solid green line in Figure 4.11e), and has biaxiality of up to $\beta \approx 0.55$, which is significantly larger than that of any of the stable biaxial critical points in the other cases. This stable

critical point is locally minimising over a small range of high temperatures, and is then globally stable, tending to zero as t decreases. This result suggests that there is a strong possibility of observing bulk biaxiality at high temperatures (approximately between $t = 0$ and $t = 2$) in the negative coupling case, $c = -1$.

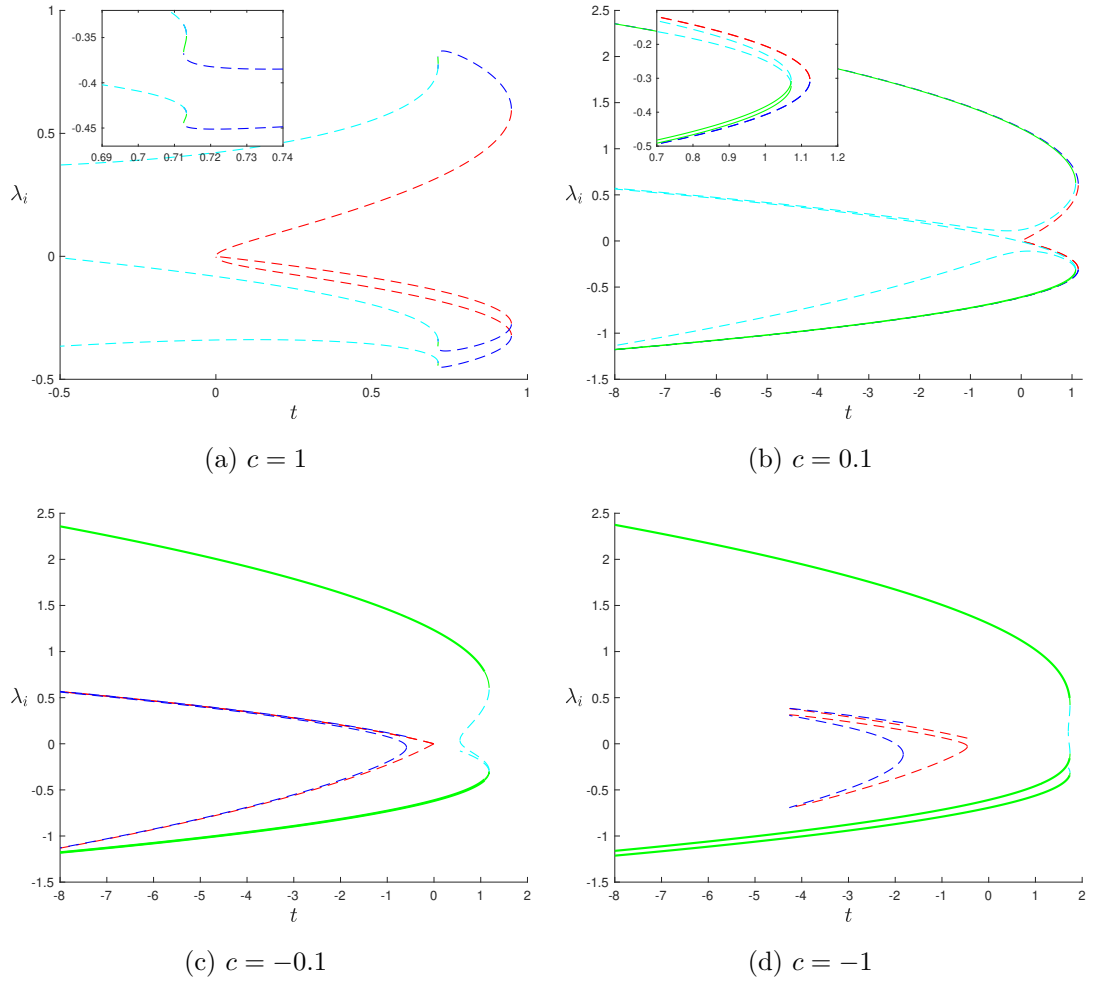


Figure 4.12: The eigenvalues, λ_i , associated with biaxial critical points of (4.28) for fixed c and $t \in [-8, 2]$. Thick solid lines indicate global minimality; thin solid lines indicate local minimality, and dashed lines indicate instability.

We plot the eigenvalues corresponding to each of the biaxial critical points in Figure 4.12, omitting the case $c = 0$, which has no biaxial critical points. We observe that the stable critical points are the points with the eigenvalues which are largest in magni-

tude. Furthermore, we plot the norm, $|\mathbf{M}| = \sqrt{m_1^2 + m_3^2}$, of the magnetisation vector associated with the biaxial critical points in Figure 4.13, again omitting the $c = 0$ case. We observe that all of the biaxial critical points have nonzero associated magnetisation vectors. We observe that the magnetisation vectors associated with stable biaxial critical points have the largest magnitude in the negative coupling cases, and the second largest magnitude in the positive coupling cases, suggesting that a magnetisation vector that is larger in magnitude plays a significant role in stabilising biaxial critical points.

We have omitted plots of the eigenvalues of the uniaxial critical points and their associated magnetisation vectors due to the fact that there are several such points, making the plots difficult to read, and therefore not particularly informative.

4.2.3 Critical Points as a Function of Nematic-Magnetic Coupling

In this section, we numerically compute critical points of the ferronematic bulk potential in (4.28) as a function of nematic-magnetic coupling strength. We consider the cases $t = 1, 0, -1, -5$, and -8 , and plot the biaxiality parameter, β , for critical points in the range $c \in [-1, 1]$, to further investigate how bulk ferronematic critical points are influenced by temperature and coupling strength. In particular, we look to track the stability and the value of the biaxiality parameter, β , of stable biaxial critical points as coupling strength varies from $c = -1$ to $c = 1$, at the given fixed temperatures.

As in the previous section, in Figure 4.14, we plot the biaxiality parameter in (4.35) of each of the critical points for each value of t , with the norm of the associated magnetisation vector, $|\mathbf{M}| = \sqrt{m_1^2 + m_3^2}$, plotted in Figure 4.15. We find at least three biaxial critical points at each temperature.

We observe that all plots in Figure 4.14 have globally minimising biaxial critical points for negative c , as is to be expected from the plots in the previous section. The

Chapter 4. Critical Points of the Ferronematic Bulk Potential

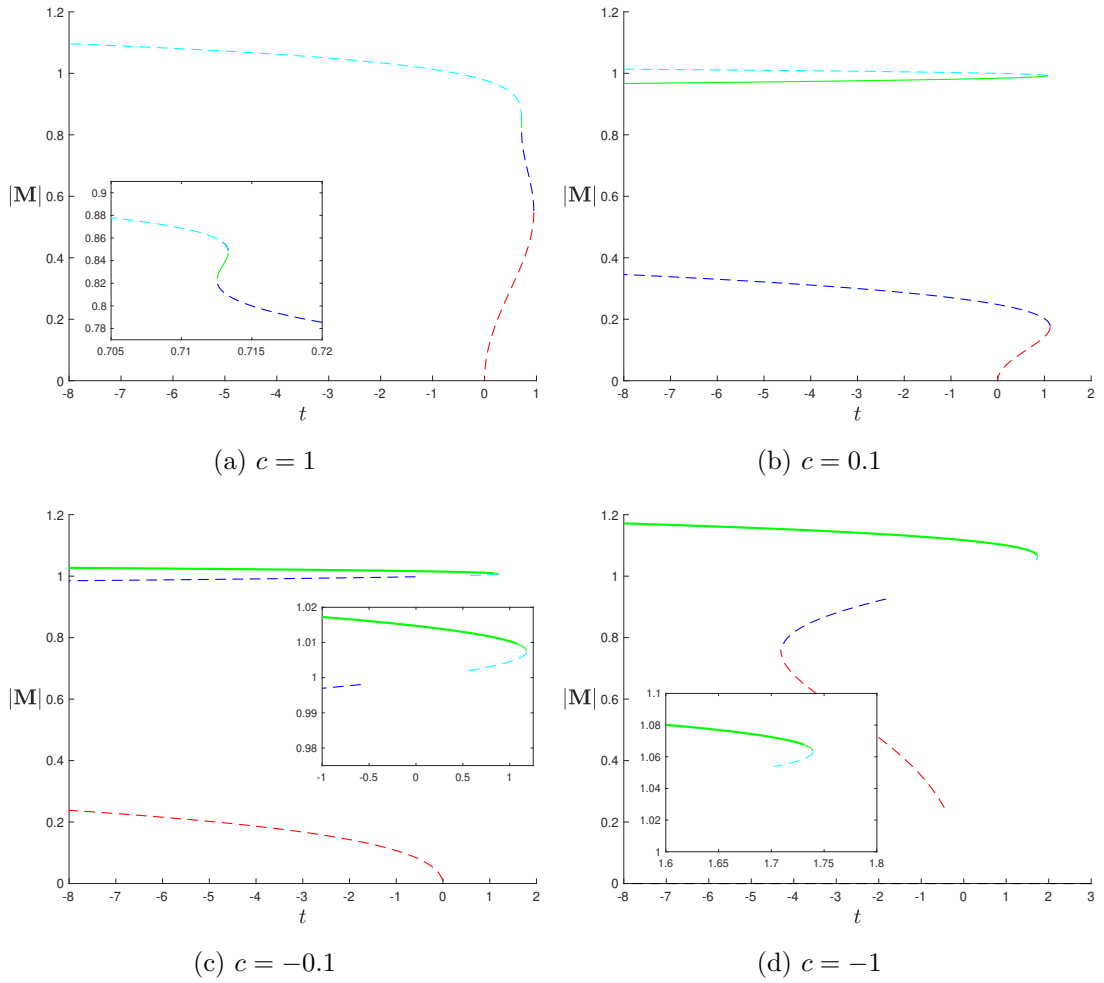


Figure 4.13: The norms of the magnetisation vectors, $|\mathbf{M}|$, associated with biaxial critical points of (4.28) for fixed c and $t \in [-8, 2]$. Thick solid lines indicate global minimality; thin solid lines indicate local minimality, and dashed lines indicate instability.

largest value of β for the globally minimising critical point (solid green line in Figure 4.14) in all cases occurs at $c = -1$ with β increasing as c decreases from $c = 0$, and this maximal value decreases with temperature, suggesting biaxiality is less favourable as temperature decreases.

As the biaxiality, β , of the global minimiser appears to increase as temperature increases and nemato-magnetic coupling decreases in Figure 4.14, we speculate that there may be a small range of high temperatures and negative coupling strengths that

Chapter 4. Critical Points of the Ferronematic Bulk Potential

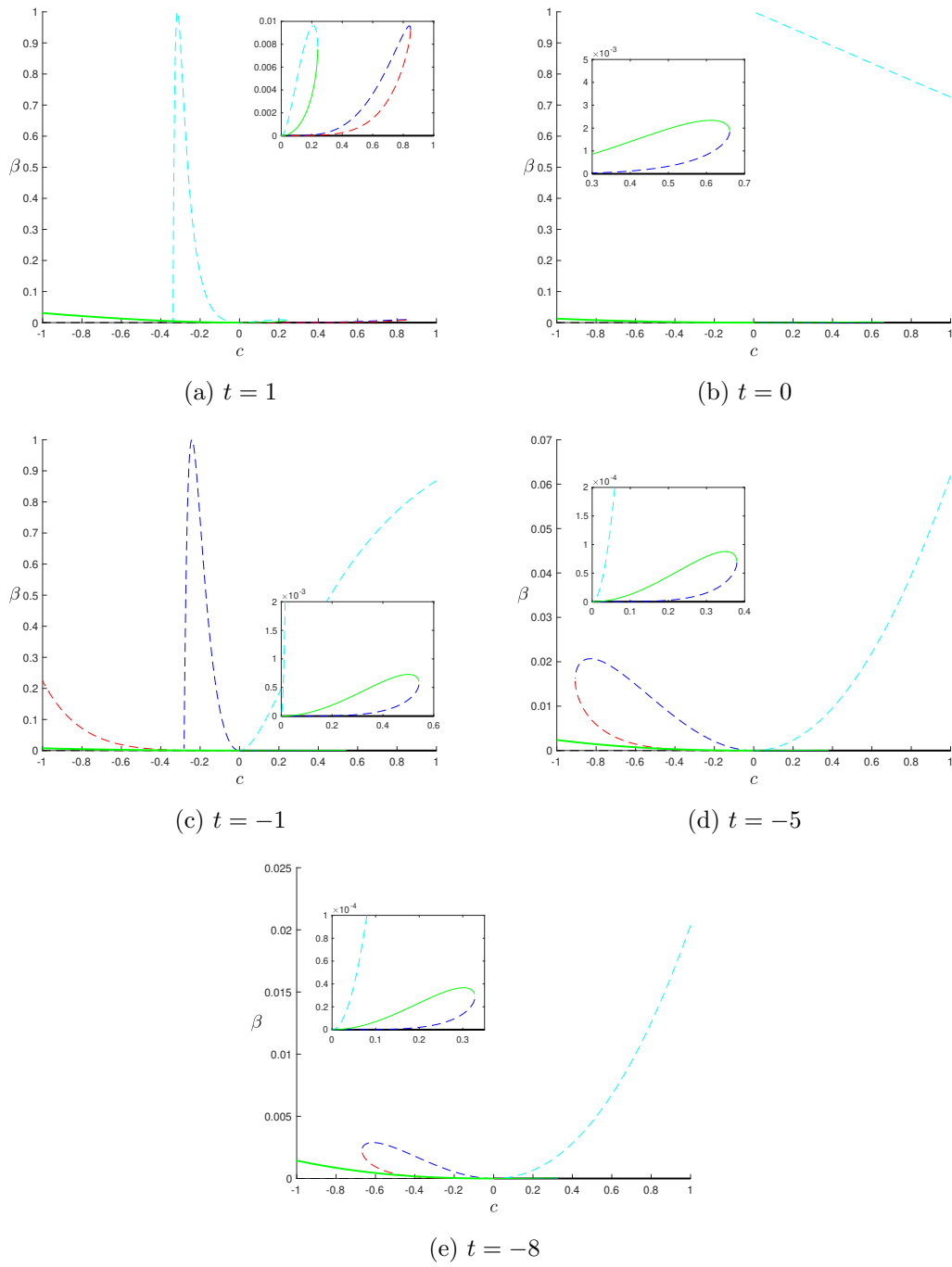


Figure 4.14: The biaxiality parameter, β , associated with biaxial critical points of (4.28) for fixed t and $c \in [-1, 1]$. Thick solid lines indicate global minimality; thin solid lines indicate local minimality, and dashed lines indicate instability.

favour significant bulk biaxiality. Let us consider again Figure 4.12. In each case, there exists some transition temperature at which biaxial critical points are first admissible, and this transition temperature appears to increase as the value of c decreases.

At all temperatures, there exists a locally minimising biaxial critical point for positive c , for c as large as $c \approx 0.7$ (see Figure 4.14b), but the corresponding biaxiality parameter in each case is very small, making it only slightly biaxial. This further reinforces the suggestion that we are unlikely to observe anything beyond approximate bulk uniaxiality in the positive coupling case.

The plots in Figure 4.14 further support our observations in Section 4.2.2: that bulk biaxiality is most likely to be physically observable within some range of higher temperatures, with negative coupling around $c = -1$.

Furthermore, we again observe that the magnetisation vector associated with the locally minimising critical point with positive coupling has the second largest magnitude at each temperature in Figure 4.15, while the magnetisation vector associated with the globally minimising critical point with negative coupling has the largest magnitude in each plot in Figure 4.15. The implication is that a magnetisation vector with a larger magnitude, of the order $|\mathbf{M}| = 1$, is required for the stability of biaxial critical points. We plot the magnetisation vector associated with certain uniaxial critical points in maroon in Figures 4.15a and 4.15c to illustrate connections between uniaxial and biaxial critical points.

4.2.4 Summary

In this chapter, we investigate the nature of critical points of the ferronematic bulk potential, first restricted to uniaxial \mathbf{Q} -tensors and a co-aligned magnetisation vector, as described in (4.2); and then in a more general setting with a \mathbf{Q} -tensor that can be

Chapter 4. Critical Points of the Ferronematic Bulk Potential

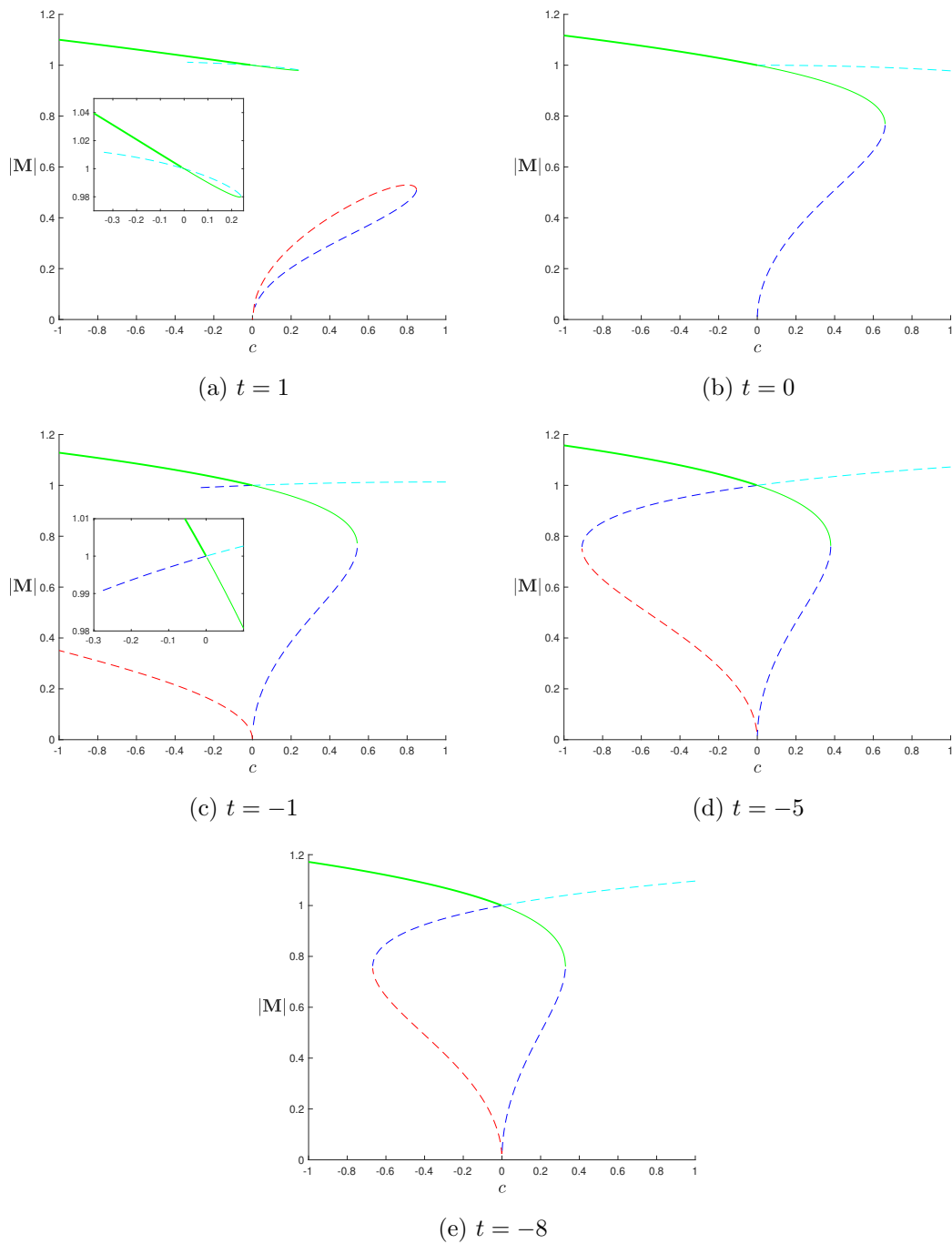


Figure 4.15: The norm of the magnetisation vector, $|\mathbf{M}|$, associated with biaxial critical points of (4.28) for fixed t and $c \in [-1, 1]$. Thick solid lines indicate global minimality; thin solid lines indicate local minimality, and dashed lines indicate instability.

biaxial, as described in (4.25).

In the uniaxial case, studied in Section 4.1, there are two key takeaways. Firstly, for any positive coupling strength c , the global minimiser is nonzero in both s and m , even at high temperatures, where $(s, m) = (0, 0)$ is the global minimiser in the uncoupled case. Secondly, we recall that s_+ is the globally minimising value of s in the uncoupled case in Figure 4.3, in agreement with the fourth-order uniaxial nematic case discussed in Section 3.2.1. We observe that the nemato-magnetic coupling has a destabilising effect on the branch $(s, m) = (s_+, 0)$, yet the branch $(s, m) = (s_-, 0)$ is locally stable at low temperatures in cases with positive c .

We also demonstrate that the bulk critical points can be approximated by polynomials in c in the weak coupling case, $c = 0.01$ in Section 4.1.3. This is useful as the analytical expressions for the roots of the polynomial in h are unwieldy. While we have not fully explored the specific contexts in which these approximations might be useful, they offer a promising alternative as long as they are used with care. Despite the need for caution, the approximate expressions have the potential to simplify calculations significantly.

In the more general case in Section 4.2, we demonstrate the existence of stable biaxial bulk critical points in both the positive and negative nemato-magnetic coupling cases. In the positive coupling case, the biaxial critical points are only locally stable, and have small maximal biaxiality, which decreases with decreasing temperature. The stable biaxial critical points are global minimisers and have larger maximal biaxiality in comparison in the negative coupling cases, which increases as the magnitude of c increases, and increases with increasing temperature. Our results suggest that bulk biaxiality is most likely to be observed experimentally in regimes with stronger negative nemato-magnetic coupling and at higher temperatures. In particular, we speculate that,

Chapter 4. Critical Points of the Ferronematic Bulk Potential

for sufficiently large and negative nemato-magnetic coupling, c , there could exist a small range of higher temperatures in which the global minimiser of the system approaches maximal biaxiality.

An important next step is to investigate the ferronematic bulk critical points in the class of \mathbf{Q} -tensors with five degrees of freedom, but we anticipate that this delicate problem will require significant computational power.

Chapter 5

The Ferronematic Radial Hedgehog Solution

The radial hedgehog solution has been studied extensively in the pure nematic case, both in the literature in the likes of [63] and [64] and in our contributions in Chapter 3. In this chapter, we consider spherical droplets of ferronematic liquid crystals and the possible equilibrium configurations. We study the qualitative properties of the radial hedgehog solution and other competing equilibria in the ferronematic case, investigating the effects of nemato-magnetic coupling strength, droplet size, and temperature on the system.

In Section 5.2, we present a range of analytical results for the ferronematic radial hedgehog solution to complement existing results on the nematic radial hedgehog solution, providing insight into the effects of magnetisation on the character of the radial hedgehog solution. We numerically explore the solution landscape of configurations on spherical droplets with rotational and mirror symmetry in Section 5.3, and we use broadly the same techniques as in the nematic case, allowing for qualitative comparison between the nematic and ferronematic cases. We note that we work with a positive cou-

pling parameter, c , throughout this chapter, so that the preferred coalignment between the nematic director and magnetisation vector is parallel.

5.1 Problem Formulation

We work with a dimensionless ferronematic free energy, in the absence of surface energies and external fields, given by

$$\begin{aligned} \mathcal{F}_F[\mathbf{Q}, \mathbf{M}] = \int_{B(0,1)} & \frac{\ell}{2} |\nabla \mathbf{Q}|^2 + \frac{t}{2} \operatorname{tr} \mathbf{Q}^2 - \sqrt{6} \operatorname{tr} \mathbf{Q}^3 + \frac{1}{2} (\operatorname{tr} \mathbf{Q}^2)^2 \\ & + \frac{\ell}{2} |\nabla \mathbf{M}|^2 + \frac{1}{4} (|\mathbf{M}|^2 - 1)^2 - c \mathbf{Q} \mathbf{M} \cdot \mathbf{M} \, dV, \end{aligned} \quad (5.1)$$

which we first introduce in Section 1.5.4, and we recall that we have rescaled the domain to the unit ball, $B(0,1)$. We capture the nematic liquid crystal configuration with the \mathbf{Q} -tensor, as in the pure nematic case, and we model the magnetisation via the magnetisation vector, \mathbf{M} . The parameter ℓ is an elastic constant which is inversely proportional to the droplet radius; the parameter t is the reduced temperature; and the parameter c is the nemato-magnetic coupling strength.

In this setting, we impose strong radial anchoring via the Dirichlet boundary condition

$$\mathbf{Q} = \mathbf{Q}_{s_f} := s_f \left(\hat{\mathbf{r}} \otimes \hat{\mathbf{r}} - \frac{1}{3} \mathbf{I} \right), \quad \mathbf{M} = \mathbf{M}_{s_f} := \sqrt{1 + \frac{4}{3} c s_f} \hat{\mathbf{r}} =: m_f \hat{\mathbf{r}}, \quad \text{on } \partial B(0,1), \quad (5.2)$$

where $\hat{\mathbf{r}}$ is the unit vector in the radial direction and s_f is the largest positive scalar order parameter corresponding to minimisers of

$$\left\{ f_F(\mathbf{Q}, \mathbf{M}) : \mathbf{Q} = s \left(\hat{\mathbf{r}} \otimes \hat{\mathbf{r}} - \frac{1}{3} \mathbf{I} \right), \mathbf{M} = m \hat{\mathbf{r}}, s, m \geq 0 \right\}, \quad (5.3)$$

and f_F is the ferronematic bulk potential

$$f_F(\mathbf{Q}, \mathbf{M}) = \frac{t}{2} \operatorname{tr} \mathbf{Q}^2 - \sqrt{6} \operatorname{tr} \mathbf{Q}^3 + \frac{1}{2} (\operatorname{tr} \mathbf{Q}^2)^2 + \frac{1}{4} (|\mathbf{M}|^2 - 1)^2 - c \mathbf{Q} \mathbf{M} \cdot \mathbf{M}. \quad (5.4)$$

We do not give an explicit expression for s_f , but instead note that the pair (s_f, m_f) minimise the function

$$g_F(s, m) := \frac{t}{3} s^2 - \frac{2\sqrt{6}}{9} s^3 + \frac{2}{9} s^4 + \frac{1}{4} (m^4 - 2m^2 + 1) - \frac{2}{3} c s m^2, \quad (5.5)$$

so that s_f is the largest positive root of

$$h(s) := s^3 - \frac{3\sqrt{6}}{4} s^2 + \left(\frac{3t}{4} - c^2 \right) s - \frac{3c}{4} = 0. \quad (5.6)$$

We note that we discuss the roots of the function h , and, more generally, the critical points of the function g_F in (5.5) in greater detail in Section 4.1.

Critical points of the ferronematic free energy then belong to the admissible space [97]

$$\mathcal{A}_{\mathbf{Q}\mathbf{M}} = \left\{ \mathbf{Q} \in W^{1,2}(B(0,1); \mathcal{S}_0), \mathbf{M} \in W^{1,2}(B(0,1); \mathbb{R}^3) : \right. \\ \left. \mathbf{Q} = \mathbf{Q}_{s_f} \text{ and } \mathbf{M} = \mathbf{M}_{s_f} \text{ on } \partial B(0,1) \right\}, \quad (5.7)$$

where the space $W^{1,2}(B(0,1); \mathcal{S}_0)$ is defined in Section 2.1, and the space $W^{1,2}(B(0,1); \mathbb{R}^3)$ is the space of all square-integrable vectors, \mathbf{M} , with square-integrable first derivatives.

Critical points of the ferronematic free energy satisfy the Euler–Lagrange equations

$$\begin{aligned} \ell \Delta Q_{ij} = t Q_{ij} + 3\sqrt{6} \left(\frac{1}{3} \operatorname{tr} \mathbf{Q}^2 \delta_{ij} - Q_{ik} Q_{kj} \right) \\ + 2Q_{ij} \operatorname{tr} \mathbf{Q}^2 + c \left(\frac{1}{3} |\mathbf{M}|^2 \delta_{ij} - M_i M_j \right), \end{aligned} \quad (5.8)$$

and

$$\ell \Delta M_i = M_i (|\mathbf{M}|^2 - 1) - 2c Q_{ij} M_j, \quad (5.9)$$

where

$$\frac{1}{3} \left(3\sqrt{6} \operatorname{tr} \mathbf{Q}^2 + c |\mathbf{M}|^2 \right) \delta_{ij} \quad (5.10)$$

is a Lagrange multiplier associated with the tracelessness constraint.

We are again interested in the radial hedgehog solution, which is an exact critical point of the ferronematic free energy in the admissible space, $\mathcal{A}_{\mathbf{QM}}$, and in the ferronematic case is of the form

$$\mathbf{Q}^*(\mathbf{r}) = s^*(r) \left(\hat{\mathbf{r}} \otimes \hat{\mathbf{r}} - \frac{1}{3} \mathbf{I} \right), \quad \mathbf{M}^*(\mathbf{r}) = m^*(r) \hat{\mathbf{r}}. \quad (5.11)$$

The functions s^* and m^* depend only on the radial distance, r , and we take the admissible space for pairs (s^*, m^*) to be

$$\mathcal{A}_{sm} = \left\{ s, m \in W^{1,2}([0, 1]; \mathbb{R}) : s(1) = s_f, m(1) = \sqrt{1 + \frac{4}{3} c s_f} \right\}. \quad (5.12)$$

As in the purely nematic case, the radial hedgehog solution is spherically symmetric and uniaxial everywhere, with the exception of the isotropic point defect at the droplet centre. The associated magnetisation vector is also oriented in the radial direction everywhere throughout the droplet.

5.2 Analysis of the Radial Hedgehog Solution

In this section, we study properties of the ferronematic radial hedgehog solution. In Chapter 3, we note that the nematic radial hedgehog solution exists with both the fourth- and sixth-order bulk potentials; and the associated scalar order parameter is positive away from the origin, unique, monotonic, and bounded in general with the fourth-order bulk potential [63], [64]. We demonstrate that these properties hold at moderately low temperatures with the sixth-order bulk potential in Chapter 3. Moreover, there exist analytical results demonstrating the stability of the radial hedgehog solution at high temperatures and in small droplets with the fourth-order bulk potential [63]; and we prove analogous results for small droplets with the sixth-order bulk potential in Chapter 3.

5.2.1 Analytical Results

Our aim in this section is to first prove the existence of the ferronematic radial hedgehog solution and then to investigate whether uniqueness, boundedness, positivity, and stability of the radial hedgehog solution are preserved in the ferronematic framework.

We begin with a general existence result for global minimisers of the ferronematic free energy defined in (5.1).

Proposition 5.1. *Consider the energy functional \mathcal{F}_F in (5.1), defined for functions $(\mathbf{Q}, \mathbf{M}) \in \mathcal{A}_{\mathbf{QM}}$, where $\mathcal{A}_{\mathbf{QM}}$ is defined in (5.7). There exists a global minimiser, $(\mathbf{Q}^*, \mathbf{M}^*) \in \mathcal{A}_{\mathbf{QM}}$ for \mathcal{F}_F .*

Proof. Firstly, the admissible space, $\mathcal{A}_{\mathbf{QM}}$ in (5.7), is nonempty since $(\mathbf{Q}_{s_f}, \mathbf{M}_{s_f}) \in \mathcal{A}_{\mathbf{QM}}$.

Furthermore, the integrand of (5.1) is quadratic in the gradient of both \mathbf{Q} and \mathbf{M} ,

so the functional (5.1) is convex and thus weakly lower-semicontinuous.

Let us now consider the coupling term in (5.1):

$$-c\mathbf{QM} \cdot \mathbf{M} = -c\left(Q_{11}M_1^2 + Q_{22}M_2^2 + Q_{33}M_3^2 + 2Q_{12}M_1M_2 + 2Q_{13}M_1M_3 + 2Q_{23}M_2M_3\right). \quad (5.13)$$

We note that, for example,

$$Q_{11}M_1^2 \leq |Q_{11}|M_1^2, \quad \text{and} \quad 2Q_{12}M_1M_2 \leq |Q_{12}|(M_1^2 + M_2^2), \quad (5.14)$$

and for some arbitrary $\lambda > 0$, it holds that

$$|Q_{11}|M_1^2 \leq \frac{1}{2}\left(\lambda Q_{11}^2 + \frac{1}{\lambda}M_1^4\right), \quad (5.15)$$

and

$$|Q_{12}|(M_1^2 + M_2^2) \leq \frac{1}{2}\left(\lambda Q_{12}^2 + \frac{1}{\lambda}(M_1^2 + M_2^2)^2\right). \quad (5.16)$$

We use the same logic for the remaining terms, so that

$$\begin{aligned} -c\mathbf{QM} \cdot \mathbf{M} &\geq -\frac{c}{2}\left(\lambda(Q_{11}^2 + Q_{22}^2 + Q_{33}^2 + Q_{12}^2 + Q_{13}^2 + Q_{23}^2) \right. \\ &\quad \left. + \frac{1}{\lambda}(M_1^4 + M_2^4 + M_3^4 \right. \\ &\quad \left. + (M_1^2 + M_2^2)^2 + (M_1^2 + M_3^2)^2 + (M_2^2 + M_3^2)^2\right) \\ &= -\frac{c}{2}\left(\lambda(\text{tr } \mathbf{Q}^2 - Q_{12}^2 - Q_{13}^2 - Q_{23}^2) \right. \\ &\quad \left. + \frac{1}{\lambda}(|\mathbf{M}|^4 + 2(M_1^4 + M_2^4 + M_3^4))\right). \end{aligned} \quad (5.17)$$

Therefore, we find that

$$\begin{aligned}
 f_F(\mathbf{Q}, \mathbf{M}) \geq & \frac{t}{2} \operatorname{tr} \mathbf{Q}^2 - \sqrt{6} \operatorname{tr} \mathbf{Q}^3 + \frac{1}{2} (\operatorname{tr} \mathbf{Q}^2)^2 + \frac{1}{4} (|\mathbf{M}|^2 - 1)^2 \\
 & - \frac{c}{2} \left(\lambda (\operatorname{tr} \mathbf{Q}^2 - Q_{12}^2 - Q_{13}^2 - Q_{23}^2) \right. \\
 & \left. + \frac{1}{\lambda} (|\mathbf{M}|^4 + 2(M_1^4 + M_2^4 + M_3^4)) \right) \quad (5.18)
 \end{aligned}$$

for an arbitrary $\lambda > 0$. We note that the ferronematic bulk potential, f_F , and the above expression, are polynomials in Q_{ij} , $i, j = 1, 2, 3$, and M_i , $i = 1, 2, 3$. The leading order terms in \mathbf{Q} are contained in the term $\frac{1}{2} (\operatorname{tr} \mathbf{Q}^2)^2$, which has a positive coefficient, as required for the above expression to be bounded from below.

Now we consider the terms

$$\begin{aligned}
 & \frac{1}{4} (|\mathbf{M}|^2 - 1)^2 - \frac{c}{2\lambda} (|\mathbf{M}|^4 + 2(M_1^4 + M_2^4 + M_3^4)) \\
 & = \left(\frac{1}{4} - \frac{3c}{2\lambda} \right) (M_1^4 + M_2^4 + M_3^4) + \left(\frac{1}{2} - \frac{c}{\lambda} \right) (M_1^2 M_2^2 + M_1^2 M_3^2 + M_2^2 M_3^2) \\
 & \quad - \frac{1}{2} |\mathbf{M}|^2 + \frac{1}{4}. \quad (5.19)
 \end{aligned}$$

Then for the leading order terms in \mathbf{M} to have positive coefficients, we require $\lambda > 6c$. Therefore, the expression (5.18) must be bounded below if $\lambda > 6c$. Thus, the bulk energy density, f_F , and hence the integrand of (5.11) is bounded from below. Therefore, the free energy (5.1) is coercive, and the existence of a global minimiser, $(\mathbf{Q}^*, \mathbf{M}^*)$, follows from the direct methods in the calculus of variations [107]. \square

Our next result is an existence result for the ferronematic radial hedgehog solution, inspired by Proposition 2.1 in [63].

Proposition 5.2. (a) Consider the energy functional

$$\begin{aligned}
 I_F[s, m] = \int_0^1 \left(\ell \left(\frac{1}{3} \left(\frac{ds}{dr} \right)^2 + \frac{2}{r^2} s^2 \right) + \frac{t}{3} s^2 - \frac{2\sqrt{6}}{9} s^3 + \frac{2}{9} s^4 \right. \\
 \left. + \frac{\ell}{2} \left(\left(\frac{dm}{dr} \right)^2 + \frac{2}{r^2} m^2 \right) \right. \\
 \left. + \frac{1}{4} (m^4 - 2m^2 + 1) - 2csm^2 \right) r^2 dr, \quad (5.20)
 \end{aligned}$$

defined for functions $(s, m) \in \mathcal{A}_{sm}$, where \mathcal{A}_{sm} is defined in (5.12). There exists a global minimiser $(s^*, m^*) \in \mathcal{A}_{sm}$ for I_F . The function s^* is a solution of the ordinary differential equation

$$\ell \left(\frac{d^2s}{dr^2} + \frac{2}{r} \frac{ds}{dr} - \frac{6}{r^2} s \right) = ts - \sqrt{6}s^2 + \frac{4}{3}s^3 - cm^2, \quad (5.21)$$

subject to the boundary conditions

$$s(0) = 0, \quad s(1) = s_f, \quad (5.22)$$

where s_f is the largest positive solution of (5.6). The function m^* is a solution of the ordinary differential equation

$$\ell \left(\frac{d^2m}{dr^2} + \frac{2}{r} \frac{dm}{dr} - \frac{2}{r^2} m \right) = m^3 - m - \frac{4}{3} csm, \quad (5.23)$$

subject to the boundary conditions

$$m(0) = 0, \quad m(1) = \sqrt{1 + \frac{4}{3} cs_f}. \quad (5.24)$$

We note that the equations (5.21) and (5.23) are the Euler–Lagrange equations

associated with (5.20).

(b) The solution $(\mathbf{Q}^*, \mathbf{M}^*)$, where

$$\mathbf{Q}^* = s^*(r) \left(\hat{\mathbf{r}} \otimes \hat{\mathbf{r}} - \frac{1}{3} \mathbf{I} \right), \quad \mathbf{M}^* = m^*(r) \hat{\mathbf{r}}, \quad (5.25)$$

where s^* and m^* are the global minimisers in part (a), is a critical point of the ferronematic free energy in (5.1).

(c) The global minimiser, (s^*, m^*) , is analytic for all $r \geq 0$.

Proof. (a) We prove existence via the direct methods in the calculus of variations, which we outline in Section 2.1. The admissible space, \mathcal{A}_{sm} , is nonempty since $(s, m) = \left(s_f, \sqrt{1 + \frac{4}{3}cs_f} \right) \in \mathcal{A}_{sm}$. The integrand of (5.20) is quadratic in $\frac{ds}{dr}$ and $\frac{dm}{dr}$, so the functional (5.20) is convex in $\frac{ds}{dr}$ and $\frac{dm}{dr}$, and thus weakly lower semicontinuous.

It holds that

$$-c\lambda \left(m^2 - \frac{1}{\lambda}s \right)^2 = -c \left(\lambda m^4 + \frac{1}{\lambda}s^2 \right) + 2csm^2 \leq 0, \quad (5.26)$$

for an arbitrary $\lambda > 0$, so we may write

$$\begin{aligned} & \frac{t}{3}s^2 - \frac{2\sqrt{6}}{9}s^3 + \frac{2}{9}s^4 + \frac{1}{4}(m^2 - 1)^2 - 2csm^2 \\ & \geq \left(\frac{t}{3} - \frac{c}{\lambda} \right) s^2 - \frac{2\sqrt{6}}{9}s^3 + \frac{2}{9}s^4 + \frac{1}{4}((1 - 4c\lambda)m^4 - 2m^2 + 1), \end{aligned} \quad (5.27)$$

which is bounded below if $\lambda < \frac{1}{4c}$. Therefore, the energy density in (5.20) is bounded from below, and the existence of a global minimiser (s^*, m^*) follows from the direct methods in the calculus of variations [107].

The boundary conditions $s^*(1) = s_f$, and $m^*(1) = \sqrt{1 + \frac{4}{3}cs_f}$ follow from the definition of the admissible space, \mathcal{A}_{sm} in (5.12). The boundary conditions $s^*(0) = m^*(0) = 0$ follow from the continuity of s^* and m^* for $r \in [0, 1]$. All functions $s \in \mathcal{A}_{sm}$ are necessarily continuous since $s \in W^{1,2}([0, 1]; \mathbb{R})$ implies $s \in C^{0,\alpha}([0, 1]; \mathbb{R})$ for some $0 < \alpha < \frac{1}{2}$ from the Sobolev embedding theorem [107], and the same is true for all functions $m \in \mathcal{A}_{sm}$. To show that $s^*(0) = m^*(0) = 0$, assume for a contradiction that $|s^*(r_0)| \geq s_0$ and $|m^*(r_0)| \geq m_0$ for some fixed s_0, m_0 and $0 < r_0 \ll 1$. Since s^* and m^* are continuous, s^* and m^* must both have a fixed sign near the origin. We further assume that $s^*(r) \geq s_0 > 0$ and $m^*(r) \geq m_0 > 0$ for $r \in [0, r_0]$. We note that the sign of $m^*(r)$ near the origin is trivial in this case, as only even powers of m^* appear in the following equations.

The equation (5.21) can be rewritten as

$$\frac{d}{dr} \left(r^2 \frac{ds}{dr} \right) = 6s + \frac{r^2}{\ell} \left(ts - \sqrt{6}s^2 + \frac{4}{3}s^3 - cm^2 \right). \quad (5.28)$$

Integrating from σ to r , where $0 < \sigma < \frac{r}{10}$, we obtain

$$\begin{aligned} & \int_{\sigma}^r \frac{d}{dr'} \left(r'^2 \frac{ds^*}{dr'} \right) dr' \\ &= \int_{\sigma}^r 6s^* dr' + \int_{\sigma}^r \frac{r'^2}{\ell} \left(ts^* - \sqrt{6}s^{*2} + \frac{4}{3}s^{*3} - cm^{*2} \right) dr', \end{aligned} \quad (5.29)$$

so that

$$\begin{aligned} & r^2 \frac{ds^*}{dr} - \sigma^2 \frac{ds^*}{dr} \Big|_{r=\sigma} \\ &= \int_{\sigma}^r 6s^* dr' + \int_{\sigma}^r \frac{r'^2}{\ell} \left(ts^* - \sqrt{6}s^{*2} + \frac{4}{3}s^{*3} - cm^{*2} \right) dr'. \end{aligned} \quad (5.30)$$

Then we may write

$$r^2 \frac{ds^*}{dr} \geq C_1 s_0 r + C_2 (r^3 - \sigma^3) + \sigma^2 s^{*\prime}(\sigma). \quad (5.31)$$

Dividing by r^2 , squaring both sides, and integrating, it is possible to show that

$$\int_{\sigma}^r \left(\frac{ds^*}{dr'} \right)^2 dr' \rightarrow \infty \quad (5.32)$$

in the limit $\sigma \rightarrow 0$, which contradicts the fact that $s^* \in W^{1,2}([0, 1]; \mathbb{R})$. An analogous argument for m^* shows that our assumption also violates $m^* \in W^{1,2}([0, 1]; \mathbb{R})$.

Therefore, we must have that $s^*(0) = 0$ and $m^*(0) = 0$ for any solution $(s^*, m^*) \in \mathcal{A}_{sm}$ of (5.21) and (5.23). Hence, (s^*, m^*) is a solution of the coupled ODEs, (5.21) and (5.23), subject to the boundary conditions

$$s^*(0) = 0 \quad \text{and} \quad s^*(1) = s_f, \quad (5.33)$$

$$m^*(0) = 0 \quad \text{and} \quad m^*(1) = \sqrt{1 + \frac{4}{3}cs_f}. \quad (5.34)$$

- (b) Firstly, we note that $(\mathbf{Q}^*, \mathbf{M}^*) \in \mathcal{A}_{\mathbf{QM}}$ in (5.7) since $(s^*, m^*) \in W^{1,2}([0, 1]; \mathbb{R})$. Furthermore, we note that $\mathcal{F}_F[\mathbf{Q}^*, \mathbf{M}^*] = 4\pi I_F[s^*, m^*]$, and it can be shown that $(\mathbf{Q}^*, \mathbf{M}^*)$ satisfies the Euler–Lagrange equations (5.8) and (5.9) since (s^*, m^*) is a solution of the ODEs (5.21) and (5.23), subject to the boundary conditions (5.22) and (5.24).
- (c) The analyticity of solutions of systems of nonlinear elliptic partial differential equations is proven in Chapter 6 of [126], and this can be applied to solutions of the ferronematic Euler–Lagrange equations (5.8) and (5.9), (\mathbf{Q}, \mathbf{M}) , subject to the boundary conditions (5.2). We note also that the analyticity of solutions of the

Landau–de Gennes free energy is proven in [49]. Therefore, the radial hedgehog solution given by (5.11), which is a solution of the ferronematic Euler–Lagrange equations, must be analytic. We have that \mathbf{Q} and \mathbf{M} are in $W^{1,2}(B(0,1); \mathcal{S}_0)$ by definition of the admissible space in (5.7). Then the right-hand sides of the Euler–Lagrange equations in (5.8) and (5.9) must belong to $L^2(B(0,1); \mathcal{S}_0)$ by the Sobolev embedding theorem. Hence, elliptic regularity and thus analyticity of solutions (\mathbf{Q}, \mathbf{M}) follows, and we refer the reader to [49] for more details.

To prove analyticity of the radial hedgehog scalar order parameter, we note that Corollary 2 in [49] implies that the eigenvectors of the radial hedgehog solution are also analytic away from the isotropic point defect at $r = 0$, so the radial hedgehog scalar order parameter s^* must also be analytic away from the origin. Furthermore, Proposition 1 in [64] can be applied to the ferronematic radial hedgehog scalar order parameter, and we may conclude that s^* is also analytic at $r = 0$.

Now, considering the associated magnetisation vector, we first note that the unit vector in the radial direction, $\hat{\mathbf{r}}$, is an eigenvector of the radial hedgehog \mathbf{Q} -tensor, and is thus analytic away from the origin, as above. Hence, m^* must also be analytic away from the origin.

□

Remark: We note that an argument first given in Proposition 1 in [64] can be used to prove that $s^{*'}(0) = 0$, but the analogous argument does not hold for m^* , so we cannot claim that $m^{*'}(0) = 0$.

In this next result, we prove the nonnegativity of the function s^* , but we note that the analogous argument does not hold for the function m^* since only even powers of m appear in the energy functional I_F in (5.20).

Proposition 5.3. *Let (s^*, m^*) be the global minimiser of I_F in (5.20), subject to the boundary conditions (5.22) and (5.24). The function s^* satisfies*

$$s^*(r) > 0 \quad \text{for } r \in (0, 1]. \quad (5.35)$$

Proof. We use the energy minimality condition to prove the lower bound $s^*(r) \geq 0$.

Suppose there exists an interior measurable subset

$$\Gamma = \{r \in (0, 1) : s^*(r) < 0\} \subset [0, 1], \quad (5.36)$$

with $s^*(r) = 0$ on $\partial\Gamma$. We note that Γ must be an interior subset because of the boundary conditions $s^*(0) = 0$, $s^*(1) = s_f$.

Define the perturbation

$$\bar{s}^*(r) = \begin{cases} s^*(r), & r \in [0, 1] \setminus \Gamma, \\ -s^*(r), & r \in \Gamma. \end{cases} \quad (5.37)$$

Then

$$I_F[\bar{s}^*, m^*] - I_F[s^*, m^*] = \int_{\Gamma} \left(\frac{4\sqrt{6}}{9} s^{*3} + \frac{4}{3} c s^* m^{*2} \right) r^2 dr < 0. \quad (5.38)$$

However, this contradicts the energy minimality of (s^*, m^*) . It follows that $s^*(r) \geq 0$ for $r \in [0, 1]$.

Next, we show that $s^*(r) > 0$ for $r > 0$. Assume for a contradiction that there exists some $r_0 \in (0, 1]$ such that $s^*(r_0) = 0$. Since we have already shown that $s^*(r) \geq 0$ on $[0, 1]$, the function s^* must therefore have a minimum at r_0 . Then

$$\left. \frac{ds^*}{dr} \right|_{r=r_0} = 0, \quad \text{and} \quad \left. \frac{d^2s^*}{dr^2} \right|_{r=r_0} \geq 0. \quad (5.39)$$

If we substitute $s^*(r_0)$ into

$$\ell \left(\frac{d^2 s}{dr^2} + \frac{2}{r} \frac{ds}{dr} - \frac{6}{r^2} s \right) = ts - \sqrt{6}s^2 + \frac{4}{3}s^3 - \frac{2}{3}cm^2, \quad (5.40)$$

we find that

$$\frac{d^2 s^*}{dr^2} \Big|_{r=r_0} = -\frac{2c}{3\ell} m^{*2}(r_0). \quad (5.41)$$

If $m^*(r_0) = 0$, we find that

$$\frac{d^2 s^*}{dr^2} \Big|_{r=r_0} = 0 \quad (5.42)$$

for all $n \in \mathbb{N}$. However, this cannot be true because s^* is analytic by Proposition 5.2, part (c), and we have the boundary condition $s^*(1) = s_f$.

If $m^*(r_0) \neq 0$, we find that

$$\frac{d^2 s^*}{dr^2} \Big|_{r=r_0} < 0, \quad (5.43)$$

which contradicts the assumption that s^* has a minimum at r_0 .

Therefore, we may conclude that $s^*(r) > 0$ for $r \in (0, 1]$. \square

Next, we prove a maximum principle, which yields upper bounds for s^* and m^* in (5.11).

Proposition 5.4. *We work in the temperature regime $t < 0$, with nonnegative nemato-magnetic coupling, c . Uniaxial minimisers, $(\mathbf{Q}^*, \mathbf{M}^*)$, of the ferronematic free energy (5.1) of the form (5.11) in the admissible space, $\mathcal{A}_{\mathbf{QM}}$ in (5.7), satisfy the upper bounds $|\mathbf{Q}^*|^2 \leq \frac{2}{3}s_f^2$ and $|\mathbf{M}^*|^2 \leq 1 + \frac{4}{3}cs_f$ on $B(0, 1)$, where s_f is the largest positive root of (5.6).*

Proof. Suppose $|\mathbf{Q}^*|$ and $|\mathbf{M}^*|$ attain maxima at two distinct points, $r_1, r_2 \in (0, 1)$,

respectively. We multiply the Euler–Lagrange equations in (5.8) by Q_{ij}^* to find that

$$\frac{1}{2}\Delta|\mathbf{Q}^*|^2 - |\nabla\mathbf{Q}^*|^2 = \frac{1}{\ell} (t|\mathbf{Q}^*|^2 - 3|\mathbf{Q}^*|^3 + 2|\mathbf{Q}^*|^2 - c\mathbf{Q}^*\mathbf{M}^* \cdot \mathbf{M}^*), \quad (5.44)$$

where we have used the fact that $|\nabla\mathbf{Q}^*|^2 + Q_{ij}^*\Delta Q_{ij}^* = \frac{1}{2}\Delta|\mathbf{Q}^*|^2$ and $\text{tr}\mathbf{Q}^{*3} = \frac{1}{\sqrt{6}}|\mathbf{Q}^*|^3$, which comes from the definition of the biaxiality parameter, $\beta = 1 - 6\frac{(\text{tr}\mathbf{Q}^3)^2}{(\text{tr}\mathbf{Q}^2)^3}$, noting that $\beta = 0$ when the \mathbf{Q} -tensor is uniaxial, and $\text{tr}\mathbf{Q}^2 = |\mathbf{Q}|^2$. Then, since \mathbf{Q}^* attains its maximum at r_1 , we must have that

$$\frac{1}{\ell} (t|\mathbf{Q}^*|^2 - 3|\mathbf{Q}^*|^3 + 2|\mathbf{Q}^*|^4 - c\mathbf{Q}^*\mathbf{M}^* \cdot \mathbf{M}^*) \Big|_{r=r_1} \leq 0. \quad (5.45)$$

Similarly, we multiply the Euler–Lagrange equations (5.9) by M_{ij}^* to obtain

$$\frac{1}{2}\Delta|\mathbf{M}^*|^2 - |\nabla\mathbf{M}^*|^2 = \frac{1}{\ell} (|\mathbf{M}^*|^2 (|\mathbf{M}^*|^2 - 1) - 2c\mathbf{Q}^*\mathbf{M}^* \cdot \mathbf{M}^*), \quad (5.46)$$

so that

$$\frac{1}{\ell} (|\mathbf{M}^*|^2 (|\mathbf{M}^*|^2 - 1) - 2c\mathbf{Q}^*\mathbf{M}^* \cdot \mathbf{M}^*) \Big|_{r=r_2} \leq 0. \quad (5.47)$$

Next, we substitute

$$\mathbf{Q}^* = s^*(r) \left(\hat{\mathbf{r}} \otimes \hat{\mathbf{r}} - \frac{1}{3}\mathbf{I} \right) \quad \text{and} \quad \mathbf{M}^* = m^*(r)\hat{\mathbf{r}} \quad (5.48)$$

into (5.45) and (5.47), which yields

$$\left(\frac{2t}{3}s^{*2} - \frac{2\sqrt{6}}{9}s^{*3} + \frac{8}{9}s^{*4} - \frac{2}{3}cs^*m^{*2} \right) \Big|_{r=r_1} \leq 0 \quad (5.49)$$

and

$$\left(m^{*2} (m^{*2} - 1) - \frac{4}{3} c s^* m^{*2} \right) \Big|_{r=r_2} \leq 0. \quad (5.50)$$

The above inequality reduces to

$$\left(m^{*2} - 1 - \frac{4}{3} c s^* \right) \Big|_{r=r_2} \leq 0, \quad (5.51)$$

and we may conclude that in fact

$$m^{*2}(r) \leq 1 + \frac{4}{3} c s^*(r_2) \quad (5.52)$$

for all $r \in [0, 1]$, as m^* attains a maximum at r_2 . Since $s^*(r_1) \geq s^*(r_2)$, we may write

$$m^{*2}(r_1) \leq 1 + \frac{4}{3} c s^*(r_1). \quad (5.53)$$

We substitute this into (5.49) to find that

$$\left(\frac{8}{9} s^{*4} - \frac{2\sqrt{6}}{3} s^{*3} + \left(\frac{2t}{3} - \frac{8}{9} c^2 \right) s^{*2} - \frac{4}{3} c s^* \right) \Big|_{r=r_1} \leq 0. \quad (5.54)$$

The left-hand side of the above equation tends to positive infinity as $s \rightarrow \infty$. In addition, the polynomial has one positive root, s_f , by Descartes' rule of signs, which states that the number of positive roots of a polynomial is at most equal to the number of sign changes in the sequence of coefficients, excluding zero coefficients. Furthermore, the difference between the number of roots and the number of sign changes is always even. In this case, with $t < 0$, there is only one sign change in the sequence of coefficients in (5.54), so there must be exactly one positive root. Furthermore, we have demonstrated that $s^*(r) \geq 0$ for $r \in [0, 1]$ in Proposition 5.3. Hence, we find that the condition in

(5.54) is satisfied if $s^*(r_1) \leq s_f$, where s_f is the largest positive root of the equation (5.6). In other words, $|\mathbf{Q}^*|$ attains a maximum at $r_1 \in [0, 1]$ if $0 \leq s^*(r_1) \leq s_f$.

Therefore, we must have $s^*(r) \leq s_f$ for $r \in [0, 1]$. We may then also conclude that $m^{*2} \leq 1 + \frac{4}{3}cs_f$.

Hence,

$$|\mathbf{Q}^*|^2 \leq \frac{2}{3}cs_f^2, \quad \text{and} \quad |\mathbf{M}^*|^2 \leq 1 + \frac{4}{3}cs_f. \quad (5.55)$$

□

The next result shows that the radial hedgehog solution is the unique critical point of the ferronematic free energy, (5.1), for droplets of sufficiently small radius. The implication is that the radial hedgehog solution is hence the globally stable critical point in sufficiently small droplets, due to the convexity of the ferronematic free energy for sufficiently large ℓ . The proof is inspired by Theorem 2.5 in [97].

Proposition 5.5. *For ℓ sufficiently large, the radial hedgehog solution, $(\mathbf{Q}^*, \mathbf{M}^*)$, defined in (5.11) is the unique critical point of the ferronematic free energy (5.1), subject to the boundary conditions (5.2).*

Proof. We want to show that there is a unique critical point of

$$\mathcal{F}_F[\mathbf{Q}, \mathbf{M}] = \int_{B(0,1)} \frac{\ell}{2} |\nabla \mathbf{Q}|^2 + \frac{\ell}{2} |\nabla \mathbf{M}|^2 + f_F(\mathbf{Q}, \mathbf{M}) dV, \quad (5.56)$$

where

$$f_F(\mathbf{Q}, \mathbf{M}) = \frac{t}{2} \text{tr } \mathbf{Q}^2 - \sqrt{6} \text{tr } \mathbf{Q}^3 + \frac{1}{2} (\text{tr } \mathbf{Q}^2)^2 + \frac{1}{4} (|\mathbf{M}|^2 - 1)^2 - c\mathbf{Q}\mathbf{M} \cdot \mathbf{M}. \quad (5.57)$$

First, we show that the free energy is strictly convex for ℓ sufficiently large. Let

$(\mathbf{Q}, \mathbf{M}), (\bar{\mathbf{Q}}, \bar{\mathbf{M}}) \in \mathcal{A}_{\mathbf{QM}}$, so that

$$(\mathbf{Q} - \bar{\mathbf{Q}}), (\mathbf{M} - \bar{\mathbf{M}}) \in W_0^{1,2}(B(0,1); \mathcal{S}_0), \quad (5.58)$$

where $W_0^{1,2}(B(0,1); \mathcal{S}_0)$ is the space of \mathbf{Q} -tensors that belong to $W^{1,2}(B(0,1); \mathcal{S}_0)$ that are zero on $\partial B(0,1)$, due to the boundary conditions (5.2).

We note that

$$\begin{aligned} & \mathcal{F}_F \left[\frac{\mathbf{Q} + \bar{\mathbf{Q}}}{2}, \frac{\mathbf{M} + \bar{\mathbf{M}}}{2} \right] \\ &= \frac{1}{2} (\mathcal{F}_F[\mathbf{Q}, \mathbf{M}] + \mathcal{F}_F[\bar{\mathbf{Q}}, \bar{\mathbf{M}}]) \\ & \quad + \int_{B(0,1)} \left(f_F \left(\frac{\mathbf{Q} + \bar{\mathbf{Q}}}{2}, \frac{\mathbf{M} + \bar{\mathbf{M}}}{2} \right) - \frac{1}{2} (f_F(\mathbf{Q}, \mathbf{M}) + f_F(\bar{\mathbf{Q}}, \bar{\mathbf{M}})) \right. \\ & \quad \quad \quad \left. - \frac{\ell}{8} |\nabla \mathbf{Q} - \nabla \bar{\mathbf{Q}}|^2 - \frac{\ell}{8} |\nabla \mathbf{M} - \nabla \bar{\mathbf{M}}|^2 \right) dV \\ & \leq \frac{1}{2} (\mathcal{F}_F[\mathbf{Q}, \mathbf{M}] + \mathcal{F}_F[\bar{\mathbf{Q}}, \bar{\mathbf{M}}]) \\ & \quad + \int_{B(0,1)} \left(f_F \left(\frac{\mathbf{Q} + \bar{\mathbf{Q}}}{2}, \frac{\mathbf{M} + \bar{\mathbf{M}}}{2} \right) - \frac{1}{2} (f_F(\mathbf{Q}, \mathbf{M}) + f_F(\bar{\mathbf{Q}}, \bar{\mathbf{M}})) \right) dV \\ & \quad \quad \quad - C_1 \ell \|\mathbf{Q} - \bar{\mathbf{Q}}\|_{L^2}^2 - C_2 \ell \|\mathbf{M} - \bar{\mathbf{M}}\|_{L^2}^2, \end{aligned} \quad (5.59)$$

where we have used the Poincaré inequalities

$$\frac{1}{8} \|\nabla(\mathbf{Q} - \bar{\mathbf{Q}})\|_{L^2}^2 \geq C_1 \|\mathbf{Q} - \bar{\mathbf{Q}}\|_{L^2}^2, \quad (5.60)$$

$$\frac{1}{8} \|\nabla(\mathbf{M} - \bar{\mathbf{M}})\|_{L^2}^2 \geq C_2 \|\mathbf{M} - \bar{\mathbf{M}}\|_{L^2}^2. \quad (5.61)$$

Note that

$$\begin{aligned} \frac{\partial^2 f_F}{\partial Q_{pq} \partial Q_{ij}} &= t \delta_{ip} \delta_{jq} - 3\sqrt{6} (\delta_{ip} Q_{jq} + \delta_{jq} Q_{ip}) + 2\delta_{ip} \delta_{jq} \operatorname{tr} \mathbf{Q}^2 + 4Q_{ij} Q_{pq}, \\ &\leq \max \left\{ 6\sqrt{6} s_f + |t|, \frac{16}{3} s_f^2 \right\} =: a_1, \end{aligned} \quad (5.62)$$

$$\frac{\partial^2 f_F}{\partial M_k \partial M_i} = -c (\delta_{ik} M_j + \delta_{jk} M_i) \leq 2c \sqrt{1 + \frac{4}{3} c s_f} =: a_2, \quad (5.63)$$

$$\begin{aligned} \frac{\partial^2 f_F}{\partial M_k \partial Q_{ij}} &= \delta_{ik} M_i M_j + 2M_i M_k^2 - \delta_{ik} - c Q_{ik} \\ &\leq 1 + \sqrt{\frac{2}{3}} c s_f + \frac{4}{3} c s_f + 2 \left(1 + \frac{4}{3} c s_f \right)^{3/2} =: a_3. \end{aligned} \quad (5.64)$$

Next, we use the fact that

$$\begin{aligned} f_F \left(\frac{\mathbf{Q} + \bar{\mathbf{Q}}}{2}, \frac{\mathbf{M} + \bar{\mathbf{M}}}{2} \right) &- \frac{1}{2} (f_F(\mathbf{Q}, \mathbf{M}) + f_F(\bar{\mathbf{Q}}, \bar{\mathbf{M}})) \\ &\leq \left| \frac{\partial^2 f_F}{\partial Q_{pq} \partial Q_{ij}} \right| \|\mathbf{Q} - \bar{\mathbf{Q}}\|_{L^2}^2 + \left| \frac{\partial^2 f_F}{\partial M_k \partial M_i} \right| \|\mathbf{M} - \bar{\mathbf{M}}\|_{L^2}^2 \\ &\quad + \left| \frac{\partial^2 f_F}{\partial M_k \partial Q_{ij}} \right| \|\mathbf{Q} - \bar{\mathbf{Q}}\|_{L^2} \|\mathbf{M} - \bar{\mathbf{M}}\|_{L^2}, \end{aligned} \quad (5.65)$$

to find that

$$\begin{aligned} \int_{B(0,1)} f_F \left(\frac{\mathbf{Q} + \bar{\mathbf{Q}}}{2}, \frac{\mathbf{M} + \bar{\mathbf{M}}}{2} \right) &- \frac{1}{2} (f_F(\mathbf{Q}, \mathbf{M}) + f_F(\bar{\mathbf{Q}}, \bar{\mathbf{M}})) \, dV \\ &\leq a_1 \|\mathbf{Q} - \bar{\mathbf{Q}}\|_{L^2}^2 + a_2 \|\mathbf{M} - \bar{\mathbf{M}}\|_{L^2}^2 + a_3 \|\mathbf{Q} - \bar{\mathbf{Q}}\|_{L^2} \|\mathbf{M} - \bar{\mathbf{M}}\|_{L^2}. \end{aligned} \quad (5.66)$$

Now, we note that

$$\|\mathbf{Q} - \bar{\mathbf{Q}}\|_{L^2} \|\mathbf{M} - \bar{\mathbf{M}}\|_{L^2} \leq \frac{1}{2} \left(\lambda \|\mathbf{Q} - \bar{\mathbf{Q}}\|_{L^2}^2 + \frac{1}{\lambda} \|\mathbf{M} - \bar{\mathbf{M}}\|_{L^2}^2 \right) \quad (5.67)$$

for any $\lambda > 0$. Let us set $\lambda = 2$, so that we have

$$\begin{aligned} \mathcal{F}_F \left[\frac{\mathbf{Q} + \bar{\mathbf{Q}}}{2}, \frac{\mathbf{M} + \bar{\mathbf{M}}}{2} \right] & \leq \frac{1}{2} (\mathcal{F}_F[\mathbf{Q}, \mathbf{M}] + \mathcal{F}_F[\bar{\mathbf{Q}}, \bar{\mathbf{M}}]) + (a_1 + a_3 - C_1 \ell) \|\mathbf{Q} - \bar{\mathbf{Q}}\|_{L^2}^2 \\ & \quad + (a_2 + a_3 - C_2 \ell) \|\mathbf{M} - \bar{\mathbf{M}}\|_{L^2}^2. \end{aligned} \quad (5.68)$$

Hence, if $\ell > \ell(c, t) = \max \left\{ \frac{1}{C_1}(a_1 + a_3), \frac{1}{C_2}(a_2 + a_3) \right\}$, we have

$$\mathcal{F}_F \left[\frac{\mathbf{Q} + \bar{\mathbf{Q}}}{2}, \frac{\mathbf{M} + \bar{\mathbf{M}}}{2} \right] < \frac{1}{2} \mathcal{F}_F[\mathbf{Q}, \mathbf{M}] + \frac{1}{2} \mathcal{F}_F[\bar{\mathbf{Q}}, \bar{\mathbf{M}}], \quad (5.69)$$

for all $\mathbf{Q}, \bar{\mathbf{Q}} \in W^{1,2}(B(0, 1); \mathcal{S}_0)$, and $\mathbf{M}, \bar{\mathbf{M}} \in W^{1,2}(B(0, 1); \mathcal{S}_0)$ such that $\mathbf{Q} \neq \bar{\mathbf{Q}}$, $\mathbf{M} \neq \bar{\mathbf{M}}$. Hence, \mathcal{F}_F is strictly convex if ℓ is large enough.

Next, assume that $\ell > \ell^*$, and that there exist two distinct solutions, $(\mathbf{Q}, \mathbf{M}), (\bar{\mathbf{Q}}, \bar{\mathbf{M}})$ of (5.1) in the admissible space $\mathcal{A}_{\mathbf{Q}\mathbf{M}}$. Then for $v \in [0, 1]$, the derivative of

$$\mathcal{F}_F[v\mathbf{Q} + (1-v)\bar{\mathbf{Q}}, v\mathbf{M} + (1-v)\bar{\mathbf{M}}] \quad (5.70)$$

vanishes at $v = 0$ and $v = 1$. However, this contradicts the strict convexity of \mathcal{F}_F , so we may conclude that a critical point of \mathcal{F}_F must be unique. \square

Remark: The values a_1, a_2, a_3 , which are functions of $|t|$, c , and s_f , increase with $|t|$, noting that s_f also increases with $|t|$. We recall that s_f is the largest positive root of

$$s^3 - \frac{3\sqrt{6}}{4}s^2 + \left(\frac{3t}{4} - c^2 \right) s - \frac{3c}{4} = 0. \quad (5.71)$$

Then, for large negative t , we have that

$$s_f \approx \left(\frac{3}{4}|t|\right)^{1/2}. \quad (5.72)$$

Therefore, a_1 increases like $|t|$; a_2 increases like $|t|^{1/4}$; and a_3 increases like $|t|^{3/4}$. Therefore, the value of ℓ required for uniqueness increases as $|t|$ increases, meaning smaller droplets are required for the uniqueness of the radial hedgehog solution at low temperatures.

In the next result, we consider the analytic form of the minimiser, (s^*, m^*) , of the functional I_F in (5.20) in Proposition 5.2 in the small droplet limit.

Proposition 5.6. *In the limit $\ell \rightarrow \infty$, the global minimiser, (s^*, m^*) , of I_F in (5.20), subject to the boundary conditions (5.22) and (5.24), is of the form*

$$(s^*, m^*) = \left(s_f r^2, \sqrt{1 + \frac{4}{3} c s_f r}\right), \quad (5.73)$$

where s_f is the largest positive root of (5.6).

Proof. We have the Euler–Lagrange equations

$$\ell \left(s'' + \frac{2}{r} s' - \frac{6}{r^2} s \right) = t s - \sqrt{6} s^2 + \frac{4}{3} s^3 - \frac{2}{3} c m^2, \quad (5.74)$$

$$\ell \left(m'' + \frac{2}{r} m' - \frac{2}{r^2} m \right) = m^3 - m - \frac{4}{3} c s m. \quad (5.75)$$

In the limit $\ell \rightarrow \infty$, these reduce to

$$s'' + \frac{2}{r} s' - \frac{6}{r^2} s = 0, \quad (5.76)$$

$$m'' + \frac{2}{r} m' - \frac{2}{r^2} m = 0. \quad (5.77)$$

It is straightforward to show that

$$s^*(r) = Ar^2, \quad \text{and} \quad m^*(r) = Br \tag{5.78}$$

solve the first and second equation, respectively. We use the boundary conditions, $s^*(1) = s_f$ and $m^*(1) = \sqrt{1 + \frac{4}{3}cs_f}$, to find that

$$s^*(r) = s_f r^2, \quad \text{and} \quad m^*(r) = \sqrt{1 + \frac{4}{3}cs_f} r. \tag{5.79}$$

□

5.2.2 Series Expansion for the Radial Hedgehog Solution

In this section, we derive series expansions for the minimisers, (s^*, m^*) , of the energy functional I_F in (5.20), inspired by Proposition 3.1 in [63]. We then numerically compute optimal coefficients for truncated versions of these series expansions.

Proposition 5.7. *Let (s^*, m^*) be a global minimiser of the energy functional (5.20), subject to the boundary conditions (5.22), (5.24). We construct power series expansions of s^* and m^* about the origin of the form*

$$s^*(r) = \sum_{n=1}^{\infty} a_n r^n, \tag{5.80}$$

$$m^*(r) = \sum_{n=1}^{\infty} b_n r^n, \quad r \leq R_c, \tag{5.81}$$

where R_c is the smaller of the two radii of convergence of the two series. Moreover, we have $a_1 = a_3 = \dots = a_{2k+1} = b_2 = b_4 = \dots = b_{2k} = 0, k \in \mathbb{N}^+$.

Proof. We have that s^* and m^* are analytic from Proposition 5.2 for $r \geq 0$. We

Chapter 5. The Ferronematic Radial Hedgehog Solution

substitute the two series, (5.80) and (5.81), into the Euler–Lagrange equations

$$\ell \left(s'' + \frac{2}{r}s' - \frac{6}{r^2}s \right) = ts - \sqrt{6}s^2 + \frac{4}{3}s^3 - \frac{2}{3}cm^2, \quad (5.82)$$

$$\ell \left(m'' + \frac{2}{r}m' - \frac{2}{r^2}m \right) = m^3 - m - \frac{4}{3}csm, \quad (5.83)$$

to obtain

$$\ell \sum_{n=1}^{\infty} (n^2 + n - 6) a_n r^{n-2} = \sum_{n=1}^{\infty} \left(ta_n - \sqrt{6}d_{2,n} + \frac{4}{3}d_{3,n} - \frac{2}{3}ce_{2,n} \right) r^n, \quad (5.84)$$

$$\ell \sum_{n=1}^{\infty} (n^2 + n - 2) b_n r^{n-2} = \sum_{n=1}^{\infty} \left(e_{3,n} - b_n - \frac{4}{3}cj_n \right) r^n, \quad (5.85)$$

where we set

$$d_{2,n} := \sum_{k=1}^{n-1} a_k a_{n-k}, \quad d_{3,n} := \sum_{k=2}^{n-1} d_{2,k}, \quad (5.86)$$

$$e_{2,n} := \sum_{k=1}^{n-1} b_k b_{n-k}, \quad e_{3,n} := \sum_{k=2}^{n-1} e_{2,k} b_{n-k}, \quad j_n := \sum_{k=1}^{n-1} a_k b_{n-k}. \quad (5.87)$$

Direct computations show that

$$a_1 = a_3 = 0, \quad b_2 = b_4 = 0, \quad (5.88)$$

$$a_2 > 0 \text{ arbitrary}, \quad a_4 = \frac{1}{14\ell} \left(ta_2 - \frac{2}{3}cb_1^2 \right), \quad (5.89)$$

$$b_1 \text{ arbitrary}, \quad b_3 = \frac{1}{10\ell}, \quad b_5 = \frac{1}{28\ell} \left(b_1^3 - \frac{1}{10\ell}b_1 - \frac{4}{3}ca_2b_1 \right), \quad (5.90)$$

where we have used the nonnegativity of s^* , as proven in Proposition 5.3.

We show by induction that (5.80) involves no odd powers of r , while (5.81) involves no even powers of r . Suppose that $a_{2n+1} = b_{2n} = 0$ for $n = 1, \dots, p$. We show that $a_{2p+3} = b_{2p+2} = 0$ also.

Comparing the coefficients of r^{2p+1} in (5.84), we find that

$$2\ell(2p^2 + 7p + 3)a_{2p+3} = ta_{2p+1} - \sqrt{6}d_{2,2p+1} + \frac{4}{3}d_{3,2p+1} - \frac{2}{3}ce_{2,2p+1}. \quad (5.91)$$

We show that each term on the right-hand side of (5.91) is zero. For the first term, we have from our assumption that $a_{2p+1} = 0$. For the second term, from our definition in (5.86), we write

$$d_{2,2p+1} = \sum_{k=1}^{2p} a_k a_{2p+1-k}. \quad (5.92)$$

Since exactly one of k and $2p+1-k$ is odd for each $k \in \{1, \dots, 2p\}$, we have $d_{2,2p+1} = 0$.

For the third term, from the definition in (5.86), we write

$$d_{3,2p+1} = \sum_{k=2}^{2p} d_{2,k} a_{2p+1-k} = d_{2,3} a_{2p-2} + d_{2,5} a_{2p-4} + \dots + d_{2,2p-3} a_4 + d_{2,2p-1} a_2, \quad (5.93)$$

where we use the assumption that $a_{2n+1} = 0$ for $n = 1, \dots, p$. It is possible to show, using an argument analogous to that for the second term, that $d_{2,q} = 0$ for any odd q such that $q \leq 2p+1$. Thus, $d_{3,2p+1} = 0$, also. Finally, for the fourth term, we write,

$$e_{2,2p+1} = \sum_{k=1}^{2p} b_k b_{2p+1-k}, \quad (5.94)$$

from the definition in (5.87). Since exactly one of k and $2p+1-k$ is odd for each $k \in \{1, \dots, 2p\}$, we may conclude that $e_{2,2p+1} = 0$ by our assumption. Therefore, the right-hand side of (5.91) is zero, which implies that a_{2p+3} , as required.

Similarly, comparing coefficients of r^{2p} in (5.85), we find that

$$2\ell(2p^2 + 5p + 2)b_{2p+2} = e_{3,2p} - b_{2p} - \frac{4}{3}cj_{2p}. \quad (5.95)$$

Chapter 5. The Ferronematic Radial Hedgehog Solution

We show that each term on the right-hand side of (5.95) is zero. For the second term, we have that $b_{2p} = 0$ by assumption. For the first term, from our definition in (5.87), we write

$$e_{3,2p} = \sum_{k=2}^{2p-1} e_{2,k} b_{2p-k} = e_{2,3} b_{2p-1} + \cdots + e_{2,2p-3} b_3 + e_{2,2p-1} b_1, \quad (5.96)$$

where we use the assumption that $b_{2n} = 0$ for $n = 1, \dots, p$. For some odd q such that $q \leq 2p - 1$, we have

$$e_{2,q} = \sum_{k=1}^{q-1} b_k b_{q-k}, \quad (5.97)$$

and we note that exactly one of k and $q - k$ is even for each $k \in \{1, \dots, q\}$. Then we may conclude that $e_{2,q} = 0$ for $q \leq 2p + 1$. Hence we may also conclude that $e_{3,2p} = 0$.

For the third term, we write

$$j_{2p} = \sum_{k=1}^{2p-1} a_k b_{2p-k}, \quad (5.98)$$

from our definition in (5.87), and we note that both k and $2p - k$ are even or both are odd, we use the assumption that $a_{2n+1} = b_{2n} = 0$ for $n = 1, \dots, p$ to conclude that $j_{2p} = 0$. Therefore, the right-hand side of (5.95) is zero, which implies that b_{2p+2} , as required.

Therefore, by the principle of mathematical induction, we may conclude that

$$a_{2n+1} = 0, \quad b_{2n} = 0, \quad \forall n \in \mathbb{N}^+. \quad (5.99)$$

Hence, the expansion (5.80) contains no odd powers of r , while the expansion (5.81) contains no even powers of r .

Next, we show by induction that a_{2n+1} and b_{2n+1} are functions of a_2, b_1, t, c , and ℓ ,

so that

$$a_{2n+2} := f_n(a_2, b_1, t, c, \ell), \quad b_{2n+1} := g_n(a_2, b_1, t, c, \ell) \quad \forall n \in \mathbb{N}^+. \quad (5.100)$$

Direct computations have shown that a_2, a_4, b_3 , and b_5 are functions of a_2, b_1, t, c , and ℓ in (5.88)-(5.90).

Suppose that

$$a_{2n+2} = f_n(a_2, b_1, t, c, \ell), \quad b_{2n+1} = g_n(a_2, b_1, t, c, \ell) \quad (5.101)$$

for $n = 1, \dots, p$. We show that

$$a_{2p+4} = f_{p+1}(a_2, b_1, t, c, \ell), \quad b_{2p+3} = g_{p+1}(a_2, b_1, t, c, \ell), \quad (5.102)$$

also.

Comparing coefficients of r^{2p+2} in (5.84), we find that

$$2\ell(2p^2 + 9p + 7)a_{2p+4} = ta_{2p+2} - \sqrt{6}d_{2,2p+2} + \frac{4}{3}d_{3,2p+2} - \frac{2}{3}ce_{2,2p+2}. \quad (5.103)$$

We show that the right-hand side of (5.103) is a function of a_2, b_1, t, c , and ℓ . For the first term, we have that $a_{2p+2} = f_p(a_2, b_1, t, c, \ell)$ by our induction assumption. For the second term, we write, from (5.86),

$$d_{2,2p+2} = \sum_{k=1}^{2p+1} a_k a_{2p+2-k} = a_2 f_{p-2} + f_1 f_{p-2} + \dots + f_{p-2} f_1 + f_{p-1} a_2, \quad (5.104)$$

where we have used the fact that $a_{2n+1} = 0 \forall n \in \mathbb{N}^+$, demonstrating that $d_{2,2p+1}$ is a

Chapter 5. The Ferronematic Radial Hedgehog Solution

function of a_2, b_1, t, c , and ℓ . For the third term, we write

$$d_{3,2p+2} = \sum_{k=2}^{2p+1} d_{2,k} a_{2p+2-k} = d_{2,2} a_{2p} + d_{2,4} a_{2p-1} + \cdots + d_{2,2p} a_2, \quad (5.105)$$

where we have used the fact that $a_{2n-1} = 0 \forall n \in \mathbb{N}^+$. The terms $d_{2,2}, \dots, d_{2,2p}$ can be expressed in terms of a_2, \dots, a_{2p-2} , so $d_{3,2p+2}$ is also a function of a_2, b_1, t, c , and ℓ . For the last term, from the definition in (5.87), we write

$$e_{2,2p+2} = \sum_{k=1}^{2p+1} b_k b_{2p+2-k}. \quad (5.106)$$

Both k and $2p+2-k$ are even or both are odd, so we may write

$$e_{2,2p+2} = b_1 g_p + g_1 g_{p-1} + \cdots + g_{p-1} g_3 + g_p b_1, \quad (5.107)$$

where we have used the fact that $b_{2n} = 0 \forall n \in \mathbb{N}^+$, showing that $e_{2,2p+2}$ is also a function of a_2, b_1, t, c , and ℓ .

Hence, the right-hand side of (5.103) is a function of a_2, b_1, t, c , and ℓ , so a_{2p+2} is also a function of a_2, b_1, t, c , and ℓ , and we write

$$a_{2p+4} = f_{p+1}(a_2, b_1, t, c, \ell). \quad (5.108)$$

Finally, we consider the coefficients of r^{2p+1} in (5.85), and find that

$$2\ell(2p^2 + 7p + 5)b_{2p+3} = e_{3,2p+1} - b_{2p+1} - \frac{4}{3}c j_{2p+1}. \quad (5.109)$$

We show that the right-hand side of (5.109) is a function of a_2, b_1, t, c , and ℓ . We have $b_{2p+1} = g_p(a_2, b_1, t, c, \ell)$ by our induction assumption, for the first term. For the second

term, from our definition in (5.87), we write

$$e_{3,2p+1} = \sum_{k=2}^{2p} e_{2,k} b_{2p+1-k} = e_{2,2} b_{2p-1} + e_{2,4} b_{2p-3} + \cdots + e_{2,2p-2} b_3 + e_{2,2p} b_1, \quad (5.110)$$

where we have used the fact that $b_{2n} = 0 \forall n \in \mathbb{N}^+$. The terms $e_{2,2}, \dots, e_{2,2p}$ can be expressed in terms of b_1, b_{2p-1} by their definition in (5.87), so $e_{3,2p+1}$ is also a function of a_2, b_1, t, c , and ℓ . Furthermore, for the third term, we write

$$j_{2p+1} = \sum_{k=1}^{2p} a_k b_{2p+1-k}, \quad (5.111)$$

and we note that exactly one of k and $2p+1-k$ is odd for each $k \in \{1, \dots, 2p\}$, so

$$j_{2p+1} = a_2 g_{p-2} + \cdots + f_{p-2} g_1 + f_{p-1} b_1, \quad (5.112)$$

where we have used the fact that $a_{2n-1} = 0 \forall n \in \mathbb{N}^+$, demonstrating that j_{2p+1} is a function of a_2, b_1, t, c , and ℓ .

Therefore, the right-hand side of (5.109) is a function of a_2, b_1, t, c , and ℓ , which implies that b_{2p+3} is also a function of a_2, b_1, t, c , and ℓ , and we write

$$b_{2p+3} = g_{p+1}(a_2, b_1, t, c, \ell). \quad (5.113)$$

Therefore, by the principle of mathematical induction, we may conclude that

$$a_{2n+2} = f_n(a_2, b_1, t, c, \ell), \quad b_{2n+1} = g_n(a_2, b_1, t, c, \ell), \quad \forall n \in \mathbb{N}^+. \quad (5.114)$$

From the above, we may write

$$s^*(r) = a_2 r^2 + f_1(a_2, b_1, t, c, \ell) r^4 + f_2(a_2, b_1, t, c, \ell) r^6 + o(r^6), \quad (5.115)$$

$$m^*(r) = b_1 r + g_1(a_2, b_1, t, c, \ell) r^3 + g_2(a_2, b_1, t, c, \ell) r^5 + o(r^5). \quad (5.116)$$

□

Remark: Using the form of s^* and m^* near the origin in Proposition 5.7, we note that we must have $s^{*'}(0) = 0$ and $m^{*'}(0) = b_1$.

Proposition 5.7 proves that we may write

$$s(r) = a_2 r^2 + a_4 r^4 + a_6 r^6 + a_8 r^8 + o(r^8), \quad (5.117)$$

$$m(r) = b_1 r + b_3 r^3 + b_5 r^5 + b_7 r^7 + o(r^7), \quad (5.118)$$

inside some radius of convergence, where a_2 and b_1 are arbitrary, and a_4, a_6, a_8, \dots , and b_3, b_5, b_7, \dots , are functions of a_2, b_1, t, c , and ℓ . In the remainder of this section, we investigate how well polynomials of the form

$$s(r) = a_2 r^2 + a_4 r^4 + a_6 r^6 + a_8 r^8, \quad (5.119)$$

$$m(r) = b_1 r + b_3 r^3 + b_5 r^5 + b_7 r^7, \quad (5.120)$$

fit minimisers, (s, m) , of (5.20), subject to the boundary conditions (5.22) and (5.24).

We numerically compute critical points, (s, m) , of (5.20) via a finite element method for specific values of t, ℓ , and c . We solve over the unit interval, $[0, 1]$, and look for

minimisers of the free energy I_F in (5.20) by considering the weak formulations

$$\begin{aligned} F_s &= \int_0^1 \ell \left(\frac{ds}{dr} \frac{dv_1}{dr} - \frac{2}{r} \frac{ds}{dr} v_1 + \frac{6}{r^2} s v_1 \right) + v_1 \left(t s - \sqrt{6} s^2 + \frac{4}{3} s^3 - \frac{2}{3} s m^2 \right) dr, \\ F_m &= \int_0^1 \ell \left(\frac{dm}{dr} \frac{dv_2}{dr} - \frac{2}{r} \frac{dm}{dr} v_2 + \frac{2}{r^2} m v_2 \right) + v_2 \left(m^3 - m - \frac{4}{3} c s m \right) dr, \end{aligned} \quad (5.121)$$

which are obtained from the Euler–Lagrange equations (5.21) and (5.23), where v_1 and v_2 are test functions. We solve for (s, m) such that $F_s = F_m = 0$.

This returns a set of values for critical points (s, m) at points $r_i \in [0, 1]$, with $0 = r_1 < r_2 < \dots < r_{n-1} < r_n = 1$. We use these data points to find optimal values for a_2 and b_1 , which minimise the residuals

$$R_{T,s}^2 = \sum_{i=1}^n [s_i - (a_2 r_i^2 + a_4 r_i^4 + a_6 r_i^6 + a_8 r_i^8)]^2, \quad (5.122)$$

$$R_{T,m}^2 = \sum_{i=1}^n [m_i - (b_1 r_i + b_3 r_i^3 + b_5 r_i^5 + b_7 r_i^7)]^2, \quad (5.123)$$

where s_i and m_i are data points from the numerically computed solutions, and the r_i are their corresponding distances from the origin. We set

$$\frac{\partial R_{T,s}^2}{\partial a_2} = 0, \quad \frac{\partial R_{T,s}^2}{\partial b_1} = 0, \quad \frac{\partial R_{T,m}^2}{\partial a_2} = 0, \quad \frac{\partial R_{T,m}^2}{\partial b_1} = 0, \quad (5.124)$$

and solve for a_2 and b_1 using the MATLAB function `vpasolve()` [125].

For comparison, we approximate s and m by the independent polynomials

$$s(r) = c_2 r^2 + c_4 r^4 + c_6 r^6 + c_8 r^8, \quad (5.125)$$

$$m(r) = c_1 r + c_3 r^3 + c_5 r^5 + c_7 r^7, \quad (5.126)$$

removing the dependence on a_2, b_1, t, ℓ and c . We minimise the residuals

$$R_{I,s}^2 = \sum_{i=1}^n [s_i - (c_2 r_i^2 + c_4 r_i^4 + c_6 r_i^6 + c_8 r_i^8)]^2, \quad (5.127)$$

$$R_{I,m}^2 = \sum_{i=1}^n [m_i - (c_1 r_i + c_3 r_i^3 + c_5 r_i^5 + c_7 r_i^7)]^2, \quad (5.128)$$

where s_i and m_i are the same data points from the numerically computed solutions as in (5.122) and (5.123), and the r_i are their corresponding distances from the origin.

Minimising the residuals in this case is equivalent to solving the linear systems

$$\begin{bmatrix} s_1 \\ s_2 \\ \vdots \\ s_n \end{bmatrix} = \begin{bmatrix} r_1^2 & r_1^4 & r_1^6 & r_1^8 \\ r_2^2 & r_2^4 & r_2^6 & r_2^8 \\ \vdots & \vdots & \vdots & \vdots \\ r_n^2 & r_n^4 & r_n^6 & r_n^8 \end{bmatrix} \begin{bmatrix} c_2 \\ c_4 \\ c_6 \\ c_8 \end{bmatrix}, \quad \text{and} \quad \begin{bmatrix} m_1 \\ m_2 \\ \vdots \\ m_n \end{bmatrix} = \begin{bmatrix} r_1 & r_1^3 & r_1^5 & r_1^7 \\ r_2 & r_2^3 & r_2^5 & r_2^7 \\ \vdots & \vdots & \vdots & \vdots \\ r_n & r_n^3 & r_n^5 & r_n^7 \end{bmatrix} \begin{bmatrix} c_1 \\ c_3 \\ c_5 \\ c_7 \end{bmatrix}, \quad (5.129)$$

which is easily done numerically, using the function *linsolve()* in MATLAB [125].

We fit Taylor and independent polynomials across a range of temperatures and values of ℓ for r in the intervals $[0, 0.05]$, $[0, 0.1]$, and $[0, 0.5]$ and calculate the value of the residuals. We plot the fourth root of the sum of the residuals, $(R_T^2)^{1/4} := (R_{T,s}^2 + R_{T,m}^2)^{1/4}$ and $(R_I^2)^{1/4} := (R_{I,s}^2 + R_{I,m}^2)^{1/4}$ in Figures 5.1, 5.2 and 5.3, as a measure of the error associated with each fit against temperature. We plot the fourth root for readability, as the values of R_T^2 and R_I^2 for different values of t and ℓ are spread over several orders of magnitude, so plotting instead, for example, the square root of the residuals is not particularly informative. We record results for $\ell = 0.1$, $\ell = 1$, and $\ell = 10$ in each plot in Figures 5.1-5.3. Dashed lines indicate the error associated with the independent polynomial fit in (5.125) and (5.126), while solid lines correspond to the Taylor polynomial fit in (5.119) and (5.120), and different colours correspond to

Chapter 5. The Ferronematic Radial Hedgehog Solution

different values of ℓ . In each case in Figures 5.1-5.3, we compute the coefficients of the Taylor and independent polynomials using 51 data points from our numerical solutions for (s, m) to limit computational time.

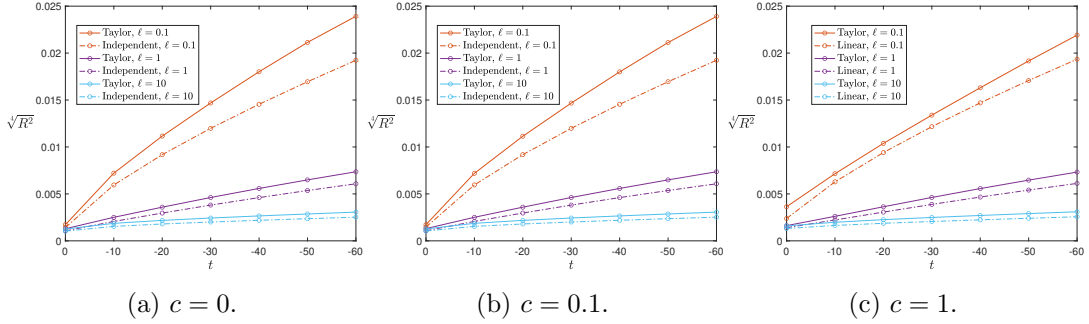


Figure 5.1: Error of each fit computed for r in the interval $[0, 0.05]$. Circles denote which fits were computed. Solid lines correspond to the Taylor polynomial fit; dashed lines correspond to the independent polynomial. Orange, purple and blue lines correspond to $\ell = 0.1$, $\ell = 1$ and $\ell = 10$, respectively.

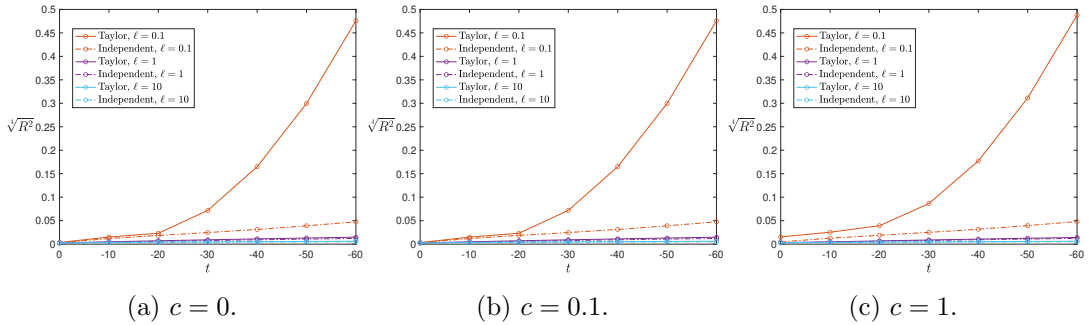


Figure 5.2: Error of each fit computed for r in the interval $[0, 0.1]$. Circles denote which fits were computed. Solid lines correspond to the Taylor polynomial fit; dashed lines correspond to the independent polynomial fit. Orange, purple and blue lines correspond to $\ell = 0.1$, $\ell = 1$ and $\ell = 10$, respectively.

There are some general trends. Firstly, the independent polynomial fit is better than the Taylor series fit in every case. This is to be expected since the coefficients of the Taylor series have the added restriction of being dependent on one another. From inspecting the plots in Figures 5.1-5.3, we observe that the error associated with both polynomial fits increases as temperature decreases; as droplet size increases (ℓ

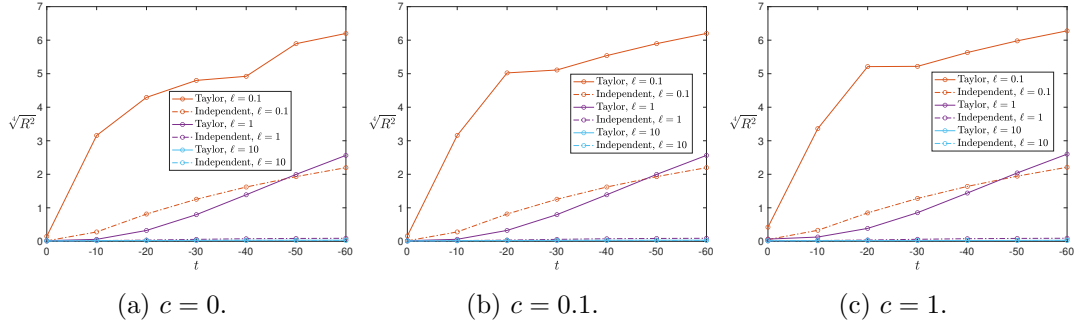


Figure 5.3: Error of each fit computed for r in the interval $[0, 0.5]$. Circles denote which fits were computed. Solid lines correspond to the Taylor polynomial fit; dashed lines correspond to the independent polynomial fit. Orange, purple and blue lines correspond to $\ell = 0.1$, $\ell = 1$ and $\ell = 10$, respectively.

decreases). We also observe that the error increases as the interval size increases. This could be related to the fact that the series expansion is valid inside some radius of convergence, which might be smaller than the intervals we use in this section.

These trends suggest that there is some loss of regularity at lower temperatures, in larger droplets, and in cases where the nemato-magnetic coupling is stronger, making the s and m profiles less suited to approximation by the polynomials.

In Figure 5.4, we plot examples of the numerically computed s and m profiles across a range of parameter values, normalised by the boundary value for ease of comparison. In general, we observe that the normalised s profiles are close to $s(r) = r^2$ and the m profiles are close to $m(r) = r$ in small droplets with $\ell = 10$, which is in agreement with Proposition 5.6. It is these profiles that are best approximated by the polynomials. In large droplets, with $\ell = 0.1$, the s profiles appear to approach a profile with a boundary layer near the origin, where $s(0) = 0$, and s close to 1 in the rest of the droplet. The polynomial fits of these profiles have the largest error.

Finally, we plot examples of the Taylor and independent polynomial fits to highlight their limitations in Figure 5.5. In Figures 5.5a and 5.5d, which correspond to the interval $[0, 0.05]$, both fits appear perfect, which is to be expected, as the error plotted

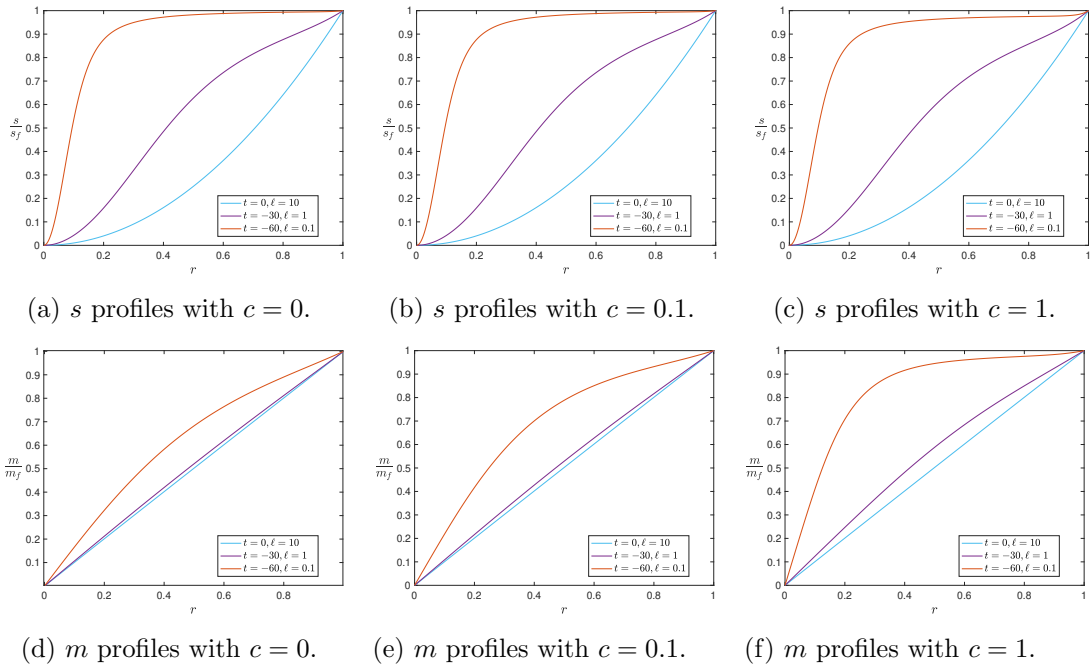


Figure 5.4: Examples of the numerically computed s and m profiles for r in the interval $[0, 1]$ with different values of the coupling parameter c . Each profile is normalised to reach a maximum value of 1 at $r = 1$, for ease of comparison. Plots (a)-(c) are s profiles, and plots (d)-(f) are the corresponding m profiles. Orange, purple and blue lines denote the parameter regimes $t = 0, \ell = 10$; $t = -30, \ell = 1$; and $t = -60, \ell = 0.1$, respectively.

in Figure 5.1b is very small. Both fits appear to approximate the numerical solutions well close to the origin in Figures 5.5b and 5.5e, corresponding to the interval $[0, 0.1]$, with the Taylor polynomial fit showing a slight deviation from the s profile closer to $r = 0.1$. It is clear that both the Taylor and independent polynomial fits fail to capture the behaviour of the numerical solution s in the interval $[0, 0.5]$ in Figures 5.5c and 5.5f.

This investigation highlights the practicality of the series expansions in (5.80) and (5.81). Series expansions can be an effective tool for approximating complicated functions, providing insight into their local behaviour. We note that the series expansions are valid in some interval $[0, R_c]$, where R_c is the smaller of the two radii of convergence of the Taylor series, though we lack an analytical expression for R_c . Our investigations

Chapter 5. The Ferronematic Radial Hedgehog Solution

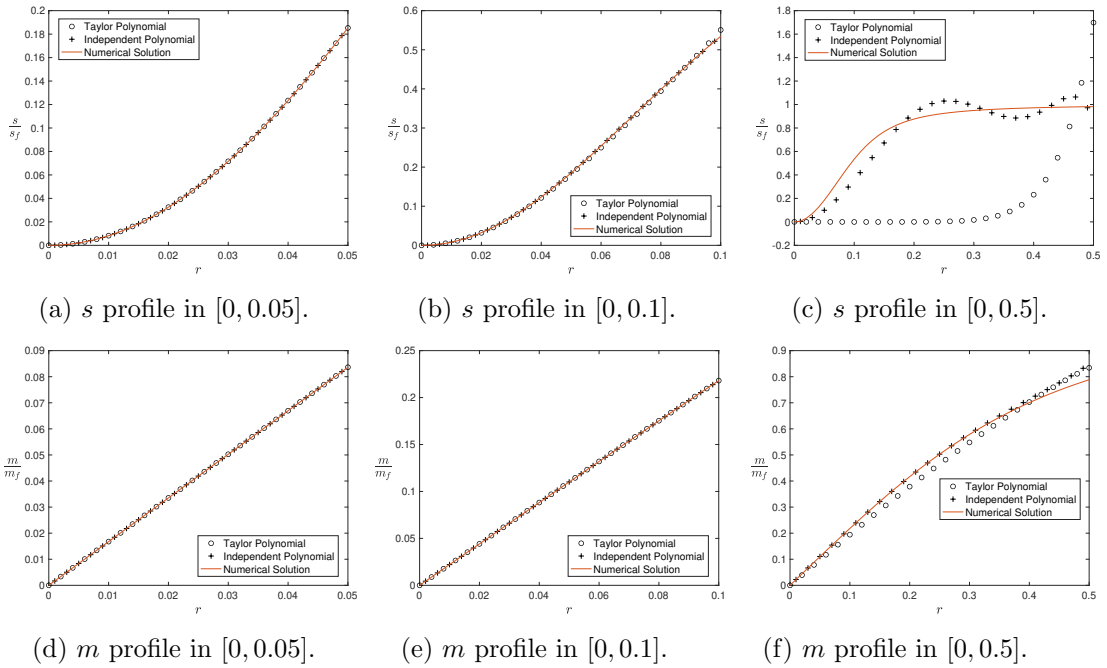


Figure 5.5: Examples of the Taylor and independent polynomial fits against the numerically computed profiles in the intervals in which they were computed, each with $c = 0.1$, $t = -60$, and $\ell = 0.1$. Solid lines correspond to the numerical solution; circles denote the Taylor polynomial; and crosses denote the independent polynomial. Plots (a)-(c) are s profiles and their fits, and plots (d)-(f) are the corresponding m profiles and fits.

suggest that the series can be useful up to distances of the order of 0.1 from the origin; and in scenarios which model small droplets at high temperatures with weak nematic-magnetic coupling. The comparison with the independent polynomial fits highlight that the Taylor polynomial fits in (5.119) and (5.120) are not the optimal polynomial fits, but they can be used in analytical scenarios, while the independent polynomial fits in (5.125) and (5.126) are perhaps more useful in a numerical framework. However, the numerical investigation underscores the effectiveness of the truncated series in approximating numerical solutions in certain scenarios, supporting the validity of the series expansions in (5.80) and (5.81) in capturing the local behavior of s and m near the origin.

5.3 Numerical Results

In Chapter 3, we numerically compute critical points of the Landau–de Gennes free energy in (3.1) with rotational symmetry about the z -axis and mirror symmetry across the xy -plane. The work in Chapter 3 focusses on the pure nematic case, with the fourth- and sixth-order bulk potentials, building upon the work in [67], to investigate the impact of a bulk potential that admits biaxiality as a bulk effect.

In this section, we numerically compute critical points of the ferronematic free energy, again with rotational and mirror symmetry, using analogous methods to those in Chapter 3, to investigate the effects of magnetic coupling on the equilibrium configurations in droplets of ferronematic liquid crystals. In Section 5.3.1, we compute critical points of the ferronematic free energy. We compute the Morse Index of the ferronematic radial hedgehog solution in Section 5.3.2, to understand its stability as a function of temperature, droplet radius and nemato-magnetic coupling strength. In Section 5.3.3, we demonstrate that an unstable radial hedgehog solution may act as a transition state between two stable states via a gradient flow method. We complete our numerical investigation in this chapter by constructing bifurcation diagrams as a function of temperature in Section 5.3.4, for a range of droplet radii and coupling strengths.

5.3.1 Critical Points of the Ferronematic Free Energy

Section 2.3.2 outlines the numerical methods for computing critical points via a finite element method in the nematic case with the fourth-order bulk potential. In the ferronematic case, we again numerically compute critical points with rotational symmetry about the z -axis and mirror symmetry across the xy -plane, and work in cylindrical polar coordinates (r, θ, z) , where $r \in [0, 1]$ and $z \in [0, 1]$, while θ is the angle in the

xy -plane, thus reducing the computational domain to a quarter circle. As such, we work with a \mathbf{Q} -tensor of the form (2.38), and we include a magnetisation vector of the form $\mathbf{M} = [m_1, m_2, m_3]^T$. The ferronematic free energy in (5.1) is then rewritten as

$$\begin{aligned}
 & \mathcal{F}_F[\mathbf{Q}, \mathbf{M}] \\
 &= \int_{B(0,1)} \frac{\ell}{2} \left(q_{1,r}^2 + q_{2,r}^2 + q_{3,r}^2 + q_{1,z}^2 + q_{2,z}^2 + q_{3,z}^2 + \frac{1}{r^2} (4q_2^2 + q_3^2) \right) \\
 & \quad + \frac{t}{2} (q_1^2 + q_2^2 + q_3^2) - q_1^3 + 3q_1q_2^2 - \frac{3}{2}q_1q_3^2 - \frac{3\sqrt{3}}{2}q_2q_3^2 \\
 & \quad + \frac{1}{2} (q_1^4 + q_2^4 + q_3^4 + 2q_1^2q_2^2 + 2q_1^2q_3^2 + 2q_2^2q_3^2) \\
 & \quad + \frac{\ell}{2} (m_{1,r}^2 + m_{2,r}^2 + m_{3,r}^2 + m_{1,z}^2 + m_{2,z}^2 + m_{3,z}^2) \\
 & \quad + \frac{1}{4} (m_1^2 + m_2^2 + m_3^2 - 1)^2 \\
 & \quad - c \left(\left(-\frac{\sqrt{6}}{6}q_1 + \frac{\sqrt{2}}{2}q_2 (\cos^2 \theta - \sin^2 \theta) \right) m_1^2 \right. \\
 & \quad \quad + \left(-\frac{\sqrt{6}}{6}q_1 + \frac{\sqrt{2}}{2}q_2 (\sin^2 \theta - \cos^2 \theta) \right) m_2^2 + \frac{\sqrt{6}}{3}q_1m_3^2 \\
 & \quad \quad + 2 \left(\sqrt{2}q_2m_1m_2 \cos \theta \sin \theta \right. \\
 & \quad \quad \quad \left. \left. + \frac{\sqrt{2}}{2}q_3m_1m_3 \cos \theta + \frac{\sqrt{2}}{2}q_3m_2m_3 \sin \theta \right) \right) dV,
 \end{aligned} \tag{5.130}$$

Chapter 5. The Ferronematic Radial Hedgehog Solution

with associated weak formulations

$$\begin{aligned}
 F_{6,1} &= 4\pi \int_0^1 \int_0^{\sqrt{1-z^2}} \ell \nabla q_1 \cdot \nabla v_1 \\
 &\quad + \left(tq_1 - 3q_1^2 + 3q_2^2 - \frac{3}{2}q_3^2 + 2q_1^3 + 2q_1q_2^2 \right. \\
 &\quad \left. + 2q_1q_3^2 + \frac{\sqrt{6}}{6}c(m_1^2 + m_2^2 - 2m_3^2) \right) v_1 r \, dr dz, \\
 F_{6,2} &= 4\pi \int_0^1 \int_0^{\sqrt{1-z^2}} \ell \nabla q_2 \cdot \nabla v_2 \\
 &\quad + \left(\frac{4\ell}{r^2}q_2 + tq_2 + 6q_1q_2 \right. \\
 &\quad \left. - \frac{3\sqrt{3}}{2}q_3^2 + 2q_2^3 + 2q_1^2q_2 + 2q_2q_3^2 \right) v_2 r \, dr dz, \\
 F_{6,3} &= 4\pi \int_0^1 \int_0^{\sqrt{1-z^2}} \ell \nabla q_3 \cdot \nabla v_3 \\
 &\quad + \left(\frac{\ell}{r^2}q_3 + tq_3 - 3q_1q_3 \right. \\
 &\quad \left. - 3\sqrt{2}q_2q_3 + 2q_3^3 + 2q_1^2q_3 + 2q_2^2q_3 \right) v_3 r \, dr dz, \\
 F_{6,4} &= 4\pi \int_0^1 \int_0^{\sqrt{1-z^2}} \ell \nabla m_1 \cdot \nabla v_4 \\
 &\quad + \left(m_1^3 + m_1m_2^2 + m_1m_3^2 - m_1 + \frac{\sqrt{6}}{3}cq_1m_2 \right) v_4 r \, dr dz, \\
 F_{6,5} &= 4\pi \int_0^1 \int_0^{\sqrt{1-z^2}} \ell \nabla m_2 \cdot \nabla v_5 \\
 &\quad + \left(m_2^3 + m_1^2m_3 + m_2m_3^2 - m_2 + \frac{\sqrt{6}}{3}cq_1m_2 \right) v_5 r \, dr dz, \\
 F_{6,6} &= 4\pi \int_0^1 \int_0^{\sqrt{1-z^2}} \ell \nabla m_3 \cdot \nabla v_6 \\
 &\quad + \left(m_3^3 + m_1^2m_3 + m_2^2m_3 - m_3 - \frac{2\sqrt{6}}{3}cq_1m_3 \right) v_6 r \, dr dz,
 \end{aligned} \tag{5.131}$$

where the functions v_i , for $i = 1, \dots, 6$, are test functions.

Chapter 5. The Ferronematic Radial Hedgehog Solution

The boundary conditions for q_1, q_2 , and q_3 on the edge of the droplet are analogous to those in (2.41) for the nematic case with the fourth-order bulk potential, and are given by

$$q_1 = \frac{\sqrt{6}}{6}(2 - 3r^2)s_f, \quad q_2 = \frac{\sqrt{2}}{2}r^2s_f, \quad q_3 = \sqrt{2}rs_f \quad \text{on } r^2 + z^2 = 1, \quad (5.132)$$

where s_f is the largest positive solution of (5.6). To compute the boundary conditions for m_1, m_2 , and m_3 , we note that we require $\mathbf{M} = m_f \hat{\mathbf{r}}$ on the droplet boundary, where m_f is defined in (5.2). Then we write

$$\mathbf{M} = m_f \hat{\mathbf{r}} = m_f (r\mathbf{e}_r + z\mathbf{e}_z) = m_f [r, 0, z]^T \quad \text{on } r^2 + z^2 = 1, \quad (5.133)$$

Comparing this with $\mathbf{M} = [m_1, m_2, m_3]^T$ results in the boundary conditions

$$m_1 = rm_f, \quad m_2 = 0, \quad m_3 = zm_f \quad \text{on } r^2 + z^2 = 1. \quad (5.134)$$

The conditions on q_1, q_2 , and q_3 on $r = 0$ and $z = 0$ are identical to those in the nematic case, and we include additional boundary conditions for m_1, m_2 , and m_3 . We have

$$q_{1,z} = q_{2,z} = q_3 = m_2 = m_3 = 0 \quad \text{on } z = 0, \quad (5.135)$$

for mirror symmetry across the xy -plane, and

$$q_{1,r} = q_2 = q_{2,r} = q_3 = m_1 = m_2 = 0 \quad \text{on } r = 0, \quad (5.136)$$

for rotational symmetry about the z -axis.

We numerically compute general critical points of the ferronematic free energy by

solving the weak formulations (5.131) with the boundary conditions (5.132)-(5.136).

The radial hedgehog solution and its associated magnetisation vector can be calculated via weak formulations in terms of the scalar order parameter, s , and the scalar associated with the magnetisation vector, m . Just as in the nematic case discussed in Section 2.3.3, we set

$$\mathbf{Q} = s(r) \left(\hat{\mathbf{r}} \otimes \hat{\mathbf{r}} - \frac{1}{3} \mathbf{I} \right), \quad \mathbf{M} = m(r) \hat{\mathbf{r}}, \quad (5.137)$$

where $\hat{\mathbf{r}}$ is the spherical radial unit vector. We convert the above to cylindrical polar coordinates for our numerical framework by setting $\hat{\mathbf{r}} = \frac{r\mathbf{e}_r + z\mathbf{e}_z}{\sqrt{r^2 + z^2}}$, where r and z are as described at the beginning of this section. Then using the form of \mathbf{Q} involving q_1, q_2 , and q_3 in (2.38), and taking $\mathbf{M} = [m_1, m_2, m_3]^T$, we find that the radial hedgehog \mathbf{Q} -tensor and associated magnetisation vector in (5.137) can be described by

$$q_1 = \frac{\sqrt{6}}{2} \left(\frac{z^2}{r^2 + z^2} - \frac{1}{3} \right) s, \quad q_2 = \frac{\sqrt{2}r^2}{2(r^2 + z^2)} s, \quad q_3 = \frac{\sqrt{2}rz}{r^2 + z^2} s, \quad (5.138)$$

and

$$m_1 = \frac{r}{\sqrt{r^2 + z^2}} m, \quad m_2 = 0, \quad m_3 = \frac{z}{\sqrt{r^2 + z^2}}, \quad (5.139)$$

in our numerical framework, noting that (s, m) is a solution of the coupled ODEs (5.21) and (5.23). To solve for critical points of the form (5.137), we substitute (5.138) and (5.139) into the free energy (5.130), and compute weak formulations in terms of s and

m , which are given by

$$\begin{aligned}
 F_{2,1} = 4\pi \int_0^1 \int_0^{\sqrt{1-z^2}} & \left(\ell \nabla s \cdot \nabla w_1 \right. \\
 & + \left(ts - \sqrt{6}s^2 + \frac{4}{3}s^3 + \frac{6\ell s}{r^2 + z^2} \right. \\
 & \quad \left. - \frac{3cm^2}{2(r^2 + z^2)} \left(\left(z^2 - \frac{1}{2}r^2 \right) \left(\frac{z^2}{r^2 + z^2} - \frac{1}{3} \right) \right. \right. \\
 & \quad \left. \left. + \frac{r^4}{2(r^2 + z^2)} + \frac{2r^2 z^2}{r^2 + z^2} \right) \right) w_1 \Big) r \, dr dz, \\
 \\
 F_{2,2} = 4\pi \int_0^1 \int_0^{\sqrt{1-z^2}} & \left(\ell \nabla m \cdot \nabla w_2 \right. \\
 & + \left(\frac{\ell m(r^2 + 1)}{r^2 + z^2} + m^3 - m \right. \\
 & \quad \left. - \frac{2csm}{r^2 + z^2} \left(\left(z^2 - \frac{1}{2}r^2 \right) \left(\frac{z^2}{r^2 + z^2} - \frac{1}{3} \right) \right. \right. \\
 & \quad \left. \left. + \frac{r^4}{2(r^2 + z^2)} + \frac{2r^2 z^2}{r^2 + z^2} \right) \right) w_2 \Big) r \, dr dz,
 \end{aligned} \tag{5.140}$$

where w_1 and w_2 are test functions.

We also consider radial hedgehog configurations without restricting the magnetisation vector to the form $\mathbf{M} = m(r)\hat{\mathbf{r}}$. In this case, we work with q_1, q_2 , and q_3 as in (5.138), and take a more general $\mathbf{M} = [m_1, m_2, m_3]^T$. To solve for critical points of this form, we substitute q_1, q_2 , and q_3 in (5.138) into the free energy (5.130), and compute

Chapter 5. The Ferronematic Radial Hedgehog Solution

weak formulations in terms of s, m_1, m_2 , and m_3 , which take the form

$$\begin{aligned}
 F_{4,1} &= 4\pi \int_0^1 \int_0^{\sqrt{1-z^2}} \left(\ell \nabla s \cdot \nabla u_1 \right. \\
 &\quad \left. + \left(ts - \sqrt{6}s^2 + \frac{4}{3}s^3 + \frac{6\ell s}{r^2+z^2} \right. \right. \\
 &\quad \left. \left. - \frac{3}{2}c \left(\frac{z^2}{r^2+z^2} - \frac{1}{3} \right) \left(m_3^2 - \frac{1}{2}m_1^2 - \frac{1}{2}m_2^2 \right) \right) u_1 \right) r \, dr dz, \\
 F_{4,2} &= 4\pi \int_0^1 \int_0^{\sqrt{1-z^2}} \left(\ell \nabla m_1 \cdot \nabla u_2 \right. \\
 &\quad \left. + \left(m_1^3 + m_1 m_2^2 + m_1 m_3^2 - m_1 \right. \right. \\
 &\quad \left. \left. + c s m_1 \left(\frac{z^2}{r^2+z^2} - \frac{1}{3} \right) \right) u_2 \right) r \, dr dz, \\
 F_{4,3} &= 4\pi \int_0^1 \int_0^{\sqrt{1-z^2}} \left(\ell \nabla m_2 \cdot \nabla u_3 \right. \\
 &\quad \left. + \left(m_2^3 + m_1^2 m_2 + m_2 m_3^2 - m_2 \right. \right. \\
 &\quad \left. \left. + c s m_2 \left(\frac{z^2}{r^2+z^2} - \frac{1}{3} \right) \right) u_3 \right) r \, dr dz, \\
 F_{4,4} &= 4\pi \int_0^1 \int_0^{\sqrt{1-z^2}} \left(\ell \nabla m_3 \cdot \nabla u_4 \right. \\
 &\quad \left. + \left(m_3^3 + m_1^2 m_3 + m_2^2 m_3 - m_3 \right. \right. \\
 &\quad \left. \left. - 2c s m_3 \left(\frac{z^2}{r^2+z^2} - \frac{1}{3} \right) \right) u_4 \right) r \, dr dz,
 \end{aligned} \tag{5.141}$$

where u_1, u_2, u_3 , and u_4 are test functions.

As in the nematic case, we plot the biaxiality parameter,

$$\beta = 1 - 6 \frac{(\text{tr } \mathbf{Q}^3)^2}{(\text{tr } \mathbf{Q}^2)^3}, \tag{5.142}$$

of the numerically computed critical points; and the leading eigenvector of the \mathbf{Q} -tensor, which models the preferred direction of the liquid crystal molecules. In addition, we plot the norm, $|\mathbf{M}| = \sqrt{m_1^2 + m_2^2 + m_3^2}$, and the direction of the associated magnetisation vector. Just as in the nematic case, the sign of the scalar order parameter is an indication of which configuration we have obtained, noting again that this is equivalent to the sign of q_1 at the origin, as discussed in Section 2.3.2. We recall that the radial hedgehog configuration has $q_1(0, 0) = 0$; the split core configuration has $q_1(0, 0) < 0$; and the biaxial torus configuration has $q_1(0, 0) > 0$.

We plot some ferronematic critical points in Figures 5.6, 5.7, and 5.8, noting that the farthest left and farthest right columns correspond to unstable radial hedgehog configurations, while the central left and right columns correspond to stable split core and biaxial torus configurations, respectively.

Let us first consider Figures 5.6a, 5.7a, and 5.8a, which correspond to the radial hedgehog solution, while Figures 5.6e, 5.7e, and 5.8e are the norms of the associated magnetisation vectors. We note that rather than solving the weak formulations (5.131), we solve the weak formulations (5.140) for the radial hedgehog solution and magnetisation vector of the form (5.137). As the radial hedgehog solution is purely uniaxial, Figures 5.6a, 5.7a, and 5.8a are identical. The magnetisation vector profiles in Figures 5.6e, 5.7e, and 5.8e each show the norm of the magnetisation vector increasing in the radial direction, with $m(0) = 0$ and $m(1) = \sqrt{1 + \frac{4}{3}cs_f}$, noting that the value on the edge of the droplet increases with the nematic-magnetic coupling strength, c .

Figures 5.6d, 5.7d, and 5.8d also correspond to the radial hedgehog solution, but with the restriction on the form of \mathbf{M} in (5.137) removed to yield Figures 5.6h, 5.7h and 5.8h, and we obtain these configurations via the weak formulations given in (5.141). The biaxiality parameters and leading eigenvectors are identical to those in Figures 5.6a,

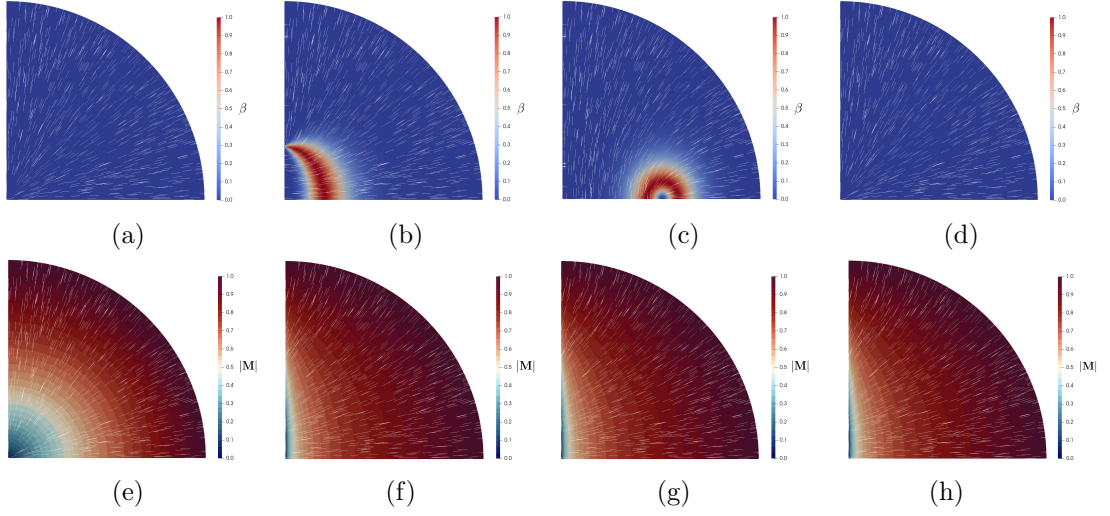


Figure 5.6: Critical points of the ferronematic free energy with $c = 0$, $t = -30$, and $\ell = 0.5$. (a)-(d) Biaxiality parameter, β , and leading eigenvector of the \mathbf{Q} -tensor of the critical point. (a), (d) Radial hedgehog solution with and without radial \mathbf{M} enforced, respectively; and (b) split core and (c) biaxial torus solution without radial \mathbf{M} enforced. (e)-(h) Norm, $|\mathbf{M}|$, and direction of the magnetisation vector associated with critical points of the ferronematic free energy. (e) Radial hedgehog solution with radial \mathbf{M} enforced; and (f) split core, (g) biaxial torus, and (h) radial hedgehog solutions without radial \mathbf{M} enforced. We plot $r \in [0, 1]$ on the horizontal axis and $z \in [0, 1]$ on the vertical axis.

5.7a, and 5.8a. However, the magnetisation vectors in Figures 5.6e, 5.7e, and 5.8e are no longer aligned purely in the radial direction, and lack spherical symmetry. Figure 5.6h is identical to Figures 5.6f and 5.6g, due to the absence of nemato-magnetic coupling, while the behaviour in Figures 5.7h and 5.8h is closer to the magnetisation vectors corresponding to the split core and biaxial torus configurations at the same values of c than those of the more restricted hedgehog configurations in Figures 5.7e and 5.8e. This suggests that the more general form of the magnetisation vector, $\mathbf{M} = [m_1, m_2, m_3]^T$, is the more natural choice, as opposed to imposing the spherically symmetric, radial structure $\mathbf{M} = m(r)\hat{\mathbf{r}}$.

We plot split core configurations in Figures 5.6b, 5.7b, and 5.8b, and their associated magnetisation vectors in Figures 5.6f, 5.7f, and 5.8f, which are obtained via the weak

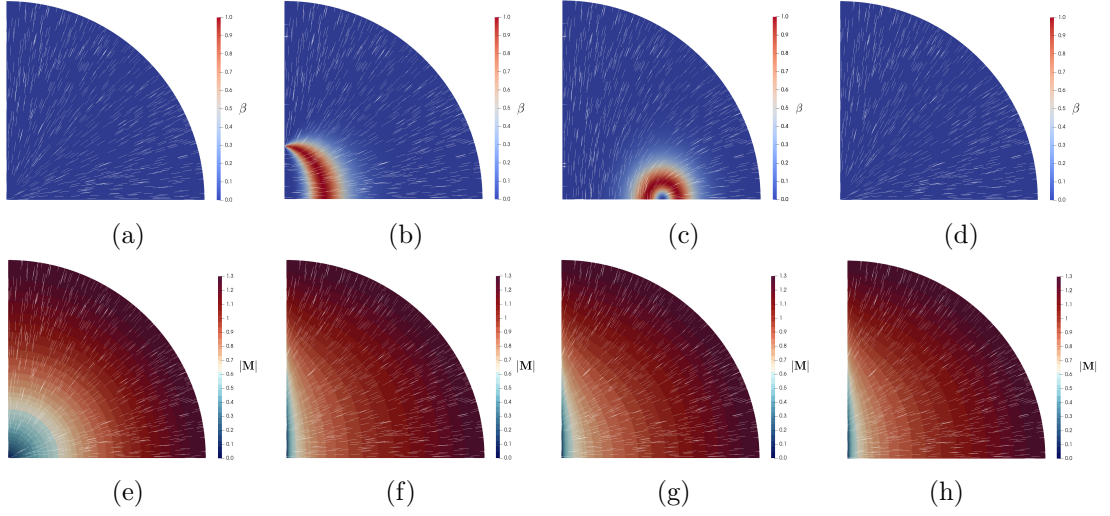


Figure 5.7: Critical points of the ferronematic free energy with $c = 0.1$, $t = -30$, and $\ell = 0.5$. (a)-(d) Biaxiality parameter, β , and leading eigenvector of the \mathbf{Q} -tensor of the critical point. (a), (d) Radial hedgehog solution with and without radial \mathbf{M} enforced, respectively; and (b) split core and (c) biaxial torus solution without radial \mathbf{M} enforced. (e)-(h) Norm, $|\mathbf{M}|$, and direction of the magnetisation vector associated with critical points of the ferronematic free energy. (e) Radial hedgehog solution with radial \mathbf{M} enforced; and (f) split core, (g) biaxial torus, and (h) radial hedgehog solutions without radial \mathbf{M} enforced. We plot $r \in [0, 1]$ on the horizontal axis and $z \in [0, 1]$ on the vertical axis.

formulations given in (5.131). We observe that the regions of biaxiality in each case are almost identical, and that the more pronounced difference across coupling strengths is in the magnetisation vector. The norms of the magnetisation vectors in the $c = 0$ and $c = 0.1$ cases are similar, but we observe a different pattern in the magnetisation vector for $c = 1$, with a region with smaller $|\mathbf{M}|$ near the droplet centre, highlighting a more pronounced effect of the nemato-magnetic coupling on the magnetisation vector than on the liquid crystal defect structure in this example.

The trend across coupling strengths for the biaxial torus configuration is similar to that of the split core configuration. We plot the biaxiality parameter corresponding to the biaxial torus solution in Figures 5.6c, 5.7c, and 5.8c, with the associated magnetisation vectors in Figures 5.6g, 5.7g, and 5.8g, respectively. The regions of biaxiality

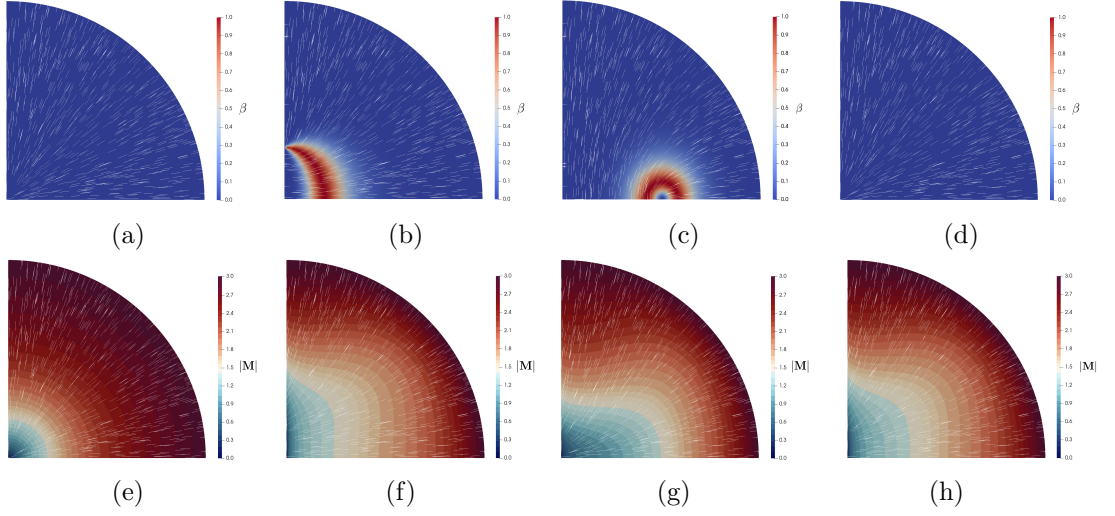


Figure 5.8: Critical points of the ferronematic free energy with $c = 1$, $t = -30$, and $\ell = 0.5$. (a)-(d) Biaxiality parameter, β , and leading eigenvector of the \mathbf{Q} -tensor of the critical point. (a), (d) Radial hedgehog solution with and without radial \mathbf{M} enforced, respectively; and (b) split core and (c) biaxial torus solution without radial \mathbf{M} enforced. (e)-(h) Norm, $|\mathbf{M}|$, and direction of the magnetisation vector associated with critical points of the ferronematic free energy. (e) Radial hedgehog solution with radial \mathbf{M} enforced; and (f) split core, (g) biaxial torus, and (h) radial hedgehog solutions without radial \mathbf{M} enforced. We plot $r \in [0, 1]$ on the horizontal axis and $z \in [0, 1]$ on the vertical axis.

are almost unchanged across values of c ; and the norms of the magnetisation vectors in the $c = 0$ and $c = 0.1$ cases in Figures 5.6g and 5.7g are similar, with a more noticeable difference in the $c = 1$ case in Figure 5.8g.

The observed trends in the split core and biaxial torus configurations across different coupling strengths raise the question of whether magnetisation meaningfully impacts the structure of defects. It is possible that the magnetisation vector simply conforms to accommodate defect structures that are almost identical to those in the pure nematic case, with minimal impact on the liquid crystal configurations. However, we note that here we only consider the a single temperature and droplet size, $t = -30$, $\ell = 0.5$, and that other temperatures and droplet sizes might see more noticeable differences in the structure of defects in comparison to the pure nematic case. Furthermore, if it is

true that magnetisation has minimal influence on the structure of defects, it could still have a stabilising or destabilising effect on certain configurations relative to the pure nematic case.

5.3.2 The Morse Index of the Radial Hedgehog Solution

We use the Morse index to characterise the stability of ferronematic critical points, just as we do in the nematic case in Section 3.4.2. We recall that the concept of the Morse index is introduced in Section 2.3.3, and that index-0 critical points are stable, while higher index critical points are unstable. In this section, we numerically compute the Morse index of the ferronematic radial hedgehog solution across a range of temperatures and droplet radii in three cases: the uncoupled case with $c = 0$; and the coupled cases $c = 0.1$ and $c = 1$. We note that our study is again limited to the class of \mathbf{Q} -tensors with three degrees of freedom. We obtain solutions of the form (5.138) and (5.139) via the weak formulations in (5.141), and compute their Morse indices as critical points of the free energy (5.130).

We tabulate the Morse index of the ferronematic radial hedgehog solution for a range of temperatures and droplet radii in Figures 5.9, 5.10, and 5.11, which correspond to $c = 0$, $c = 0.1$, and $c = 1$, respectively. We do not record the index of the radial hedgehog solution in the case $c = 0$, $t = 2$, since the ferronematic bulk potential does not have any uniaxial critical points with real, positive scalar order parameter, s , above $t = \frac{9}{8}$ in the uncoupled case (see Section 4.1), so the boundary value s_f is undefined in this context.

In all three cases, we observe that the radial hedgehog solution is stable at higher temperatures and in smaller droplets (with larger ℓ). The $c = 0$ and $c = 0.1$ cases are identical, with one exception at $t = -4$, $\ell = 0.001$, where the radial hedgehog solution

Chapter 5. The Ferronematic Radial Hedgehog Solution

	$t = 2$	$t = 0$	$t = -2$	$t = -4$	$t = -6$	$t = -8$	$t = -10$	$t = -15$	$t = -20$	$t = -25$	$t = -30$	$t = -40$	$t = -50$	$t = -60$
$\ell = 0.001$	-	Index-0	Index-0	Index-1	Index-1	Index-1	Index-1	Index-1	Index-1	Index-1	Index-1	Index-1	Index-1	Index-1
$\ell = 0.005$	-	Index-0	Index-0	Index-0	Index-1	Index-1	Index-1	Index-1	Index-1	Index-1	Index-1	Index-1	Index-1	Index-1
$\ell = 0.05$	-	Index-0	Index-0	Index-0	Index-1	Index-1	Index-1	Index-1	Index-1	Index-1	Index-1	Index-1	Index-1	Index-1
$\ell = 0.1$	-	Index-0	Index-0	Index-0	Index-1	Index-1	Index-1	Index-1	Index-1	Index-1	Index-1	Index-1	Index-1	Index-1
$\ell = 0.2$	-	Index-0	Index-0	Index-0	Index-0	Index-1	Index-1	Index-1	Index-1	Index-1	Index-1	Index-1	Index-1	Index-1
$\ell = 0.3$	-	Index-0	Index-0	Index-0	Index-0	Index-0	Index-1							
$\ell = 0.4$	-	Index-0	Index-0	Index-0	Index-0	Index-0	Index-1							
$\ell = 0.5$	-	Index-0	Index-0	Index-0	Index-0	Index-0	Index-0	Index-1						
$\ell = 0.75$	-	Index-0	Index-0	Index-0	Index-0	Index-0	Index-0	Index-0	Index-1	Index-1	Index-1	Index-1	Index-1	Index-1
$\ell = 1$	-	Index-0	Index-0	Index-0	Index-0	Index-0	Index-0	Index-0	Index-1	Index-1	Index-1	Index-1	Index-1	Index-1
$\ell = 1.25$	-	Index-0	Index-0	Index-0	Index-0	Index-0	Index-0	Index-0	Index-0	Index-1	Index-1	Index-1	Index-1	Index-1
$\ell = 1.5$	-	Index-0	Index-0	Index-0	Index-0	Index-0	Index-0	Index-0	Index-0	Index-0	Index-1	Index-1	Index-1	Index-1
$\ell = 1.75$	-	Index-0	Index-0	Index-0	Index-0	Index-0	Index-0	Index-0	Index-0	Index-0	Index-0	Index-1	Index-1	Index-1
$\ell = 2$	-	Index-0	Index-0	Index-0	Index-0	Index-0	Index-0	Index-0	Index-0	Index-0	Index-0	Index-1	Index-1	Index-1

Figure 5.9: The Morse index of the radial hedgehog solution for the given value of t and ℓ as a critical point of the ferronematic free energy in (5.130) with $c = 0$. Each index is assigned a different colour for readability.

	$t = 2$	$t = 0$	$t = -2$	$t = -4$	$t = -6$	$t = -8$	$t = -10$	$t = -15$	$t = -20$	$t = -25$	$t = -30$	$t = -40$	$t = -50$	$t = -60$
$\ell = 0.001$	Index-0	Index-0	Index-0	Index-0	Index-1	Index-1	Index-1	Index-1	Index-1	Index-1	Index-1	Index-1	Index-1	Index-1
$\ell = 0.005$	Index-0	Index-0	Index-0	Index-0	Index-1	Index-1	Index-1	Index-1	Index-1	Index-1	Index-1	Index-1	Index-1	Index-1
$\ell = 0.05$	Index-0	Index-0	Index-0	Index-0	Index-1	Index-1	Index-1	Index-1	Index-1	Index-1	Index-1	Index-1	Index-1	Index-1
$\ell = 0.1$	Index-0	Index-0	Index-0	Index-0	Index-1	Index-1	Index-1	Index-1	Index-1	Index-1	Index-1	Index-1	Index-1	Index-1
$\ell = 0.2$	Index-0	Index-0	Index-0	Index-0	Index-0	Index-1	Index-1	Index-1	Index-1	Index-1	Index-1	Index-1	Index-1	Index-1
$\ell = 0.3$	Index-0	Index-0	Index-0	Index-0	Index-0	Index-0	Index-1							
$\ell = 0.4$	Index-0	Index-0	Index-0	Index-0	Index-0	Index-0	Index-1							
$\ell = 0.5$	Index-0	Index-0	Index-0	Index-0	Index-0	Index-0	Index-0	Index-1						
$\ell = 0.75$	Index-0	Index-0	Index-0	Index-0	Index-0	Index-0	Index-0	Index-0	Index-1	Index-1	Index-1	Index-1	Index-1	Index-1
$\ell = 1$	Index-0	Index-0	Index-0	Index-0	Index-0	Index-0	Index-0	Index-0	Index-1	Index-1	Index-1	Index-1	Index-1	Index-1
$\ell = 1.25$	Index-0	Index-0	Index-0	Index-0	Index-0	Index-0	Index-0	Index-0	Index-0	Index-1	Index-1	Index-1	Index-1	Index-1
$\ell = 1.5$	Index-0	Index-0	Index-0	Index-0	Index-0	Index-0	Index-0	Index-0	Index-0	Index-0	Index-1	Index-1	Index-1	Index-1
$\ell = 1.75$	Index-0	Index-0	Index-0	Index-0	Index-0	Index-0	Index-0	Index-0	Index-0	Index-0	Index-0	Index-1	Index-1	Index-1
$\ell = 2$	Index-0	Index-0	Index-0	Index-0	Index-0	Index-0	Index-0	Index-0	Index-0	Index-0	Index-0	Index-1	Index-1	Index-1

Figure 5.10: The Morse index of the radial hedgehog solution for the given value of t and ℓ as a critical point of the ferronematic free energy in (5.130) with $c = 0.1$. Each index is assigned a different colour for readability.

is an index-1 critical point with $c = 0$, and an index-0 critical point with $c = 0.1$. We observe that the radial hedgehog solution is stable for a larger temperature range and in larger droplets in the $c = 1$ case, suggesting that the nemato-magnetic coupling has a stabilising effect on the radial hedgehog solution. For example, at $t = -8$, the radial hedgehog solution is an index-0 critical point in the $c = 1$ case in Figure 5.11 for all droplet sizes from $\ell = 0.001$ to $\ell = 2$. In contrast, the radial hedgehog solution is an

Chapter 5. The Ferronematic Radial Hedgehog Solution

	$t = 2$	$t = 0$	$t = -2$	$t = -4$	$t = -6$	$t = -8$	$t = -10$	$t = -15$	$t = -20$	$t = -25$	$t = -30$	$t = -40$	$t = -50$	$t = -60$
$\ell = 0.001$	Index-0	Index-0	Index-0	Index-0	Index-0	Index-0	Index-1							
$\ell = 0.005$	Index-0	Index-0	Index-0	Index-0	Index-0	Index-0	Index-1							
$\ell = 0.05$	Index-0	Index-0	Index-0	Index-0	Index-0	Index-0	Index-1							
$\ell = 0.1$	Index-0	Index-0	Index-0	Index-0	Index-0	Index-0	Index-1							
$\ell = 0.2$	Index-0	Index-0	Index-0	Index-0	Index-0	Index-0	Index-1							
$\ell = 0.3$	Index-0	Index-0	Index-0	Index-0	Index-0	Index-0	Index-0	Index-1						
$\ell = 0.4$	Index-0	Index-0	Index-0	Index-0	Index-0	Index-0	Index-0	Index-1						
$\ell = 0.5$	Index-0	Index-0	Index-0	Index-0	Index-0	Index-0	Index-0	Index-1						
$\ell = 0.75$	Index-0	Index-0	Index-0	Index-0	Index-0	Index-0	Index-0	Index-0	Index-1	Index-1	Index-1	Index-1	Index-1	Index-1
$\ell = 1$	Index-0	Index-0	Index-0	Index-0	Index-0	Index-0	Index-0	Index-0	Index-0	Index-1	Index-1	Index-1	Index-1	Index-1
$\ell = 1.25$	Index-0	Index-0	Index-0	Index-0	Index-0	Index-0	Index-0	Index-0	Index-0	Index-0	Index-1	Index-1	Index-1	Index-1
$\ell = 1.5$	Index-0	Index-0	Index-0	Index-0	Index-0	Index-0	Index-0	Index-0	Index-0	Index-0	Index-0	Index-1	Index-1	Index-1
$\ell = 1.75$	Index-0	Index-0	Index-0	Index-0	Index-0	Index-0	Index-0	Index-0	Index-0	Index-0	Index-0	Index-0	Index-1	Index-1
$\ell = 2$	Index-0	Index-0	Index-0	Index-0	Index-0	Index-0	Index-0	Index-0	Index-0	Index-0	Index-0	Index-0	Index-1	Index-1

Figure 5.11: The Morse index of the radial hedgehog solution for the given value of t and ℓ as a critical point of the ferronematic free energy in (5.130) with $c = 1$. Each index is assigned a different colour for readability.

index-1 critical point at $t = -8$ in large droplets described by $\ell = 0.001$ to $\ell = 0.2$ in the $c = 0$ and $c = 0.1$ cases in Figures 5.9 and 5.10. Similarly, for $\ell = 0.1$, the radial hedgehog solution in droplets is an index-0 critical point at temperatures as low as $t = -8$ in the $c = 1$ case; yet it is an index-1 critical point for temperatures from $t = -6$ and below in the $c = 0$ and $c = 0.1$ cases.

5.3.3 The Radial Hedgehog Solution as an Index-1 Transition State

In this section, we attempt to identify scenarios in which the ferronematic radial hedgehog solution is an index-1 saddle point because, just as in the nematic case in Section 3.4.3, such saddle points can be referred to as transition states, playing a role in switching mechanisms between two stable states [116]. Specifically, we investigate whether an index-1 radial hedgehog solution can mediate transitions between stable split core and biaxial torus configurations in the ferronematic case.

We consider example values for t and ℓ in the $c = 0$ and $c = 1$ cases for which the ferronematic radial hedgehog solution is an index-1 critical point of the ferronematic free energy in (5.130). Using a method analogous to that outlined in Section 2.3.4 for

the fourth-order nematic case, we compute a transition pathway between two index-0 ferronematic critical points, through an index-1 radial hedgehog solution, \mathbf{q}^* , where

$$\mathbf{q}^* = [q_1, q_2, q_3, m_1, m_2, m_3]^T, \quad (5.143)$$

where q_1, q_2 , and q_3 are of the form (5.138) and m_1, m_2 , and m_3 are of the form (5.139). We use a gradient flow method, taking small perturbations of the radial hedgehog solution along the direction of the eigenvector associated with the negative eigenvalue of the Hessian as an initial condition, thus solving the initial value problem

$$\begin{aligned} \frac{\partial \mathbf{q}}{\partial \tau} &= -\nabla \mathcal{F}_F(\mathbf{q}, \nabla \mathbf{q}) \quad \text{in } B(0, 1) \text{ for } \tau > 0, \\ \mathbf{q} &= \mathbf{q}_0 = \mathbf{q}^* \pm \lambda \mathbf{u} \quad \text{in } B(0, 1) \text{ at } \tau = 0, \end{aligned} \quad (5.144)$$

with boundary conditions (5.132)-(5.136), where \mathcal{F}_F is the ferronematic free energy (5.130); the quantity λ is a small positive constant; and \mathbf{u} is the unstable eigendirection of the radial hedgehog solution. We refer the reader to Section 2.3.4 for more details on the initial value problem in the fourth-order nematic case, which is analogous to the ferronematic case.

We take $t = -30$, $\ell = 0.5$ with $c = 0$ and $c = 1$ for consistency with Section 5.3.1. We note that an unstable eigendirection of the radial hedgehog solution at the origin in the case $t = -30$, $\ell = 0.5$, and $c = 1$ is given by $\mathbf{u} = [3.08 \times 10^{-2}, 0, 0, 0, 0, 0]^T$, and that a perturbation of the radial hedgehog solution, $\mathbf{q}_0 = \mathbf{q}^* + \lambda \mathbf{u}$, yields the biaxial torus solution, while a perturbation $\mathbf{q}_0 = \mathbf{q}^* - \lambda \mathbf{u}$ yields the split core configuration. This is in agreement with the fact that $q_1 > 0$ at the origin for a biaxial torus solution, and $q_1 < 0$ at the origin for a split core solution. We note that the first term in \mathbf{u} is several orders of magnitude larger than the other terms (which are of the order 10^{-18} or

smaller, so are the numerical equivalent of zero and we write them as such), indicating that the searching direction of our gradient flow method is driven by a perturbation of q_1 .

We show an index-1 radial hedgehog solution connected to index-0 split core and biaxial torus configurations in Figures 5.12a and 5.12b, corresponding to the $c = 0$ and $c = 1$ cases, respectively, with the associated magnetisation vectors given in Figures 5.12c and 5.12d. These examples demonstrate that the radial hedgehog solution can act as a transition state between the split core and biaxial torus configurations in both uncoupled and coupled systems for our choice of t and ℓ .

5.3.4 Bifurcation Diagrams

We numerically compute bifurcation diagrams as a function of temperature with the ferronematic free energy, plotted in Figure 5.13, using methods outlined in Section 2.3.5. We plot the value of the scalar order parameter, s , of each configuration at the origin against temperature, recalling that $s(0, 0) = \sqrt{\frac{3}{2}}q_1(0, 0)$, and that all configurations are necessarily uniaxial at the origin in our numerical framework, due to the boundary conditions (5.135) and (5.136). We restrict the associated magnetisation vector to be proportional to the radial unit vector, as described in (5.137), so that we can compare our numerical results in this section with the analytical results in Section 5.2.

Let us first consider the uncoupled cases in Figures 5.13a, 5.13d, 5.13g and 5.13j. We observe the same qualitative behaviour as in the nematic cases in Section 3.4.4, and we again recover the predictions of [67]. To recap: the radial hedgehog solution is the unique global minimiser at high temperatures; the stable biaxial torus solution is the global minimiser at all temperatures at which it is defined; the radial hedgehog solution is locally stable at intermediate temperatures and coexists with the globally

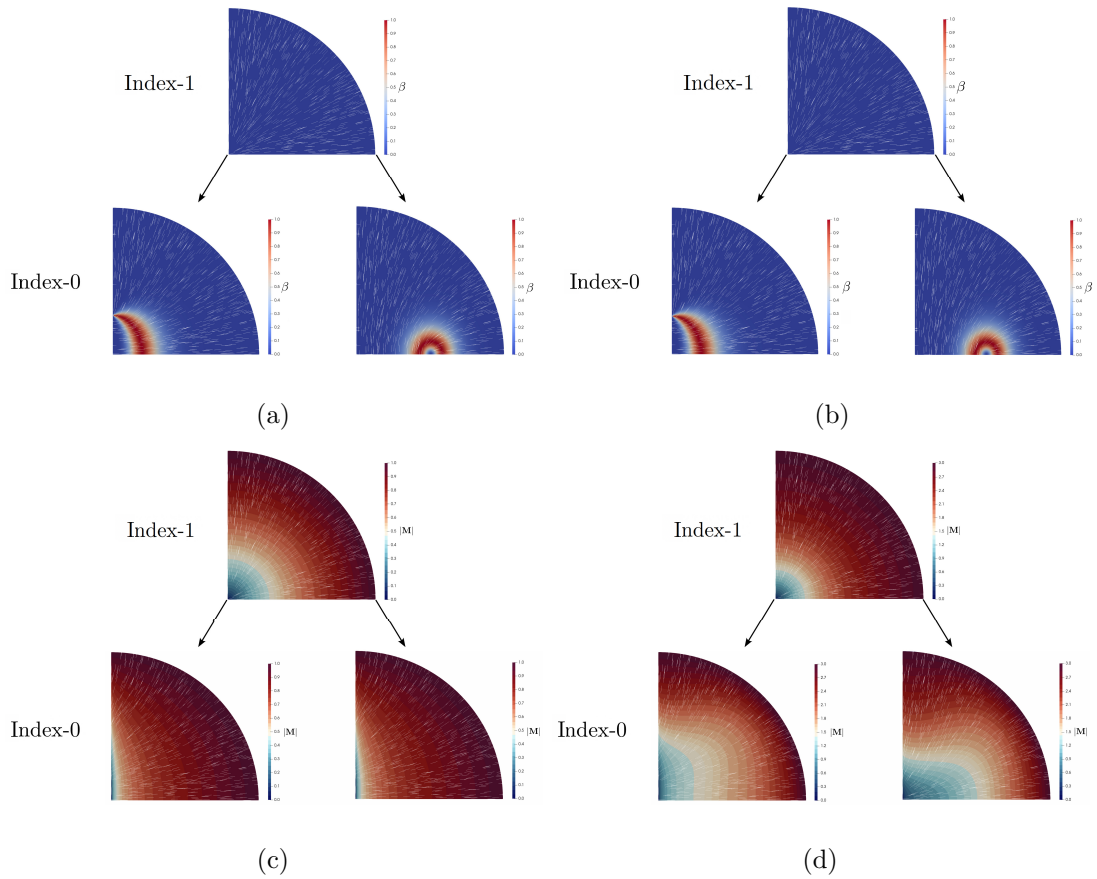


Figure 5.12: The transition pathways between two stable states. Transition between split core and biaxial torus configurations via index-1 radial hedgehog configuration for (a) the ferronematic free energy (5.130) with $c = 0$, $t = -30$, and $\ell = 0.5$, and (b) the ferronematic free energy (5.130) with $c = 1$, $t = -30$, and $\ell = 0.5$. We plot the associated magnetisation vectors in (c) and (d), respectively. We plot $r \in [0, 1]$ on the horizontal axis and $z \in [0, 1]$ on the vertical axis.

minimising and unstable biaxial torus configurations; and the radial hedgehog solution loses stability at sufficiently low temperatures, where the unstable biaxial torus solution vanishes and a locally minimising split core solution emerges. The bifurcation points shift to lower temperatures as droplet size decreases (or ℓ increases). We only plot the radial hedgehog solution up to $t = \frac{9}{8}$ in the $c = 0$ cases because the boundary value, s_f , is complex for $t > \frac{9}{8}$.

The diagrams in the coupled case with $c = 0.1$ are qualitatively similar and are

Chapter 5. The Ferronematic Radial Hedgehog Solution

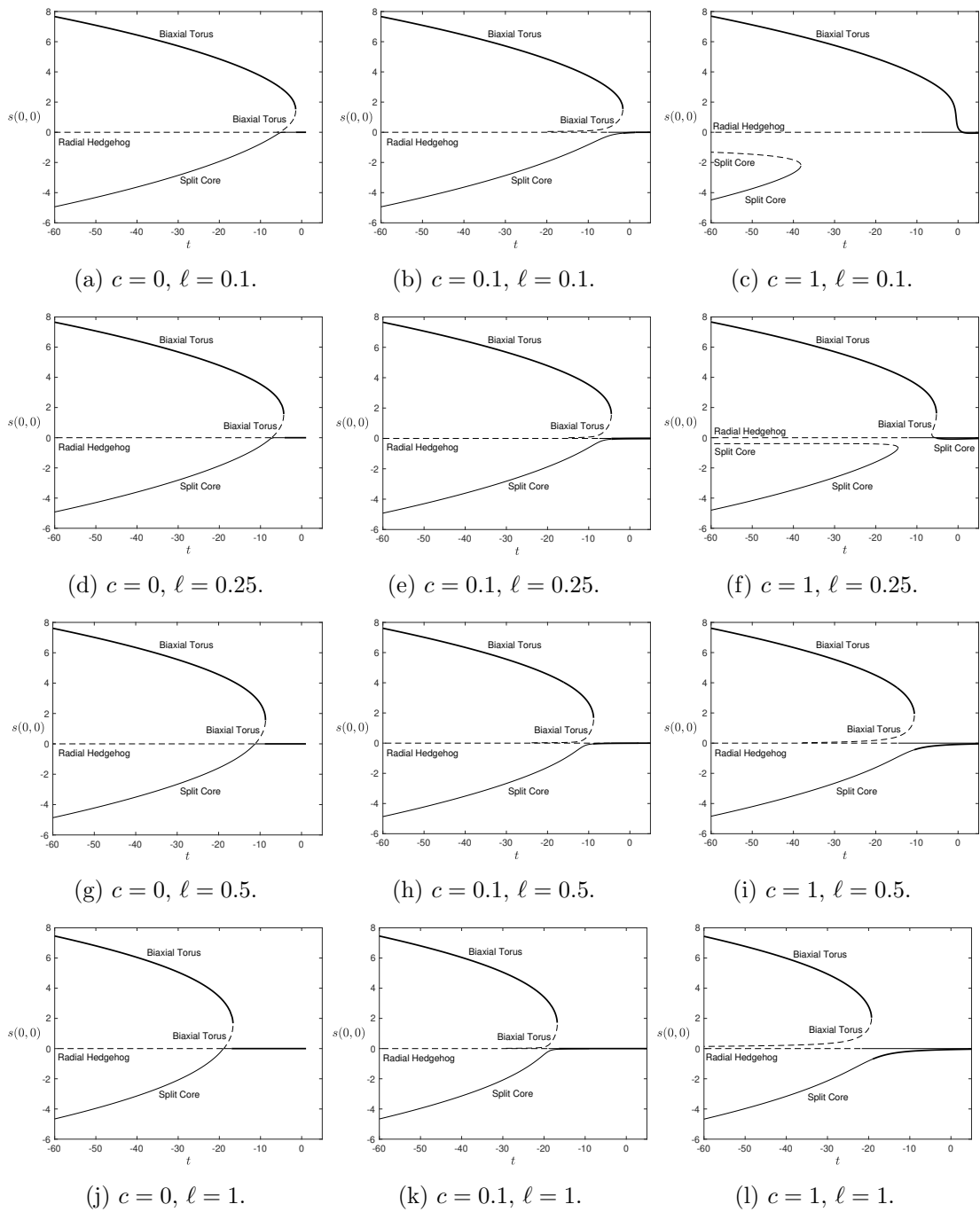


Figure 5.13: Bifurcation diagrams for critical points of the ferronematic free energy (5.130) for a range of values of c and ℓ . We plot the scalar order parameter of each configuration at the origin. Bold solid lines indicate global minimality; thin solid lines indicate local minimality; and dashed lines indicate instability.

given in Figures 5.13b, 5.13e, 5.13h, and 5.13k. We note the following trends. As in the uncoupled case, the radial hedgehog solution is the unique global minimiser at high temperatures and the stable biaxial torus solution is the global minimiser at all temperatures at which it is defined. There is an intermediate temperature range in which locally stable split core and unstable biaxial torus solutions coexist, in contrast to the uncoupled case, with the split core solution converging to the radial hedgehog solution as temperature increases and the unstable biaxial torus solution converging to the radial hedgehog solution as temperature decreases. Finally, at low temperatures, there exists the unstable radial hedgehog solution; a locally stable split core solution; and a globally minimising biaxial torus solution, just as in the uncoupled case. The bifurcation points again shift to lower temperatures as droplet radius decreases, or ℓ increases.

We observe certain behaviours that are common to each diagram with strong coupling, described by $c = 1$, and given in Figures 5.13c, 5.13f, 5.13i, and 5.13l. Firstly, the stable biaxial torus configuration is again globally minimising at all temperatures at which it is defined. Secondly, the radial hedgehog solution is never the global minimiser for the temperature range plotted, and there instead exists a globally minimising split core solution.

The qualitative behaviour in the strongly coupled case varies with droplet size. Let us first consider smaller droplets, described by $\ell = 0.5$ and $\ell = 1$ in Figures 5.13i and 5.13l, respectively. We observe that there is an intermediate temperature range in which locally stable split core and unstable biaxial torus solutions coexist, analogously to the $c = 0.1$ case. Furthermore, as in the $c = 0$ and $c = 0.1$ cases, the radial hedgehog solution is unstable at low temperatures; there exists a locally minimising split core solution; and the stable biaxial torus solution is the global minimiser.

Now, let us consider larger droplets in the $c = 1$ case, described by $\ell = 0.1$ and $\ell = 0.25$ in Figures 5.13c and 5.13f, respectively. In both diagrams, there is an intermediate temperature range in which there is no split core solution, and the only configurations present are the globally minimising biaxial torus solution and the locally minimising or unstable radial hedgehog solution. Furthermore, at low temperatures, we observe both locally stable and unstable split core solutions, which coexist with the unstable radial hedgehog and globally minimising biaxial torus solutions. We speculate that the unstable split core solution will converge to the unstable radial hedgehog solution at sufficiently low temperatures. In the $\ell = 0.25$ case in Figure 5.13f, the unstable biaxial torus branch connects to a globally minimising split core branch; while in the $\ell = 0.1$ case in Figure 5.13c, there is no unstable biaxial torus branch.

We present examples of stable and unstable split core configurations at $t = -60$, $\ell = 0.1$, and $c = 1$ in Figure 5.14. We note that the stable solution has a larger region of biaxiality than its unstable counterpart, and that the norms and directions of the associated magnetisation vectors are almost identical.

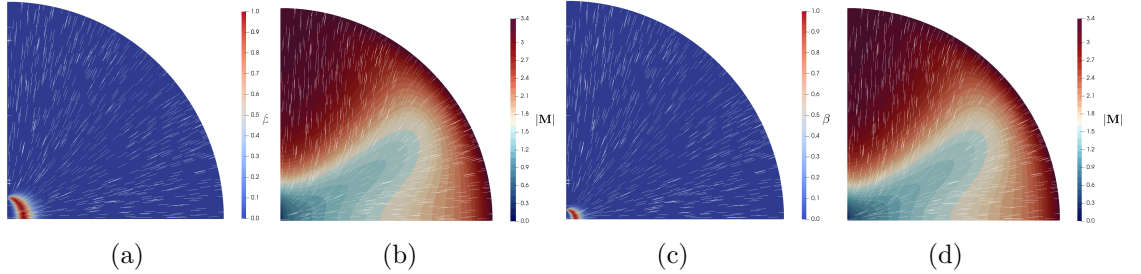


Figure 5.14: Biaxiality parameter, β , and leading eigenvector of \mathbf{Q} -tensor of (a) stable, and (c) unstable split core configurations at $t = -60$ with $c = 1$ and $\ell = 0.1$. Associated norm, $|\mathbf{M}|$, and direction of the magnetisation vector in (b) and (d), respectively. We plot $r \in [0, 1]$ on the horizontal axis and $z \in [0, 1]$ on the vertical axis.

The bifurcation diagrams corresponding to $c = 0.1$ and $c = 1$ with $\ell = 0.1$ in Figures 5.13b and 5.13c are quite qualitatively different, with the unstable biaxial torus and split core configurations each only present in one of the diagrams. We reproduce these

diagrams in Figures 5.15a and 5.15c, respectively, together with a bifurcation diagram with the intermediate coupling strength $c = 0.5$ in Figure 5.15b. The intermediate bifurcation diagram provides some insight into how the stability and existence of solutions evolves as the nemato-magnetic coupling strength, c , changes. Specifically, there is an intermediate temperature range in which a stable split core solution does not exist which grows as c increases; an unstable split core solution emerges at sufficiently low temperatures with higher values of c ; and the unstable biaxial torus solution exists over a smaller temperature range with $c = 0.5$ than with $c = 0.1$, and is inadmissible with $c = 1$. Overall, as c increases, the system evolves from one with an unstable biaxial torus solution at intermediate temperatures and a stable split core at all temperatures plotted to one which lacks a split core solution at intermediate temperatures, but admits an unstable split core solution at sufficiently low temperatures and never admits an unstable biaxial torus solution.

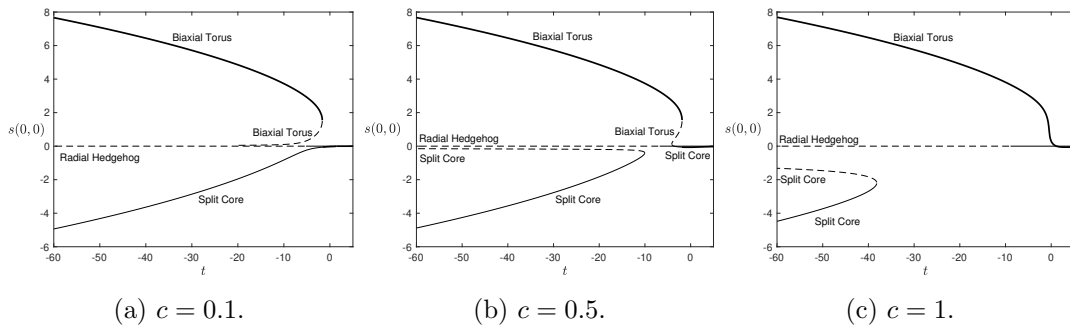


Figure 5.15: Bifurcation diagrams for the ferronematic free energy (5.130) for $c = 0.1$, $c = 0.5$, and $c = 1$, with $\ell = 0.1$. We plot the scalar order parameter of each configuration at the origin. Bold solid lines indicate the global minimiser; thin solid lines indicate local minimality; and dashed lines indicate instability.

The above discussion highlights key differences between the coupled and uncoupled cases. Most significantly, a stable split core solution is typically admissible at higher temperatures in cases with nonzero c , in comparison to the uncoupled case; and in fact the split core solution is the global minimiser at higher temperatures for $c = 1$ with

$\ell = 0.1$ and $\ell = 0.25$. We speculate that this preference for the split core solution at higher temperatures in coupled cases in comparison to the uncoupled case is due to the natural coalignment of the magnetisation vector and the nematic director. We note that the direction of the magnetisation vector is almost parallel to the plane of symmetry near the droplet centre in Figures 5.6f, 5.7f, and 5.8f, and that the same is true of the leading eigenvector associated with the split core solution in Figures 5.6b, 5.7b and 5.8b. The contrary is true of the biaxial torus solution, with the leading eigenvector almost orthogonal to the plane of symmetry in Figures 5.6c, 5.7c, and 5.8c, opposing the preferred direction of the magnetisation vector. It is possible that the agreement in alignment between the leading eigenvector of the split core solution and the magnetisation vector is what leads to the emergence of stable split core configurations at higher temperatures in contrast to the uncoupled cases.

Furthermore, we speculate that the split core solution is perhaps only the global minimiser at high temperatures for $c = 1$ with $\ell = 0.1$ and $\ell = 0.25$ due to the restriction of the form of the magnetisation vector associated with the radial hedgehog solution in (5.11). We note that the direction of the unrestricted magnetisation vector associated with the radial hedgehog solution in Figures 5.6h, 5.7h, and 5.8h is not approximately radially aligned at the droplet centre, suggesting a radially oriented magnetisation vector is not energetically preferable. It is possible that were we to construct bifurcation diagrams without restricting the form of the magnetisation vector associated with the radial hedgehog solution, we might not observe a globally minimising split core solution at high temperatures.

It is notable that the global minimality of the biaxial torus solution at lower temperatures is not lost in the coupled cases we have studied, despite the opposition in alignment between the nematic director and magnetisation vector. Let us consider the

form of the ferronematic free energy in (5.1) for a possible explanation. The only temperature dependence is in the Landau–de Gennes energy density, which captures the preferred nematic liquid crystal behaviour. As temperature decreases, the magnitude of this contribution increases and the nematic behaviour dominates. Therefore, since the biaxial torus solution is the global minimiser in the pure nematic case, it remains so at sufficiently low temperatures in the presence of nemato-magnetic coupling.

In general, the behaviour in all diagrams in Figure 5.13 suggests we may reasonably conclude the radial hedgehog solution will be the unique global minimiser at sufficiently high temperatures for any positive values of c and ℓ , in agreement with Proposition 5.5. Furthermore, we suspect that for any positive values of c and ℓ , there is some sufficiently low temperature below which there are only three configurations: the globally minimising biaxial torus solution; the locally minimising split core solution; and the unstable radial hedgehog solution. Therefore, ferronematic solution landscapes with positive coupling resemble the nematic solution landscapes in Section 3.4.4 at sufficiently high and sufficiently low temperatures, with the key differences in behaviour occurring at intermediate temperatures.

5.4 Summary

In this chapter, we perform some analytical and numerical studies of critical points of a ferronematic free energy (5.1) to investigate the effects of nemato-magnetic coupling on equilibrium configurations in spherical droplets of ferronematic liquid crystals.

In Section 5.2.1, we prove a selection of analytical results for the ferronematic radial hedgehog solution in (5.11), by analogy with certain results for the nematic radial hedgehog solution with the sixth-order bulk potential in Section 3.3, which in turn extend existing results in the literature regarding the nematic radial hedgehog solution with

the fourth-order bulk potential. We prove existence of the ferronematic radial hedgehog solution in (5.11), and a maximum principle for the ferronematic radial hedgehog \mathbf{Q} -tensor and the associated magnetisation vector. Moreover, we prove nonnegativity of the ferronematic radial hedgehog scalar order parameter and uniqueness of the ferronematic radial hedgehog solution in small droplets and at high temperatures. We conclude Section 5.2.1 by proving that, in the small droplet limit, the radial hedgehog scalar order parameter is quadratic, while the associated magnetisation parameter is linear.

We focus our efforts on power series expansions of the ferronematic radial hedgehog scalar order parameter and the associated magnetisation about the droplet centre in (5.11), inspired by Proposition 3.1 in [63] in Section 5.2.2. We prove that the scalar order parameter expansion contains only even powers of r , while the magnetisation parameter expansion contains only odd powers of r . We then explore how well truncations of these series fit numerically computed s and m profiles. We find evidence that suggests that such truncations are best used to approximate local behaviour of the radial hedgehog scalar order parameter and the associated magnetisation parameter about the origin at high temperatures, in small droplets, and in weakly coupled systems.

Section 5.3 contains our numerical results in droplets with rotational and mirror symmetry, and we perform a similar numerical investigation here as is done in Section 3.4. We give examples of ferronematic critical points in Section 5.3.1, again finding radial hedgehog, split core and biaxial torus configurations. We confirm that the ferronematic radial hedgehog solution is stable in small droplets and at high temperatures in Section 5.3.2, and we observe that nemato-magnetic coupling has a stabilising effect on the ferronematic radial hedgehog solution. Furthermore, we confirm that the fer-

ronematic radial hedgehog solution can act as a transition state between stable split core and biaxial torus configurations in Section 5.3.3. Finally, we construct a range of bifurcation diagrams in Section 5.3.4. Our results suggest that the limiting high and low temperature behaviour of the solution landscapes is similar to that in the nematic case, with a unique, globally minimising radial hedgehog solution at sufficiently high temperatures; and a globally minimising biaxial torus solution, a locally minimising split core solution, and an unstable radial hedgehog solution at sufficiently low temperatures. The uniqueness of the radial hedgehog solution at high temperatures is in agreement with Proposition 5.5 in Section 5.2, and we speculate that the ferronematic solution landscape agrees with its nematic counterpart at low temperatures as the Landau–de Gennes contribution to the ferronematic free energy in (5.1) increases in magnitude as temperature decreases, meaning the nematic behaviour dominates at low temperatures. We do observe some interesting contrasting behaviour to the nematic case at intermediate temperatures, however. We see the emergence of an unstable split core solution in certain parameter regimes, which is absent in the nematic case; and the split core solution is globally stable at higher temperatures, which we suspect can be attributed to the natural coalignment of the magnetisation vector and the nematic director associated with the split core configuration.

We note that the critical points in this chapter again only exploit three of the five degrees of freedom. An interesting question is whether there exist any new biaxial critical points induced by nemato-magnetic coupling without the imposed mirror and rotational symmetry. The existence of such critical points could have important implications in applications, as it is possible that the ferronematic solution landscape with five degrees of freedom is richer than the corresponding pure nematic solution landscape. If transition pathways between stable states can be identified, it might be

Chapter 5. The Ferronematic Radial Hedgehog Solution

possible to apply magnetic fields to guide switching between stable states with more precision than in the nematic case.

Chapter 6

Stochastic Effects on Deterministic Solutions

The purpose of this chapter is to consider the effects of random noise on radial hedgehog scalar order parameter profiles in the nematic and ferronematic cases, which we have studied in a deterministic context in Chapters 3 and 5. We incorporate random noise via the inclusion of an additional stochastic term in the relevant gradient flow equations. This term simulates random fluctuations throughout the material, which can arise due to material imperfections or thermal fluctuations, or as a result of the inherent uncertainties and variabilities present in experimental conditions. In this work, we model the effects of random perturbations on the stability of fixed point in nematic and ferronematic systems.

We generate noise via a Q -Wiener stochastic process [106]. It is reasonable to expect that the alignment of liquid crystal molecules at one point typically influences the alignment of nearby molecules, and a Q -Wiener process is well suited to modelling uncertainties in a liquid crystalline system as uncertainties are correlated, by design. A Q -Wiener process is comparable to coloured noise, which has spatial correlation,

unlike white noise, which is uniform throughout space and can be modelled via a simpler Wiener process. A Wiener process uses standard Brownian motion [106], which is a stochastic process characterised by independent increments that are normally distributed; and exhibits randomness in space and time with uncorrelated increments. A Q -Wiener process extends the concept of a Wiener process in that it also employs Brownian motion, and introduces spatial correlation through some covariance operator, Q , so that the increments of the process at different spatial points are correlated. We refer the reader to [106] for a formal definition of a Q -Wiener process.

In this chapter, we work with additive noise in nematic and ferronematic systems, which does not depend on the unknown variables we are solving for (s in the nematic cases, and (s, m) in the ferronematic case). We observe that random noise in this framework has the greatest impact on the radial hedgehog solution in large droplets and at higher temperatures, and we find that the effects on small droplets and at low temperatures are unremarkable. We do, however, observe that random noise breaks the perfect rotational symmetry of the radial hedgehog solution in every case. We clarify that as we solve for the radial hedgehog scalar order and magnetisation parameters in this chapter, the preferred direction of the liquid crystal molecules and the direction of the magnetisation vector are fixed. As such, we do not perturb the preferred orientation of the liquid crystal molecules nor the direction of the magnetisation, and therefore, symmetry is lost in the degree of ordering and the magnitude of the magnetisation vector throughout the droplet, but the inclusion of additive noise does not influence the preferred direction of liquid crystal molecule orientation or the direction of the associated magnetisation vector.

Although we observe some more notable differences between deterministic and stochastic solutions in large droplets and at higher temperatures, and perfect rota-

tional symmetry is lost in all cases, we find that, in general, stochastic solutions remain similar to their deterministic counterparts across all scenarios we consider. This confirms the robustness of the deterministic models employed in Chapters 3 and 5.

This chapter is organised as follows. In Section 6.1, we recall the form of the nematic and ferronematic radial hedgehog solutions, and the associated Euler–Lagrange equations and boundary conditions. In Section 6.2, we outline the numerical methods employed in both the deterministic and stochastic cases. In Section 6.3, we present our results, first in the nematic case, considering both the fourth- and sixth-order bulk potentials; and then in the ferronematic case, where we consider three different values of c : $c = 0$, $c = 0.1$, and $c = 1$, which correspond to the uncoupled case, a weakly coupled case, and a strongly coupled case, respectively. Finally, we summarise our findings in Section 6.4.

6.1 Problem Formulation

In this chapter, we consider droplets of nematic and ferronematic liquid crystals. We revisit the Landau–de Gennes free energy

$$\begin{aligned} \mathcal{F}[\mathbf{Q}] = \int_{B(0,1)} & \frac{\varepsilon^2}{2} |\nabla \mathbf{Q}|^2 + \frac{t}{2} \operatorname{tr} \mathbf{Q}^2 - \sqrt{6} \operatorname{tr} \mathbf{Q}^3 + \frac{1}{2} (\operatorname{tr} \mathbf{Q}^2)^2 \\ & + \frac{d}{5} \operatorname{tr} \mathbf{Q}^2 \operatorname{tr} \mathbf{Q}^3 + \frac{e}{6} (\operatorname{tr} \mathbf{Q}^2)^3 + \frac{f-e}{6} (\operatorname{tr} \mathbf{Q}^3)^2 \, dV, \end{aligned} \quad (6.1)$$

which we work with in Chapter 3, to which we refer the reader for more details. We work with the fourth-order bulk potential,

$$f_B(\mathbf{Q}) = \frac{t}{2} \operatorname{tr} \mathbf{Q}^2 - \sqrt{6} \operatorname{tr} \mathbf{Q}^3 + \frac{1}{2} (\operatorname{tr} \mathbf{Q}^2)^2, \quad (6.2)$$

setting $d = e = f = 0$ in (6.1); and with the sixth-order bulk potential,

$$f_B(\mathbf{Q}) = \frac{t}{2} \operatorname{tr} \mathbf{Q}^2 - \sqrt{6} \operatorname{tr} \mathbf{Q}^3 + \frac{1}{2} (\operatorname{tr} \mathbf{Q}^2)^2 + \frac{d}{5} \operatorname{tr} \mathbf{Q}^2 \operatorname{tr} \mathbf{Q}^3 + \frac{e}{6} (\operatorname{tr} \mathbf{Q}^2)^3 + \frac{f-e}{6} (\operatorname{tr} \mathbf{Q}^3)^2, \quad (6.3)$$

in the case $d = 1$, $e = 0$, and $f = 1$. We recall that we impose strong homeotropic anchoring on the droplet boundary via the Dirichlet condition

$$\mathbf{Q}_{s_+} = s_+ \left(\hat{\mathbf{r}} \otimes \hat{\mathbf{r}} - \frac{1}{3} \mathbf{I} \right), \quad \text{on } \partial B(0, 1), \quad (6.4)$$

where $\hat{\mathbf{r}}$ is the unit vector in the radial direction, and s_+ is the largest positive minimiser of the function

$$g(s) = \frac{t}{3} s^2 - \frac{2\sqrt{6}}{9} s^3 + \frac{2}{9} s^4 + \frac{4d}{135} s^5 + \frac{4e}{81} s^6 + \frac{(f-e)}{6} s^6, \quad (6.5)$$

in both the fourth- and sixth-order bulk potential cases. We recall that the nematic radial hedgehog solution is of the form

$$\mathbf{Q}^*(\mathbf{r}) = s^*(r) \left(\hat{\mathbf{r}} \otimes \hat{\mathbf{r}} - \frac{1}{3} \mathbf{I} \right), \quad (6.6)$$

where s^* is a solution of the ordinary differential equation

$$\varepsilon^2 \left(\frac{d^2 s}{dr^2} + \frac{2}{r} \frac{ds}{dr} - \frac{6}{r^2} s \right) = ts - \sqrt{6} s^2 + \frac{4}{3} s^3 + \frac{2d}{9} s^4 + \frac{4e}{9} s^5 + \frac{2(f-e)}{27} s^5, \quad (6.7)$$

subject to the boundary conditions

$$s(0) = 0, \quad s(1) = s_+. \quad (6.8)$$

We also work again with the ferronematic free energy in this chapter, which is given by

$$\begin{aligned} \mathcal{F}_F[\mathbf{Q}, \mathbf{M}] = \int_{B(0,1)} & \frac{\ell}{2} |\nabla \mathbf{Q}|^2 + \frac{\hat{t}}{2} \operatorname{tr} \mathbf{Q}^2 - \sqrt{6} \operatorname{tr} \mathbf{Q}^3 + \frac{1}{2} (\operatorname{tr} \mathbf{Q}^2)^2 \\ & + \frac{\ell}{2} |\nabla \mathbf{M}|^2 + \frac{1}{4} (|\mathbf{M}|^2 - 1)^2 - c \mathbf{Q} \mathbf{M} \cdot \mathbf{M} \, dV, \end{aligned} \quad (6.9)$$

and we denote the reduced temperature by \hat{t} in this chapter to highlight the fact that the reduced temperature has a slightly different definition in the nematic case compared the ferronematic case, as a result of the choice of nondimensionalisation. We refer the reader to the definitions of the dimensionless parameters in each free energy in Section 2.2. Strong homeotropic anchoring in the ferronematic case is imposed via the Dirichlet boundary conditions

$$\mathbf{Q}_{s_f} = s_f \left(\hat{\mathbf{r}} \otimes \hat{\mathbf{r}} - \frac{1}{3} \mathbf{I} \right), \quad \mathbf{M}_{s_f} = m_f \hat{\mathbf{r}} = \sqrt{1 + \frac{4}{3} c s_f} \hat{\mathbf{r}} \quad \text{on } \partial B(0, 1), \quad (6.10)$$

where s_f is the largest positive root of the function

$$h(s) = s^3 - \frac{3\sqrt{6}}{4} s^2 + \left(\frac{3\hat{t}}{4} - c^2 \right) s - \frac{3c}{4} = 0. \quad (6.11)$$

The ferronematic radial hedgehog solution is of the form

$$\mathbf{Q}^* = s^*(r) \left(\hat{\mathbf{r}} \otimes \hat{\mathbf{r}} - \frac{1}{3} \mathbf{I} \right), \quad \mathbf{M}^* = m^*(r) \hat{\mathbf{r}}, \quad (6.12)$$

where s^* and m^* are solutions of the ordinary differential equations

$$\ell \left(\frac{d^2 s}{dr^2} + \frac{2}{r} \frac{ds}{dr} - \frac{6}{r^2} s \right) = \hat{t}s - \sqrt{6}s^2 + \frac{4}{3}s^3 - cm^2, \quad (6.13)$$

$$\ell \left(\frac{d^2 m}{dr^2} + \frac{2}{r} \frac{dm}{dr} - \frac{2}{r^2} m \right) = m^3 - m - \frac{4}{3}csm, \quad (6.14)$$

subject to the boundary conditions

$$s(0) = m(0) = 0, \quad s(1) = s_f, \quad m(1) = m_f. \quad (6.15)$$

6.2 Numerical Methods

We follow the strategy set out in [73] and compute deterministic and stochastic radial hedgehog scalar order parameter profiles in the nematic case with the fourth- and sixth-order bulk potentials, and scalar order parameter and magnetisation parameter profiles in the ferronematic case. We use a finite difference method to discretise the relevant differential equations, and implement a fourth-order Runge-Kutta method [127] in MATLAB [125] to obtain solutions. In this Chapter the domain is the unit disc, which we describe using polar coordinates, (r, θ) , where $r \in [0, 1]$ and $\theta \in [0, 2\pi]$. In our numerical framework, we work on a 100×100 grid over the rectangle $[0, 1] \times [0, 2\pi]$. We follow the work in [73], in which the authors solve on a 100×100 grid. It is possible that simulations could be performed on a coarser grid to reduce computational time, showing the same behaviour, but we do not test different meshes in this thesis.

6.2.1 Deterministic Solutions

In this section, we outline the numerical methods implemented to obtain deterministic solutions in the nematic sixth-order bulk potential case, noting that the methods in the

fourth-order bulk potential case simply correspond to the special case $d = e = f = 0$.

We then outline the numerical methods in the ferronematic case.

The Nematic Radial Hedgehog Solution

In the nematic case, we use a fourth-order Runge-Kutta method to numerically solve the gradient flow equation

$$\frac{\partial s}{\partial \tau} = \varepsilon^2 \left(\frac{\partial^2 s}{\partial r^2} + \frac{2}{r} \frac{\partial s}{\partial r} - \frac{6}{r^2} s \right) - \left(ts - \sqrt{6}s^2 + \frac{4}{3}s^3 + \frac{2d}{9}s^4 + \frac{4e}{9}s^5 + \frac{2(f-e)}{27}s^5 \right), \quad (6.16)$$

subject to the boundary conditions (6.8).

We discretise the gradient flow equation above over a uniform, 100×100 grid of points on $[0, 1] \times [0, 2\pi]$, following [73], so that the spatial step size is $k = 1/99$, and solve over some time interval, $[0, T]$. We note that this choice of grid has a finer resolution near the origin, and a coarser resolution near the outer boundary. We argue that this choice of grid is sufficient as more interesting behaviour tends to occur closer to the origin, but it would be interesting to repeat this study on a grid which has a more regular resolution throughout the disc.

We choose a time step size, $\Delta\tau$, that is small enough such that the deterministic numerical simulations converge, but large enough to minimise the computational time. Typically, once a small enough step size is found for convergence, a smaller step size would also lead to convergence to the same solution, but the time taken to reach convergence would be increased. The value of T in the deterministic case is not predetermined and is simply equal to $N_t \Delta\tau$, where N_t is the number of iterations required for convergence, the criteria for which we define later in this section. We find that the

time step size, $\Delta\tau = 2 \times 10^{-5}$, as used in [73], is sufficient, except in the small droplet cases. It is possible that a larger step size may also lead to convergence but we do not investigate whether that is the case in this thesis. We find that a significantly smaller step size is required for convergence in small droplets, and we find a suitable step size, $\Delta\tau = 1.25 \times 10^{-6}$, through a process of trial and error. We do not claim to find the optimal step size, as we tested step sizes in decreasing increments of 0.5×10^{-7} and select the first step size in this sequence that leads to convergence. We fix the value of T at the beginning of the stochastic simulations based on the number of iterations required for convergence in each deterministic simulations using the same time step size. We set $T = N_t\Delta\tau$ to one significant figure such that N_t is greater than the number of iterations required for convergence in the deterministic simulations. In each case, we work with a random initial guess for s , where the value of s at each grid point is generated via a random selection from the standard normal distribution.

The fourth-order Runge-Kutta method computes the value of s at time $\tau_{n+1} = (n + 1)\Delta\tau$, using the formula [127]

$$s_{n+1} = s_n + \frac{\Delta\tau}{6} (k_1 + 2k_2 + 2k_3 + k_4), \quad (6.17)$$

where s_n is the matrix containing the values of the function s at each grid point at time τ_n ;

$$\begin{aligned} k_1 &= f(\tau_n, s_n), \\ k_2 &= f\left(\tau_n + \frac{\Delta\tau}{2}, s_n + \frac{\Delta\tau}{2}k_1\right), \\ k_3 &= f\left(\tau_n + \frac{\Delta\tau}{2}, s_n + \frac{\Delta\tau}{2}k_2\right), \\ k_4 &= f(\tau_{n+1}, s_n + \Delta\tau k_3); \end{aligned} \quad (6.18)$$

and f is the spatially-discretised version of the right-hand side of the gradient flow

equation (6.16).

We recall that we impose boundary conditions at $r = 0$ and $r = 1$, so that we require $s_n(0, \theta_j) = 0$ and $s_n(1, \theta_j) = s_+$ for $n = 1, \dots, N_t$ and $j = 1, \dots, 100$. Hence, we apply the Runge-Kutta method to the 98×100 grid over the domain $[0 + k, 1 - k] \times [0, 2\pi]$, and at each time step we work with the matrix

$$s_n = \begin{bmatrix} s_n(r_2, \theta_1) & s_n(r_2, \theta_2) & \cdots & s_n(r_2, \theta_{99}) & s_n(r_2, \theta_{100}) \\ s_n(r_3, \theta_1) & s_n(r_3, \theta_2) & \cdots & s_n(r_3, \theta_{99}) & s_n(r_3, \theta_{100}) \\ \vdots & \vdots & \ddots & \vdots & \vdots \\ s_n(r_{98}, \theta_1) & s_n(r_{98}, \theta_2) & \cdots & s_n(r_{98}, \theta_{99}) & s_n(r_{98}, \theta_{100}) \\ s_n(r_{99}, \theta_1) & s_n(r_{99}, \theta_2) & \cdots & s_n(r_{99}, \theta_{99}) & s_n(r_{99}, \theta_{100}) \end{bmatrix}, \quad (6.19)$$

where $n = 1, \dots, N_\tau$, $r_u = u/99$, $\theta_v = (v - 1)2\pi/99$, for $u = 1, \dots, 98$ and $v = 1, \dots, 100$, so that $(s_n)_{i,j} = s_n(r_{i+1}, \theta_j)$ for $i = 1, \dots, 98, j = 1, \dots, 100$.

Let us work with a spatially-discretised version of

$$ts - \sqrt{6}s^2 + \frac{4}{3}s^3 + \frac{2d}{9}s^4 + \frac{4e}{9}s^5 + \frac{2(f-e)}{27}s^5, \quad (6.20)$$

given by

$$(G_n)_{i,j} = t(s_n)_{i,j} - \sqrt{6}(s_n)_{i,j}^2 + \frac{4}{3}(s_n)_{i,j}^3 + \frac{2d}{9}(s_n)_{i,j}^4 + \frac{4e}{9}(s_n)_{i,j}^5 + \frac{2(f-e)}{27}(s_n)_{i,j}^5, \quad (6.21)$$

for $i = 1, \dots, 98, j = 1, \dots, 100$.

Then, implementing the central difference formulae [127], we write, for $j = 1, \dots, 100$

and $n = 1, \dots, N_\tau$,

$$\begin{aligned}
 f(\tau_n, s_n)_{1,j} &= \varepsilon^2 \left(\frac{(s_n)_{2,j} - 2(s_n)_{1,j}}{k^2} + \frac{2}{r_2} \frac{(s_n)_{2,j}}{2k} - \frac{6}{r_2^2} (s_n)_{1,j} \right) - (G_n)_{1,j}, \\
 f(\tau_n, s_n)_{i,j} &= \varepsilon^2 \left(\frac{(s_n)_{i+1,j} - 2(s_n)_{i,j} + (s_n)_{i-1,j}}{k^2} \right. \\
 &\quad \left. + \frac{2}{r_{i+1}} \frac{(s_n)_{i+1,j} - (s_n)_{i-1,j}}{2k} - \frac{6}{r_{i+1}^2} (s_n)_{i,j} \right) - (G_n)_{i,j}, \quad i = 2, \dots, 97, \\
 f(\tau_n, s_n)_{98,j} &= \varepsilon^2 \left(\frac{s_+ - 2(s_n)_{98,j} + (s_n)_{97,j}}{k^2} \right. \\
 &\quad \left. + \frac{2}{r_{99}} \frac{s_+ - (s_n)_{97,j}}{2k} - \frac{6}{r_{99}^2} (s_n)_{98,j} \right) - (G_n)_{98,j}.
 \end{aligned} \tag{6.22}$$

We assume convergence of the deterministic simulations when the norm of the spatially discretised version of $\frac{\partial s}{\partial \tau}$ in (6.16), $f(\tau_n, s_n)$, is less than 10^{-6} , as this is several orders of magnitude smaller than the norm of $\frac{\partial s}{\partial r}$ at an energy maximum, and is sufficient to indicate that we are converging to an energy minimum and terminate the simulations when this threshold is reached.

The Ferronematic Radial Hedgehog Solution

The ferronematic case is analogous to the nematic case. In this case, we again use the fourth-order Runge-Kutta method to numerically solve the coupled gradient flow equations

$$\begin{aligned}
 \frac{\partial s}{\partial \tau} &= \ell \left(\frac{\partial^2 s}{\partial r^2} + \frac{2}{r} \frac{\partial s}{\partial r} - \frac{6}{r^2} s \right) - \left(\hat{t}s - \sqrt{6}s^2 + \frac{4}{3}s^3 - cm^2 \right), \\
 \frac{\partial m}{\partial \tau} &= \ell \left(\frac{\partial^2 m}{\partial r^2} + \frac{2}{r} \frac{\partial m}{\partial r} - \frac{2}{r^2} m \right) - \left(m^3 - m - \frac{4}{3}csm \right),
 \end{aligned} \tag{6.23}$$

subject to the boundary conditions (6.15). The domain and spatial and time step sizes are the same as in the previous section, and we again solve over some time interval

$[0, T]$. Furthermore, in each case, we work with a random initial guess for (s, m) , where the values of s and m at each grid point are generated via random selections from the standard normal distribution.

The fourth-order Runge-Kutta method computes the values of s and m at τ_{n+1} using the formulae

$$\begin{aligned} s_{n+1} &= s_n + \frac{\Delta\tau}{6} (k_{s,1} + 2k_{s,2} + 2k_{s,3} + k_{s,4}), \\ m_{n+1} &= m_n + \frac{\Delta\tau}{6} (k_{m,1} + 2k_{m,2} + 2k_{m,3} + k_{m,4}), \end{aligned} \quad (6.24)$$

where s_n and m_n are matrices containing the values of the functions s and m at each grid point at time τ_n , and

$$\begin{aligned} k_{s,1} &= f_s(\tau_n, s_n, m_n), \\ k_{s,2} &= f_s\left(\tau_n + \frac{\Delta\tau}{2}, s_n + \frac{\Delta\tau}{2}k_{s,1}, m_n + \frac{\Delta\tau}{2}k_{m,1}\right), \\ k_{s,3} &= f_s\left(\tau_n + \frac{\Delta\tau}{2}, s_n + \frac{\Delta\tau}{2}k_{s,2}, m_n + \frac{\Delta\tau}{2}k_{m,2}\right), \\ k_{s,4} &= f_s(\tau_{n+1}, s_n + \Delta\tau k_{s,3}, m_n + \Delta\tau k_{m,3}), \\ k_{m,1} &= f_m(\tau_n, s_n, m_n), \\ k_{m,2} &= f_m\left(\tau_n + \frac{\Delta\tau}{2}, s_n + \frac{\Delta\tau}{2}k_{s,1}, m_n + \frac{\Delta\tau}{2}k_{m,1}\right), \\ k_{m,3} &= f_m\left(\tau_n + \frac{\Delta\tau}{2}, s_n + \frac{\Delta\tau}{2}k_{s,2}, m_n + \frac{\Delta\tau}{2}k_{m,2}\right), \\ k_{m,4} &= f_m(\tau_{n+1}, s_n + \Delta\tau k_{s,3}, m_n + \Delta\tau k_{m,3}). \end{aligned} \quad (6.25)$$

Here, f_s and f_m are the spatially discretised versions of the right-hand side of the first and second equation in (6.23), respectively.

Due to the boundary conditions at $r = 0$ and $r = 1$, we again apply the Runge-Kutta method to the 98×100 grid over the domain $[0 + k, 1 - k] \times [0, 2\pi]$, recalling that

$k = 1/99$, and we again note that it is possible that a coarser grid would be sufficient, but we do not investigate this question in this thesis. Thus, we work with the same matrix s_n as in (6.19) at each time step, and the equivalent matrix for m , given by

$$m_n = \begin{bmatrix} m_n(r_2, \theta_1) & m_n(r_2, \theta_2) & \cdots & m_n(r_2, \theta_{99}) & m_n(r_2, \theta_{100}) \\ m_n(r_3, \theta_1) & m_n(r_3, \theta_2) & \cdots & m_n(r_3, \theta_{99}) & m_n(r_3, \theta_{100}) \\ \vdots & \vdots & \ddots & \vdots & \vdots \\ m_n(r_{98}, \theta_1) & m_n(r_{98}, \theta_2) & \cdots & m_n(r_{98}, \theta_{99}) & m_n(r_{98}, \theta_{100}) \\ m_n(r_{99}, \theta_1) & m_n(r_{99}, \theta_2) & \cdots & m_n(r_{99}, \theta_{99}) & m_n(r_{99}, \theta_{100}) \end{bmatrix}, \quad (6.26)$$

where $n = 1, \dots, N_\tau$, $r_u = u/99$, $\theta_v = (v-1)2\pi/99$, for $u = 1, \dots, 98$ and $v = 1, \dots, 100$, so that $(m_n)_{i,j} = m_n(r_{i+1}, \theta_j)$ for $i = 1, \dots, 98, j = 1, \dots, 100$.

We work with spatially discretised versions of the expressions

$$\hat{t}s - \sqrt{6}s^2 + \frac{4}{3}s^3 - cm^2, \quad \text{and} \quad m^3 - m - \frac{4}{3}csm, \quad (6.27)$$

given by

$$\begin{aligned} (G_{s,n})_{i,j} &= \hat{t}(s_n)_{i,j} - \sqrt{6}(s_n)_{i,j}^2 + \frac{4}{3}(s_n)_{i,j}^3 - c(m_n)_{i,j}^2, \\ (G_{m,n})_{i,j} &= (m_n)_{i,j}^3 - (m_n)_{i,j} - \frac{4}{3}(s_n)_{i,j}(m_n)_{i,j}, \end{aligned} \quad (6.28)$$

for $i = 1, \dots, 98, j = 1, \dots, 100$. Again implementing the central difference formulae [127], the expressions for f_s are analogous to those for f in (6.22), with s_+ replaced by s_f

and G_n replaced by $G_{s,n}$. The expressions for f_m are given by

$$\begin{aligned}
 f_m(\tau_n, s_n, m_n)_{1,j} &= \varepsilon^2 \left(\frac{(m_n)_{2,j} - 2(m_n)_{1,j}}{k^2} + \frac{2}{r_2} \frac{(m_n)_{2,j}}{2k} - \frac{2}{r_2^2} (m_n)_{1,j} \right) - (G_{m,n})_{1,j}, \\
 f_m(\tau_n, s_n, m_n)_{i,j} &= \varepsilon^2 \left(\frac{(m_n)_{i+1,j} - 2(m_n)_{i,j} + (m_n)_{i-1,j}}{k^2} \right. \\
 &\quad \left. + \frac{2}{r_{i+1}} \frac{(m_n)_{i+1,j} - (m_n)_{i-1,j}}{2k} - \frac{2}{r_{i+1}^2} (m_n)_{i,j} \right) - (G_{m,n})_{i,j}, \\
 &\hspace{25em} i = 2, \dots, 97, \\
 f_m(\tau_n, s_n, m_n)_{98,j} &= \varepsilon^2 \left(\frac{1 - 2(m_n)_{98,j} + (m_n)_{97,j}}{k^2} \right. \\
 &\quad \left. + \frac{2}{r_{99}} \frac{1 - (m_n)_{97,j}}{2k} - \frac{2}{r_{99}^2} (m_n)_{98,j} \right) - (G_{m,n})_{98,j}.
 \end{aligned} \tag{6.29}$$

for $j = 1, \dots, 100$ and $n = 1, \dots, N_\tau$.

We assume convergence of the deterministic simulations when the norm of the spatially discretised version of $\left(\frac{\partial s^2}{\partial \tau} + \frac{\partial m^2}{\partial \tau}\right)^{1/2}$, where the partial derivatives are defined in (6.23), or $(f_s(\tau_n, s_n, m_n)^2 + f_m(\tau_n, s_n, m_n)^2)^{1/2}$, is less than 10^{-6} , and terminate the simulations when this threshold is reached.

6.2.2 Stochastic Solutions

We include additive noise in our models by working with a stochastic version of the gradient flow equations in the nematic case in (6.16) and in the ferronematic case in (6.23). The stochastic gradient flow equation in the nematic case is given by [73], [106]

$$\begin{aligned}
 \frac{\partial s}{\partial \tau} &= \varepsilon^2 \left(\frac{\partial^2 s}{\partial r^2} + \frac{2}{r} \frac{\partial s}{\partial r} - \frac{6}{r^2} s \right) \\
 &\quad - \left(ts - \sqrt{6}s^2 + \frac{4}{3}s^3 + \frac{2d}{9}s^4 + \frac{4e}{9}s^5 + \frac{2(f-e)}{27}s^5 \right) + \sigma dW(\tau, \mathbf{x}), \\
 &\hspace{25em} \mathbf{x} \in [0, 1] \times [0, 2\pi], \tag{6.30}
 \end{aligned}$$

subject to the boundary conditions (6.8); and the stochastic gradient flow equations in the ferronematic case are given by

$$\begin{aligned}\frac{\partial s}{\partial \tau} &= \ell \left(\frac{\partial^2 s}{\partial r^2} + \frac{2}{r} \frac{\partial s}{\partial r} - \frac{6}{r^2} s \right) - \left(\hat{t}s - \sqrt{6}s^2 + \frac{4}{3}s^3 - cm^2 \right) + \sigma dW(\tau, \mathbf{x}), \\ \frac{\partial m}{\partial \tau} &= \ell \left(\frac{\partial^2 m}{\partial r^2} + \frac{2}{r} \frac{\partial m}{\partial r} - \frac{2}{r^2} m \right) - \left(m^3 - m - \frac{4}{3} csm \right) + \sigma dW(\tau, \mathbf{x}),\end{aligned}\tag{6.31}$$

$$\mathbf{x} \in [0, 1] \times [0, 2\pi],$$

where, in each case, noise is generated via the Q -Wiener process $W(\tau, \mathbf{x})$ and σ is a parameter included to scale the strength of additive noise.

We give a brief outline of the discrete approximation of $dW(\tau, \mathbf{x})$, following Theorem 10.7 in [106]. We may write a Q -Wiener process, $W(\tau, \mathbf{x})$, as

$$W(\tau, \mathbf{x}) := \sum_{j=1}^{\infty} \sqrt{p_j} \chi_j(\mathbf{x}) B_j(\tau),\tag{6.32}$$

where spatial correlations are incorporated through the eigenvalues, p_j , of the Q -Wiener process and the associated eigenfunctions, χ_j , and we refer the reader to [106] for further details. The B_j terms are independent identically distributed (iid) Brownian motions. A Q -Wiener process can be approximated by a finite sum analogous to that in Example 10.12 in [106] for use in numerical simulations.

In our case, we include additive noise on the 98×100 grid over the domain $\Omega = [0 + k, 1 - k] \times [0, 2\pi]$ to account for the boundary conditions at $r = 0$ and $r = 1$. Then we work with points $\mathbf{x}_{i_1, i_2} = [r_{i_1}, \theta_{i_2}] = [i_1/99, 2\pi(i_2 - 1)/99]$, for $i_1 = 1, \dots, 98$, and $i_2 = 1, \dots, 100$. We suppose that $Q : L^2(\Omega) \rightarrow L^2(\Omega)$ is a bounded linear operator with eigenvalues $p_{j_1, j_2} = e^{-\alpha \gamma_{j_1, j_2}}$, where $\alpha > 0$ controls the decay rate of the noise and $\gamma_{j_1, j_2} = j_1^2 + j_2^2$. The associated eigenfunctions are $\chi_{j_1, j_2}(\mathbf{x}) = \frac{1}{\sqrt{2\pi}} e^{2\pi i j_1 x_1} e^{2\pi i j_2 x_2}$. The

Q -Wiener process is then approximated by the finite sum

$$W^J(t, \mathbf{x}) := \sum_{j_1=-J_1/2+1}^{J_1/2} \sum_{j_2=-J_2/2+1}^{J_2/2} \sqrt{p_{j_1, j_2}} \chi_{j_1, j_2}(\mathbf{x}) B_{j_1, j_2}(\tau), \quad (6.33)$$

where $J_1 = 98$ and $J_2 = 100$ and the B_{j_1, j_2} are iid Brownian motions. We then approximate $dW(\tau, (r_{i_1}, \theta_{i_2}))$ in (6.30) and (6.31) with the difference

$$\Delta W_n^J = W^J(\tau + \Delta\tau, (r_{i_1}, \theta_{i_2})) - W^J(\tau, (r_{i_1}, \theta_{i_2})). \quad (6.34)$$

We compute the above difference using Algorithms 10.5 and 10.6 in [106]. We note that the additive noise will not be a rotationally symmetric Gaussian in coordinate space as a consequence of the choice of grid. However, we argue that it will still provide useful insight into imperfect systems, although it would be interesting to investigate the effects of a spherically symmetric Gaussian.

We again apply the Runge-Kutta method discussed in the previous section to obtain solutions to the stochastic gradient flow equations (6.30) and (6.31). We again take random initial guesses for s in the nematic case, and we compute the value of s at each grid point at the n^{th} time step, τ_n , using the formula

$$s_{n+1} = s_n + \frac{\Delta\tau}{6} (k_1 + 2k_2 + 2k_3 + k_4), \quad (6.35)$$

where in the stochastic case we have

$$\begin{aligned}
 k_1 &= f(\tau_n, s_n) + \sigma \frac{\Delta W_n^J}{\Delta \tau}, \\
 k_2 &= f\left(\tau_n + \frac{\Delta \tau}{2}, s_n + \frac{\Delta \tau}{2} k_1\right) + \sigma \frac{\Delta W_n^J}{\Delta \tau}, \\
 k_3 &= f\left(\tau_n + \frac{\Delta \tau}{2}, s_n + \frac{\Delta \tau}{2} k_2\right) + \sigma \frac{\Delta W_n^J}{\Delta \tau}, \\
 k_4 &= f(\tau_{n+1}, s_n + \Delta \tau k_3) + \sigma \frac{\Delta W_n^J}{\Delta \tau},
 \end{aligned} \tag{6.36}$$

as is done in [73], where f is as described in (6.22).

Analogously, in the ferronematic case, the values of s and m at each grid point are computed using the formulae

$$\begin{aligned}
 s_{n+1} &= s_n + \frac{\Delta \tau}{6} (k_{s,1} + 2k_{s,2} + 2k_{s,3} + k_{s,4}), \\
 m_{n+1} &= m_n + \frac{\Delta \tau}{6} (k_{m,1} + 2k_{m,2} + 2k_{m,3} + k_{m,s}),
 \end{aligned} \tag{6.37}$$

where each $k_{s,i}$ and $k_{m,i}$, $i = 1, \dots, 4$ are as in the deterministic case (6.25), with the addition of $\sigma \frac{\Delta W_n^J}{\Delta \tau}$, as in the stochastic nematic case in (6.36). Just as in the nematic stochastic case, we take random initial guesses for s and m .

The value $\alpha > 0$ in the exponent of the eigenvalues of the Q -Wiener process influences the strength of the spatial variation of the noise. We previously noted that we also include the term σ to scale the strength of the noise in (6.30) and (6.31). To avoid complication, we only vary the strength of the noise through the term α , and set $\sigma = 1$, as is done in [73]. Small values of α ($\alpha < 0.1$) result in larger values for the p_{j_1, j_2} terms away from $j_1 = j_2 = 0$ and signify large spatial variation in strong noise. Conversely, large values of α ($\alpha > 1$) result in smaller values for the p_{j_1, j_2} terms and denote less spatial variation in weak noise. The stochastic solutions we present in the following sections are each the average of 100 independent stochastic simulations.

In [73], the authors discuss the concept of the invariant measure, which essentially indicates that the output of stochastic simulations will approach the same equilibrium state over a sufficiently large time interval [128]. The authors in [73] note that Proposition 4.1 in [129] can be applied to equations of the form (6.30) and (6.31) to guarantee the existence of an invariant measure, which means that there is some equilibrium state to which each stochastic numerical simulation will approach. In practice, we would expect the output of each individual stochastic simulation, if run over a sufficiently large time interval, to exhibit small fluctuations around some such equilibrium state. Furthermore, we would expect the averages of two sets of, say, 100 stochastic simulations, each run over the same sufficiently large time interval, to be almost identical, and at the very least display the same qualitative behaviour. We give an example of this behaviour in the next section, indicating that once the system has reached the equilibrium state, the solution simply exhibits small random fluctuations about this state for long time.

6.3 Numerical Results

6.3.1 The Nematic Radial Hedgehog Solution

Fourth-Order Bulk Potential

In this section, we present a range of results in the nematic case with the fourth-order bulk potential, summarising our investigation into the effects of additive noise on the nematic radial hedgehog solution with the fourth-order bulk potential. The solution profiles presented here and in the following sections are taken from solutions computed on the 100×100 grid corresponding to the disc over $[0, 1] \times [0, 2\pi]$, which are then averaged in the θ -direction. In other words, one simulation is an average over the 100 grid points in the θ -direction. This allows us to better visually examine solutions

for properties such as monotonicity and nonnegativity, but tells us nothing about the symmetry of solutions about the origin.

We plot examples of the scalar order parameter of deterministic radial hedgehog profiles in Figure 6.1, which solve the ODE (6.16) with $d = e = f = 0$, subject to the boundary conditions (6.8), and are obtained via the Runge-Kutta method described in (6.17) and (6.18). Figure 6.1a corresponds to large droplets, with $\varepsilon = 0.1$; Figure 6.1b corresponds to the intermediate droplet size described by $\varepsilon = 1$; while Figure 6.1c corresponds to small droplets given by $\varepsilon = 5$. We obtain solutions for $t = -1$, $t = -10$, and $t = -100$ for each value of ε . As discussed in the preceding section, we assume that we have achieved an equilibrium state through a numerical simulation when the norm of $\frac{\partial s}{\partial \tau}$ is less than 10^{-6} , and terminate the simulation when this condition is satisfied. We use a step size of $\Delta\tau = 2 \times 10^{-5}$ in the simulations with $\varepsilon = 0.1$ and 1 , as discussed in the preceding section. The small droplet case described by $\varepsilon = 5$ is more sensitive to step size and requires a smaller step size for convergence, so we set $\Delta\tau = 1.25 \times 10^{-6}$, as discussed in Section 6.2, in simulations with $\varepsilon = 5$. We find that convergence is achieved in each case in fewer than 100,000 iterations. The key observations are that the degree of nematic ordering throughout the droplet increases as droplet size increases and temperature decreases, and that each profile is nonnegative, monotonic increasing, and bounded above by s_+ , where

$$s_+ = \sqrt{\frac{3}{2} \frac{3 + \sqrt{9 - 8t}}{4}}, \quad (6.38)$$

in the fourth-order case, as required from the analytical results reviewed in Sections 1.5.2 and 3.3.

In Figure 6.2, we present the stochastic counterparts to the deterministic solutions in Figure 6.1, with strong noise described by $\alpha = 0.1$ in (6.30). We use the same step

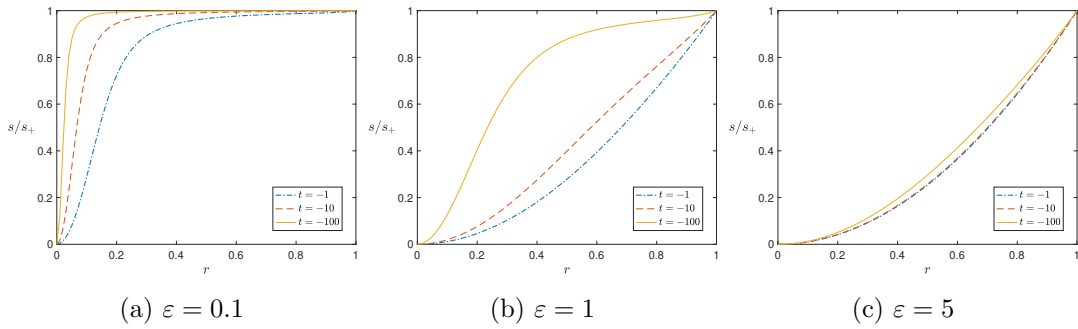


Figure 6.1: Deterministic radial hedgehog scalar order parameter profiles obtained from (6.16) in the fourth-order case with $d = e = f = 0$ in (a) large droplets ($\varepsilon = 0.1$); (b) intermediate droplets ($\varepsilon = 1$); and (c) small droplets ($\varepsilon = 5$). Dashed and dotted blue lines correspond to $t = -1$; dashed orange lines correspond to $t = -10$; and solid yellow lines correspond to $t = -100$.

sizes in the numerical simulations as in the deterministic case: $\Delta\tau = 2 \times 10^{-5}$ when $\varepsilon = 0.1$ and $\varepsilon = 1$; and $\Delta\tau = 1.25 \times 10^{-6}$ when $\varepsilon = 5$. As convergence is reached in fewer than 100,000 iterations in the deterministic cases, we run the stochastic simulations over the time interval $[0, T]$, setting $T = 2$ when $\varepsilon = 0.1$ and $\varepsilon = 1$; and setting $T = 0.2$ when $\varepsilon = 5$. In Figure 6.2, we plot the average of 100 numerical solutions of the stochastic differential equation in (6.30), which is also averaged in the θ -direction, with $d = e = f = 0$, subject to the boundary conditions (6.8). We observe that Figures 6.2b and 6.2c, corresponding to $\varepsilon = 1$ and $\varepsilon = 5$ are indistinguishable from the deterministic equivalents in Figures 6.1b and 6.1c. We observe slight differences between Figures 6.2a and 6.1a in the large droplet case. Interestingly, the value of the scalar order parameter is slightly reduced away from $r = 0$ and $r = 1$ in each case, suggesting that the degree of ordering away from the droplet centre and boundary in large droplets in a more realistic system is more relaxed than that predicted via the deterministic model. The value of the scalar order parameter is also slightly larger than the boundary value s_+ close to $r = 1$ at $t = -1$ in the stochastic case, violating the monotonicity and upper bound predicted by the analytical results discussed in Sections 1.5.2 and 3.3. This

suggests that stochastic effects are most pronounced at higher temperatures, closer to the isotropic-nematic transition temperature, and in larger droplets, where there is more space for liquid crystal molecules to deviate from the predicted configuration. We note, however, that these differences between the deterministic and stochastic cases are small, and that the qualitative behaviour of the stochastic solutions approximates that of the deterministic solutions in each case presented.

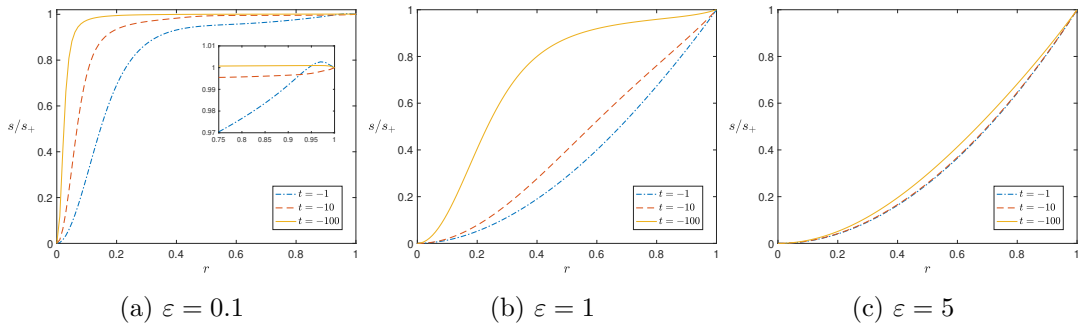


Figure 6.2: Stochastic radial hedgehog scalar order parameter profiles obtained from (6.30) in the fourth-order case with $d = e = f = 0$, strong noise ($\alpha = 0.1$), and in (a) large droplets ($\varepsilon = 0.1$); (b) intermediate droplets ($\varepsilon = 1$); and (c) small droplets ($\varepsilon = 5$). Dashed and dotted blue lines correspond to $t = -1$; dashed orange lines correspond to $t = -10$; and solid yellow lines correspond to $t = -100$.

In Figure 6.3, we plot the average of 100 independent numerical solutions of the stochastic differential equation in (6.30) with $\varepsilon = 0.1$, $t = -1$, and $d = e = f = 0$ at $T = 2$ and $T = 10$. We observe that the solutions are almost identical, suggesting that the system has reached an equilibrium state, in agreement with the existence of an invariant measure [73], as discussed in the preceding section. In other words, in this example, we expect all results of stochastic simulations, run over a sufficiently long time, to exhibit small fluctuations about the same equilibrium state shown in Figure 6.3, and expect the same to be true for different values of t and ε .

We consider the cases $t = -1$, $\varepsilon = 0.1$ and $t = -100$, $\varepsilon = 5$ in Figure 6.4. We plot the deterministic solution of (6.16), together with the average of 100 numerical solutions

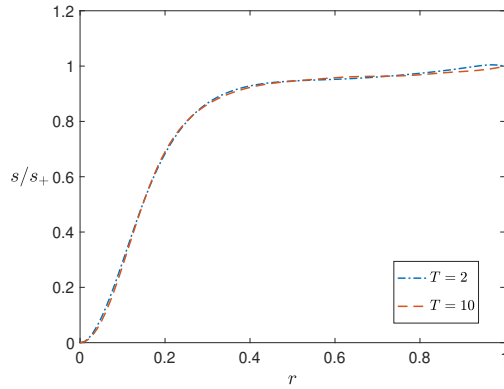


Figure 6.3: The average of 100 numerical solutions of (6.31) with $d = e = f = 0$ and $\alpha = 0.1$ for $t = -1$, $\varepsilon = 0.1$ at (a) $T = 2$, and (b) $T = 10$.

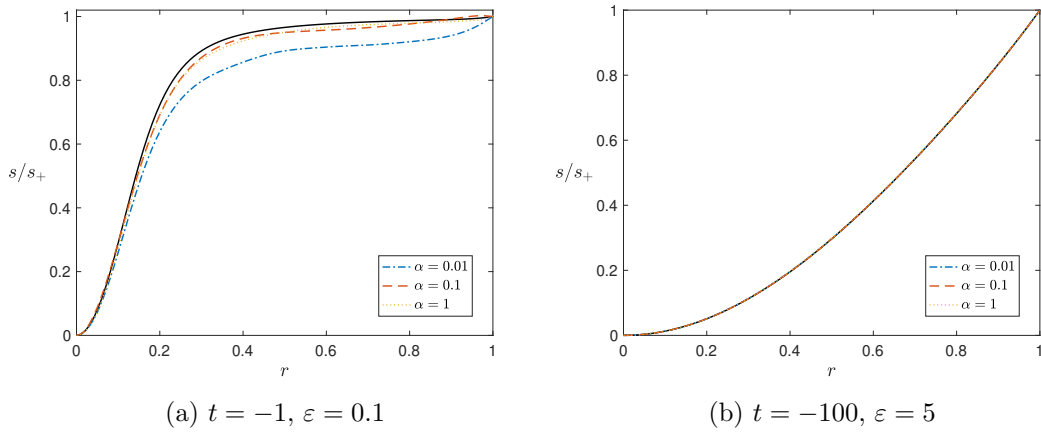


Figure 6.4: Comparison of deterministic and stochastic radial hedgehog scalar order parameter profiles obtained from (6.16) and (6.30) in the fourth-order case with $d = e = f = 0$ with different strengths of noise. Black solid lines correspond to the deterministic profile, while dashed and dotted blue, dashed orange, and dotted yellow lines correspond to stochastic profiles with very strong noise ($\alpha = 0.01$), strong noise ($\alpha = 0.1$), and weak noise ($\alpha = 1$), respectively. We plot profiles for (a) a large droplet at a higher temperature ($t = -1$, $\varepsilon = 0.1$) and (b) a small droplet at a low temperature ($t = -100$, $\varepsilon = 5$).

of (6.30) in the stochastic case, with three different strengths of noise, described by $\alpha = 0.01$, $\alpha = 0.1$, and $\alpha = 1$, recalling that $\alpha = 0.01$ corresponds to strong noise, while $\alpha = 1$ corresponds to weak noise. In the higher temperature, large droplet case in Figure 6.4a, we observe that stronger noise results in a larger deviation from the

deterministic solution, and we reproduce the solution which exceeds s_+ in (6.38). We also see that in each case, the stochastic solution has a lower value for s away from $r = 0$ and $r = 1$, supporting the hypothesis that more realistic systems could be slightly less ordered than the deterministic predictions. Conversely, we observe no noticeable differences between the deterministic and stochastic scalar order parameter profiles in the low temperature and small droplet case in Figure 6.4b, even with strong noise.

The scalar order parameter profiles plotted in Figures 6.1-6.4 are in fact an average of the scalar order parameter throughout the droplet. In Figures 6.5a and 6.5b, we present deterministic and stochastic solutions, respectively, on the disc on which they were computed in the case $t = -1$, $\varepsilon = 0.1$, with $d = e = f = 0$, with strong noise, $\alpha = 0.1$, in the stochastic case. We observe that the solutions are very similar, although the value of s is slightly lower in the bulk of the droplet (denoted by a slightly darker yellow). To better illuminate the differences between the two solutions, we subtract the stochastic solution from the deterministic solution and plot this in Figure 6.5c. The key feature of Figure 6.5c is the lack of symmetry, meaning that the rotational symmetry of the radial hedgehog scalar order parameter is lost in the stochastic case. We omit the plots, but we note that there is a loss of spherical symmetry to some degree for every value of t and ε we have considered. Furthermore, we observe that the difference between the deterministic and stochastic solutions is mostly positive away from the origin and the droplet surface, suggesting the inclusion of additive noise results in a reduction of nematic ordering in the interior of the droplet, although small in this case.

We draw two fundamental conclusions from this numerical investigation in the fourth-order nematic case. Firstly, the inclusion of additive noise can result in the violation of key properties inherent in deterministic solutions at high temperatures and in large droplets, namely: monotonicity, the upper bound, and rotational symmetry;

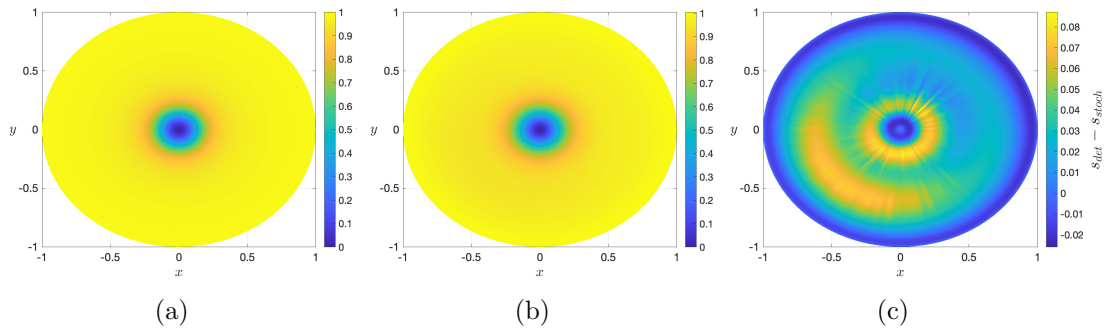


Figure 6.5: Value of s/s_+ throughout the domain (a) in the deterministic case from (6.16); and (b) in the stochastic case with strong noise, $\alpha = 0.1$, from (6.30), each with $t = -1$, $\varepsilon = 0.1$, and $d = e = f = 0$. (c) The difference between the deterministic and stochastic solutions in (a) and (b), respectively.

and additive noise reduces the degree of ordering away from the droplet centre and boundary in such systems. Secondly, and perhaps more importantly, the effects of additive noise are more pronounced in larger droplets and at higher temperatures, but even in the more extreme cases, the qualitative behaviour still approximates that of the corresponding deterministic solutions. Thus, while one might expect some differences in the radial hedgehog scalar order parameter in the deterministic and stochastic cases at high temperatures and in large droplets, our findings support the use of the deterministic model in (6.16) in the fourth-order case as a reliable tool to predict the form of the radial hedgehog solution in general.

Sixth-Order Bulk Potential

In this section, we present results in the nematic case with the sixth-order bulk potential. Analogously to the preceding section, we summarise the effects of the inclusion of additive noise on the nematic radial hedgehog solution with the sixth-order bulk potential.

We first plot examples of deterministic radial hedgehog scalar order parameter profiles in Figure 6.6, which are solutions of the ODE (6.30) with $d = 1$, $e = 0$, and

$f = 1$, subject to the boundary conditions (6.8), and are obtained via the Runge-Kutta method described in (6.17) and (6.18). We plot profiles in droplets with large ($\varepsilon = 0.1$), intermediate ($\varepsilon = 1$), and small ($\varepsilon = 5$) radii in Figures 6.6a, 6.6b, and 6.6c, respectively; and in each plot we include profiles corresponding to the temperatures $t = -1$, $t = -10$, and $t = -100$. We use the same step sizes and convergence criteria as in the fourth-order bulk potential case. The key observations are the same as in the fourth-order case: the degree of ordering throughout the droplet increases with droplet size and decreases with increasing temperature; and each profile is nonnegative, monotonic increasing and bounded above by s_+ . We recall that scalar order parameter profiles which take negative values are admissible in certain parameter regimes with the sixth-order bulk potential (see Proposition 3.4 and Figure 3.6 in Chapter 3), but we consider only nonnegative deterministic solutions here.

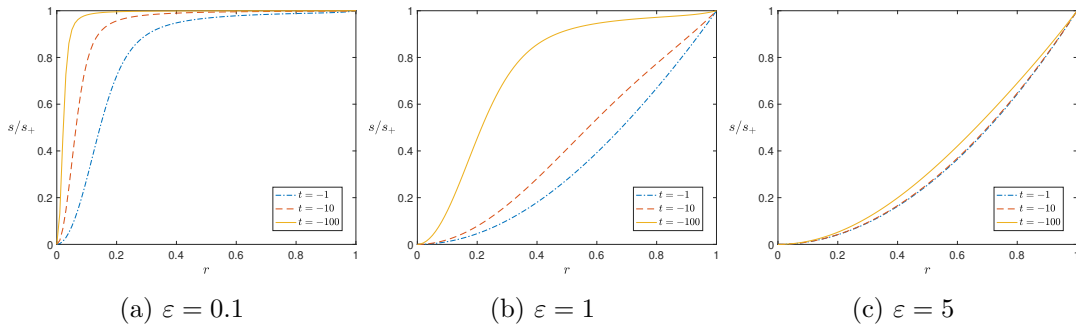


Figure 6.6: Deterministic radial hedgehog scalar order parameter profiles obtained from (6.16) in the sixth-order case with $d = 1$, $e = 0$, and $f = 1$ in (a) large droplets ($\varepsilon = 0.1$); (b) intermediate droplets ($\varepsilon = 1$); and (c) small droplets ($\varepsilon = 5$). Dashed and dotted blue lines correspond to $t = -1$; dashed orange lines correspond to $t = -10$; and solid yellow lines correspond to $t = -100$.

Next, we plot a range of stochastic radial hedgehog scalar order parameter profiles in Figure 6.7 with the same values of ε and t as the deterministic profiles plotted in Figure 6.6. We set $d = 1$, $e = 0$, $f = 1$ and $\alpha = 0.1$ in (6.30) and obtain solutions via the Runge-Kutta method described in (6.35) and (6.36), plotting the average of

100 simulations in each case. We use the same values of $\Delta\tau$ as in the deterministic simulations and solve over the time interval $[0, T]$, setting $T = 4$ when $\varepsilon = 0.1$ and $\varepsilon = 1$; and $T = 0.4$ when $\varepsilon = 5$ since the deterministic simulations converge in fewer than 200,000 iterations. We draw similar conclusions to those in the fourth-order case: the stochastic solutions with $\varepsilon = 1$ and $\varepsilon = 5$ in Figures 6.7b and 6.7c, respectively, are indistinguishable from their deterministic counterparts in Figures 6.2b and 6.2c, so the inclusion of additive noise has little impact.

We observe slight differences in the large droplet case with $\varepsilon = 0.1$ in Figure 6.7a. In the higher temperature case, $t = -1$, the value of the scalar order parameter profile is reduced in the interior of the droplet. At $t = -10$, the value of the scalar order parameter appears to decrease slightly between approximately $r = 0.5$ and $r = 0.8$, so that the profile is not monotonic; and appears to attain values slightly larger than s_+ near the droplet boundary, so that $s(r) > s_+$. Proposition 3.3 in Chapter 3 requires that $s(r) \leq \max\{s_+, |s_-|\}$, $r \in [0, 1]$, where s_- is the negative minimiser of the function g in (6.5) with $t = -10$, $d = 1$, $e = 0$ and $f = 1$. In this case, we note that $s_+ \approx 2.96$, while $s_- \approx -2.55$, meaning that we require $s(r) \leq s_+$, hence the stochastic solution at $t = -10$ in Figure 6.6a violates Proposition 3.3 in Chapter 3. Furthermore, Proposition 3.4 in Chapter 3 defines conditions under which the radial hedgehog scalar order parameter must be monotonic. We find that these conditions are satisfied in the case $t = -10$, $d = 1$, $e = 0$ and $f = 1$, so the stochastic solution at $t = -10$ in Figure 6.7a also violates Proposition 3.4 in Chapter 3.

We find that the qualitative behaviour is close to that of the deterministic scalar order parameter profiles in Figure 6.6a. However, we note that the discrepancies between the deterministic and stochastic solutions appear larger in the sixth-order case compared to the fourth-order case.

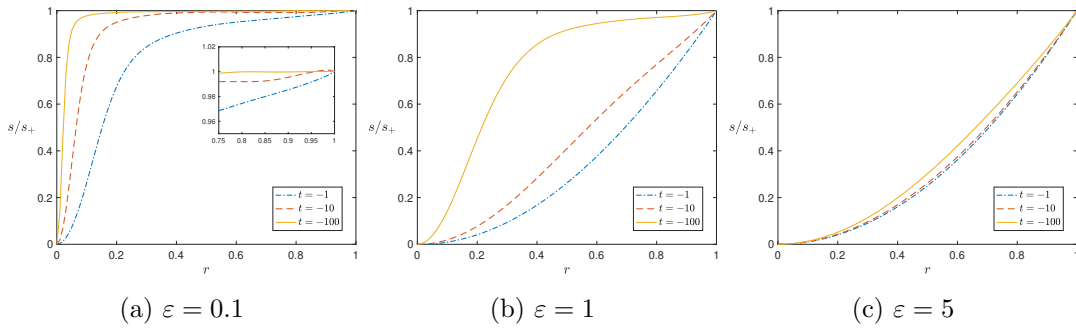


Figure 6.7: Stochastic radial hedgehog scalar order parameter profiles obtained from (6.30) in the sixth-order case with $d = 1$, $e = 0$ and $f = 1$, with strong noise ($\alpha = 0.1$), and in (a) large droplets ($\varepsilon = 0.1$); (b) intermediate droplets ($\varepsilon = 1$); and (c) small droplets ($\varepsilon = 5$). Dashed and dotted blue lines correspond to $t = -1$; dashed orange lines correspond to $t = -10$; and solid yellow lines correspond to $t = -100$.

In Figure 6.8, we consider the specific cases $t = -1$, $\varepsilon = 0.1$ and $t = -100$, $\varepsilon = 5$, again taking $d = 1$, $e = 0$ and $f = 1$, plotting three stochastic solutions with different strengths of noise against the deterministic solution in each plot. Each stochastic solution is the average of 100 simulations, and we consider very strong ($\alpha = 0.01$), strong ($\alpha = 0.1$), and weak ($\alpha = 1$) noise. Figure 6.4b again indicates that the inclusion of additive noise has no discernible impact in small droplets and at low temperatures. In Figure 6.8a, we observe that the additive noise does affect the radial hedgehog scalar order parameter in large droplets and at higher temperatures, with each stochastic profile having lower interior order than the deterministic solution, with stronger noise resulting in a greater deviation from the deterministic radial hedgehog scalar order parameter profile.

Just as in the preceding section, we plot deterministic and stochastic solutions on the disc, and their difference, obtained by subtracting the stochastic solution from the deterministic solution, in Figure 6.9, in the case $t = -1$, $\varepsilon = 0.1$, $d = 1$, $e = 0$, and $f = 1$. The stochastic solution is again the average of 100 simulations with strong noise described by $\alpha = 0.1$. The qualitative deductions are the same as in the fourth-order

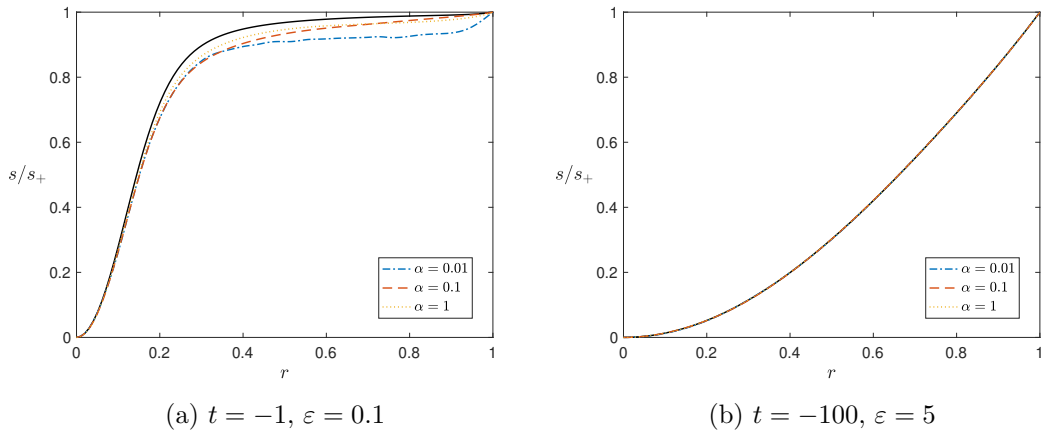


Figure 6.8: Comparison of deterministic and stochastic radial hedgehog scalar order parameter profiles obtained from (6.16) and (6.30) in the sixth-order case with $d = 1, e = 0$ and $f = 1$ with different strengths of noise. Black solid lines correspond to the deterministic profile, while dashed and dotted blue, dashed orange, and dotted yellow lines correspond to stochastic profiles with very strong noise ($\alpha = 0.01$), strong noise ($\alpha = 0.1$), and weak noise ($\alpha = 1$), respectively. We plot profiles for (a) $t = -1, \varepsilon = 0.1$ and (b) $t = -100, \varepsilon = 5$.

case. We note that the lack of symmetry is less clear in Figure 6.9c in comparison to Figure 6.5c, however the difference between the stochastic and deterministic solutions is larger throughout the domain in the sixth-order case, and this might disguise the lack of symmetry.

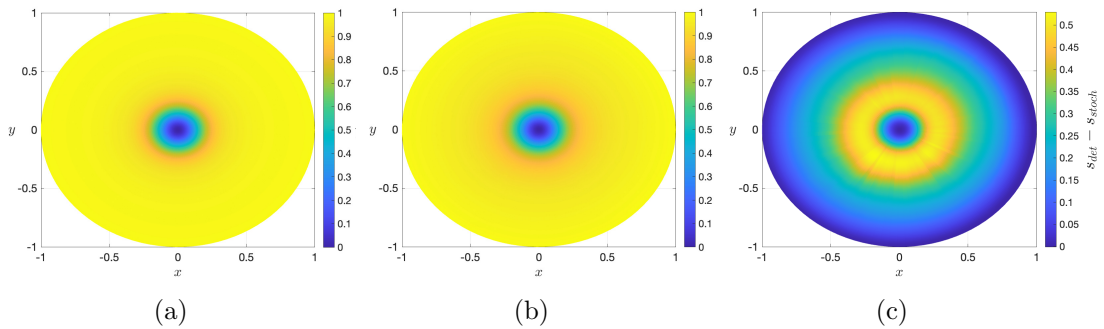


Figure 6.9: Value of s/s_+ throughout the domain (a) in the deterministic case from (6.16); and (b) in the stochastic case with strong noise, $\alpha = 0.1$, from (6.30), each with $t = -1, \varepsilon = 0.1, d = 1, e = 0$ and $f = 1$. (c) The difference between deterministic and stochastic solutions in (a) and (b), respectively.

The key observations in this section are as follows: the inclusion of additive noise

breaks the rotational symmetry; can result in non-monotonic scalar order parameter profiles or profiles which violate the upper bound in large droplets and at higher temperatures; and reduces the interior ordering. A difference between the fourth- and sixth-order cases is that where we do observe discrepancies between the stochastic and deterministic solutions, they are typically more pronounced in the sixth-order case.

6.3.2 The Ferronematic Radial Hedgehog Solution

In the following sections, we plot the same sequence of four sets of plots in the uncoupled case, $c = 0$, a weakly coupled case, $c = 0.1$, and a strongly coupled case, $c = 1$.

We first plot examples of the scalar order parameter of the deterministic radial hedgehog solution and the associated magnetisation profiles, which solve the coupled PDEs (6.23), subject to the boundary conditions (6.15), and are obtained via the Runge-Kutta method described in (6.24) and (6.25). We present solutions in large droplets with $\ell = 0.1$; in intermediate droplets with $\ell = 1$; and in small droplets with $\ell = 5$, at the temperatures $\hat{t} = -1$, $\hat{t} = -10$, and $\hat{t} = -100$ in each case. We assume that the numerical simulation has converged when $\left(\frac{\partial s}{\partial \tau}^2 + \frac{\partial m}{\partial \tau}^2\right)^{1/2} < 10^{-6}$. We use a step size of $\Delta\tau = 2 \times 10^{-5}$ in the simulations with $\ell = 0.1$ and $\ell = 1$, and $\Delta\tau = 1.25 \times 10^{-6}$ in the simulations with $\ell = 5$, and taking random initial guesses for both s and m , we find that convergence is reached in fewer than 200,000 iterations in each case.

We then plot the stochastic counterparts to the deterministic solutions obtained from (6.31) with strong noise, $\alpha = 0.1$, subject to the boundary conditions (6.15). We run the stochastic Runge-Kutta method outlined in (6.24) and (6.25) over the time interval $[0, T]$, setting $T = 4$ when $\ell = 0.1$ and $\ell = 1$; and setting $T = 0.4$ when $\ell = 5$, using step sizes of $\Delta\tau = 2 \times 10^{-5}$ with $\ell = 0.1$ and $\ell = 1$ and $\Delta\tau = 1.25 \times 10^{-6}$ with $\ell = 5$. We plot the average of 100 stochastic numerical simulations in each case.

Next, we plot the average of 100 stochastic simulations against the deterministic solutions in the specific cases $\hat{t} = -1$, $\ell = 0.1$ and $\hat{t} = -100$, $\ell = 5$ with weak noise, $\alpha = 1$, strong noise, $\alpha = 0.1$, and very strong noise, $\alpha = 0.01$.

Finally, we plot deterministic and stochastic solutions on the disc with $\hat{t} = -1$ and $\ell = 0.1$, with strong noise, $\alpha = 0.1$, in the stochastic case, and their difference obtained from subtracting the stochastic solution from the deterministic solution at each point. We note that the stochastic solution is again the average of 100 stochastic simulations.

The Uncoupled Case

In this section, we consider the ferronematic case in the absence of nemato-magnetic coupling, with $c = 0$. Setting $c = 0$ renders the problem analogous to the nematic case with the fourth-order bulk potential, and as such the qualitative behaviour of the radial hedgehog scalar order parameter is the same as in the pure nematic case.

The key observations regarding the deterministic radial hedgehog scalar order parameter profiles in Figure 6.10 are the same as in the nematic case. The associated magnetisation vector profiles in Figures 6.10d-6.10f do not vary with temperature. This is because, in the uncoupled case, the magnetisation vector depends only on droplet size, described by ℓ , and has no dependence on temperature.

Regarding the stochastic magnetisation profiles in Figures 6.11d-6.11f, we observe that the profiles are no longer identical at each value of ℓ . However, we see no clear trends in the variation of the magnetisation profile with respect to droplet size or temperature, and as such we speculate that the differences in the magnetisation profiles are purely random variations as a result of the inclusion of additive noise in the model.

In the large droplet, higher temperature case with very strong noise in Figure 6.12c, we observe that the magnetisation profile is reduced in magnitude in the droplet interior,

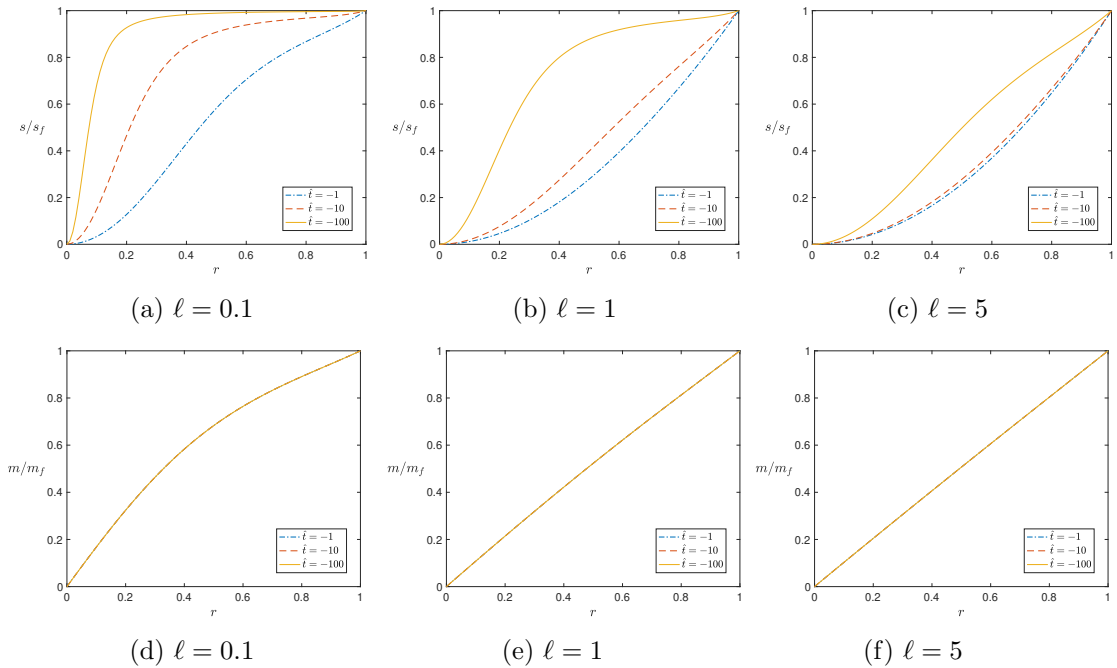


Figure 6.10: Deterministic radial hedgehog scalar order parameter profiles (a)-(c) and magnetisation profiles (d)-(f) obtained from (6.23) in the ferronematic case with zero nemato-magnetic coupling, $c = 0$, in (a), (d) large droplets ($\ell = 0.1$); (b), (e) intermediate droplets ($\ell = 1$); (c), (f) and small droplets ($\ell = 5$). Dashed and dotted blue lines correspond to $\hat{t} = -1$; dashed orange lines correspond to $\hat{t} = -10$; and solid yellow lines correspond to $\hat{t} = -100$.

approaching a linear profile. We see slight fluctuations in the magnetisation parameter with very strong noise in the small droplet, low temperature case in Figure 6.12d, but we speculate that these are merely random fluctuations about the deterministic solution. Figure 6.12 indicates that large droplets of ferronematic liquid crystals have slightly weaker spontaneous magnetisation than predicted by the deterministic model in (6.23).

Figures 6.13a and 6.13d are the solutions for s and m in the deterministic case, respectively; Figures 6.13b and 6.13e are the stochastic solutions for s and m , respectively; and Figures 6.13c and 6.13f are the differences between the deterministic and stochastic solutions for s and m , respectively. The value for both s and m throughout

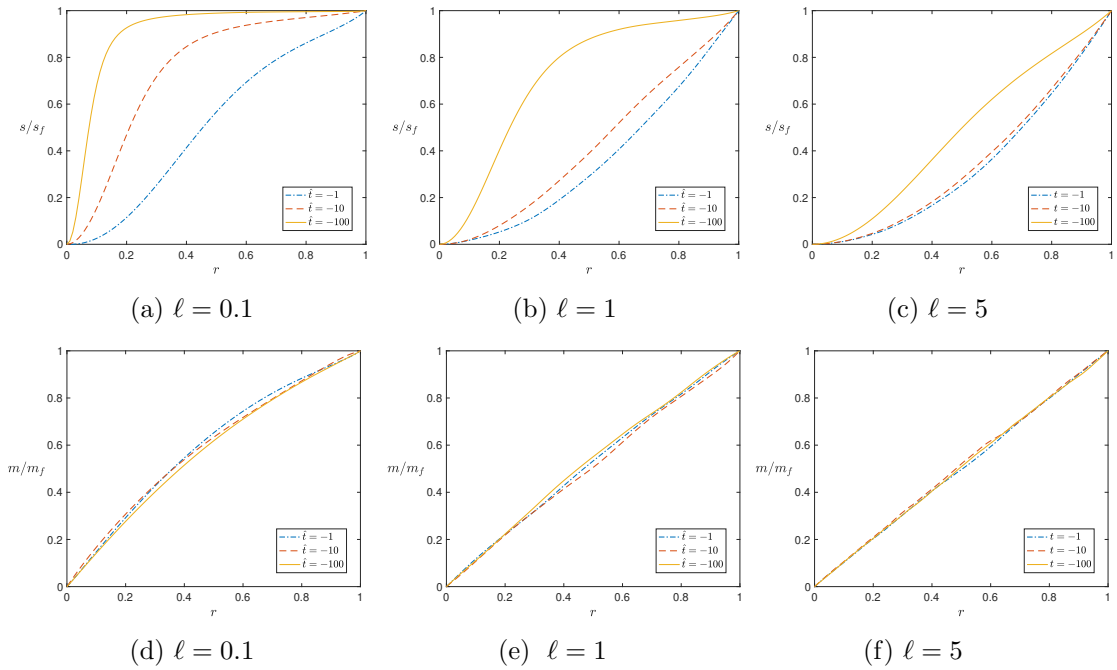


Figure 6.11: Stochastic radial hedgehog scalar order parameter profiles (a)-(c) and magnetisation profiles (d)-(f) obtained from (6.31) in the ferronematic case with strong noise, $\alpha = 0.1$; and zero nemato-magnetic coupling, $c = 0$, in (a), (d) large droplets ($\ell = 0.1$); (b), (e) intermediate droplets ($\ell = 1$); (c), (f) and small droplets ($\ell = 5$). Dashed and dotted blue lines correspond to $\hat{t} = -1$; dashed orange lines correspond to $\hat{t} = -10$; and solid yellow lines correspond to $\hat{t} = -100$.

the domain in the stochastic case is lower than in the deterministic case, although this is difficult to see in Figures 6.13b and 6.13e. This is more obvious in Figures 6.13c and 6.13f, which shows there is a clear difference between both the s and the m solutions, and demonstrates that rotational symmetry is lost in the stochastic case. We make two further observations: firstly, the difference between the deterministic and stochastic solutions is nonnegative everywhere in the domain, highlighting that the inclusion of additive noise results in a reduction in ordering throughout the droplet, at least in this case. Secondly, the greatest differences between the deterministic and stochastic solutions are not at the same points in the domain for the solutions for s and m , which is to be expected since there is no nemato-magnetic coupling, meaning the fluctuations

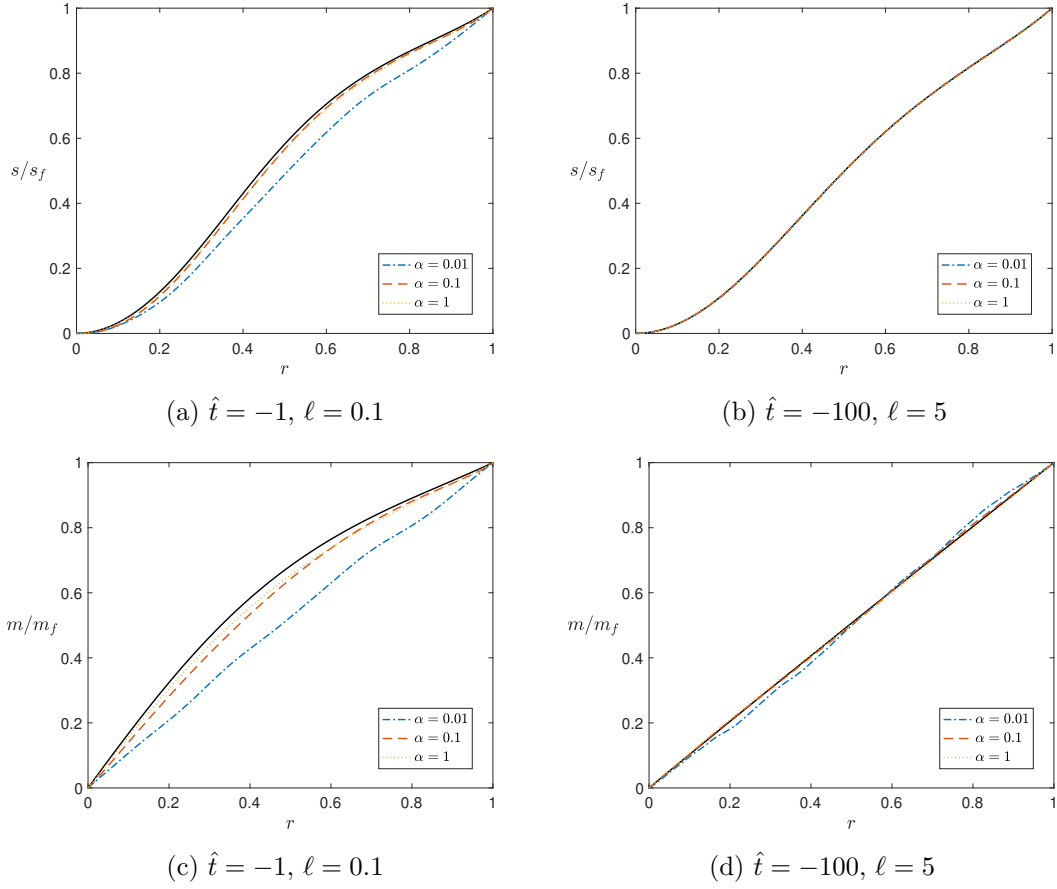


Figure 6.12: Comparison of deterministic and stochastic radial hedgehog scalar order parameter profiles (a), (b), and the associated magnetisation profiles (c), (d), obtained from (6.23) and (6.31), respectively, with zero nemato-magnetic coupling, $c = 0$ with different strengths of noise. Black solid lines correspond to the deterministic profile, while dashed and dotted blue, dashed orange, and dotted yellow lines correspond to stochastic profiles with very strong noise ($\alpha = 0.01$), strong noise ($\alpha = 0.1$), and weak noise ($\alpha = 1$), respectively. We plot profiles for (a), (c) $\hat{t} = -1, \ell = 0.1$; and (b), (d) $\hat{t} = -100, \ell = 5$.

in the value of m are not dependent on fluctuations in the value of s . Finally, it is important to point out that while there are differences between the stochastic and deterministic solutions, these differences are very small in magnitude, as can be seen from the scales in Figures 6.13c and 6.13f.

As there are no observed violations of properties such as nonnegativity or monotonicity, the effects of additive noise in the uncoupled ferronematic case is arguably

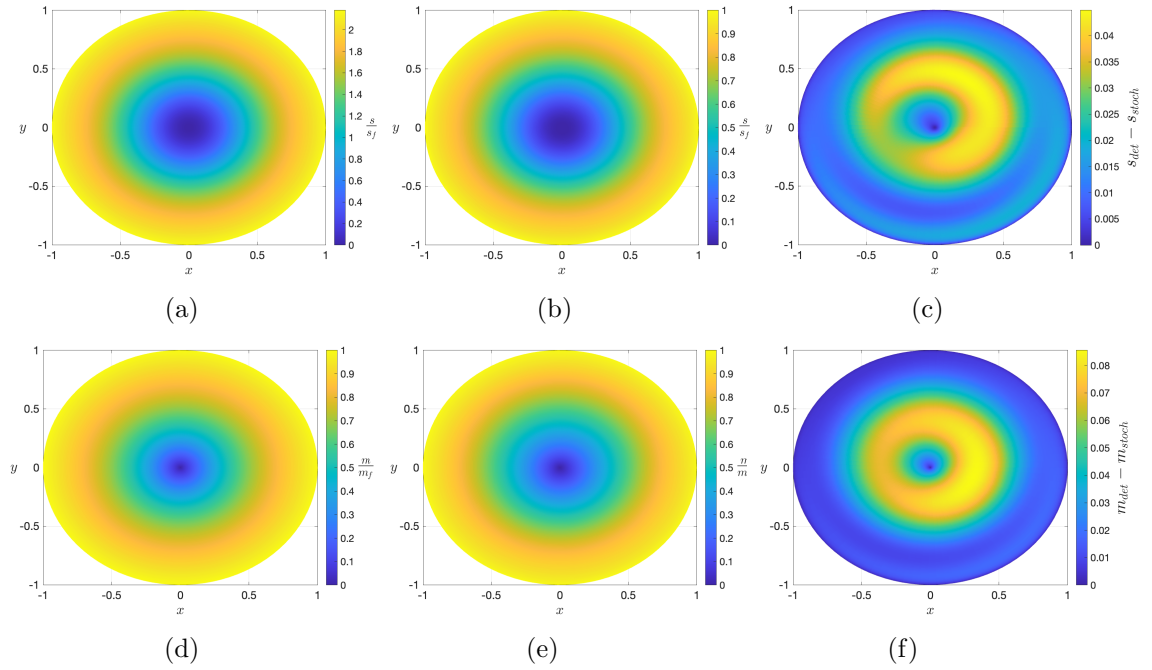


Figure 6.13: Value of s/s_f throughout the domain (a) in the deterministic case from (6.16); and (b) in the stochastic case with strong noise, $\alpha = 0.1$, from (6.30), each with $\hat{t} = -1$, $\ell = 0.1$, and $c = 0$. (c) The difference between the deterministic and stochastic scalar order parameter in (a) and (b), respectively. Value of m/m_f , throughout the domain (d) deterministic case from (6.16); and (e) in the stochastic case from (6.31). (f) The difference between the deterministic and stochastic magnetisation parameter in (d) and (e), respectively.

weaker than in the nematic cases studied. However, we must note that the parameter regimes for the nematic and ferronematic cases are slightly different due to the choice of nondimensionalisation in Section 2.2, so care must be taken when comparing the two systems.

A Weakly Coupled Case

We next consider a weakly coupled case, $c = 0.1$, in this section.

In Figure 6.14, we see that the radial hedgehog scalar order parameter profiles are almost identical to those in the uncoupled case plotted in Figure 6.10, with each solution being monotonic, nonnegative, and attaining its maximum on the droplet

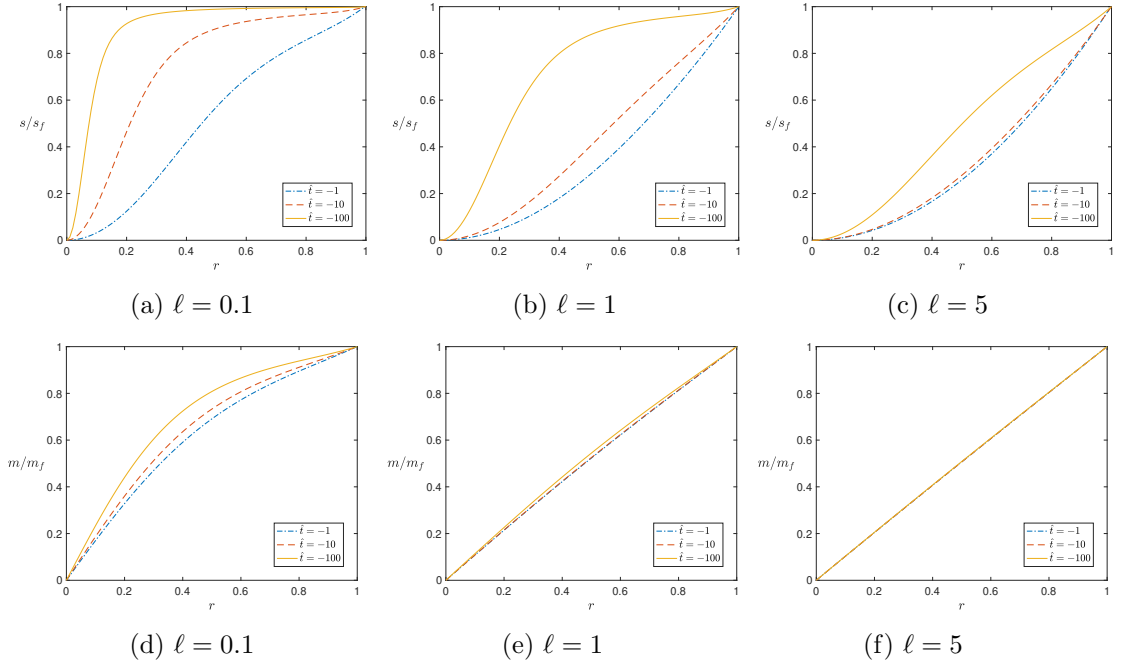


Figure 6.14: Deterministic radial hedgehog scalar order parameter profiles (a)-(c) and magnetisation profiles (d)-(f) obtained from (6.23) in the ferronematic case with weak nemato-magnetic coupling, $c = 0.1$, in (a), (d) large droplets ($\ell = 0.1$); (b), (e) intermediate droplets ($\ell = 1$); (c), (f) and small droplets ($\ell = 5$). Dashed and dotted blue lines correspond to $\hat{t} = -1$; dashed orange lines correspond to $\hat{t} = -10$; and solid yellow lines correspond to $\hat{t} = -100$.

boundary. The difference between the deterministic solutions in the $c = 0$ and $c = 0.1$ cases is in the magnetisation profiles in Figures 6.14d-6.14f. We observe that there are slight differences in the magnetisation profiles at different temperatures in this weakly coupled case in Figures 6.14d-6.14f, which can be attributed to the nemato-magnetic coupling introducing some level of temperature-dependence in the magnetisation. The differences are most pronounced in large droplets described by $\ell = 0.1$ in Figure 6.14d, with the magnitude of the magnetisation parameter, m , decreasing in the droplet bulk for higher temperatures.

Comparing Figures 6.15a-6.15c to Figures 6.14a-6.14c, we are unable to detect any clear differences between the deterministic and stochastic radial hedgehog scalar or-

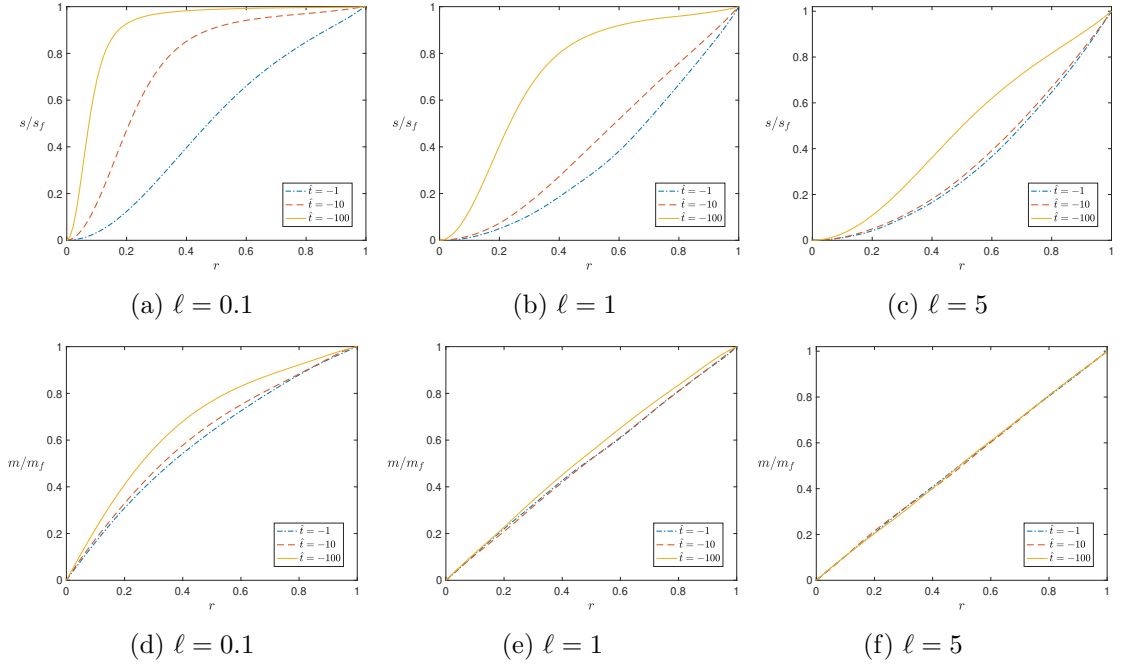


Figure 6.15: Stochastic radial hedgehog scalar order parameter profiles (a)-(c) and magnetisation profiles (d)-(f) obtained from (6.31) in the ferronematic case with strong noise, $\alpha = 0.1$ and weak nemato-magnetic coupling, $c = 0.1$, in (a), (d) large droplets ($\ell = 0.1$); (b), (e) intermediate droplets ($\ell = 1$); (c), (f) and small droplets ($\ell = 5$). Dashed and dotted blue lines correspond to $\hat{t} = -1$; dashed orange lines correspond to $\hat{t} = -10$; and solid yellow lines correspond to $\hat{t} = -100$.

der parameter profiles with the inclusion of strong additive noise, and we note that monotonicity, nonnegativity and the upper bound are preserved. Comparing Figures 6.15d-6.15f to Figures 6.14d-6.14f, we observe that the magnitude of the radial hedgehog magnetisation profile is slightly reduced with the inclusion of strong noise in the cases $\hat{t} = -1$ and $\hat{t} = -10$ with $\ell = 0.1$ and $\ell = 1$.

Additive noise appears to reduce the degree of nematic ordering and strength of spontaneous magnetisation in the large droplet, higher temperature case, as shown in Figures 6.16a and 6.16c, with stronger noise resulting in a greater reduction. We do not observe any differences in the radial hedgehog scalar order parameter with the inclusion of additive noise in the small droplet, low temperature case in Figure 6.16b, and we

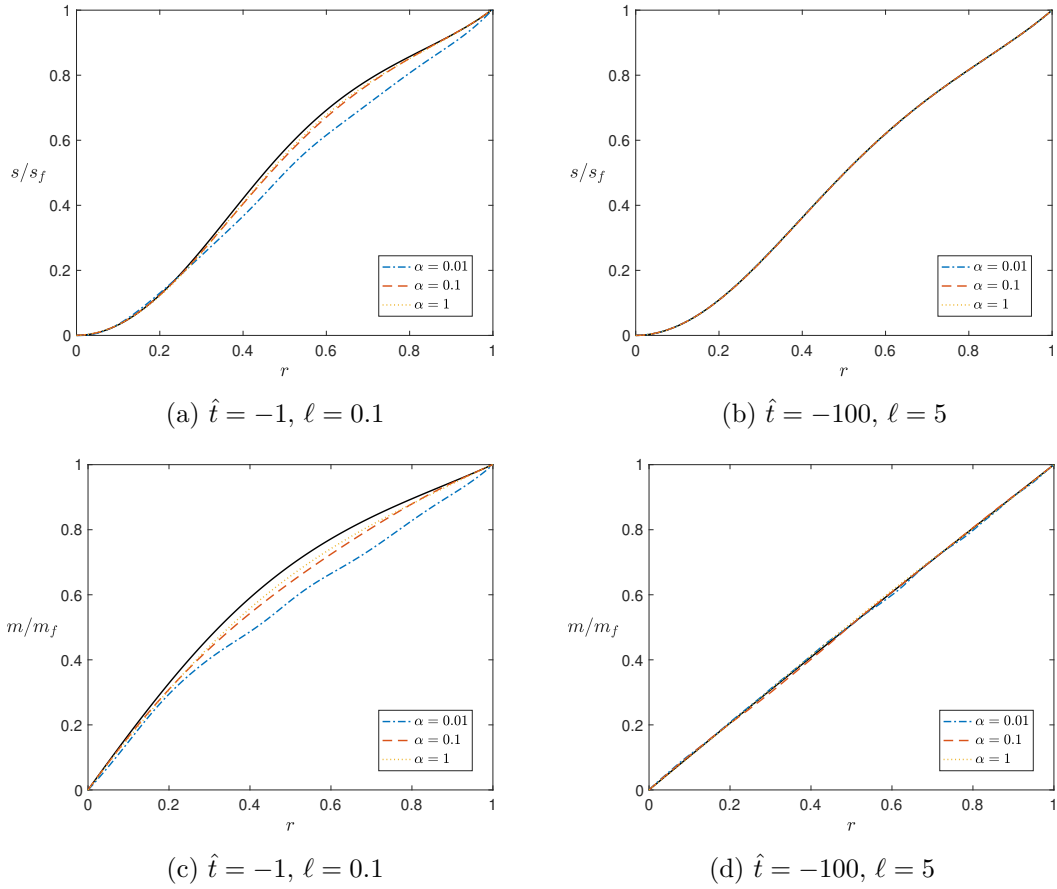


Figure 6.16: Comparison of deterministic and stochastic radial hedgehog scalar order parameter profiles (a), (b), and the associated magnetisation profiles (c), (d), obtained from (6.23) and (6.31), respectively, with weak nematic-magnetic coupling, $c = 0.1$, with different strengths of noise. Black solid lines correspond to the deterministic profile, while dashed and dotted blue, dashed orange, and dotted yellow lines correspond to stochastic profiles with very strong noise ($\alpha = 0.01$), strong noise ($\alpha = 0.1$), and weak noise ($\alpha = 1$), respectively. We plot profiles for (a), (c) $\hat{t} = -1, \ell = 0.1$; and (b), (d) $\hat{t} = -100, \ell = 5$.

observe slight random fluctuations in the magnetisation parameter in Figure 6.16d.

Furthermore, the differences in Figures 6.17c and 6.17f are mostly positive, so we conclude that additive noise results in a reduction in the nematic ordering and the strength of the spontaneous magnetisation throughout the droplet. In this weakly coupled case, comparing the patterns in Figures 6.17c and 6.17f, while the patterns in the differences between the values of s and m in the deterministic and stochastic

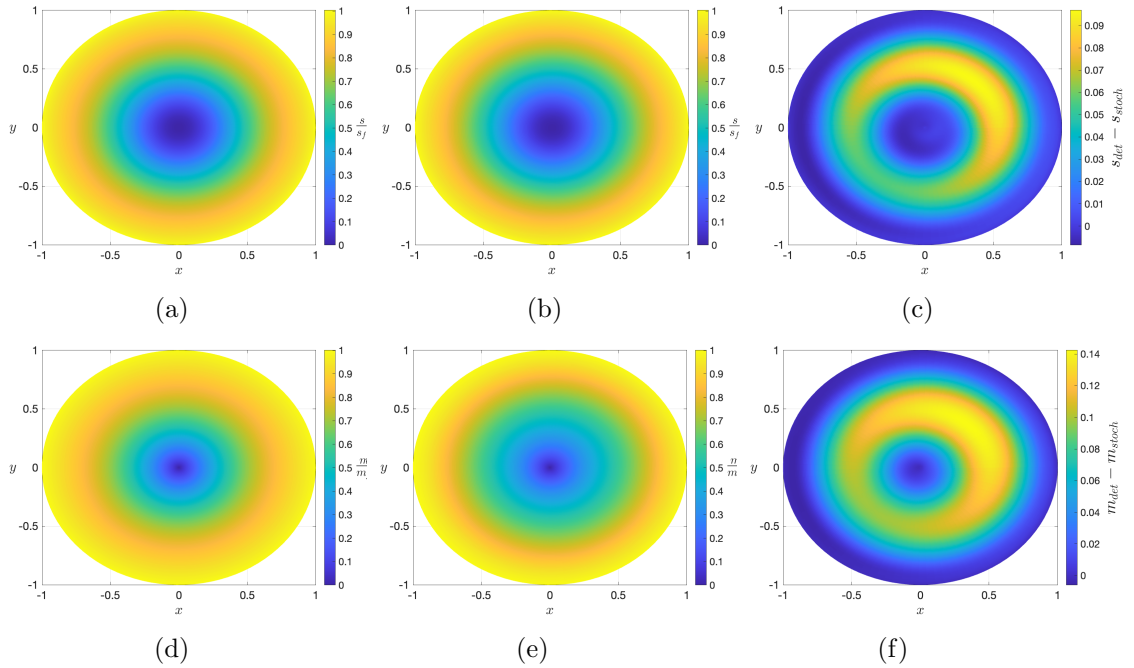


Figure 6.17: Value of s/s_f throughout the domain (a) in the deterministic case from (6.16); and (b) in the stochastic case with strong noise $\alpha = 0.1$, from (6.30), each with $\hat{t} = -1$, $\ell = 0.1$, and $c = 0.1$. (c) The difference between the deterministic and stochastic scalar order parameter in (a) and (b), respectively. Value of m/m_f , throughout the domain (d) deterministic case from (6.16); and (e) in the stochastic case from (6.31). (f) The difference between the deterministic and stochastic magnetisation parameter in (d) and (e), respectively.

cases are not identical, or in other words the largest differences between solutions are not in the exact same locations, one could argue that they are similar, and indeed appear more correlated than in the uncoupled case, in this example at least. This is in keeping with the fact that nonzero nemato-magnetic coupling introduces some interdependence between the values of s and m , so it is natural that fluctuations in m have some dependence on fluctuations in s , and vice-versa.

A Strongly Coupled Case

In this final section, we consider strong nemato-magnetic coupling described by $c = 1$.

In Figure 6.19, we see the stochastic radial hedgehog scalar order parameter take

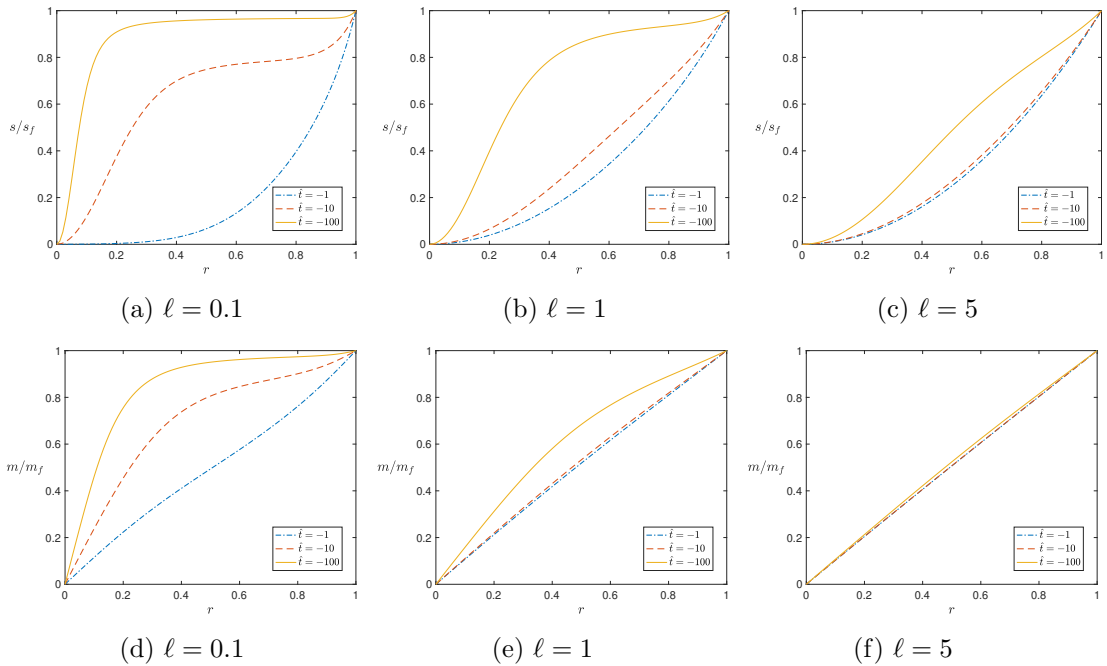


Figure 6.18: Deterministic radial hedgehog scalar order parameter profiles (a)-(c) and magnetisation profiles (d)-(f) obtained from (6.23) in the ferronematic case with strong nemato-magnetic coupling, $c = 1$, in (a), (d) large droplets ($\ell = 0.1$); (b), (e) intermediate droplets ($\ell = 1$); (c), (f) and small droplets ($\ell = 5$). Dashed and dotted blue lines correspond to $\hat{t} = -1$; dashed orange lines correspond to $\hat{t} = -10$; and solid yellow lines correspond to $\hat{t} = -100$.

negative values near the origin in the case $\ell = 1$, $t = -1$, which violates Proposition 5.3 in Chapter 5. In the deterministic case, there is almost no ordering near the droplet centre at this temperature and droplet size, while in the stochastic case we observe slight negative ordering near the centre of the droplet before the nematic ordering increases towards the edge of the droplet. Furthermore, this is the first example in a ferronematic system in which the scalar order parameter is nonmonotonic. Regarding the magnetisation parameter profiles in Figures 6.19d-6.19f, there are no observable differences to the deterministic case in small droplets; we observe slight differences at lower temperatures in intermediate droplets; and clearer differences in the larger droplet case, with each magnetisation profile being pulled closer to the shape of the corresponding scalar

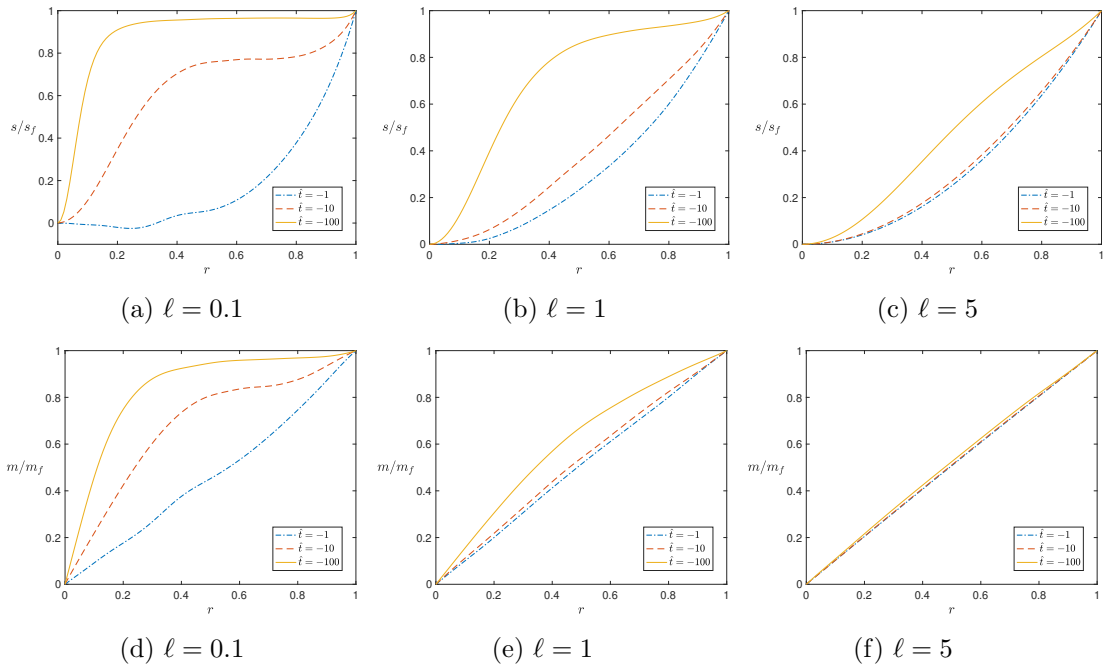


Figure 6.19: Stochastic radial hedgehog scalar order parameter profiles (a)-(c) and magnetisation profiles (d)-(f) obtained from (6.31) in the ferronematic case with strong noise, $\alpha = 0.1$ and strong nemato-magnetic coupling, $c = 1$, in (a), (d) large droplets ($\ell = 0.1$); (b), (e) intermediate droplets ($\ell = 1$); (c), (f) and small droplets ($\ell = 5$). Dashed and dotted blue lines correspond to $\hat{t} = -1$; dashed orange lines correspond to $\hat{t} = -10$; and solid yellow lines correspond to $\hat{t} = -100$.

order parameter in comparison to the deterministic case. The qualitative behaviour of the stochastic magnetisation profiles is similar to the deterministic counterparts. The higher temperature, large droplet example here represents the largest departure from the deterministic solution, suggesting the inclusion of additive noise has the greatest impact in strongly coupled ferronematic systems at higher temperatures and in larger droplets. However, one could still argue that the effects are small.

In Figure 6.20, there are no clear differences between the deterministic and stochastic radial hedgehog scalar order parameter profiles in the small droplet, low temperature case, and there are only slight fluctuations in the associated magnetisation profiles. In the large droplet, higher temperature case, additive noise again appears to reduce

the degree of ordering throughout the droplet, and reduces the value of the associated magnetisation. This again reinforces that the inclusion of additive noise has a more pronounced effect on large droplets and at higher temperatures, and that noise typically reduces the degree of nematic ordering and the strength of the spontaneous magnetisation.

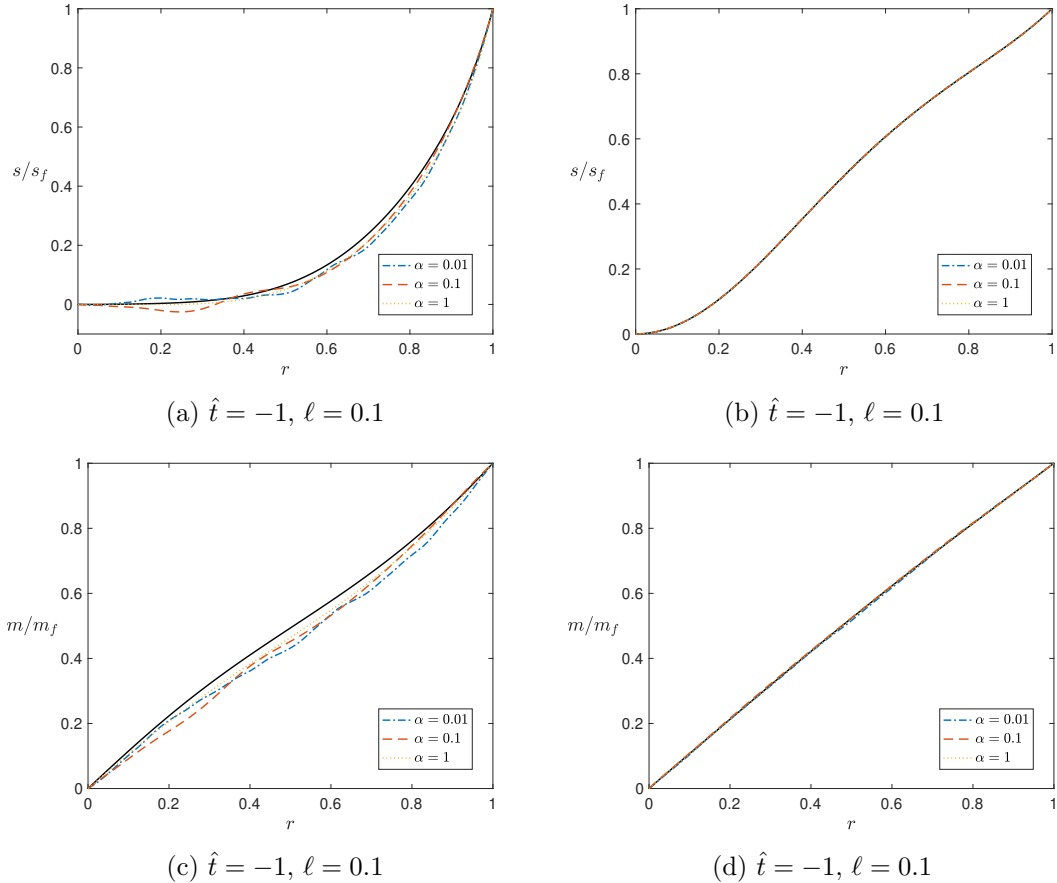


Figure 6.20: Comparison of deterministic and stochastic radial hedgehog scalar order parameter profiles (a), (b), and the associated magnetisation profiles (c), (d), obtained from (6.23) and (6.31), respectively, with strong nemato-magnetic coupling, $c = 1$, with different strengths of noise. Black solid lines correspond to the deterministic profile, while dashed and dotted blue, dashed orange, and dotted yellow lines correspond to stochastic profiles with very strong noise ($\alpha = 0.01$), strong noise ($\alpha = 0.1$), and weak noise ($\alpha = 1$), respectively. We plot profiles for (a), (c) $\hat{t} = -1, \ell = 0.1$; and (b), (d) $\hat{t} = -100, \ell = 5$.

In Figure 6.21b, we observe a darker ring around the origin corresponding to roughly

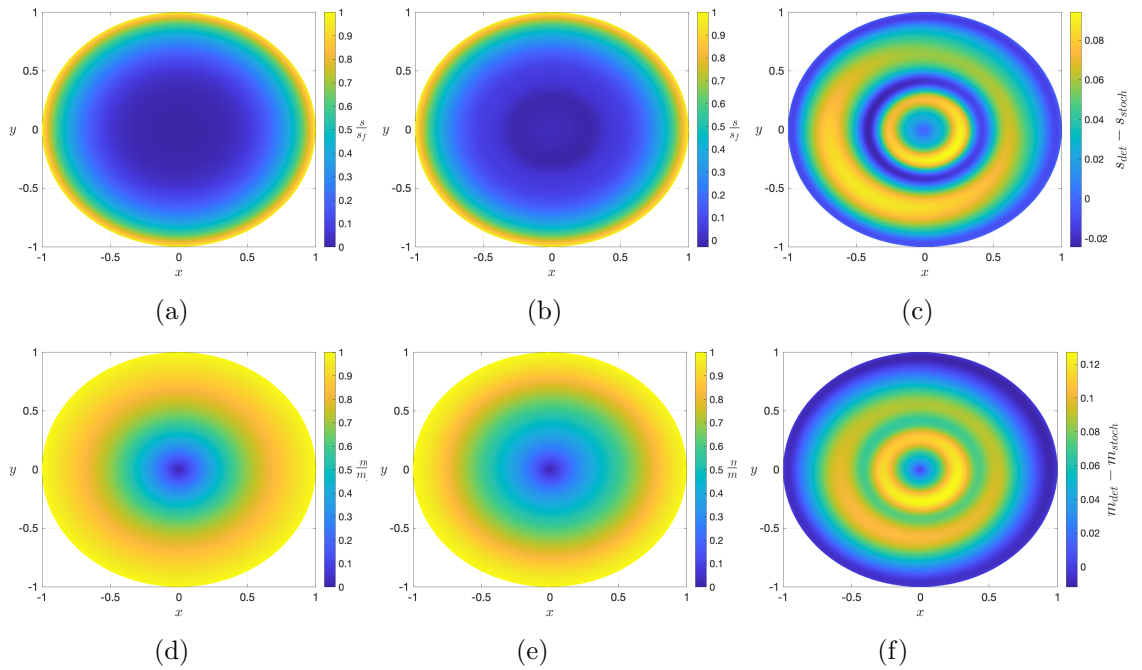


Figure 6.21: Value of s/s_f throughout the domain (a) in the deterministic case from (6.16); and (b) in the stochastic case with strong noise $\alpha = 0.1$, from (6.30), each with $\hat{t} = -1$, $\ell = 0.1$, and $c = 1$. (c) The difference between the deterministic and stochastic scalar order parameter in (a) and (b), respectively. Value of m/m_f , throughout the domain (d) deterministic case from (6.16); and (e) in the stochastic case from (6.31). (f) The difference between the deterministic and stochastic magnetisation parameter in (d) and (e), respectively.

where the scalar order parameter is negative in the stochastic case, which is absent in the deterministic case in Figure 6.21a. Furthermore, we also see that the patterns in the two difference plots in Figures 6.21c and 6.21f are very similar. In particular, while different in magnitude, looking at the two yellow bands each figure, we observe that the greatest differences in the scalar order parameter solutions appear to be in the same locations as the greatest differences in the magnetisation solutions, which is to be expected with strong nemato-magnetic coupling.

This section concludes our numerical investigations and our observations in this strongly coupled case are in approximate agreement with our observations in the earlier sections. The differences observed with the inclusion of additive noise are arguably the

most pronounced in this strongly coupled case, in comparison to the weakly coupled and uncoupled ferronematic systems. The key finding in this section is the example in which monotonicity and nonnegativity are violated with the inclusion of strong additive noise.

6.4 Summary

In this chapter, we perform a numerical investigation of the effects of the inclusion of additive noise in rotational droplets of nematic and ferronematic liquid crystals. This noise models factors such as material imperfections, thermal fluctuations, and flaws in experimental setup. Including noise is also an effective way to test how well the existing deterministic models capture the qualitative behaviour of more realistic systems.

Our investigation suggests that the radial hedgehog configuration in more realistic systems may not be perfectly rotationally symmetric and may be slightly less ordered than expected from deterministic predictions. Moreover, in ferronematic systems we might also expect slightly weaker spontaneous magnetisation. However, we make these observations in larger droplets and at higher temperatures, and find that the degree of nematic ordering and strength of spontaneous magnetisation in other scenarios is largely unaffected by the inclusion of noise. Therefore, in smaller droplets and at lower temperatures, we would expect the deterministic predictions to be very accurate. We observe that rotational symmetry is lost in every case with the inclusion of additive noise.

Furthermore, we find examples of radial hedgehog scalar order parameter profiles which violate the monotonicity and nonnegativity and the upper bounds predicted in Chapters 3 and 5. This suggests that these properties may not hold in every case in reality, but we note that the deviations from the deterministic solutions in the examples

presented are small.

In the nematic case, we find that additive noise has a greater impact on solutions with a sixth-order bulk potential. In the ferronematic case, we observe that the greatest differences between deterministic and stochastic solutions occurs in the strongly coupled case.

Despite the observed differences between deterministic and stochastic solutions throughout this chapter, the qualitative behaviour between deterministic and stochastic solutions is generally preserved, supporting the use of the existing deterministic models as valuable tools to capture the behaviour of the nematic and ferronematic radial hedgehog solutions.

The investigation in this chapter is limited to the radial hedgehog solution on a disc, only. A key next step would be to study more general equilibrium configurations on the sphere with additive noise, which would allow for randomness in the preferred direction of the nematic liquid crystal molecules as well as in the degree of ordering. It would be useful to include additive noise into the models used in Sections 3.4 and 5.3 to understand the impact of noise on the structure and stability of equilibrium configurations in spherical droplets of nematic and ferronematic liquid crystals. However, such a numerical investigation would require significant computational power, so careful consideration regarding factors such as the numerical methods, mesh size, and time step size would be required. Another potential next step would be to repeat our investigation with multiplicative noise instead, to understand whether the dependence of noise on the unknown variable would have any material impact on solutions.

Chapter 7

Conclusions and Future Work

The aim of this thesis has been twofold: to investigate biaxiality as a bulk effect in liquid crystalline systems; and to study the character of defect structures in equilibrium in spherical droplets of nematic liquid crystals and ferronematic liquid crystals.

Throughout this thesis, we model nematic liquid crystals using the Landau–de Gennes theory, with the addition of magnetisation and nemato-magnetic coupling energies in the ferronematic case. We recall that the commonly used fourth-order bulk potential does not admit biaxiality as a bulk effect in the absence of magnetisation. We demonstrate that biaxiality can be a bulk effect under the more complicated sixth-order bulk potential in the pure nematic case, and that it is also admissible in the ferronematic case, where magnetisation is induced by a dilute suspension of magnetic nanoparticles in systems of nematic liquid crystals.

We investigate the character and stability of the canonical radial hedgehog configuration and other equilibrium configurations in spherical droplets of nematic and ferronematic liquid crystals. We first focus on the pure nematic case with the sixth-order bulk potential, and then study equilibrium configurations in ferronematic systems. We determine how factors such as droplet size, temperature, and nemato-magnetic coupling

influence the stability and extent of biaxiality in such equilibrium configurations.

Finally, we consider the nematic and ferronematic radial hedgehog solution in a stochastic context, to investigate if and how the inclusion of random noise in the system influences the properties of the radial hedgehog solution, providing insight into the robustness of the deterministic models used throughout this thesis. To conclude this thesis, we present a brief summary of each chapter, and indicate some directions for future study, building upon this work.

Chapter 3 contains some analytical and numerical studies of a Landau–de Gennes free energy with a sixth-order bulk potential, and is divided into three main sections. We first consider critical points of the sixth-order bulk potential, and find that the global minimiser has negative scalar order parameter at low temperatures in the class of uniaxial \mathbf{Q} -tensors and is indeed biaxial in the more general class of \mathbf{Q} -tensors which can be biaxial. This is in contrast to the fourth-order bulk potential, which has a uniaxial global minimiser with nonnegative scalar order parameter at low temperatures in the class of uniaxial \mathbf{Q} -tensors, and does not admit biaxial critical points in the more general case. This is of interest since bulk biaxiality is typically challenging to induce experimentally.

The second key component of Chapter 3 is an analytical exploration of the canonical radial hedgehog solution with the sixth-order bulk potential. We find some analogies with the radial hedgehog solution with the fourth-order bulk potential for moderately low temperatures. Specifically, we prove uniqueness, monotonicity and nonnegativity of the radial hedgehog scalar order parameter at moderately low temperatures. However, these properties need not hold at low temperatures, and we provide an example of a second radial hedgehog solution at a low temperature which has negative scalar order parameter away from $r = 0$ and $r = 1$. This is in contrast to the radial hedgehog solu-

tion with the fourth-order bulk potential, which is unique, nonnegative and monotonic at low temperatures.

Finally, we numerically compute critical points with rotational and mirror symmetry, namely the radial hedgehog, split core, and biaxial torus solutions, with the sixth-order bulk potential to complete Chapter 3. The essential findings are that the biaxial regions in the split core and biaxial torus configurations are larger under the sixth-order potential than with the fourth-order potential, and the split core and biaxial torus configurations have larger domains of stability with the sixth-order bulk potential as opposed to with the fourth-order bulk potential. Otherwise, we find that the critical points of the Landau–de Gennes free energy with the sixth-order bulk potential are qualitatively similar to those with the fourth-order bulk potential.

The numerical study in Chapter 3 exploits only three of the five possible degrees of freedom. A natural extension to this work would be to study the solution landscape in the absence of rotational and mirror symmetry, with both the fourth- and sixth-order bulk potentials. In [1], the authors demonstrate the existence of a new biaxial solution with five degrees of freedom under the sixth-order bulk potential. It would be interesting to explore the stability of such a solution as a function of temperature and droplet radius; and investigate the role of solutions with rotational and mirror symmetry in this more general system. Another avenue to explore would be to weaken the anchoring conditions. We only consider strong anchoring in this work, but this is perhaps quite a strict condition that is difficult to replicate in experiments. It would be interesting to work instead with some form of weak anchoring, with an associated free energy, which might better capture the behaviour at the boundary in real-world systems.

In Chapter 4, we consider the critical points of the ferronematic bulk potential for

different coupling strengths across a range of temperatures. We first consider critical points in the class of uniaxial \mathbf{Q} -tensors with the associated magnetisation vector oriented in the same direction as the nematic director. We find that the system generally favours critical points with nonzero magnetisation, with the exception of the point $(s_-, 0)$, where s_- is defined in (4.7), which gains local stability at low temperatures. We then study critical points with a \mathbf{Q} -tensor and magnetisation vector which each have two degrees of freedom. We find that for each value we consider of the nemato-magnetic coupling, c , there is some temperature at which the system admits at least a locally stable biaxial critical point. Globally stable critical points with the largest biaxiality parameter typically occur at higher temperatures just above the nematic supercooling temperature, where the isotropic phase loses stability, and with larger negative values of the nemato-magnetic coupling parameter. This suggests that bulk biaxiality is perhaps most likely to be observed experimentally at such high temperatures and in systems which are strongly coupled, with the nematic director and magnetisation vector aligned perpendicular to one another. A worthwhile further investigation would be to consider critical points of the ferronematic bulk potential in the class of \mathbf{Q} -tensors with five degrees of freedom with an associated magnetisation vector with three degrees of freedom to discern whether biaxiality is truly favourable as a bulk effect in ferronematic systems.

Much of the work in Chapter 5 is analogous to that in Chapter 3: we perform an analytical and numerical study on a ferronematic free energy. We prove a range of analytical results for the ferronematic radial hedgehog solution, including existence and uniqueness results, and a maximum principle, which allow us to draw comparisons between the nematic and ferronematic radial hedgehog solutions. We also perform an analogous numerical study to that in Chapter 3 of equilibrium configurations on the

sphere with rotational and mirror symmetry. We find that the ferronematic solution landscape is richer than the nematic solution landscape in systems with strong positive nemato-magnetic coupling; and that the presence of magnetisation has a stabilising effect on the split core configuration at high temperatures. We do not consider a negative nemato-magnetic coupling parameter at any point in Chapter 5. As such, an immediate next step would be to investigate whether the analytical results hold with a negative coupling parameter, and to perform the same numerical study with a negative coupling parameter to understand the effects of a magnetisation vector which is perpendicular to the nematic director on the solution landscape. As in the nematic case, it would also be interesting to study the problem with five degrees of freedom, and to replace the strong anchoring with weak anchoring.

In Chapter 6, we introduce a stochastic term into the nematic and ferronematic models for the radial hedgehog solution. We perform a comprehensive numerical investigation into the effects of additive noise on the nematic and ferronematic radial hedgehog solution in domains of different sizes and at different temperatures, with the fourth- and sixth-order bulk potentials in the nematic case; and in uncoupled, weakly coupled, and strongly coupled ferronematic systems. We find that rotational symmetry is lost, and there are slight differences between the stochastic and deterministic radial hedgehog solutions in larger domains and at higher temperatures. A clear trend is that, in such domains, additive noise can reduce the degree of nematic ordering in the interior, and can slightly reduce the strength of the spontaneous magnetisation. We also find examples in which the monotonicity and nonnegativity predicted by the analytical results in Chapters 3 and 5 are violated. On the whole, however, any differences between deterministic and stochastic solutions observed are minimal and do not significantly alter the qualitative behaviour of the nematic and ferronematic radial

Chapter 7. Conclusions and Future Work

hedgehog solutions. This indicates that the deterministic models in both the nematic and ferronematic cases are robust and can be relied upon to capture the character of the nematic and ferronematic radial hedgehog solutions. A natural extension to this work would be to consider more general equilibrium configurations on the sphere in both the nematic and ferronematic cases. It would be interesting to study the effects of additive noise on the stability and structure of equilibrium configurations, and investigate whether the inclusion of noise results in any new equilibrium configurations not observed under the deterministic models.

Bibliography

- [1] S. McLauchlan, Y. Han, M. Langer, and A. Majumdar, “The radial hedgehog solution in the Landau–de Gennes theory: Effects of the bulk potentials,” *Physica D: Nonlinear Phenomena*, vol. 459, p. 134019, 2024.
- [2] P. G. de Gennes and J. Prost, *The physics of liquid crystals*. Oxford University Press, Oxford, 1974.
- [3] E. G. Virga, *Variational theories for liquid crystals*. Berlin, Germany: Chapman and Hall/CRC, 1994.
- [4] S. Chandrasekhar, B. K. Sadashiva, and K. A. Suresh, “Liquid crystals of disc-like molecules,” *Pramana Journal of Physics*, vol. 9, pp. 471–480, 5 1977.
- [5] E. van den Pol, D. M. E. Thies–Weesie, A. V. Petukhov, D. V. Byelov, and G. J. Vroege, “Uniaxial and biaxial liquid crystal phases in colloidal dispersions of board-like particles,” *Liquid Crystals*, vol. 37, pp. 641–651, 6-7 2010.
- [6] J. P. F. Lagerwall and G. Scalia, “A new era for liquid crystal research: Applications of liquid crystals in soft matter nano-, bio- and microtechnology,” *Current Applied Physics*, vol. 12, pp. 1387–1412, 2012.
- [7] F. Reinitzer, “Contributions to the knowledge of cholesterol,” *Liquid Crystals*, vol. 5, pp. 7–18, 1 1889.

Bibliography

- [8] H. Kelker, "History of liquid crystals," *Molecular Crystals and Liquid Crystals*, vol. 21, pp. 1–48, 1-2 1973.
- [9] D. Dunmur and T. Sluckin, *Soap, science, and flat-screen TVs: a history of liquid crystals*, eng. Oxford University Press, 2011.
- [10] M. Mitov, "Liquid-crystal science from 1888 to 1922: Building a revolution," *ChemPhysChem*, vol. 15, pp. 1245–1250, 7 2014.
- [11] G. W. Gray, K. J. Harrison, and J. A. Nash, "New family of nematic liquid crystals for displays," *Electronics Letters*, vol. 9, 130–131(1), 6 1973.
- [12] A. A. Collyer, "Lyotropic liquid crystal polymers for engineering applications," *Materials Science and Technology*, vol. 6, pp. 981–992, 10 1990.
- [13] G. Friedel, "Les états mésomorphes de la matière," *Annales de Physique*, vol. 9, pp. 273–474, 18 1922.
- [14] I. W. Stewart, *The static and dynamic continuum theory of liquid crystals: a mathematical introduction*. Taylor & Francis, 2004.
- [15] J. De, R. A. K. Yadav, R. S. Yadav, *et al.*, "Molecular engineering for the development of a discotic nematic mesophase and solid-state emitter in deep-blue oleds," *Journal of Organic Chemistry*, vol. 86, pp. 7256–7262, 10 2021.
- [16] N. J. Mottram and C. J. P. Newton, *Introduction to Q-tensor theory*, 2014. [Online]. Available: <https://arxiv.org/abs/1409.3542v2>.
- [17] J. Ball, E. Feireisl, F. Otto, and E. Rocca, *Mathematical thermodynamics of complex fluids*. Springer, 2017.
- [18] P. J. Collings and M. Hird, *Introduction to liquid crystals chemistry and physics*. Taylor & Francis, 1997.
- [19] G. Chartier, *Introduction to Optics*. Springer, 2005.

Bibliography

- [20] J. C. Jones, “The fiftieth anniversary of the liquid crystal display,” *Liquid Crystals Today*, vol. 27, pp. 44–70, 3 2018.
- [21] T. P. Brody, J. A. Asars, and G. D. Dixon, “A 6×6 inch 20 lines-per-inch liquid-crystal display panel,” *IEEE Transactions on Electron Devices*, vol. 20, pp. 995–1001, 11 1973.
- [22] T. J. Spencer, C. M. Care, R. M. Amos, and J. C. Jones, “Zenithal bistable device: Comparison of modeling and experiment,” *Physical Review E*, vol. 82, pp. 021–702, 2 2010.
- [23] A. Raisch and A. Majumdar, “Order reconstruction phenomena and temperature-driven dynamics in a 3D zenithally bistable device,” *Europhysics Letters*, vol. 107, pp. 1–6, 1 2014.
- [24] M.-M. Giraud-Guille, E. Belamie, G. Mosser, C. Helary, F. Gobeaux, and S. Vigier, “Liquid crystalline properties of type i collagen: Perspectives in tissue morphogenesis,” *Comptes Rendus Chimie*, vol. 11, pp. 245–252, 3 2008.
- [25] F. Livolant and Y. Bouligand, “New observations on the twisted arrangement of Dinoflagellate chromosomes,” *Chromosoma*, vol. 68, no. 1, pp. 21–44, 1978.
- [26] Z. Dogic and S. Fraden, “Development of model colloidal liquid crystals and the kinetics of the isotropic–smectic transition,” *Philosophical Transactions of the Royal Society of London. Series A: Mathematical, Physical, and Engineering sciences*, vol. 359, pp. 997–1015, 1782 2001.
- [27] R. Qu and G. Li, “Overview of liquid crystal biosensors: From basic theory to advanced applications,” *Biosensors*, vol. 12, 4 2022.

Bibliography

- [28] V. K. Gupta, J. J. Skaife, T. B. Dubrovsky, and N. L. Abbott, “Optical amplification of ligand-receptor binding using liquid crystals,” *Science*, vol. 279, pp. 2077–2080, 5359 1998.
- [29] S. H. Yoon, K. C. Gupta, J. S. Borah, *et al.*, “Folate ligand anchored liquid crystal microdroplets emulsion for in vitro detection of kb cancer cells,” *Langmuir*, vol. 30, no. 35, pp. 10 668–10 677, 2014.
- [30] S. Sivakumar, K. L. Wark, J. K. Gupta, N. L. Abbott, and F. Caruso, “Liquid crystal emulsions as the basis of biological sensors for the optical detection of bacteria and viruses,” *Advanced Functional Materials*, vol. 19, pp. 2260–2265, 14 2009.
- [31] H. Coles and S. Morris, “Liquid-crystal lasers,” *Nature Photonics*, vol. 4, pp. 676–685, 10 2010.
- [32] J. Mysliwiec, A. Szukalska, A. Szukalski, and L. Sznitko, “Liquid crystal lasers: The last decade and the future,” *Nanophotonics*, vol. 10, pp. 2309–2346, 9 2021.
- [33] P. J. W. Hands, C. M. Brown, D. K. Dickinson, S. M. Morris, and J.-D. Lin, “36-1: Invited paper: Liquid-crystal lasers: Recent advances and future opportunities,” *SID Symposium Digest of Technical Papers*, vol. 53, pp. 440–443, 1 2022.
- [34] J. W. Dobrucki and U. Kubitscheck, *Fluorescence Microscopy*. John Wiley & Sons, Ltd, 2017, ch. 3.
- [35] M. Humar, M. Ravnik, S. Pajk, and I. Muševič, “Electrically tunable liquid crystal optical microresonators,” *Nature Photonics*, vol. 3, pp. 595–600, 10 2009.
- [36] M. Humar, “Liquid-crystal-droplet optical microcavities,” *Liquid Crystals*, vol. 43, pp. 1937–1950, 13-15 2016.

Bibliography

- [37] H. K. Bisoyi and S. Kumar, “Discotic nematic liquid crystals: Science and technology,” *Chemical Society Reviews*, vol. 39, pp. 264–285, 1 2010.
- [38] C. W. Oseen, “The theory of liquid crystals,” *Transactions of the Faraday Society*, vol. 29, pp. 883–899, 140 1933.
- [39] F. C. Frank, “I. Liquid crystals: On the theory of liquid crystals,” *Discussions of the Faraday Society*, vol. 25, pp. 19–28, 1958.
- [40] I. Haller, “Elastic constants of the nematic liquid crystalline phase of p-methoxybenzylidene-p-n-butylaniline (MBBA),” *The Journal of Chemical Physics*, vol. 57, pp. 1400–1405, 4 1972.
- [41] J. L. Ericksen, “Liquid crystals with variable degree of orientation,” *Archive for Rational Mechanics and Analysis*, vol. 113, pp. 97–120, 2 1991.
- [42] M. Kleman and O. D. Lavrentovich, “Topological point defects in nematic liquid crystals,” *Philosophical Magazine*, vol. 86, pp. 4117–4137, 25-26 2006.
- [43] Y.-K. Kim, S. V. Shiyankovskii, and O. D. Lavrentovich, “Morphogenesis of defects and tactoids during isotropic–nematic phase transition in self-assembled lyotropic chromonic liquid crystals,” *Journal of Physics: Condensed Matter*, vol. 25, p. 404 202, 40 2013.
- [44] B. F. de Oliveira, P. P. Avelino, F. Moraes, and J. C. R. E. Oliveira, “Nematic liquid crystal dynamics under applied electric fields,” *Physical Review E*, vol. 82, p. 041 707, 4 2010.
- [45] E. Willman, F. A. Fernández, R. James, and S. E. Day, “Switching dynamics of a post-aligned bistable nematic liquid crystal device,” *Journal of Display Technology*, vol. 4, pp. 276–281, 3 2008.

Bibliography

- [46] S. Steinberg, “Accurate rendering of liquid-crystals and inhomogeneous optically anisotropic media,” *ACM Transactions on Graphics*, vol. 39, pp. 1–23, 2020.
- [47] L. D. Landau, “On the theory of phase transitions,” *Soviet Journal of Experimental and Theoretical Physics*, vol. 7, pp. 19–32, 1937.
- [48] P. G. de Gennes, “Short range order effects in the isotropic phase of nematics and cholesterics,” *Molecular Crystals and Liquid Crystals*, vol. 12, pp. 193–214, 3 1971.
- [49] A. Majumdar and A. Zarnescu, “Landau–de Gennes theory of nematic liquid crystals: The Oseen–Frank limit and beyond,” vol. 196, pp. 227–280, 1 2010.
- [50] E. C. Gartland, P. Palffy-Muhoray, and R. S. Varga, “Numerical minimization of the Landau-de Gennes free energy: Defects in cylindrical capillaries,” *Molecular Crystals and Liquid Crystals*, vol. 199, pp. 429–452, 1 1991.
- [51] A. Sonnet, A. Kilian, and S. Hess, “Alignment tensor versus director: Description of defects in nematic liquid crystals,” *Physical Review E*, vol. 52, pp. 718–722, 1995.
- [52] A. Majumdar and Y. Wang, “Remarks on uniaxial solutions in the landau–de gennes theory,” *Journal of Mathematical Analysis and Applications*, vol. 464, pp. 328–353, 1 2018.
- [53] E. F. Gramsbergen, L. Longa, and W. H. de Jeu, “Landau theory of the nematic-isotropic phase transition,” *Physics Reports*, vol. 135, pp. 195–257, 1986.
- [54] G. De Matteis, A. Sonnet, and E. Virga, “Landau theory for biaxial nematic liquid crystals with two order parameter tensors,” *Continuum Mechanics and Thermodynamics*, vol. 20, pp. 347–374, 6 2008.

Bibliography

- [55] P. Kaiser, W. Wiese, and S. Hess, “Stability and instability of an uniaxial alignment against biaxial distortions in the isotropic and nematic phases of liquid crystals,” *Journal of Non-Equilibrium Thermodynamics*, vol. 17, pp. 153–170, 1992.
- [56] A. Majumdar, “Equilibrium order parameters of nematic liquid crystals in the Landau–de Gennes theory,” *European Journal of Applied Mathematics*, vol. 21, pp. 181–203, 2010.
- [57] R. Alben, “Liquid crystal phase transitions in mixtures of rodlike and platelike molecules,” *The Journal of Chemical Physics*, vol. 59, pp. 4299–4304, 8 1973.
- [58] P. B. Vigman, A. I. Larkin, and V. M. Filev, “Isolated point on a first-order transition curve,” *Soviet Journal of Experimental and Theoretical Physics*, vol. 41, p. 944, 1975.
- [59] D. W. Allender and M. A. Lee, “Landau theory of biaxial nematic liquid crystals,” *Molecular Crystals and Liquid Crystals*, vol. 110, pp. 331–339, 1-4 1984.
- [60] D. W. Allender, M. A. Lee, and N. Hafiz, “Landau theory of biaxial and uniaxial nematic liquid crystals,” *Molecular Crystals and Liquid Crystals*, vol. 124, pp. 45–52, 1 1985.
- [61] D. Allender and L. Longa, “Landau–de Gennes theory of biaxial nematics reexamined,” *Physical Review E*, vol. 78, p. 011 704, 2008.
- [62] S. Singh, “Phase transitions in liquid crystals,” *Physics Reports*, vol. 324, pp. 107–269, 2 2000.
- [63] A. Majumdar, “The radial-hedgehog solution in Landau–de Gennes’ theory for nematic liquid crystals,” *European Journal of Applied Mathematics*, vol. 23, pp. 61–97, 2012.

Bibliography

- [64] X. Lamy, “Some properties of the nematic radial hedgehog in the Landau–de Gennes theory,” *Journal of Mathematical Analysis and Applications*, vol. 69, p. 026 113, 2004.
- [65] E. Penzenstadler and H.-R. Trebin, “Fine structure of point defects and soliton decay in nematic liquid crystals,” *Journal de Physique*, vol. 50, pp. 1027–1040, 9 1989.
- [66] N. Schopohl and T. J. Sluckin, “Defect core structure in nematic liquid crystals,” *Physical Review Letters*, vol. 59, pp. 2582–2584, 22 1987.
- [67] S. Mkaddem and E. C. Gartland, “Fine structure of defects in radial nematic droplets,” *Physical Review E*, vol. 62, pp. 6694–6705, 2000.
- [68] R. Ignat, L. Nguyen, V. Slastikov, and A. Zarnescu, “Stability of the melting hedgehog in the Landau–de Gennes theory of nematic liquid crystals,” *Archive for Rational Mechanics and Analysis*, vol. 215, pp. 633–673, 2015.
- [69] S. Kralj and E. G. Virga, “Universal fine structure of nematic hedgehogs,” *Journal of Physics A: Mathematical and General*, vol. 34, p. 829, 4 2001.
- [70] R. Rosso and E. G. Virga, “Metastable nematic hedgehogs,” *Journal of Physics A: Mathematical and General*, vol. 29, pp. 4247–4264, 1996.
- [71] D. Henao, A. Majumdar, and A. Pisante, “Uniaxial versus biaxial character of nematic equilibria in three dimensions,” *Calculus of Variations and Partial Differential Equations*, p. 55, 56 2017.
- [72] E. C. Gartland and S. Mkaddem, “Instability of radial hedgehog configurations in nematic liquid crystals under Landau–de Gennes free-energy models,” *Physical Review E*, vol. 59, pp. 563–567, 1999.

Bibliography

- [73] J. Dalby, A. Majumdar, Y. Wu, and A. Dond, “Stochastic effects on solution landscapes for nematic liquid crystals,” *Liquid Crystals*, vol. 51, pp. 276–296, 2 2024.
- [74] T. Lopez-Leon and A. Fernandez-Nieves, “Drops and shells of liquid crystal,” *Colloid & Polymer Science*, vol. 289, pp. 345–359, 4 2011.
- [75] D. S. Miller, X. Wang, and N. L. Abbott, “Design of functional materials based on liquid crystalline droplets,” *Chemistry of materials*, vol. 26, pp. 496–506, 1 2014.
- [76] Y. Hu, Y. Qu, and P. Zhang, “On the disclination lines of nematic liquid crystals,” *Communications in Computational Physics*, vol. 19, pp. 354–379, 2 2016.
- [77] D. An, W. Wang, and P. Zhang, “On equilibrium configurations of nematic liquid crystals droplet with anisotropic elastic energy,” *Research in the Mathematical Sciences*, vol. 4, pp. 1–18, 1 2017.
- [78] H. Zhang, H. Liu, Z. Zhang, and G. Zheng, “Stability of a split-core configuration induced by saddle-splay elasticity in a submicron nematic liquid crystal spherical droplet,” *Liquid Crystals*, vol. 49, pp. 1746–1752, 13 2022.
- [79] F. Brochard and P.-G. de Gennes, “Theory of magnetic suspensions in liquid crystals,” *Journal de Physique*, vol. 31, pp. 691–708, 7 1970.
- [80] S. Burylov and Y. Raikher, “Ferro-nematics: On the development of the continuum theory approach,” *Journal of Magnetism and Magnetic Materials*, vol. 85, pp. 74–76, 1 1990.
- [81] S. V. Burylov and Y. L. Raikher, “Macroscopic properties of ferro-nematics caused by orientational interactions on the particle surfaces. I. Extended contin-

Bibliography

- uum model,” *Molecular Crystals and Liquid Crystals Science and Technology. Section A. Molecular Crystals and Liquid Crystals*, vol. 258, pp. 107–122, 1 1995.
- [82] S. V. Burylov and Y. L. Raikher, “Ferronematics: Enhanced magneto-optical response of a liquid crystalline system,” *Materials Science and Engineering: C*, vol. 2, pp. 235–241, 4 1995.
- [83] M. C. Calderer, A. DeSimone, D. Golovaty, and A. Panchenko, “An effective model for nematic liquid crystal composites with ferromagnetic inclusions,” *SIAM Journal on Applied Mathematics*, vol. 74, pp. 237–262, 2 2014.
- [84] G. Zarubin, M. Bier, and S. Dietrich, “A ferronematic slab in external magnetic fields,” *Soft Matter*, vol. 14, pp. 9806–9818, 48 2018.
- [85] S. Burylov and Y. Raikher, “Macroscopic properties of ferronematics caused by orientational interactions on the particle surfaces. II. Behavior of real ferronematics in external fields,” *Molecular Crystals and Liquid Crystals Science and Technology. Section A. Molecular Crystals and Liquid Crystals*, vol. 258, pp. 123–141, 1995.
- [86] V. I. Zadorozhnii, A. N. Vasilev, V. Y. Reshetnyak, K. S. Thomas, and T. J. Sluckin, “Nematic director response in ferronematic cells,” *Europhysics Letters*, vol. 73, p. 408, 3 2005.
- [87] J. Rault, P. E. Cladis, and J. P. Burger, “Ferronematics,” *Physics Letters A*, vol. 32, pp. 199–200, 3 1970.
- [88] A. Mertelj, D. Lisjak, M. Drogenik, and M. Copic, “Ferromagnetism in suspensions of magnetic platelets in liquid crystal,” *Nature*, vol. 504, pp. 237–241, 2013.
- [89] A. Mertelj and D. Lisjak, “Ferromagnetic nematic liquid crystals,” *Liquid Crystals Reviews*, vol. 5, pp. 1–33, 1 2017.

Bibliography

- [90] B. J. Liang and S.-H. Chen, “Electric-field-induced molecular reorientation of a magnetically biased ferronematic liquid-crystal film,” *Physical Review A*, vol. 39, pp. 1441–1446, 3 1989.
- [91] Q. Liu, P. J. Ackerman, T. C. Lubensky, and I. I. Smalyukh, “Biaxial ferromagnetic liquid crystal colloids,” *Proceedings of the National Academy of Sciences*, vol. 113, pp. 10 479–10 484, 38 2016.
- [92] M. F. Prodanov, O. G. Buluy, E. V. Popova, S. A. Gamzaeva, Y. O. Reznikov, and V. V. Vashchenko, “Magnetic actuation of a thermodynamically stable colloid of ferromagnetic nanoparticles in a liquid crystal,” *Soft Matter*, vol. 12, pp. 6601–6609, 31 2016.
- [93] I. Appel, H. Nádasi, C. Reitz, *et al.*, “Doping of nematic cyanobiphenyl liquid crystals with mesogen-hybridized magnetic nanoparticles,” *Physical Chemistry Chemical Physics*, vol. 19, pp. 12 127–12 135, 19 2017.
- [94] I. Appel and S. Behrens, “Influence of the particle parameters on the stability of magnetic dopants in a ferrolyotropic suspension,” *Journal of Magnetism and Magnetic Materials*, vol. 431, pp. 49–53, 2017.
- [95] K. Koch, M. Kundt, A. Eremin, H. Nadasi, and A. M. Schmidt, “Efficient ferronematic coupling with polymer-brush particles,” *Physical Chemistry Chemical Physics*, vol. 22, pp. 2087–2097, 4 2020.
- [96] J. C. Jones and S. Beldon, “10.4: High image-content zenithal bistable devices,” *SID Symposium Digest of Technical Papers*, vol. 35, pp. 140–143, 1 2004.
- [97] J. Dalby, P. Farrell, A. Majumdar, and J. Xia, “One-dimensional ferronematics in a channel: Order reconstruction, bifurcations, and multistability,” *SIAM Journal on Applied Mathematics*, vol. 82, pp. 694–719, 2 2022.

Bibliography

- [98] K. Bisht, V. Banerjee, P. Milewski, and A. Majumdar, “Magnetic nanoparticles in a nematic channel: A one-dimensional study,” *Physical Review E*, vol. 100, 1 2019.
- [99] K. Bisht, Y. Wang, V. Banerjee, and A. Majumdar, “Tailored morphologies in two-dimensional ferronematic wells,” *Physical Review E*, vol. 101, p. 022 706, 2 2020.
- [100] G. Zarubin, M. Bier, and S. Dietrich, “A ferronematic slab in external magnetic fields,” *Soft Matter*, vol. 14, pp. 9806–9818, 48 2018.
- [101] Z. Brzezniak, E. Hausenblas, and P. Razafimandimby, “Some results on the penalised nematic liquid crystals driven by multiplicative noise: Weak solution and maximum principle,” *Stochastic Partial Differential Equations: Analysis and Computations*, 2019.
- [102] Z. Brzezniak, U. Manna, and A. Panda, “Large deviations for stochastic nematic liquid crystals driven by multiplicative gaussian noise,” *Potential Analysis*, 2019.
- [103] B. Guo, G. Zhou, and W. Zhou, “Asymptotic behavior of two-dimensional stochastic nematic liquid crystal flows with multiplicative noise,” *Journal of Mathematical Analysis and Applications*, vol. 496, p. 124 791, 1 2021.
- [104] A. De Bouard, A. Hocquet, and A. Prohl, “Existence, uniqueness and regularity for the stochastic ericksen–leslie equation,” *Nonlinearity*, vol. 34, p. 4057, 6 2021.
- [105] L. Wang, J.-L. Wu, and G. Zhou, “Global well-posedness of stochastic nematic liquid crystals with random initial and boundary conditions driven by multiplicative noise,” *Applied Mathematics & Optimization*, vol. 87, 2019.
- [106] G. J. Lord, C. E. Powell, and T. Shardlow, *An Introduction to Computational Stochastic PDEs*, ser. Cambridge Texts in Applied Mathematics. 2014.

Bibliography

- [107] L. C. Evans, *Partial Differential Equations*, 2nd ed., ser. Graduate studies in mathematics; v. 19. American Mathematical Society, 2010.
- [108] T. A. Davis and E. C. Gartland, “Finite element analysis of the landau-de gennes minimization problem for liquid crystals,” *SIAM Journal on Numerical Analysis*, vol. 35, pp. 336–362, 1 1998.
- [109] E. B. Priestly, P. J. Wojtowicz, and P. Sheng, “Introduction to liquid crystals,” Springer New York, NY, 1976.
- [110] A. Logg, K.-A. Mardal, and G. N. Wells, *Automated Solution of Differential Equations by the Finite Element Method: The FEniCS Book*. Springer, 2012.
- [111] Y. Han, A. Majumdar, and L. Zhang, “A reduced study for nematic equilibria on two-dimensional polygons,” *SIAM Journal on Applied Mathematics*, vol. 80, pp. 1678–1703, 4 Jul. 2020.
- [112] J. Yin, L. Zhang, and P. Zhang, “High-index optimization-based shrinking dimer method for finding high-index saddle points,” *SIAM Journal on Scientific Computing*, vol. 41, A3576–A3595, 2019.
- [113] *The Visualization Handbook*. Elsevier Butterworth-Heinemann, 2005.
- [114] J. W. Milnor, M. Spivak, and R. Wells, *Morse Theory. (AM-51), Volume 51*. Princeton University Press, 1963.
- [115] V. Hernandez, J. E. Roman, and V. Vidal, “SLEPc: A scalable and flexible toolkit for the solution of eigenvalue problems,” *ACM Transactions on Mathematical Software*, vol. 31, pp. 351–362, 2005.
- [116] H. Kusumaatmaja and A. Majumdar, “Free energy pathways of a multistable liquid crystal device,” *Soft Matter*, vol. 11, pp. 4809–4817, 24 2015.

Bibliography

- [117] S. P. Boyd and L. Vandenberghe, *Convex Optimization*. Cambridge University Press, 2004.
- [118] J. Butcher, *Numerical Methods for Ordinary Differential Equations*, 2nd ed. John Wiley & Sons, 2008.
- [119] J. Yin, Y. Wang, J. Z. Y. Chen, P. Zhang, and L. Zhang, “Construction of a pathway map on a complicated energy landscape,” *Physical Review Letters*, vol. 124, p. 090 601, 9 2020.
- [120] E. L. Rees, “Graphical discussion of the roots of a quartic equation,” *The American Mathematical Monthly*, vol. 29, pp. 51–55, 2 1922.
- [121] X. Lamy, “Bifurcation analysis in a frustrated nematic cell,” *Journal of Nonlinear Science*, vol. 24, pp. 1197–1230, 6 2014.
- [122] J. H. Noh, Y. Wang, H. L. Liang, V. S. R. Jampani, A. Majumdar, and J. P. F. Lagerwall, “Dynamic tuning of the director field in liquid crystal shells using block copolymers,” *Physical Review Research*, vol. 2, p. 033 160, 3 2020.
- [123] R. Irving, *Beyond the Quadratic Formula*, 1st ed. Mathematical Association of America, 2013.
- [124] A. Vats, S. Puri, and V. Banerjee, “Emergence of biaxiality in nematic liquid crystals with magnetic inclusions: Some theoretical insights,” *Physical Review E*, vol. 106, p. 044 701, 4 2022.
- [125] The MathWorks Inc., *MATLAB*, Version 23.2.0.2380103 (R2023b), 2023.
- [126] C. Morrey, *Multiple Integrals in the Calculus of Variations*. American Mathematical Society, 1964.
- [127] J. C. Butcher, *The Numerical Analysis of Ordinary Differential Equations: Runge-Kutta and General Linear Methods*. John Wiley & Sons, 1987.

Bibliography

- [128] L. Arnold, *Random Dynamical Systems*. Springer, 1998.
- [129] C. Feng, Y. Wu, and H. Zhao, “Anticipating random periodic solutions–ii. spdes with multiplicative linear noise,” *arXiv.org*, 2018.